NUREG/CR-0762
LA-7769-PR

Informal Report

IORA

Nuclear Reactor Safety

Quarterly Progress Report

October 1—December 31, 1978

University of California

LOS ALAMOS SCIENTIFIC LABORATORY
Post Office Box 1663 Los Alamos, New Mexico 87545

The four most recent reports in this series, unclassified, are LA-7195-PR, NUREG/CR-0062 LA-7278-PR, NUREG/CR-0385 LA-7481-PR, and NUREG/CR-0522 LA-7567-PR.

This report was not edited by the Technical Information staff.

This work was partially supported by the US Department of Energy, Division of Reactor Development and Demonstration.

NUREG/CR-0762
LA-7769-PR
Informal Report
R4, R7, and R8

Nuclear Reactor Safety

Quarterly Progress Report

October 1—December 31, 1978

Compiled by

James F. Jackson
Michael G. Stevenson

Manuscript submitted: March 1979
Date published: May 1979

Prepared for
Office of Nuclear Regulatory Research
Division of Reactor Safety Research
Office of Nuclear Reactor Regulation
Division of Systems Safety
US Nuclear Regulatory Commission
Washington, DC 20555

UNITED STATES
DEPARTMENT OF ENERGY
CONTRACT W-7405-ENG. 36

CONTENTS

CONTENTS (cont)

557 007

FIGURES

FIGURES (cont)

FIGURES (cont)

FIGURES (cont)

TABLES

TABLES (cont)

ABSTRACT

The LWR safety computer code, TRAC-P1A, was completed during this quarter. Considerable progress was also made toward the completion of the set of experimental assessment calculations that is to accompany the public release of the code. A very coarse-node LOCA calculation was performed on a U.S. PWR model using TRAC. This was the first step in a noding study that is part of an effort to reduce TRAC running times. The complete LOCA sequence was calculated with about 1 h or CDC-7600 CPU time. The results agreed surprisingly well with the initial phases of an earlier fine-node calculation.

A series of TRAC calculations were performed to determine the influence of several operational parameters on the transient behavior of the proposed Japanese Slab Core Test Facility. Preliminary calculations for the Japanese Cylindrical Core Test Facility were also performed. A posttest calculation of LOFT Test L1-5 was completed, as well as a pretest prediction of the first LOFT nuclear test, L2-2. Comparisons of the calculated results with the experimental data are presented.

A numerical study of scale effects on ECC bypass was performed with the K-TIF code. A new momentum exchange formulation was implemented into K-TIF that accurately predicts the results from several CREARE bypass experiments. The SOLA-SPRAY code for analyzing dispersed droplet flow was improved by including compressibility and phase change effects. Finally, a seismic response capability was added to the SOLA-FLX code.

SIMMER LMFBR disrupted core analysis code development and applications work reported in this quarter includes improvements in the analytic equation-of-state and in the pressure and component density solution iteration technique. Mechanistic analyses of transition phase dynamics and calculations of above-core structure behavior are reported. SIMMER testing and verification work reported includes analyses of UKAEA COVA and SRI International bubble expansion experiments and of Sandia (PBE-SG2) and ANL (AX-1) in-pile experiments investigating carbide fuel behavior under rapid transient conditions. Also in the LMFBR area, development and testing of the LAFM code continued, and a significant nonprototypical failure mechanism was discovered in low ramp rate TOP fuel failure tests carried out in static capsules.

In the HTGR safety research work, the last in a series of one-dimensional core block system model seismic response tests was completed. The final version of the NONSAP-C finite element concrete structural analysis code was released to the BNL and ANL code libraries. Full system test analyses with the CHAP Ft. St. Vrain and large HTGR system response models were performed.

Work continued in the design, fabrication, and analysis of the GCFR core disruptive test program. Postmortem analysis of the FLS 1 test indicated that 18 of the 34 rods failed.

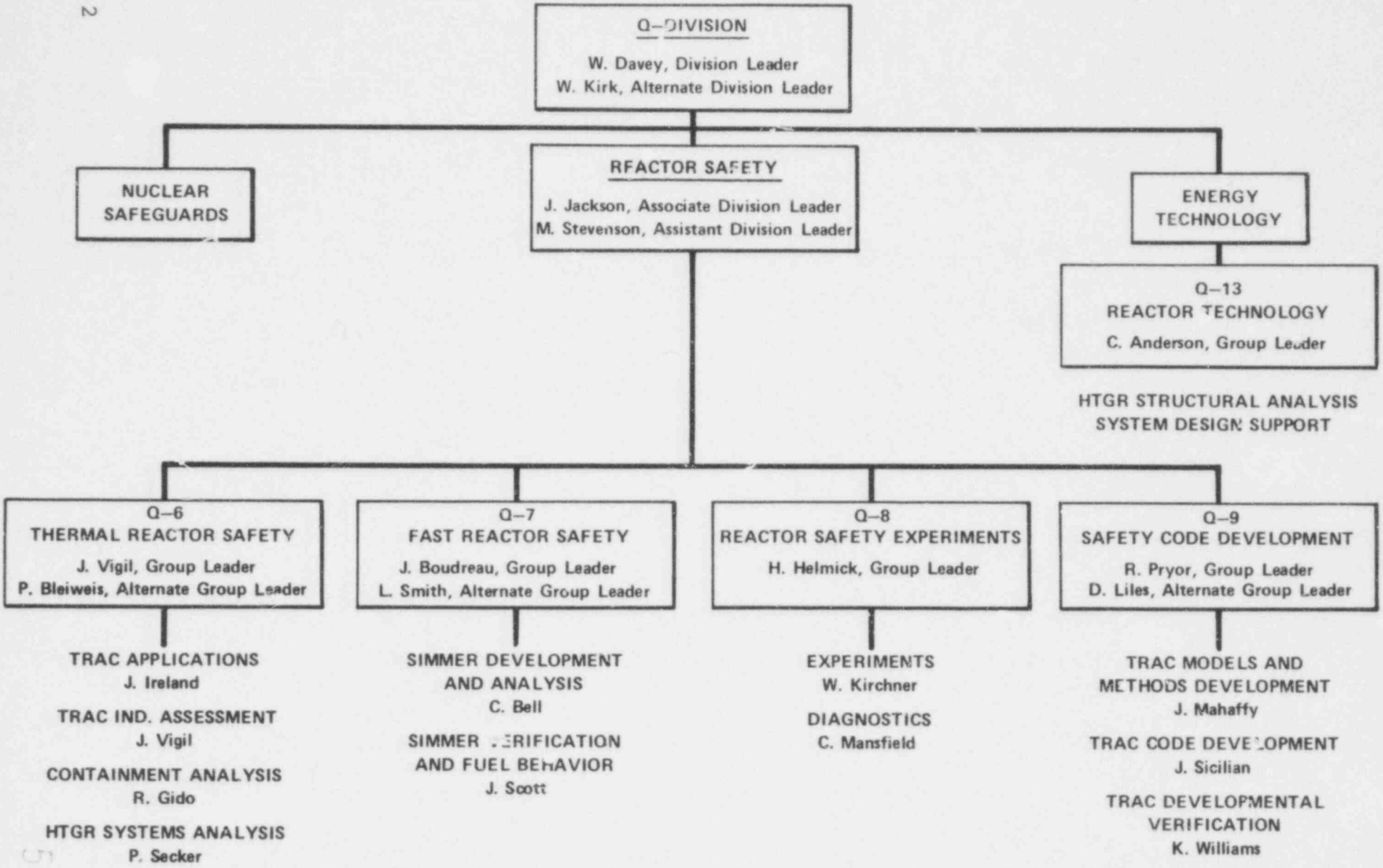

Fig. 1. Q-Division Reactor Safety Organization Chart (March 1979).

NUCLEAR REACTOR SAFETY

Compiled by

James F. Jackson
and
Michael G. Stevenson

I. INTRODUCTION

(J. F. Jackson and M. G. Stevenson, Q-DO)

This quarterly report summarizes technical progress from a continuing nuclear reactor safety research program conducted at the Los Alamos Scientific Laboratory (LASL). This research effort concentrates on providing an accurate and detailed understanding of the response of nuclear reactor systems to a broad range of postulated accident conditions. The bulk of the funding is provided by the U.S. Nuclear Regulatory Commission (NRC), with part of the advanced reactor work funded by the U.S. Department of Energy (DOE).

The report is mainly organized according to reactor type. Major sections deal with Light Water Reactors (LWRs), Liquid Metal Fast Breeder Reactors (LMFBRs), High-Temperature Gas-Cooled Reactors (HTGRs), and Gas-Cooled Fast Reactors (GCFRs).

The research discussed was performed by several divisions and groups within LASL. The names and group affiliations of the individual staff members responsible for the work are given at the beginning of each section. Most of the work was performed in the reactor safety portion of the Energy (Q) Division. An organization chart showing the groups with major reactor safety activities is presented on the facing page (Fig. 1). It reflects the formation of a new group, Q-9, and indicates the people responsible for key

technical areas. Other divisions contributing to the program were the Theoretical (T) Division, Computer Science and Services (C) Division, the Systems, Analysis, and Assessment (S) Division, and the Dynamic Testing (M) Division.

II. LWR SAFETY RESEARCH

(J. F. Jackson, Q-DO)

Three of the major projects in LASL's light water reactor safety research program are reported in this section. The first is the development, testing against experimental data, and application of the Transient Reactor Analysis Code (TRAC). The second involves thermal-hydraulic research in key problem areas of importance to water reactor safety. The third is an experimental program that supports model development activities and investigates new instrumentation techniques for safety experiments.

A. TRAC Code Development and Assessment

(R. J. Pryor, Q-9)

TRAC is an advanced, best estimate computer program for the analysis of postulated accidents in LWRs. It features a nonhomogeneous, nonequilibrium, multidimensional fluid dynamics treatment; detailed heat transfer and reflood models; and a flow-regime-dependent constitutive equation package to describe the basic physical phenomena that occur under accident conditions. It calculates initial steady-state conditions and complete accident sequences in a continuous and consistent manner.

The first version of TRAC, called TRAC-P1, is primarily directed toward loss-of-coolant accidents (LOCAs) in pressurized water reactors (PWRs). A refinement of this version, called TRAC-P1A, will be released through the National Energy Software Center (NESC) in February. Later versions of the code will treat boiling water reactors (BWRs) and provide capabilities for Anticipated Transients Without Scram (ATWS), Reactivity Insertion Accident (RIA), and operational transient analyses.

As part of a closely coupled code assessment effort, TRAC is being applied to a broad range of water reactor safety experiments. These experiments are designed to study separate and integral effects that occur during all phases of a LOCA. TRAC posttest calculations are compared with experimental results to evaluate the

thermal-hydraulic models in the code. Pretest calculations are made to test the predictive capability of TRAC. Both types of analyses are in progress and will continue to receive increased emphasis.

During the past quarter, progress was made on several fronts. Most importantly, TRAC version P1A was completed. In preparation for the release of TRAC-P2 later this year, progress was made on the addition of a droplet field. Also, improvements were made to the HORSE maintenance program and the TRAC graphics processor. Finally, a number of developmental assessment calculations were performed in preparation for the release of TRAC-P1A.

1. Fluid Dynamics and Heat Transfer Methods

(D. R. Liles, Q-9)

The quarterly progress consisted of the development of an implicit heat transfer coupling procedure and work on implementing the FRAP[1] nuclear fuel rod code at the LASL computing facility. In addition, work proceeded on debugging the droplet field for inclusion in TRAC version P2. Additional effort was placed on improving the reflood heat transfer and in developing a two-fluid, one-dimensional model for future TRAC versions.

a. Implicit Heat Transfer Calculation

(F. L. Addessio, Q-9)

The conduction calculation in the reactor vessel and the loop components is being modified to allow for an implicit coupling with the fluid dynamics computations. This effort has been undertaken to eliminate possible numerical instabilities when the calculational time step sizes are increased.

The coupling of the conduction solution and the fluid dynamics occurs as a result of the wall heat transfer terms in the energy equation. Such terms were formerly written as

$$q_w = h^n A \left(T_w^n - T_f^{n+1} \right) , \qquad (1)$$

where the superscripts denote the time levels and the subscripts indicate wall and fluid properties, respectively. An implicit coupling is obtained by defining the wall temperature at the new

time level, i.e.,

$$q_w = h^n A \left(T_w^{n+1} - T_f^{n+1} \right) . \tag{2}$$

An expression for the wall surface temperature (T_w^{n+1}) is derived from a heat transfer analysis of the wall. From the finite difference form of the conduction equation, a vector equation for the temperature distribution in the wall may be expressed in the form

$$A \vec{T}_w^{n+1} = \vec{B} + \vec{C} \, \delta T_f , \tag{3}$$

where $\delta T_f = T_f^{n+1} - T_f^n$. Multiplying by the inverse of A provides the wall temperature distribution in terms of the fluid temperature

$$\vec{T}_w^{n+1} = \vec{D} + \frac{\partial \vec{T}_w}{\partial T_f} \delta T_f . \tag{4}$$

The wall surface temperature dependance on the fluid temperature is extracted from the above equation. It is this relation that may then be used in the wall heat transfer expression [Eq. (2)] for the fluid dynamics calculations.

The technique which was developed to accomplish an implicit coupling between the heat transfer and fluid mechanis computations may be summarized as follows.

1. A wall conduction analysis is performed to obtain an expression for the wall temperature in terms of the fluid temperature for each cell [Eq. (4)].

2. Using this expression for T_w^{n+1} in the energy Eq. (2), the fluid dynamics equations are solved, resulting in a solution for T_f^{n+1}.

3. With the fluid temperature known, the conduction Eq. (3) is used to obtain the wall temperature distribution $\vec{T}_w^{n+1}$.

b. Steam Generator Modifications

(F. L. Addessio, Q-9)

The initial formulation of the U-tube-type steam generator module in TRAC was based on the assumption that the heat transfer coefficients for the up and down tubes in a given cell are equal. This simplification has now been eliminated.

A consequence of this modification is a change in the definition of the effective wall temperature ($\hat{T}_w$) and heat transfer coefficient ($\hat{h}$) used in the fluid dynamics calculations for the secondary fluid cells. By using a simple energy balance (e.g., consider secondary cell 5 in Fig. 2):

$$\hat{h}_5 \; 2A\left(\hat{T}_{w5} - T_f\right) = h_6 \; A\left(T_{w6} - T_f\right) + h_7 \; A\left(T_{w7} - T_f\right), \tag{5}$$

the effective values may be readily determined,

$$\hat{h}_5 = 0.5(h_6 + h_7), \tag{6}$$

and

$$\hat{T}_{w5} = \left(h_6 \; T_{w6} + h_7 \; T_{w7}\right) \Big/ \left(h_6 + h_7\right) . \tag{7}$$

A similar expression applies for the effective rate of change of the wall temperature necessary for the implicit computations, i.e.,

$$\left(\frac{\partial \hat{T}_w}{\partial T_F}\right)_5 = \left[h_6 \left(\frac{\partial T_w}{\partial T_f}\right)_6 + h_7 \left(\frac{\partial T_w}{\partial T_F}\right)_7\right] \Big/ (h_6 + h_7) . \tag{8}$$

c. Gap Conductance

(D. A. Mandell and J. M. Silician, Q-9)

The present gap conductance model in the TRAC code assumes that the fuel-clad gap is a constant.[2] Since the stored energy, which is significantly influenced by the gap conductance, has an important influence on the peak clad temperature,[3] more detailed fuel rod models are being examined.

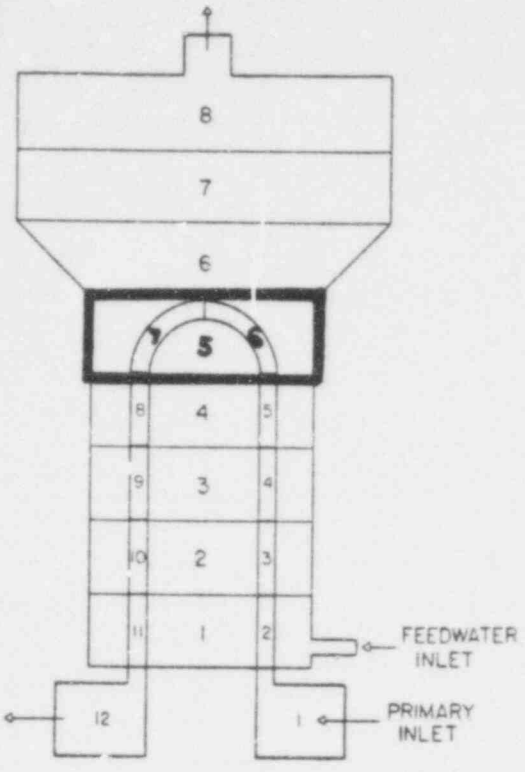

Fig. 2. U-tube-type steam generator geometry in TRAC.

A number of options exist for implementing a more detailed fuel mechanical model in the TRAC code. Separate codes, such as FRAP-S3[4] and FRAP-T4[4] could be coupled to TRAC as was done with RELAP.[5] A concern in this approach would be the possibility of substantially increased computer running times. With FRAP-T coupled to RELAP, experience has shown that the running times are only slightly increased for typical calculations, however.[6]

A second option is to remove specific subroutines from FRAP-T and put them into TRAC. This results in complicated coding and does not take full advantage of the extensive experimental assessment of FRAP-T.

A third option is to initialize the gap conductance calculation by using the steady-state version of FRAP, or a similar code, and then use a simplified transient model as is done in the CHASTE code.[7] Here again, one would have to consider an extensive independent experimental assessment activity.

In order to better understand the models and methods used in the FRAP codes, these codes were obtained from the Idaho National Engineering Laboratory (INEL). Problems were encountered in implementing FRAP-S3 and FRAP-T4 on the LASL CDC-7600 due to differences in the LASL and INEL computer operating systems. The INEL system has more small core memory (SCM) and in order to run FRAP-S3 at LASL, it was necessary to separate the main program into several parts and use overlays. FRAP-S3 is now running at LASL and the test cases give identical results to those obtained at INEL.

FRAP-T4 is considerably larger than FRAP-S3 (FRAP-T4 is slightly smaller than TRAC) and uses the CDC segmented loader

system at INEL. This system is not commonly used at LASL (overlays are used) and it is necessary to use the LASL SLOPE2 interface in order to use segments.[8] The FRAP-T segmented structure cannot be converted to an overlay structure without making major changes to the code structure. Since the SLOPE2 system uses part of SCM and due to other system differences, it was necessary to reduce the size of FRAP-T. This was done by placing the RESTART common in large core memory (LCM). After reducing the size of FRAP-T, it was found that an error exists in either the LASL segmented loader or in the SLOPE2 system. This error is now being investigated.

2. TRAC Code Development

(J. M. Sicilian, Q-9)

Programming of TRAC-P1A was completed this quarter. This version of TRAC will be released to the public upon completion of a set of assessment problems. Testing of the improved TRAC graphics postprocessor and the HORSE code maintenance program was completed. Also, an investigation of TRAC Central Processor Unit (CPU) utilization was begun and preliminary results obtained.

a. Completion of TRAC-P1A

(J. M. Sicilian, Q-9)

Programming of TRAC-P1A was completed this quarter. Numerous model improvements and programming advances have been implemented and the assessment process was initiated for this version. The program, together with sample problems, will be released to the NESC once assessment is completed. A draft of the first volume of the TRAC-P1A manual has been completed and is being brought into final form.

Significant programming improvements incorporated into TRAC-P1A this quarter include the addition of information to the dump file for consistent problem restarts, the addition of a short edit, and the removal of all nonstandard CDC FORTRAN statements.

b. TRAC Graphics Postprocessor Testing

(J. C. Ferguson, Q-9)

A special update library was made for the TRAC code so it can produce graphics output files which can be utilized by the

improved graphics postprocessor, TRCPLOT. A file format conversion program, CONVERT, was also written to improve the overall efficiency of the graphics package. The full system of programs, TRAC - CONVERT - TRCPLOT, has been tested using the U.S. PWR sample problem and was made available to LASL users. The update library will be permanently incorporated into the standard TRAC code once version TRAC-P1A has been released.

c. HORSE Code Improvements

(R. P. Harper, Q-9)

The new version of HORSE, which permits simultaneous development of multiple TRAC versions has been completed and the TRAC library files converted to a new format. These changes are presently being tested and will be implemented once TRAC-P1A is released. Conversion of associated programs to the new file format has begun and will improve programmer efficiency when completed.

d. TRAC CPU Utilization Study

(I. F. Weeks, Q-9)

Specialized techniques available on LTSS have been applied to investigating the CPU utilization of the current TRAC code. Preliminary results suggest that CPU utilization is not concentrated at specific locations within TRAC, although it shows that the handling of large argument lists is a major source of TRAC execution cost. Confirmation of these results is being pursued and plans for dealing with large argument lists are being considered.

3. TRAC Code Assessment

(K. A. Williams, Q-9)

The primary accomplishment of this quarter's code assessment effort was the pretest prediction and posttest analysis of the first LOFT Nuclear Test L2-2. Several calculations of the LOFT-L1-5 test were also performed to prepare for the L2-2 blind prediction, as well as to aid in interpreting the results. All of the calculations are reported in Sec. II.C, below.

TRAC-P1A is being used for the final recalculation of the code assessment problems to be included as part of the code documentation.

Selected results are reported for Standard Problem 5 (SP5), a Semiscale heated blowdown test, and for the Edwards unheated pipe blowdown experiment.

In addition, analyses of several tests from the new Semiscale MOD 3 facility were initiated. In particular, test S-07-6, a heated blowdown through reflood has been calculated out to 120 s. The main objective of this calculation was to ascertain if TRAC can predict the long-term (about 110 s) oscillations that were experimentally measured after reflood. These results will be reported in the next quarterly.

a. TRAC-P1A Analysis of SP5

(J. K. Meier, Q-9)

A recalculation of SP5 was performed as a part of the developmental assessment of TRAC-P1A. Some preliminary results of this calculation are presented below; a more complete discussion will be included in the TRAC-P1A Users Manual, Vol. II.

A comparison of calculated hot- and cold-leg break mass flow rate with test data is presented in Figs. 3 and 4. Both the calculated hot- and cold-leg break mass flow rates agree well with the test data. In Fig. 5, the predicted mass flow rate through the pump (intact loop) is also seen to agree well with the test data.

Figure 6 compares the lower plenum pressure calculated by TRAC with SP5 test data. The code does an excellent job of matching the test until 10 s after the rupture. At this time, heat transfer and thermocouple data from the test indicate that the core dries out and the vapor within it superheats. This superheating causes a decrease in the rate of pressure decay. Since TRAC calculations do not exhibit as much superheating of the vapor during this time period, the prediction of lower plenum pressure continues to decay. Further study of this situation is now in progress.

A comparison of the rod temperature at the high power elevation in the core is shown in Fig. 7. Since there are a number of thermocouples at this elevation, an upper and lower limit is presented for the test data. The largest divergence between the test data and the code predictions occurs just after 10 s, the times at which the semiscale core superheats. At later times, the TRAC

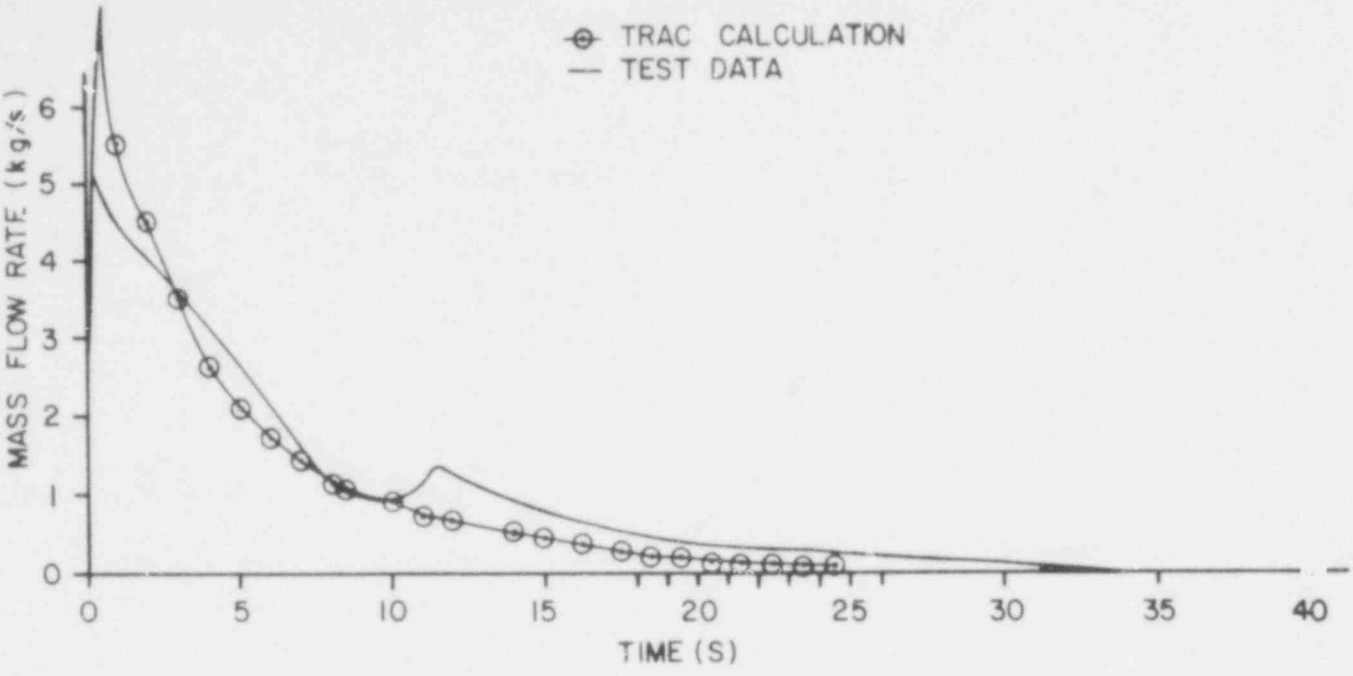

Fig. 3. Standard Problem 5: Hot-leg mass flow rate based on FDB-42, GB-42.

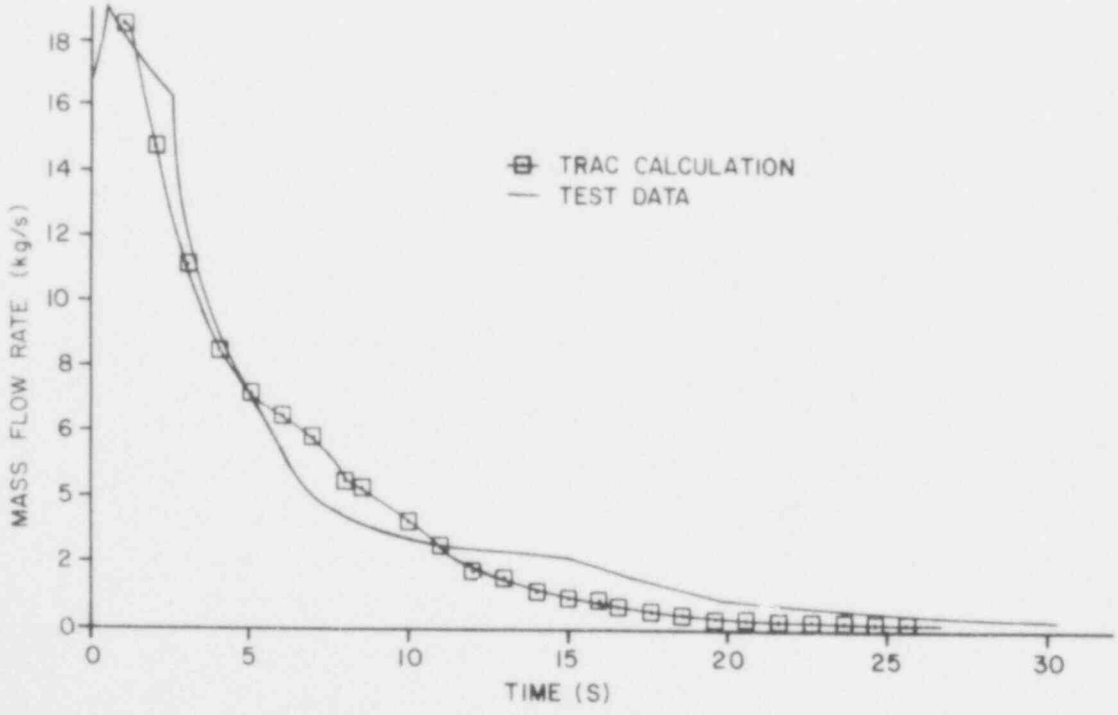

Fig. 4. Standard Problem 5: Cold-leg mass flow rate on FTB-21, GB-21VR).

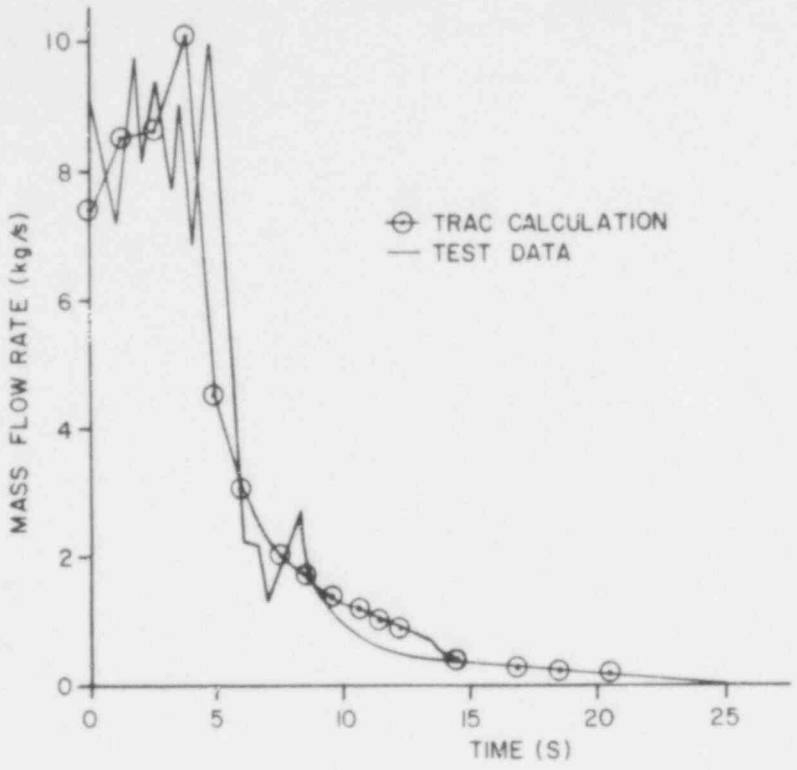

Fig. 5. Standard Problem 5: Pump inlet mass flow rate based on FDU-10, GU-10.

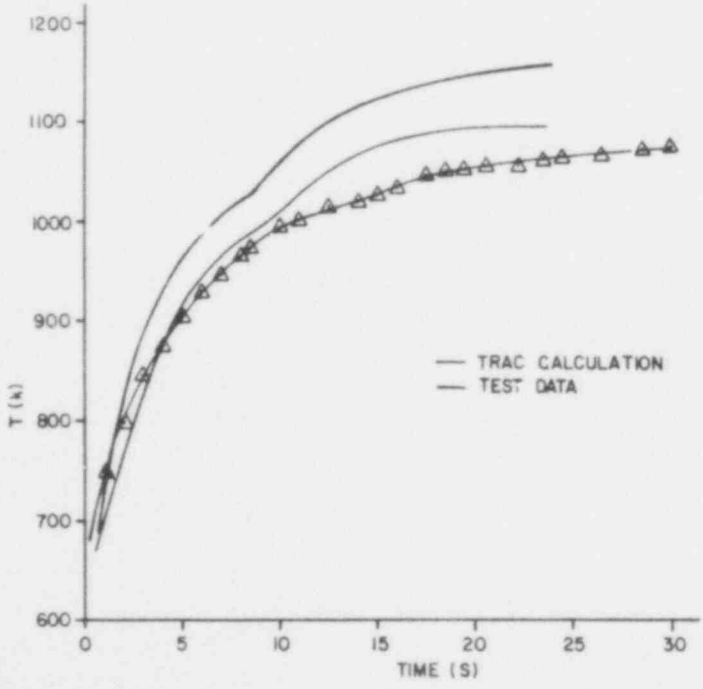

Fig. 6. Standard Problem 5: Experimental lower plenum pressure.

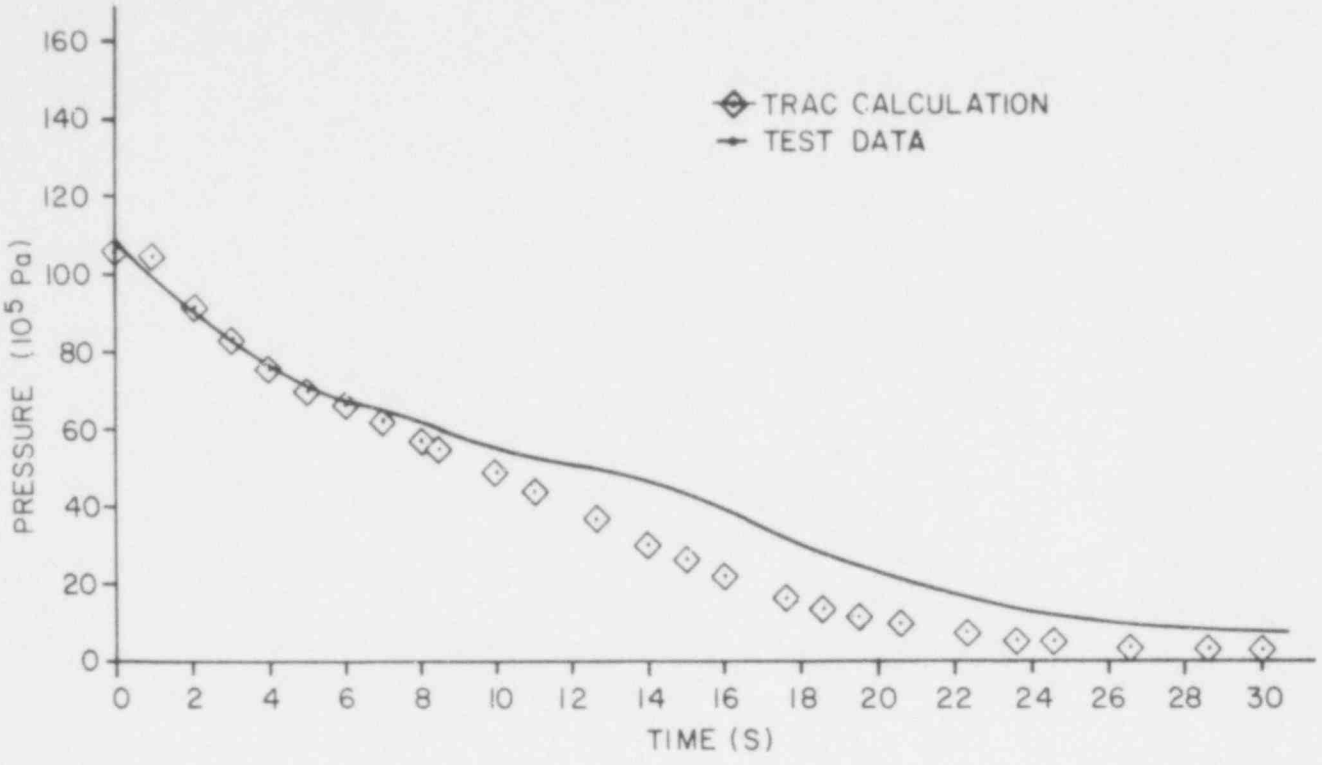

Fig. 7. Standard Problem 5: Band of experimental cladding temperatures at 22-26 in. elevations.

results converge on the test data until the difference is less than 20 K at 30 s after rupture.

b. TRAC-P1A Analysis of Edwards Blowdown Experiment

(J. S. Gilbert, Q-6)

The Edwards horizontal pipe blowdown experiment studied depressurization phenomena of initially nonflowing subcooled water[9] and was Reactor Safety Research (RSR) Standard Problem 1 (SP1). This problem has been recently recalculated in preparation for the code assessment volume to be included with the TRAC-P1A release documentation. The experimental apparatus consisted of a straight steel pipe 4.096 m in length and 0.073 m in internal diameter and was filled with demineralized water. A hydraulic pump and a control valve regulated the pressure in the system. Air in the pipe was evacuated with a vacuum pump before filling the pipe with water. Prior to rupturing the glass disk, the pipe was isolated from the supply tank, thus preventing the discharge of cold water into the pipe during blowdown. Pressure and temperature

transducers were located at gage stations GS-1 to GS-7 (see Fig. 8). Also provided at GS-2 and GS-5 were two diametrically opposed aluminum alloy disks for transient void fraction measurements using an x-ray absorption system. The pipe was heated electrically using heaters formed to the curvature of the pipe and was insulated with asbestos insulation. The temperature variation along the pipe was limited by adjustment of the voltage control for each heater. The system was brought to an initial approximately isothermal temperature of 515 K and initial pressure of 7 MPa. Once the isolating valve between the pipe and the storage tank closed, the glass disk was ruptured and the data were automatically recorded.

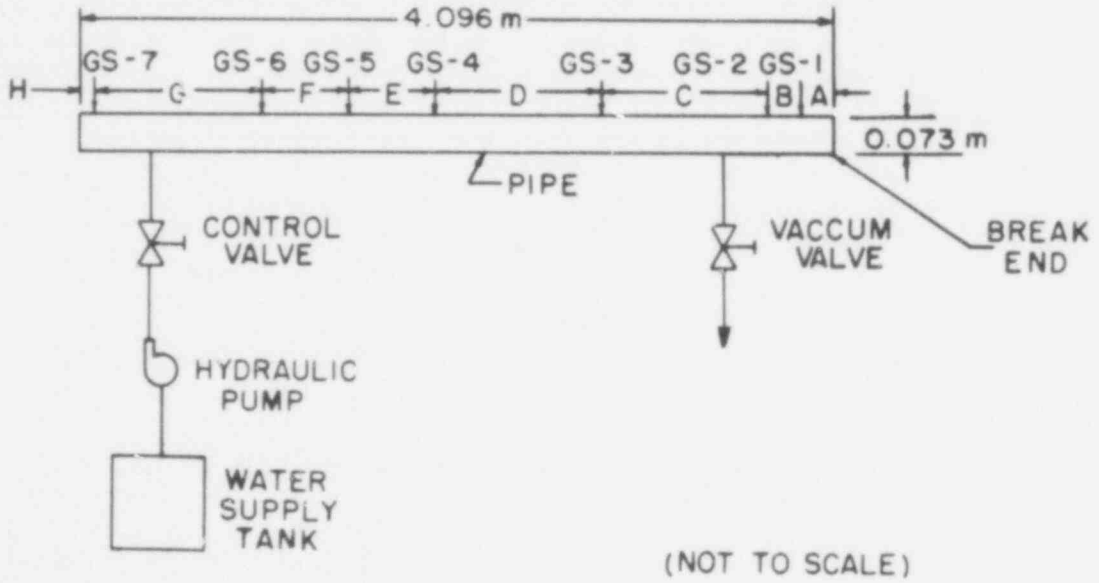

DIMENSION	m
A	0.168
B	0.158
C	0.835
D	0.911
E	0.555
F	0.555
G	0.835
H	0.079

Fig. 8. Schematic of Edwards horizontal pipe blowdown experiment adapted from Ref. 9.

The TRAC-P1A model of the Edwards experiment consists of four components (a fill, two PIPES, and a BREAK) coupled in series. The system is a straight horizontal pipe except for an abrupt area change at the exit. The two pipe components are subdivided into 46 fluid cells. The noding given in Fig. 9 was determined by performing a noding sensitivity study. Based on a parametric study the annular flow friction factor correlation option (NFF=4) was used.[10] An additive loss coefficient (FRIC=1.436) was used for the exit flow cell to account for form losses at the break due to two-dimensional effects which cannot be treated with the one-dimensional model.

Since the initial conditions were uniform pressure, approximately uniform temperature, and zero flow velocity, no steady-state calculations were required. Because the temperature distribution along the pipe may have varied as much as 9 K an adjusted temperature distribution was used as suggested by Garner.[11] Due to the reduced flow area at the break, the cell sizes were decreased along the pipe in the direction of the break. The consequences of various cell sizes near the break were studied. The selected cell length of 0.005 m at the break is 1/25 of the cell length at the closed end of the pipe.

Calculations were performed with the 5 different friction factor correlation options (NFF = 1, 2, 3, 4, and 5) in TRAC. These results were generally bracketed by the annular flow friction factor (NFF=4) which yielded maximum pressures and the CISE friction factor (NFF=3) which yielded maximum pressures throughout the pipe. Friction factor option, NFF=4, was chosen for the study since it agreed better with the data.

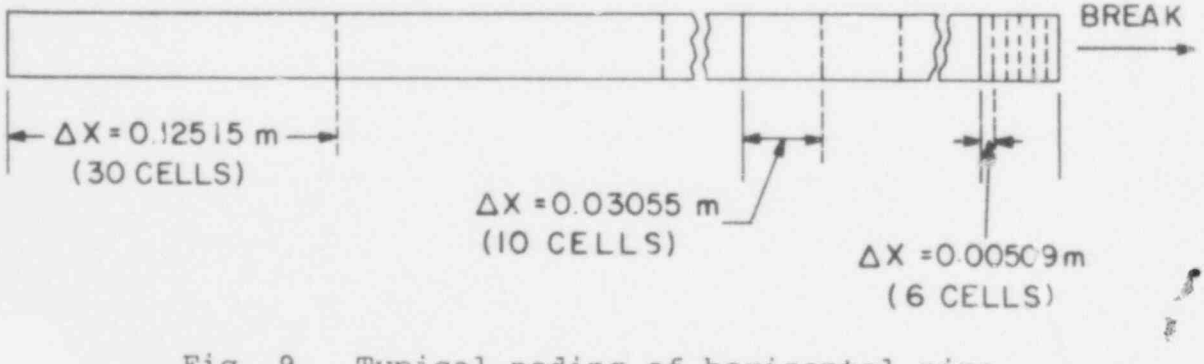

Fig. 9. Typical noding of horizontal pipe.

When the glass disk was ruptured some of the glass was retained around the circumference of the disk support assembly, thereby reducing the discharge area by 10-15%. To model this flow, areas of 60, 70, 85, 87, and 90% at the break were studied. To approximate the actual flow area (the vena contracta), the 60 and 70% flow areas were studied first. With these two cases, the pressures were significantly higher than the experimental data. For the 85, 87, and 90% flow area cases, only minor increases in pressure occurred. The nominal value of 87% was selected.

The calculated pressure comparison with experimental results at GS-5 is typical of all gage stations (see Fig. 10). The following observations apply to all the pressure results. From 0.0 to 0.2 s the maximum variations between calculated and experimental pressures are +0.4 MPa to -0.2 MPa. During the mid-range of the transient, 0.2-0.4 s, a faster rate of depressurization was predicted than observed. The maximum difference was -0.8 MPa at 0.25 s for GS-6. For the balance of the transient, 0.4-0.6 s, the calculated results were in good agreement with the experimental results. Experimental error bar information was not available; however, a deviation of ± 0.3 MPa was suggested.[11] In summary, agreement between calculated pressure and experimental data for all pressures is good during the first and last one-third of the transient.

In Fig. 11, a temperature comparison is made at GS-5 with the only available temperature data. The plotted temperature is the liquid temperature. After 0.2 s, the calculated saturation, liquid, and vapor temperatures are equal. At 0.4 s, the calculated value is approximately 30 K below the experimental data.

The comparison in Fig. 12 between calculated and measured void fraction is fair from 0.0-0.3 s and good after 0.3 s. Note that the void fraction is greater than 0.9 after 0.3 s. The difficulty in measuring void fraction using the x-ray absorption technique partially explains deviations between the calculated curve and the experimental data.

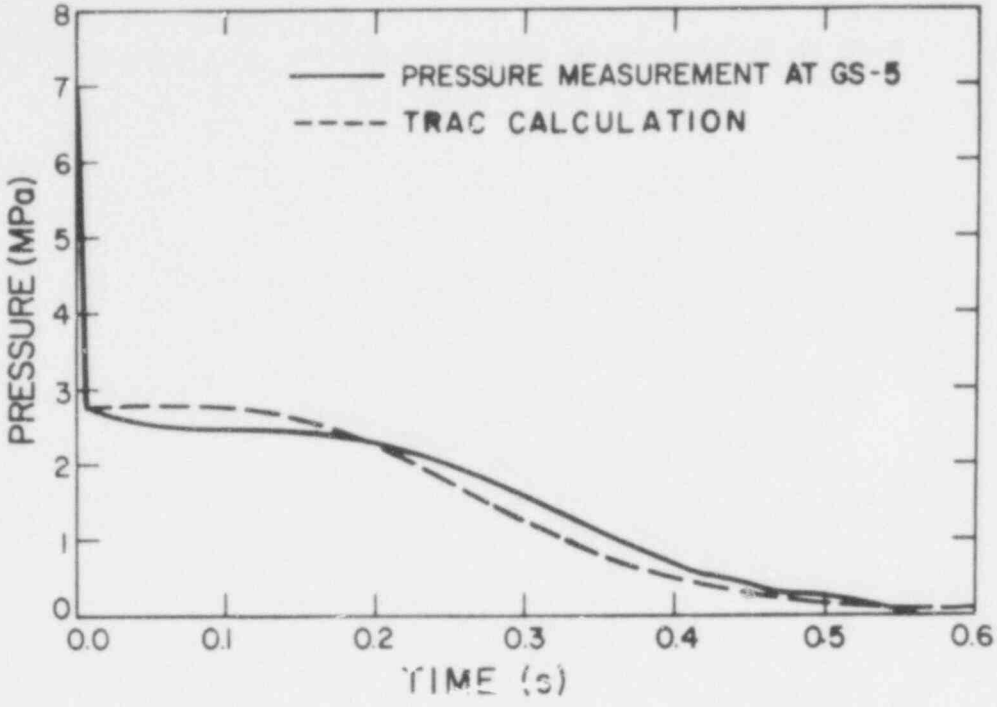

Fig. 10. Calculated and experimental fluid pressure for Edwards blowdown experiment at location GS-5.

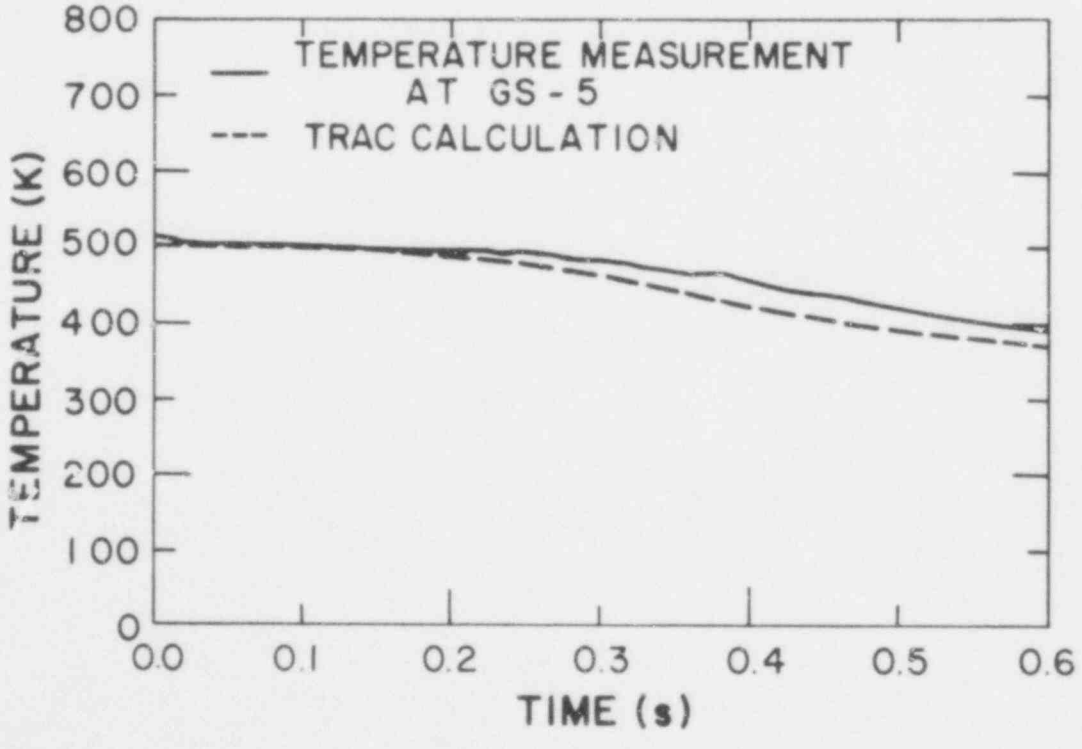

Fig. 11. Calculated and experimental fluid temperature for Edwards blowdown experiment at location GS-5.

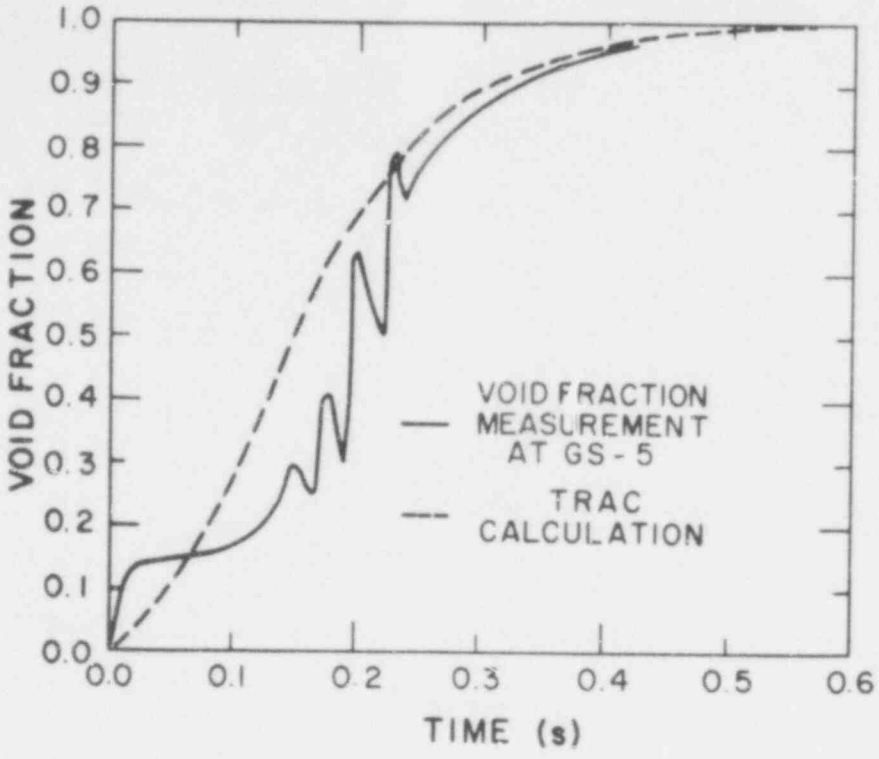

Fig. 12. Calculated and experimental void fraction for Edwards blowdown experiment at location GS-5.

In summary, the Edwards problem provided assessment of the TRAC-P1A analytical features for a simple blowdown experiment without heat transfer. In general, agreement was good between calculated results and experimental data. A complete comparison between experimental measurements and the calculation, as well as the results of the sensitivity study, will appear in the TRAC-P1A documentation.

B. TRAC Applications

(J. C. Vigil and P. B. Bleiweis, Q-6)

The work described in this section includes the application of TRAC to full-scale LWR transients and to the planned large-scale German and Japanese 2D/3D experiments. In general, these applications are used to help with the planning, coordination, and analyses of the experiments by providing design assistance, pretest

predictions, and posttest analyses. TRAC applications to the experiments also help validate the code for use on full-scale LWR systems. Applications of TRAC to full-scale LWR systems provide best estimate predictions of the consequences of postulated transients. In addition to the above activities, TRAC is being used to analyze a variety of other tests and problems for NRC and outside users.

The TRAC noding model and steady-state calculation of a typical German PWR, which includes both hot- and cold-leg emergency core cooling (ECC) injection, were completed during the quarter and the transient calculation was begun. A TRAC noding sensitivity study was also initiated. As part of this study, the typical U.S. PWR model reported previously[12] was renoded very coarsely and results obtained with this coarse model were compared with a recalculation (using the same TRAC version) of the more finely noded PWR. Analysis work for the 2D/3D program continued with a variety of Slab Core Test Facility (SCTF) design assistance calculations to determine the sensitivity of the current SCTF design to initial containment and vessel liquid levels, valve opening times, and ECC delay times. Finally, based on the results of the first TRAC simulation of the Japanese Cylindrical Core Test Facility (CCTF),[13] an improved calculation was performed and the results are reported below.

1. Typical German PWR TRAC Model and Steady-State Results

(J. R. Ireland, Q-6)

A steady-state calculation for a four-loop German PWR was completed and a LOCA transient was initiated. The TRAC model for this system was revised from that reported previously[14] and is shown in Fig. 13. The hot legs were modified to model the hot-leg injection system more accurately by using zero-angle tees. This modification reduced the number of connections to the vessel. Figure 14 shows the new vessel noding. In addition to the above modifications, the ECC system was deleted from the broken cold leg for a more accurate representation of a best estimate calculation. This new noding scheme results in 59 components and 62 junctions for a total of about 800 TRAC cells.

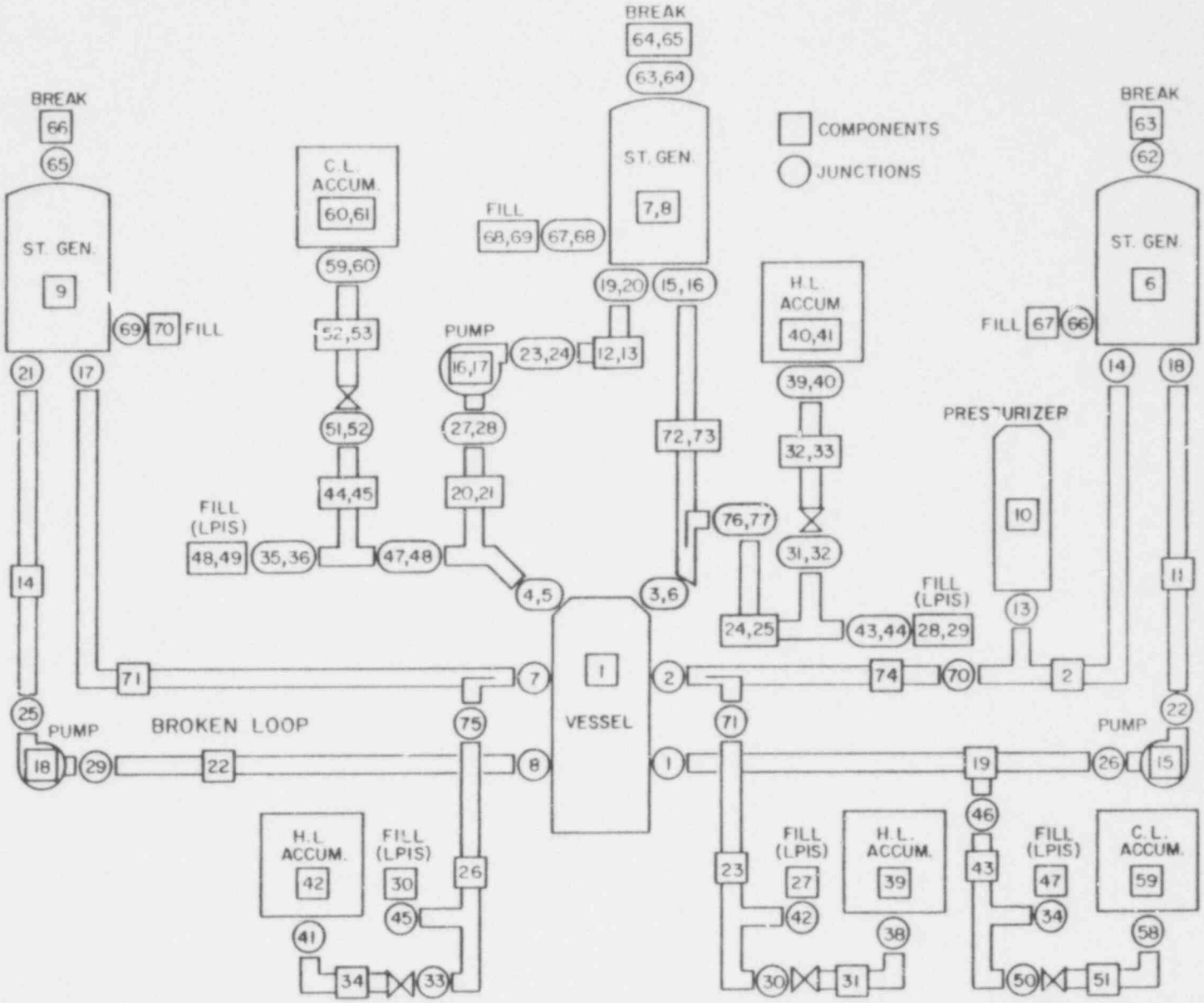

Fig. 13. German PWR schematic.

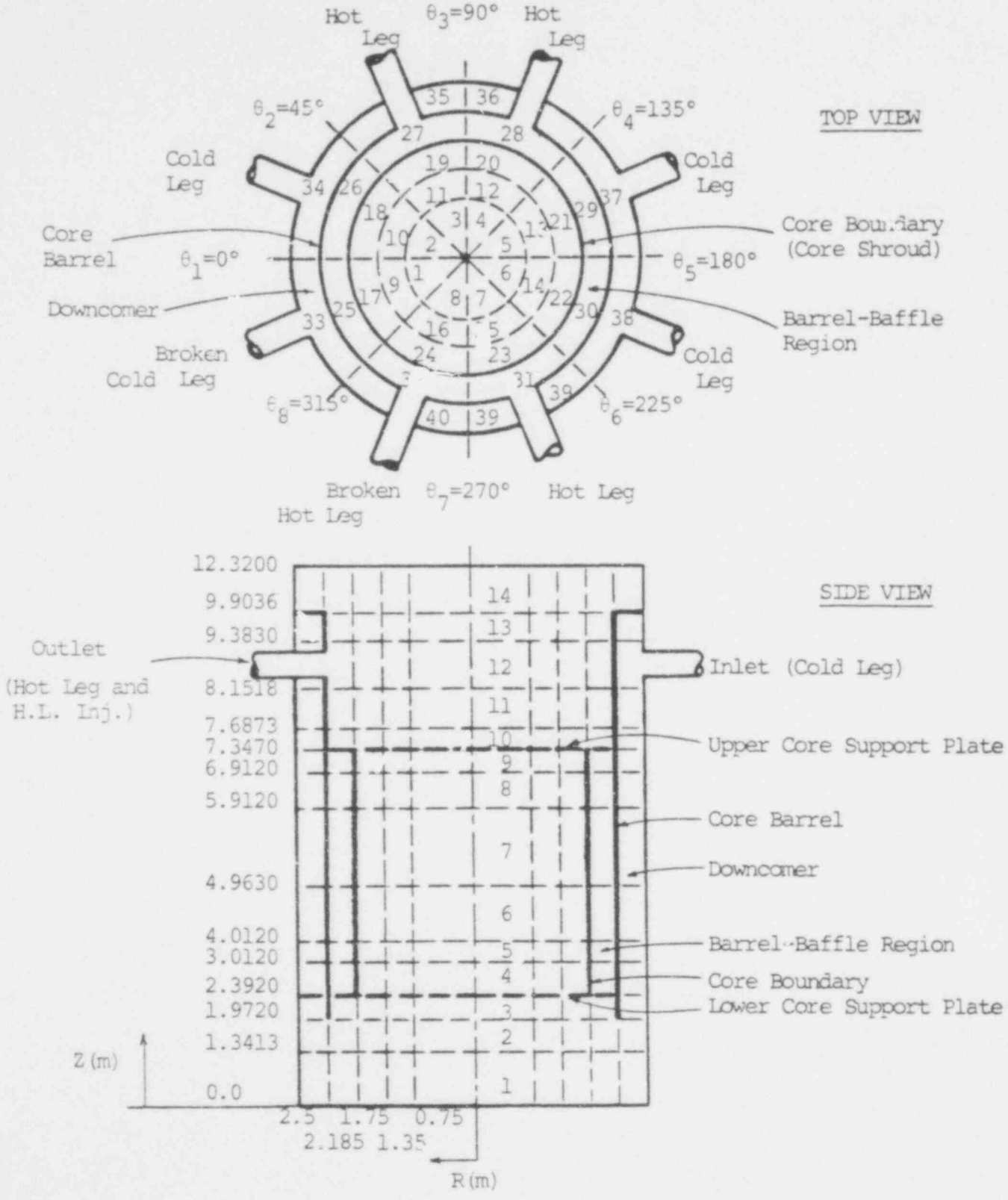

Fig. 14. TRAC noding for German PWR vessel.

Based on the geometry and noding described above, a steady-state calculation was performed using the generalized steady-state option in TRAC. Due to the complexity of the system, 300 s of reactor time were required for the velocities, temperatures, and pressures throughout the system to converge to a steady state.

Table I shows some of the important input and calculated steady-state parameters from the calculation. The inlet-to-outlet coolant temperature rise of 36.7 K is very close to the design value and the other steady-state parameters appear to be quite reasonable. Using these steady-state results, a 200%, double-ended, cold-leg break was initiated in component #22 (Fig. 13) 6.0 m from the vessel. This calculation is continuing and will be reported in detail next quarter.

TABLE I

GERMAN PWR INPUT AND STEADY-STATE INITIAL CONDITIONS

Parameter	Value
Initial Power	3.765×10^9 W
Relative Axial Power Shape (4 levels-bottom to top)	0.532 5, 1.121 4, 1.121 4, 0.532 5
Relative Radial Power Shape (average-center to core shroud)	1.137 2, 1.108 0, 0.861 6
Core Average Linear Power	2.11×10^4 W/m
Peak Rod Linear Power	2.90×10^4 W/m
Hot Rod Linear Power	3.90×10^4 W/m
Pump Speed (each)	135 rad/s
Pump Suction Side Pressure (av)	$1.540\ 2 \times 10^6$ Pa
Pump Discharge Side Pressure (av)	$1.582\ 8 \times 10^7$ Pa
Cold-Leg Temperature at Vessel Inlet (av)	546.6 K
Hot-Leg Temperature at Vessel Outlet (av)	601.3 K
Cold-Leg Pressure at Vessel Inlet (av)	$1.582\ 3 \times 10^7$ Pa
Hot-Leg Pressure at Vessel Outlet (av)	$1.561\ 1 \times 10^7$ Pa
Total Primary System Flow Rate (4 loops)	$1.931\ 3 \times 10^4$ kg/s
Steam Generator Secondary Side Average Pressure	6.9×10^6 Pa

TABLE I (cont)

Parameter	Value
Steam Generator Secondary Side Total Flow Rate (4 loops)	$1.068\ 08 \times 10^4$ kg/s
Cladding Surface Temperatures at Core Level 3 (average rod for each of 3 radial rings - center-to-core shroud)	626.7, 626.7, 612.7 K
Total System Water Mass	7.03×10^5 kg
Accumulator Setpoint	26.0×10^5 Pa
Low Pressure Injection System (LPIS) Setpoint	10.0×10^5 Pa +34.0 s Delay
ECC Water Temperature	308.0 K
Cold-Leg Break Location (component 22-distance from vessel)	6.0 m

2. Initial PWR Noding Sensitivity Study

(J. R. Ireland, Q-6)

The U.S. PWR model reported previously[13] was renoded very coarsely in order to substantially decrease the running time and to determine how well the results compare with a more finely noded calculation. Figure 15 shows the coarse-node TRAC component schematic. The three intact loops were combined into one loop in this model. Figure 16 shows the vessel noding, which consists of 28 mesh cells (as opposed to 440 mesh cells for the finely noded vessel), with 3 axial core levels, 2 lower plenum levels, 1 upper plenum level, and 1 upper head level. Two theta segments and two radial rings were used. The first radial ring extends to the core barrel, while the second extends to the vessel inner wall. The barrel-baffle region has been omitted but the downcomer gap size has been preserved. All loop components remained identical to the finely noded case except that much larger mesh cells were used. This coarse noding resulted in 20 components, 21 junctions, and a total of 73 mesh cells (about a factor of 10 less than the finely noded model).

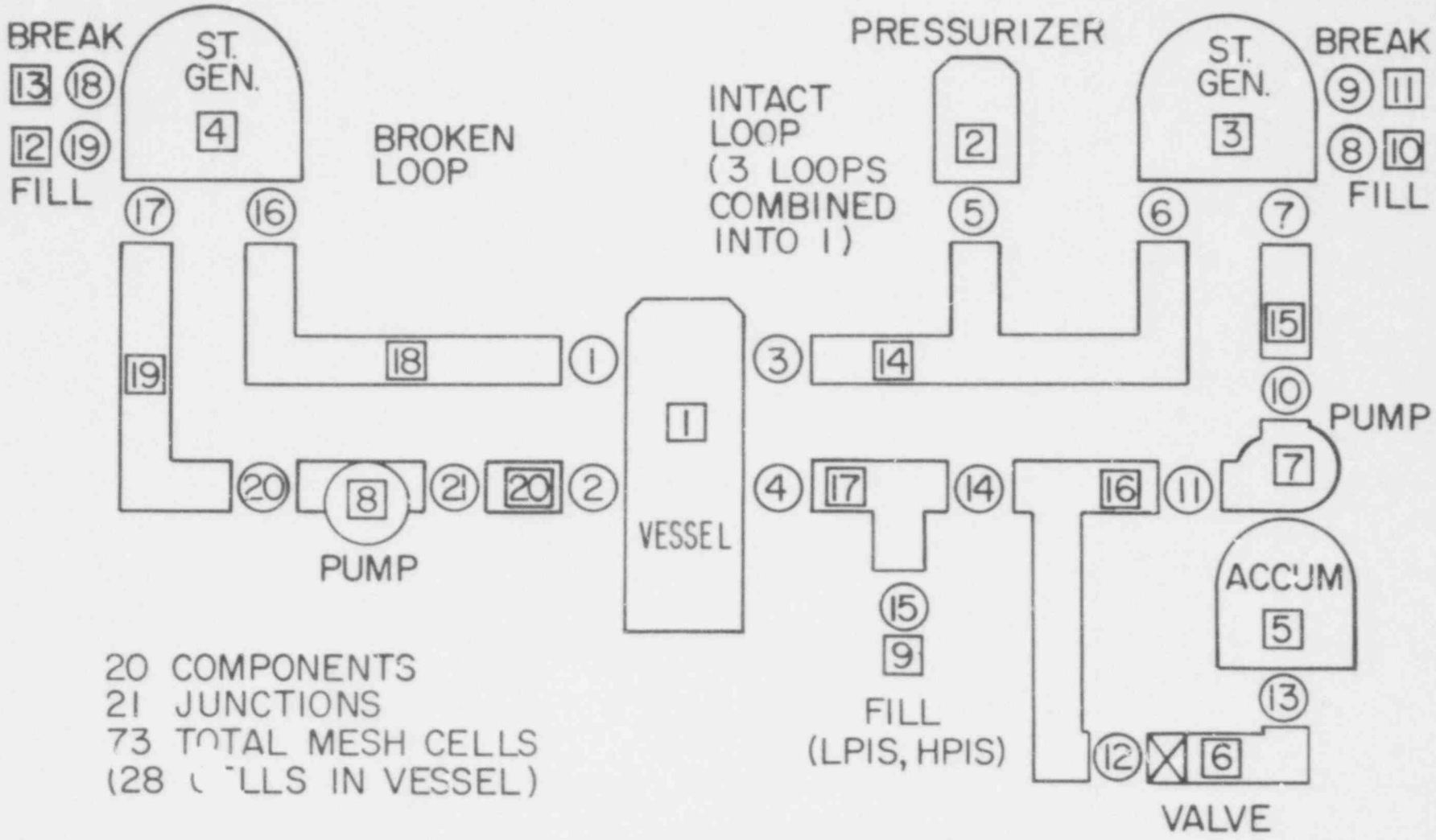

Fig. 15. Coarse-node U.S. PWR schematic.

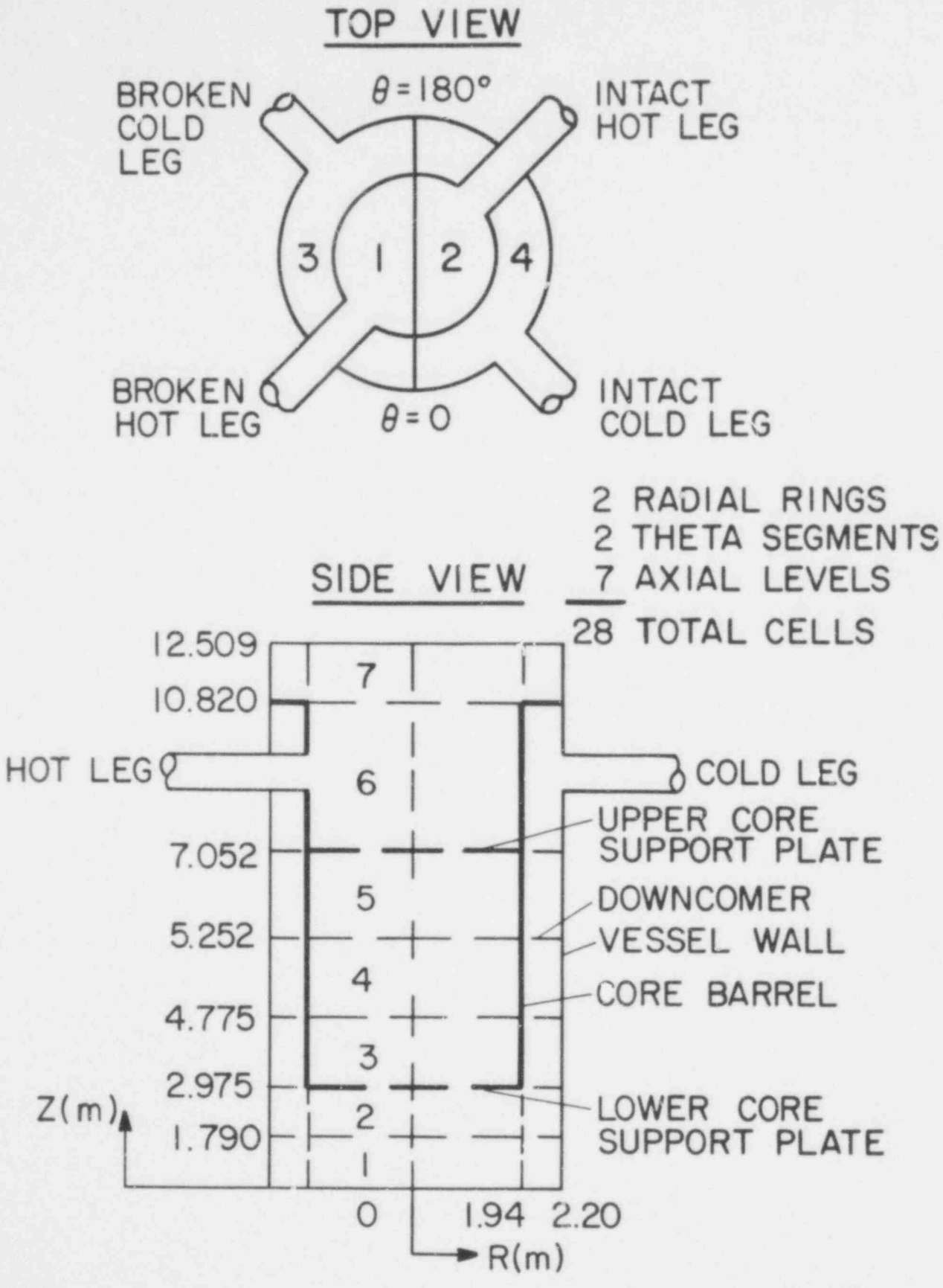

Fig. 16. TRAC noding for coarse node U.S. PWR calculation.

Table II shows some of the important input and calculated initial conditions for the steady-state calculation prior to transient initiation and compares the coarse vs the fine node results. As can be seen, the overall agreement is quite good. Note that the coolant temperature rise across the vessel differs by less than 1 K. Also, the clad surface temperatures at the core midplane are in reasonably close agreement, as is the total system water mass.

TABLE II

U.S. PWR INPUT AND STEADY-STATE INITIAL CONDITIONS

Parameter	Fine Node	Coarse Node
Initial Power	3.238×10^9 W	(same)
Relative Axial Power Shape (bottom to top)	0.75, 1.125, 1.185, 1.10, 0.64	0.9, 1.185, 0.795
Relative Radial Power Shape (center-to-core shroud)	0.99, 1.14, 0.88	1.0
Peak Rod Linear Power	3.6×10^4 W/m	(same)
Core Average Linear Power	2.3×10^4 W/m	(same)
Pump Suction Side Pressure (av)	1.500×10^6 Pa	1.515×10^7 Pa
Pump Discharge Side Pressure (av)	1.555×10^7 Pa	1.567×10^7 Pa
Cold-Leg Temperature at Vessel (av)	558.9 K	562.6 K
Hot-Leg Temperature at Vessel Outlet (av)	594.0 K	596.6 K
Cold-Leg Pressure at Vessel Inlet (av)	1.559×10^7 Pa	1.560×10^7 Pa
Hot-Leg Pressure at Vessel Outlet (av)	1.524×10^7 Pa	1.530×10^7 Pa
Total Primary System Flow Rate	$1.838\ 3 \times 10^4$ kg/s	$1.831\ 0 \times 10^4$ kg/s
Steam Generator Secondary Side Average Pressure	5.828×10^6 Pa	5.825×10^6 Pa
Steam Generator Secondary Side Total Flow Rate	$9.654\ 6 \times 10^3$ kg/s	$9.683\ 1 \times 10^3$ kg/s
Average Cladding Surface Temperature at Core Midplane	618.3 K	607.2 K
Total System Water Mass	5.00×10^5 kg	4.98×10^5 kg
Accumulator Setpoint	4.08×10^6 Pa	(same)

TABLE II (cont)

Parameter	Fine Node	Coarse Node
ECC Water Temperature	325.0 K	(same)
Break Location (distance from vessel)	6.25 m	(same)

Some of the important events which occur during the transient calculation from blowdown through reflood are compared in Table III. Note that refilling of the lower plenum and reflooding of the core are delayed in the coarse-node calculation. Figure 17 shows the lower plenum pressure during blowdown for the two cases. The coarse-node calculation blows down slightly faster than the fine-node calculation probably due to the larger nodes in the core. Figure 18 shows the break mass flow rates for the two cases; the agreement is quite good. Since the coarse-node case depressurizes

TABLE III

TABLE OF EVENTS FOR U.S. PWR LOCA CALCULATION

	Time of Event (s)	
Event	Fine Node	Coarse Node
200% Double-Ended Cold-Leg Break	0.0	(same)
Begin High-Pressure Injection System (HPIS) Flows (setpoint 1.02×10^7 Pa)	0.9	0.8
Peak Clad Temperature Reached (986 K fine, 1 000 K coarse)	3.0	6.5
Accumulator Flows Begin	10.0	9.3
Pressurizer Empties (level below 0.1 m)	15.1	18.3
LPIS Flows Begin	15.8	15.1
Lower Plenum Refilled	40.0	60.0
Accumulators Empty	41.0	50.0
Peak Rod Quenched Through Core Midplane	152	205

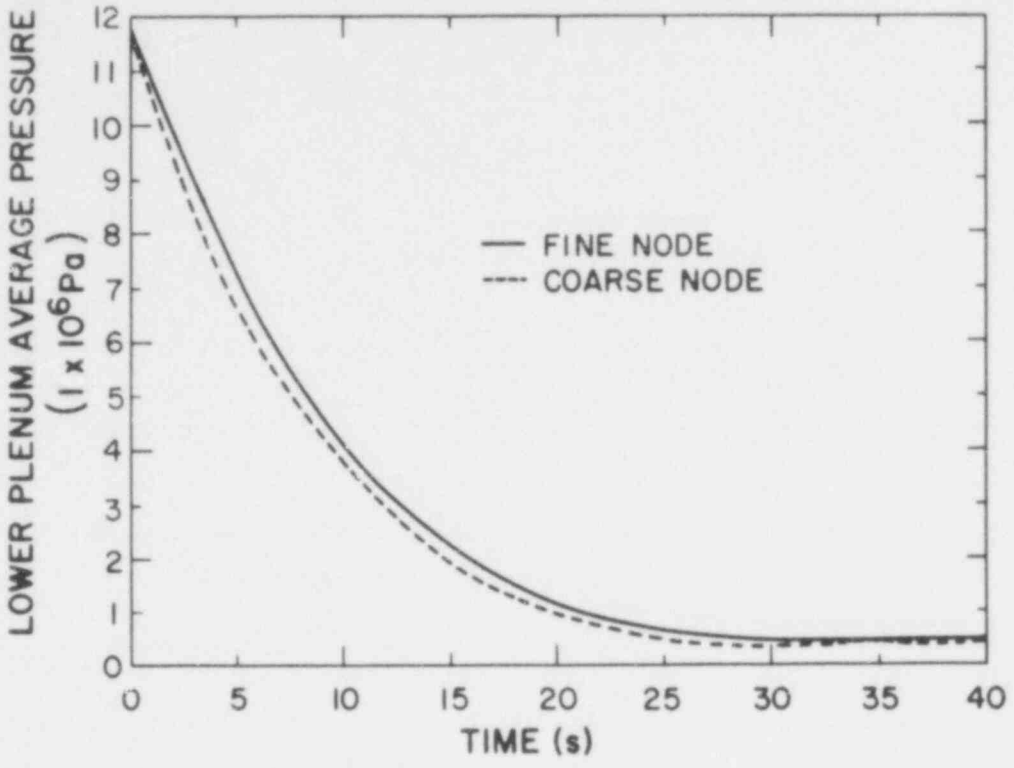

Fig. 17. U.S. PWR lower plenum average pressure.

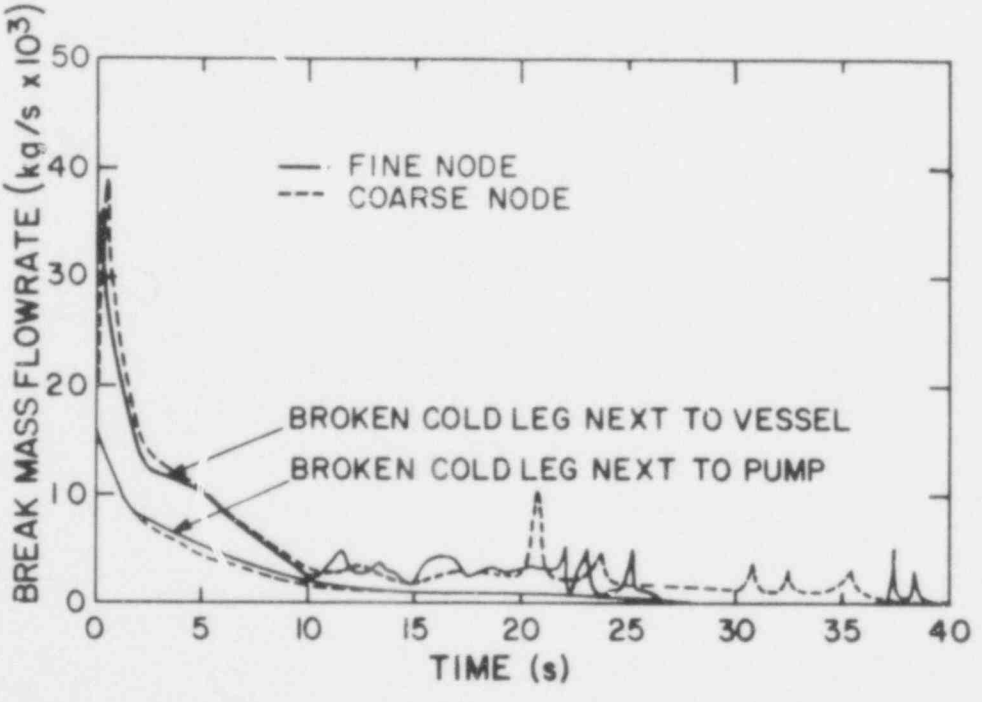

Fig. 18. U.S. PWR break mass flow rate.

faster, the initial break mass flow rate is slightly higher than the fine-node case. Figure 19 shows the mixture density in the broken pipe next to the vessel. This figure gives some indication of the bypass period during the transient. The density spikes occurring at about 35 s (fine node) and 42 s (coarse node) are due to the large surge of accumulator flow before the accumulators empty. Figure 20 shows the pressurizer water level for both cases. Note that the finely noded case empties faster, although the system depressurizes more slowly. The reason for this is that in the finely noded case the loops are modeled separately and the pressurizer loop is located next to the broken loop. Hence, the pressurizer loop blows down faster than the remaining intact loops. In the coarse-node case, however, the three intact loops are combined and this single intact loop is located 180° away from the broken loop.

Lower plenum liquid fractions are compared in Fig. 21. Note that the agreement is quite good until the ECC systems are in full operation at about 20 s. From this point on, the two cases deviate somewhat. In the fine-node case the lower plenum refills at about 40 s, while the coarse-node case refills at about 60 s. This difference is believed to be due to coarse noding in the lower plenum region and to the combined accumulator response. Figure 22 shows the vessel liquid mass for the two cases. The differences during refill can be attributed to the removal of the barrel-baffle region for the coarse-node case.

Figure 23 is a plot of the peak clad temperature at the core midplane for both cases. Since only two theta segments were used in the vessel, with one radial ring in the core, only two average rods are used for feedback to the fluid dynamics in the coarse-node case as opposed to 24 rods for the fine-node case. It is seen that the two cases compare well through refill and during the initial part of the reflood phase. The blowdown peak for the coarse-node case is slightly higher than the finely noded case (1 000 K vs 986 K) and occurs at about the same time. The temperature response looks quite good until the bottom quench fronts begin to move into the high-power central region of the core. The fine-node case predicts quenching through the core midplane at about 150 s,

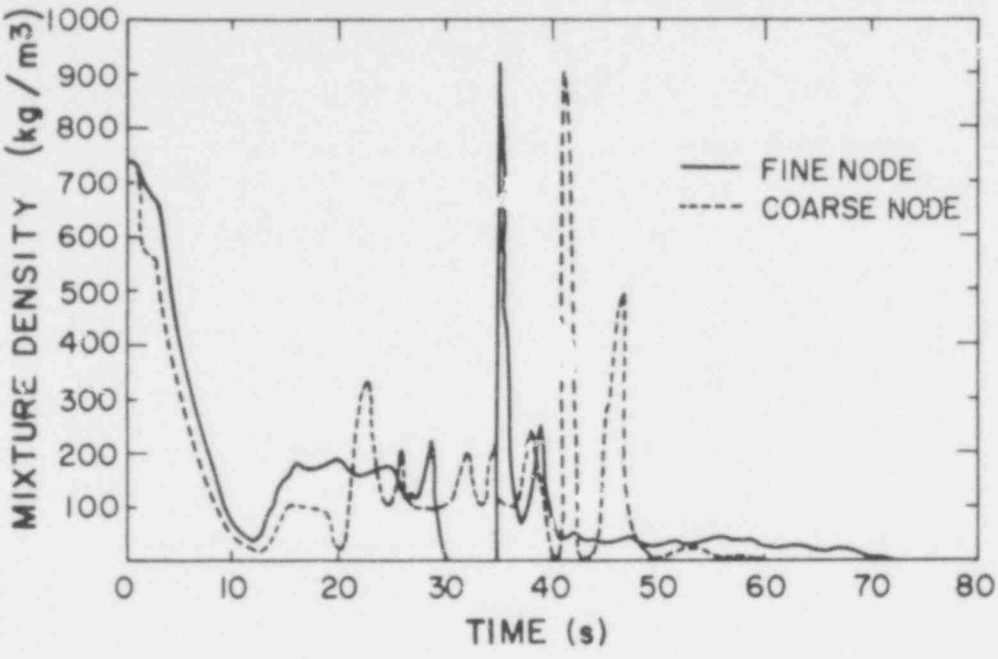

Fig. 19. U.S. PWR mixture density in broken pipe next to vessel.

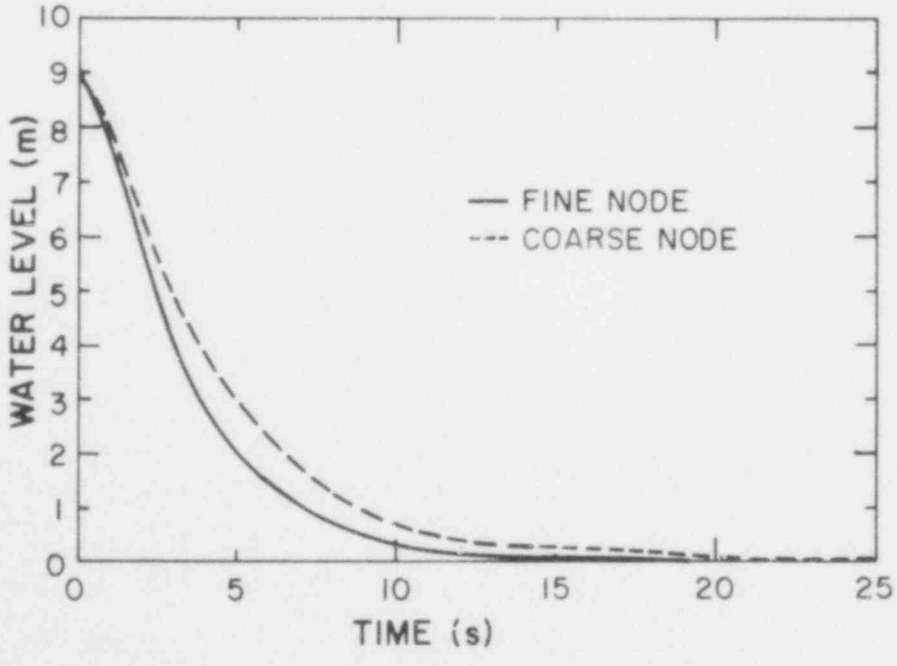

Fig. 20. U.S. PWR pressurizer water level.

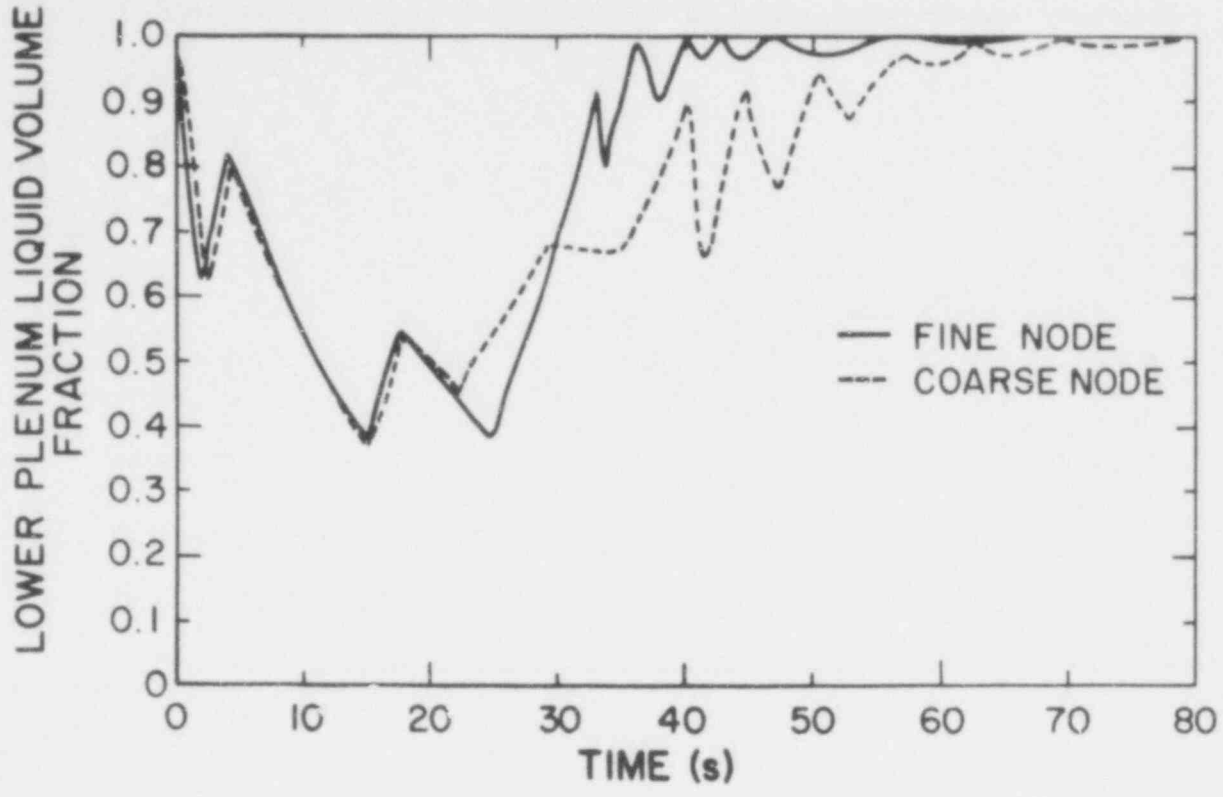

Fig. 21. U.S. PWR lower plenum liquid volume fraction.

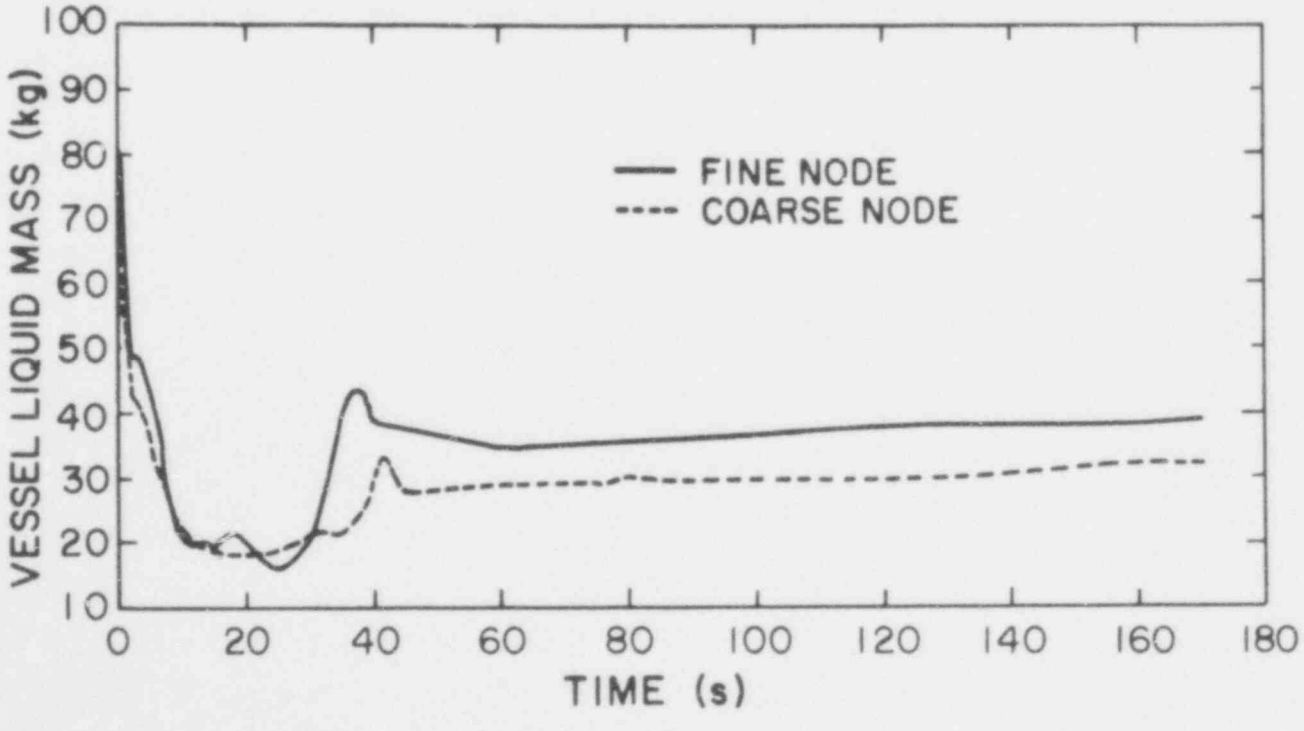

Fig. 22. U.S. PWR vessel liquid mass.

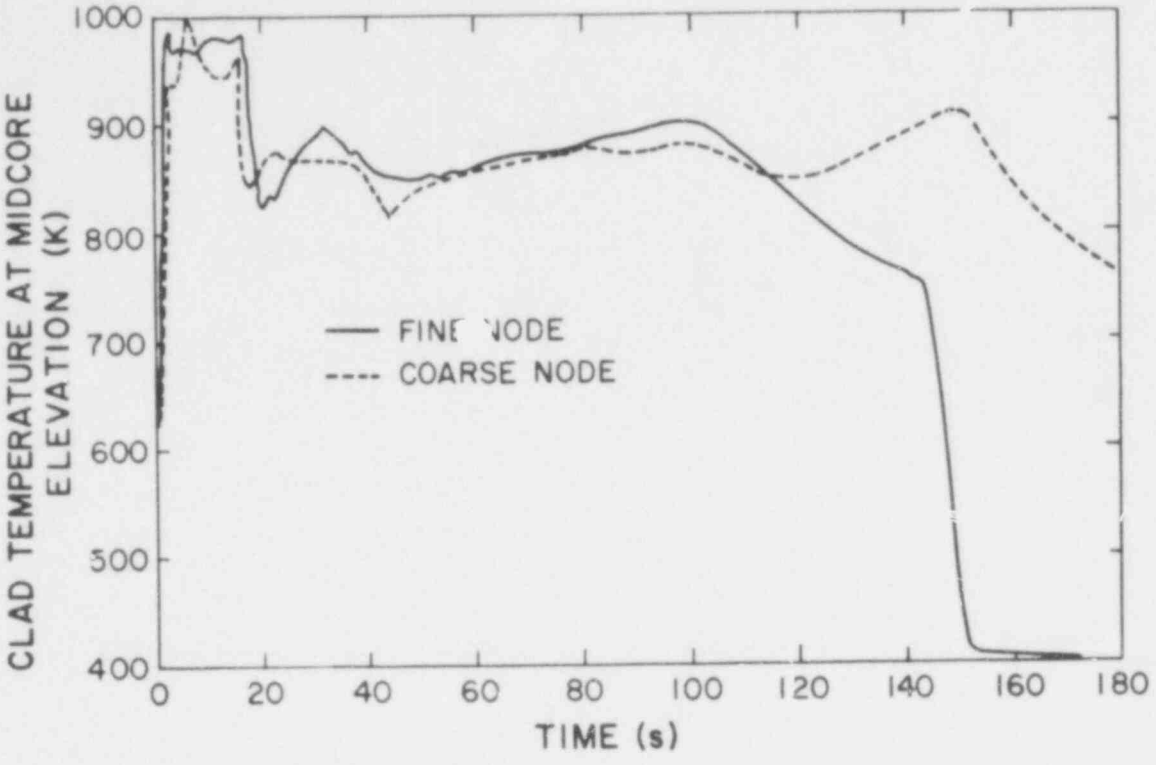

Fig. 23. U.S. PWR peak clad temperature.

but due to the coarse noding in the core and large cell sizes, the coarse-node case does not quench until about 200 s. More nodes in the vessel may be necessary and future noding studies will investigate this further.

Although the reflood portion of the coarse-node transient does not match the fine-node case, the coarse-node model does give excellent agreement through refill and offers the advantage of fast running capability. A coarse-node steady-state calculation can be run in about 6 CPU minutes (on a CDC-7600 computer) as opposed to 90 CPU minutes for the fine-node case. The transient calculation can be run in about 1 CPU hr compared to 19 CPU hr for the fine-node case.

From a comparison of results of the coarse- and fine-node PWR calculations, it is apparent that reasonable results can be obtained for the blowdown and refill phases with a dramatic decrease in CPU time. The calculations described above are the first for the noding sensitivity study and are judged to represent upper and

lower noding bounds for a PWR LOCA. Future studies will concentrate on specific areas of the system, such as the lower plenum, to determine the sensitivity of the results to noding. It appears, however, that reasonable results can be obtained for a full PWR LOCA with a TRAC calculation that requires on the order of a few CPU hours or less.

3. Design Assistance TRAC Calculations for SCTF

(D. Dobranich, Q-6)

The SCTF was modeled using the two-dimensional TRAC capability and parametric calculations were performed. The two-dimensional vessel shown in Fig. 24 contains 11 axial levels and 6 radial segments for a total of 66 mesh cells. Connected to the upper plenum is a hot leg which represents the hot legs of a four-loop PWR. The broken cold leg and intact cold leg (representing three loops) are connected into the downcomer at two different axial levels. The system schematic is shown in Fig. 25. ECC water is injected into the intact cold leg, while the broken cold leg is connected to a large pipe which models the containment. A series of tees are used to model the steam-water separator which allows a mixture void fraction of 0.95 to exit. The initial conditions for the facility are shown in Table IV.

TABLE IV
SCTF INITIAL CONDITIONS

System Pressure	6×10^5 Pa
Containment Tank Pressure	3×10^5 Pa
Core Power	11 MW (ANS decay)
Clad Temperature	885 K
Vessel Internals Temperature	430 K
Pipe Wall Temperature	430 K
Lower Plenum Liquid Temperature	430 K
Containment Liquid Temperature	405 K
ECC Liquid Temperature	330 K
ECC Flow Rate	Scaled from U.S. PWR

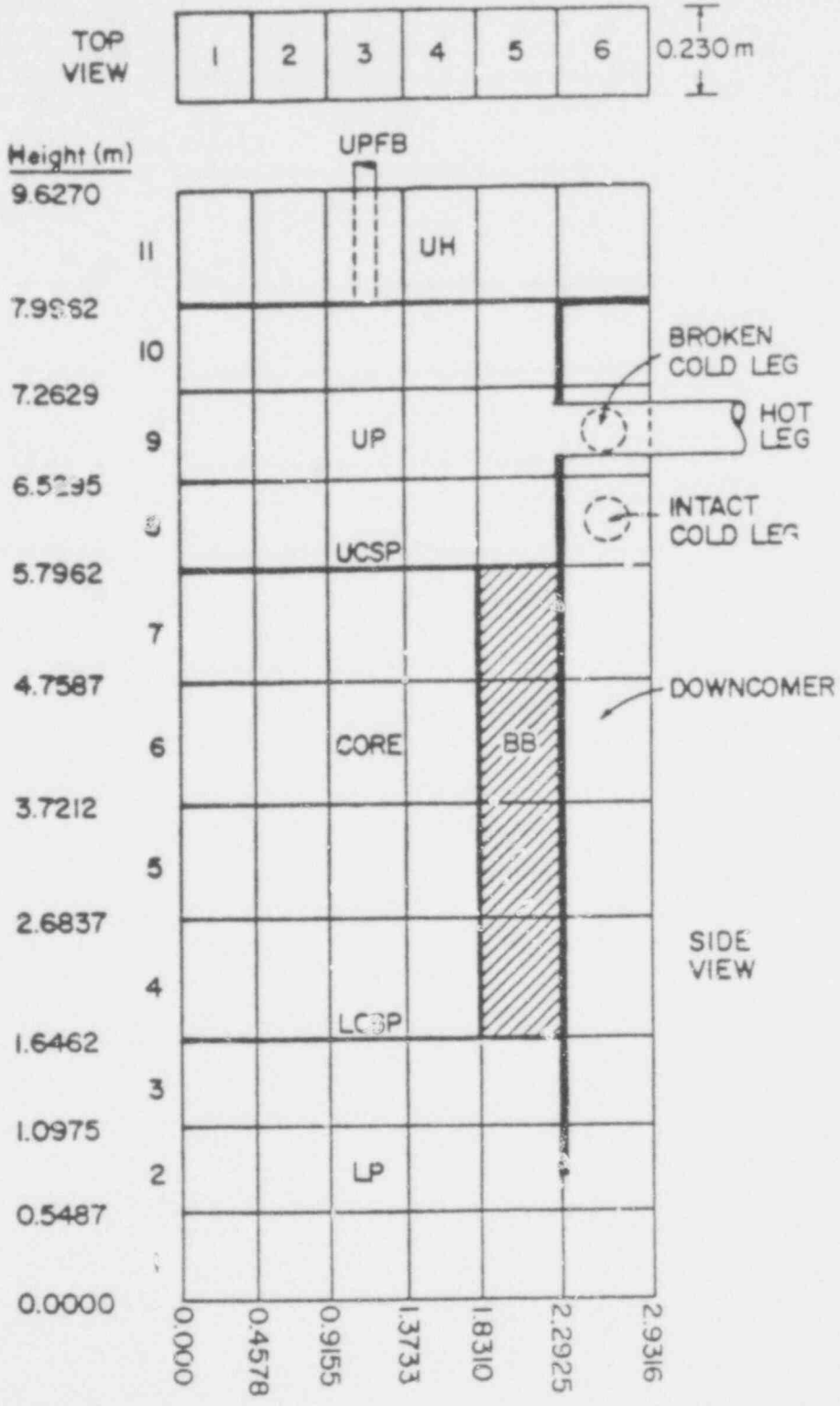

Fig. 24. SCTF two-dimensional vessel model.

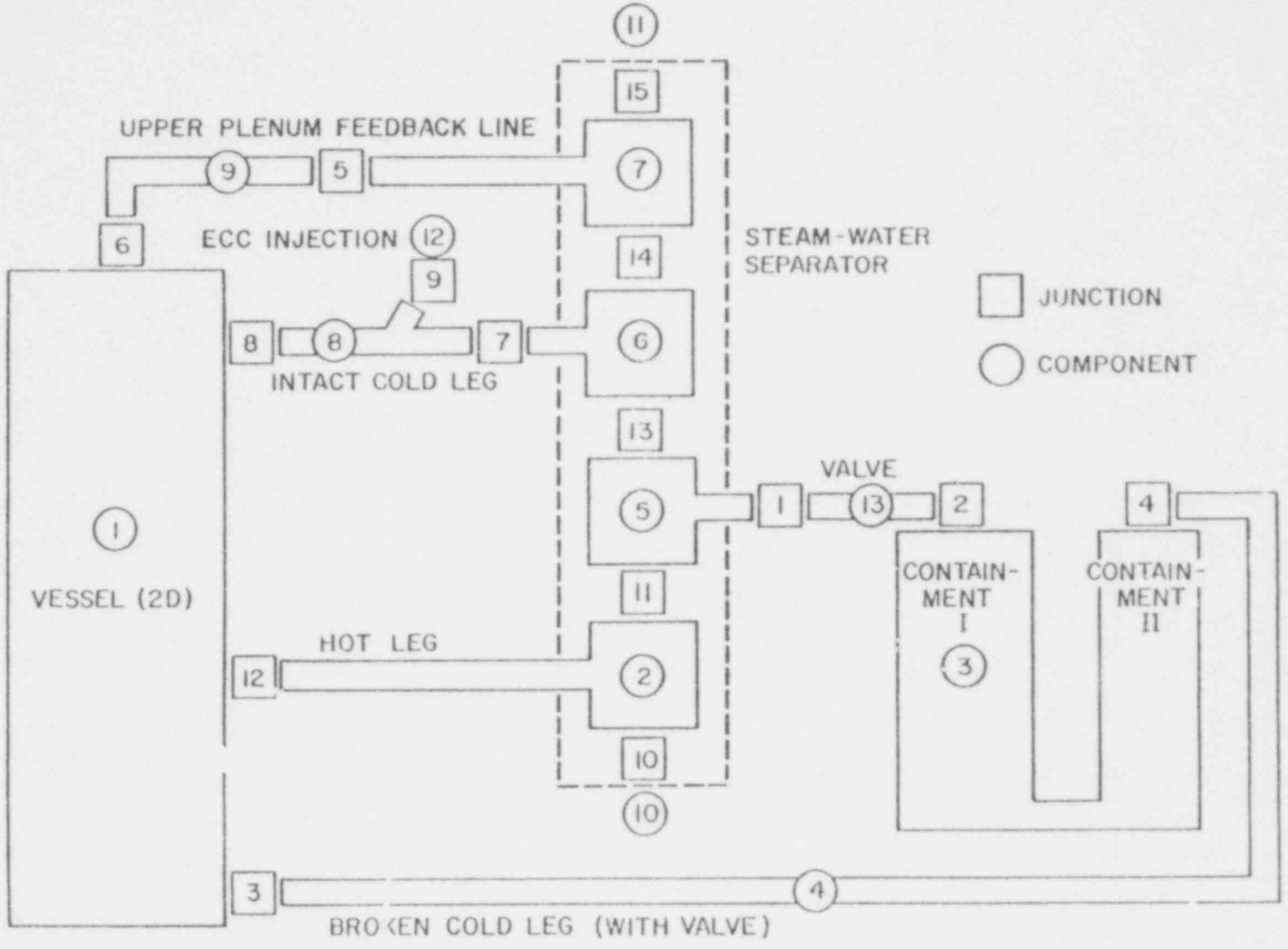

Fig. 25. SCTF system schematic.

A series of TRAC calculations (Table V) were performed to determine the effects of several parameters on the initial (until lower plenum refill) operation of SCTF. The parameters examined were:

1. valve opening time on the broken loops,
2. amount of initial liquid in the lower plenum,
3. ECC delay time, and
4. amount of initial liquid in the containment tanks.

The major influence of these parameters during the initial operation of the SCTF was on the amount of ECC bypass and the amount of initial liquid swept out of the lower plenum. Figures 26-28 show the lower plenum liquid mass vs time for various cases. Figure 26 indicates that by opening the break valves instantaneously, more liquid is swept out of the lower plenum due to the large initial pressure differential between the vessel and the break. The case with the slow opening valve takes longer to refill

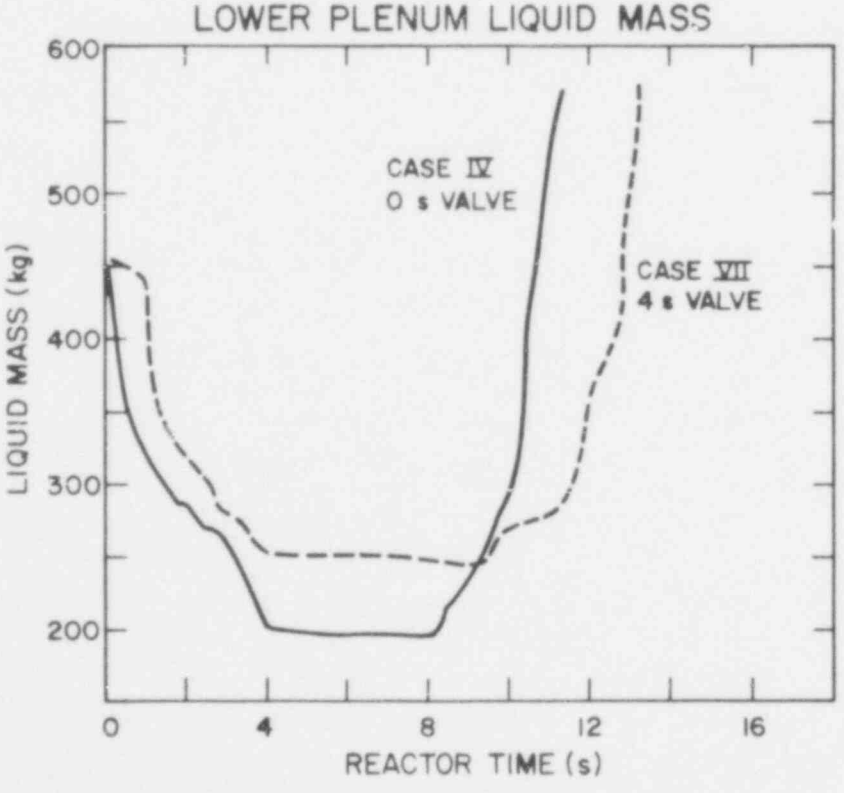

Fig. 26. Effect of valve opening time on SCTF lower plenum sweepout and refill.

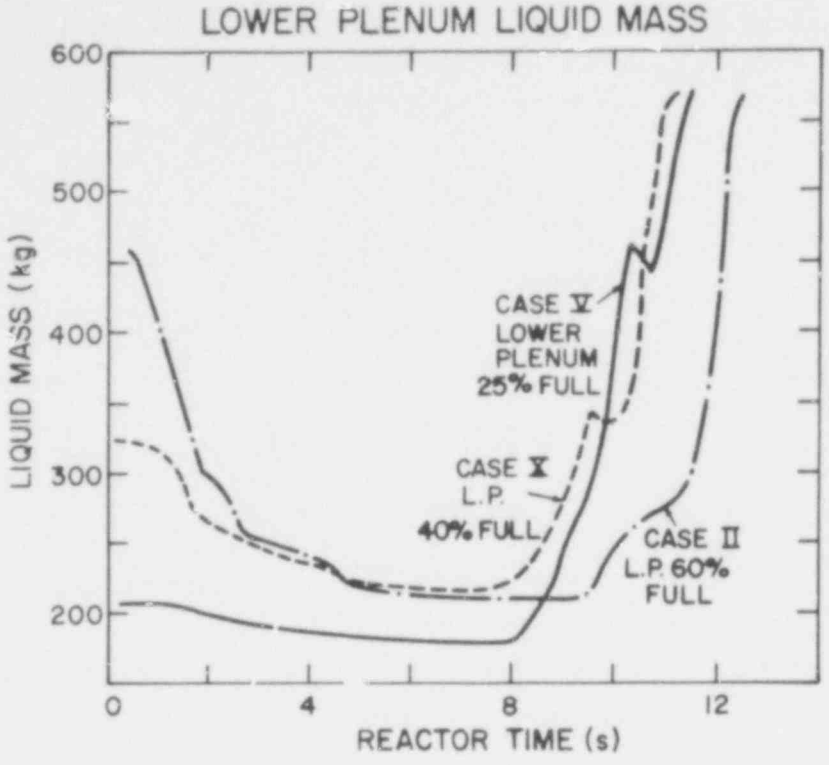

Fig. 27. Effect of initial liquid level on SCTF lower plenum sweepout and refill.

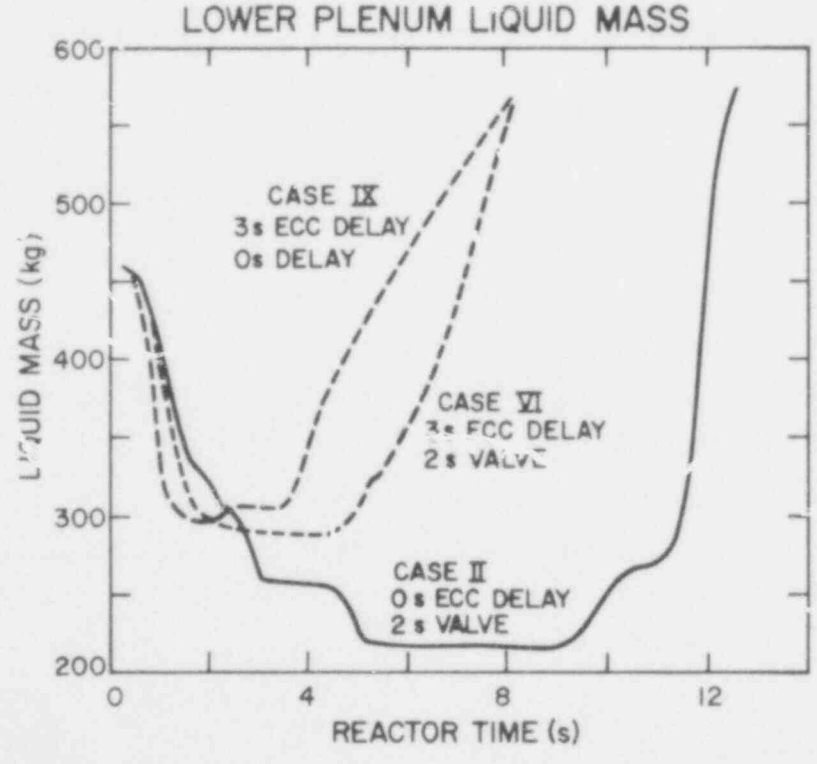

Fig. 28. Effect of ECC delay on SCTF lower plenum sweepout and refill.

TABLE V

SCTF COLD-LEG INJECTION CALCULATIONS

Case	% Liquid in Containment	% Liquid in Lower Plenum	Valve Opening Time (s)	ECC Starting Time (s)
I	0.0	58.3	2.0	0.0
II	25.0	58.3	2.0	0.0
IV	0.0	58.3	0.0	0.0
V	25.0	25.0	2.0	0.0
VI	25.0	58.3	2.0	3.0
VII	0.0	58.3	4.0	0.0
IX	25.0	58.3	0.0	3.0
X	25.0	40.0	2.0	0.0
XI	25.0	40.0	3.0	3.0
XII	25.0	58.3	2.0	1.0
XIII	25.0	58.3	2.0	5.0

because the ECC bypass time is extended due to the longer time required for the vessel and break pressures to equalize.

Figure 27 shows the effect of varying the amount of liquid initially in the lower plenum. In all cases the amount of liquid decreased to the level roughly equal to that of the bottom of the downcomer. This lower plenum sweepout continues until the pressures equalize, which occurs when the liquid level drops below the downcomer wall. This phenomenon may be dependent on the lower plenum axial noding scheme and will be studied further.

The effect of delaying the ECC injection time is shown in Fig. 28. By delaying the ECC injection for several seconds, the lower plenum refills faster than the case with no ECC delay. This effect is related to ECC bypass and to lower plenum sweepout. With a delay in ECC injection, the pressure between the downcomer and the break equalizes rapidly, minimizing lower plenum sweepout once ECC injection begins. Without ECC delay, the initial ECC liquid

is swept out the break. In addition, condensation from the subcooled liquid lowers the pressure at the top of the downcomer which enhances the amount of lower plenum sweepout. Figure 29 indicates that the optimum ECC delay time exists at approximately 3 s for this particular slab core case. The final parameter, which is the amount of initial liquid in the containment tanks, was found to have only a very small affect on the system performance.

One of the reasons for the parametric study was to determine if the conditions in the lower plenum at the end of blowdown are prototypical of a full-scale PWR. Figures 30 and 31 are plots taken from the TRAC simulation of a U.S. PWR with two slab core cases superimposed for comparison. It was found that all the slab core cases compared reasonably well with respect to lower plenum conditions in the PWR. An additional slab core case was run which did not include a blowdown period (Fig. 32). Again, the lower plenum conditions compare reasonably well with the U.S. PWR results. Finally, the liquid and vapor velocities in the vessel (shown in

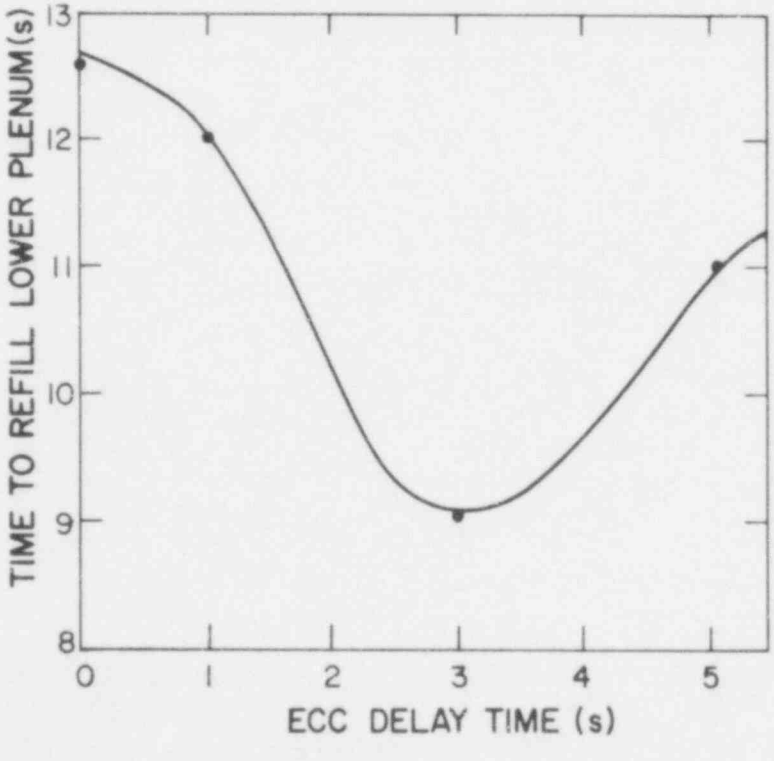

Fig. 29. Effect of ECC delay time on SCTF refill time.

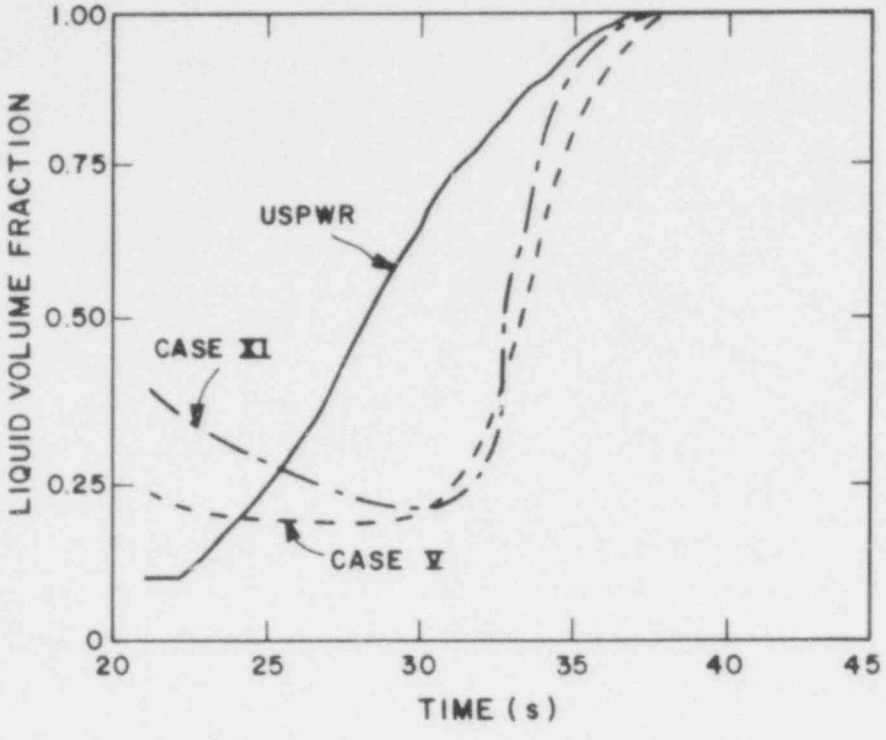

Fig. 30. PWR and SCTF refill behavior.

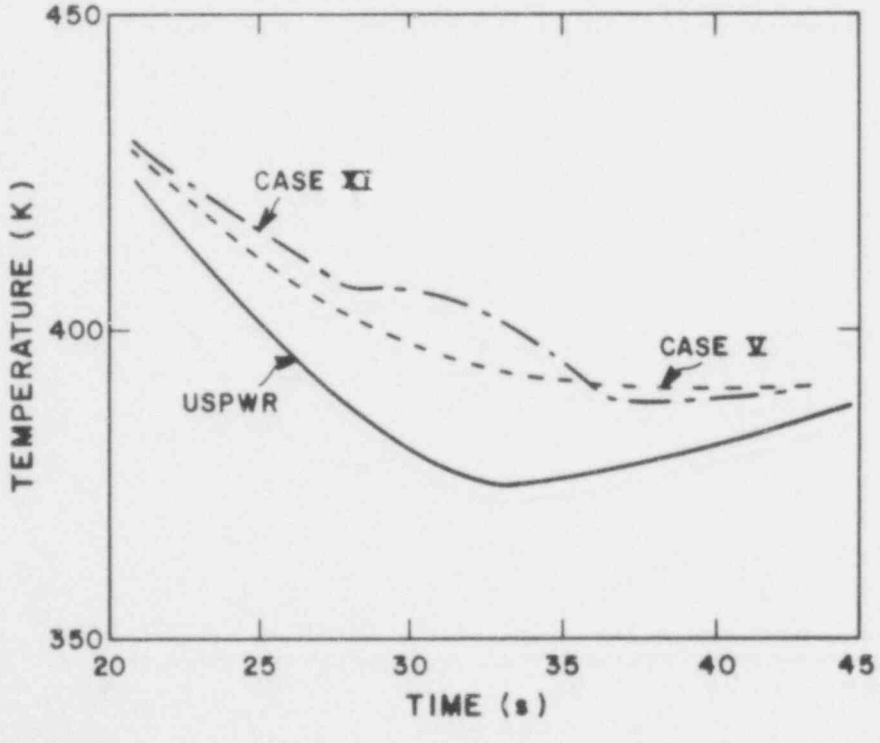

Fig. 31. PWR and SCTF lower plenum liquid temperature during refill.

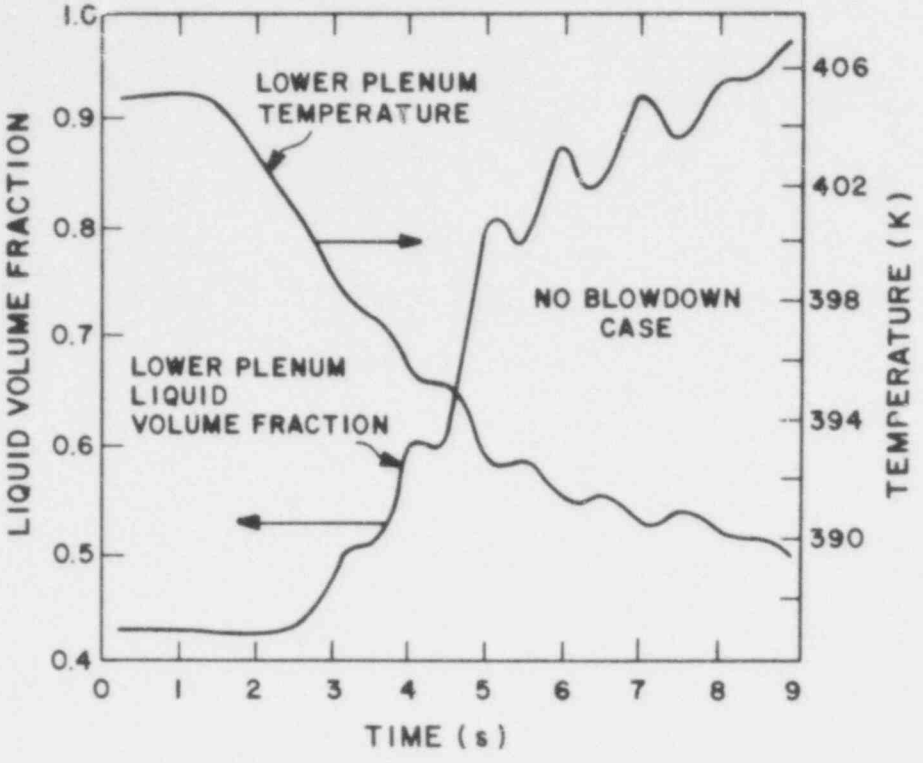

Fig. 32. SCTF lower plenum refill behavior without blowdown.

Figs. 33-36) were found to be typical of those calculated for the U.S. PWR during the same time interval.

Calculations performed to date indicate that some ECC delay and a finite valve opening time are probably necessary to generate prototypical initial conditions in the SCTF. However, some of the results described above may be sensitive to noding and this possibility is being investigated.

4. Recalculation of the CCTF

(D. Dobranich, Q-6)

Results of the initial CCTF calculation (Case 1) were reported last quarter.[13] A new calculation (Case 2) with several noding changes and altered initial conditions was performed this quarter. Two major changes were made from the first case. The amount of liquid in the lower plenum was decreased and the liquid volume in the accumulator was increased. The primary result of the first case, as reported in the last quarterly, was that the accumulator contained insufficient liquid to refill the lower plenum and that

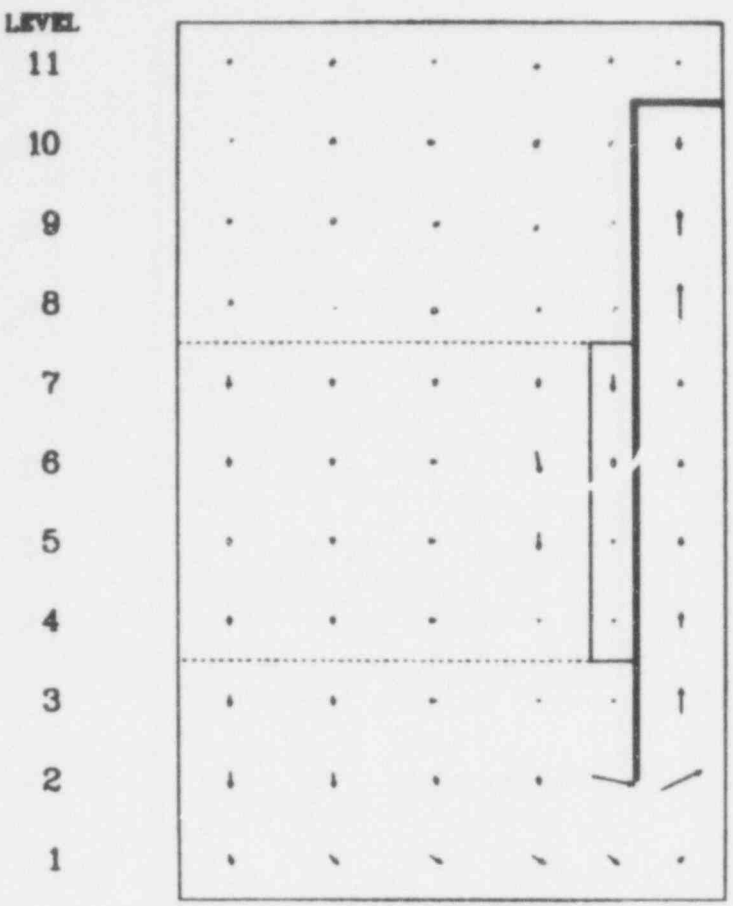

Fig. 33. SCTF vessel liquid velocities during blowdown.

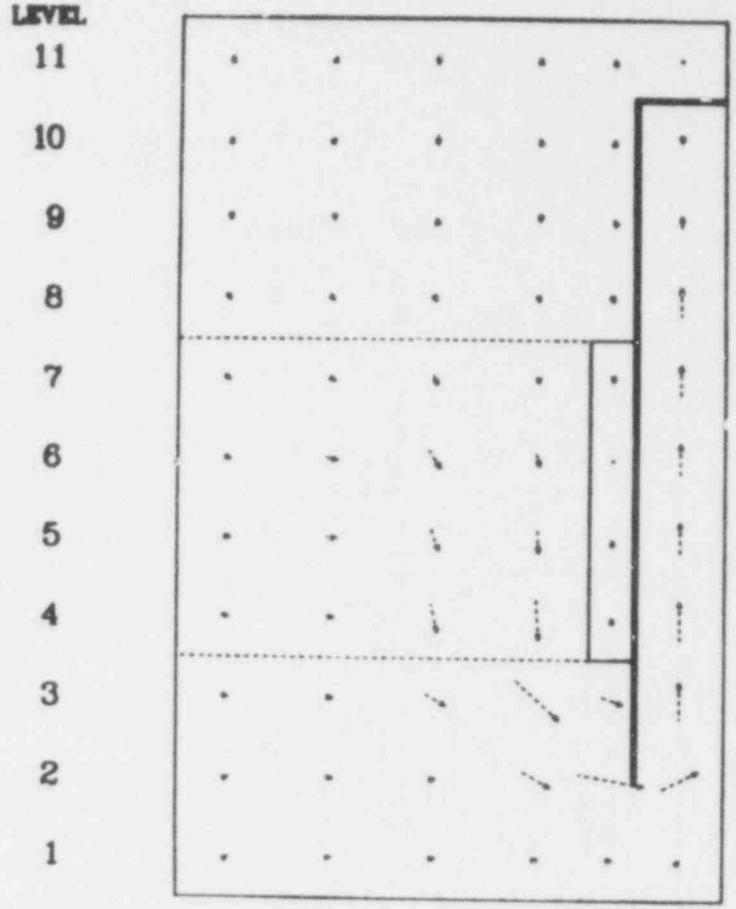

Fig. 34. SCTF vessel vapor velocities during blowdown.

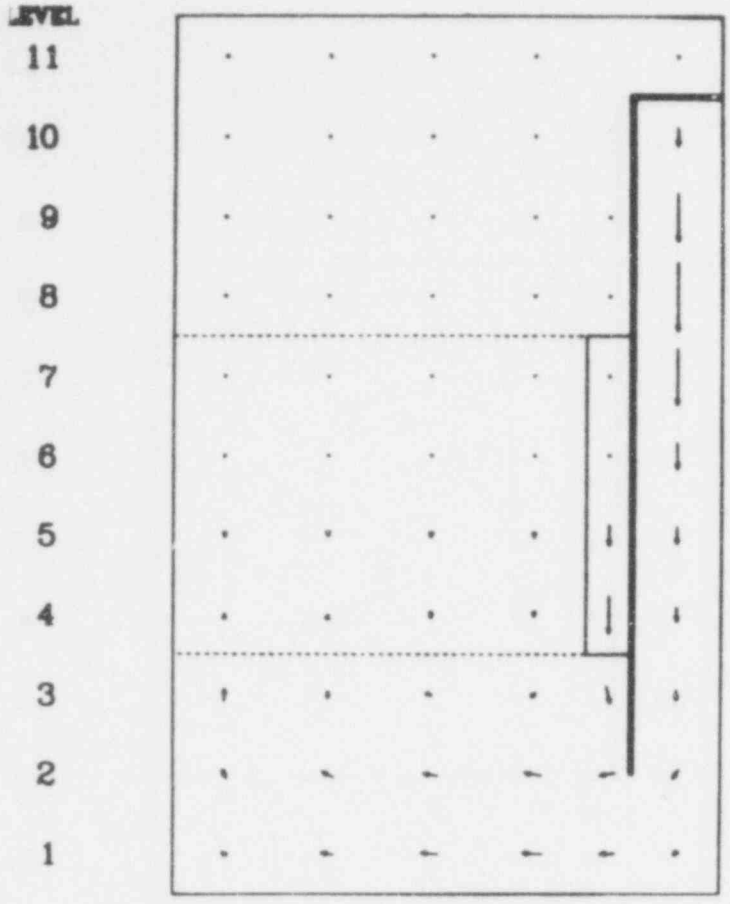

Fig. 35. SCTF vessel liquid velocities during refill.

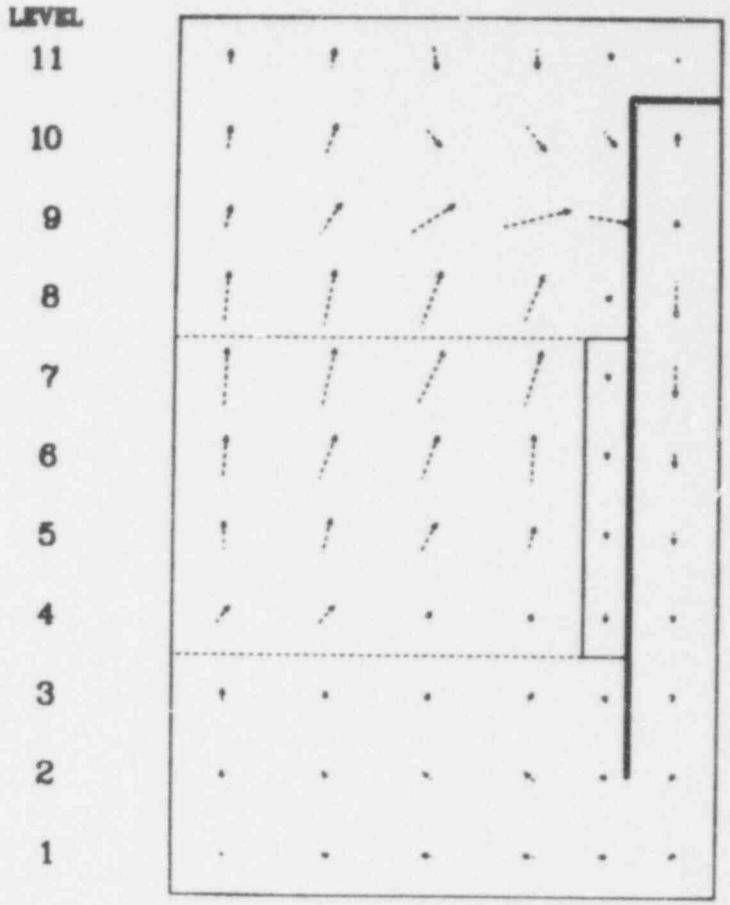

Fig. 36. SCTF vessel vapor velocities during refill.

the LPIS would be ineffective if this occurred. Increasing the initial accumulator liquid volume from 4-5.5 m^3 proved to be sufficient to refill the lower plenum and initiate reflood. Lower plenum conditions during the transient are shown in Figs. 37-39. The results for Case 2 are quite similar to those for Case 1 until the accumulators empty in Case 1.

Results from this TRAC calculation, along with new design information, have been used as an aid in renoding of the CCTF system in preparation for the initial pretest prediction.

C. Independent TRAC Assessment

(J. C. Vigil, Q-6 and K. A. Williams, Q-9)

The TRAC Development Program (Sec. II.A) includes developmental assessment prior to external release of a particular code version. Developmental assessment involves testing of the code by performing posttest analyses of a broad range of applicable

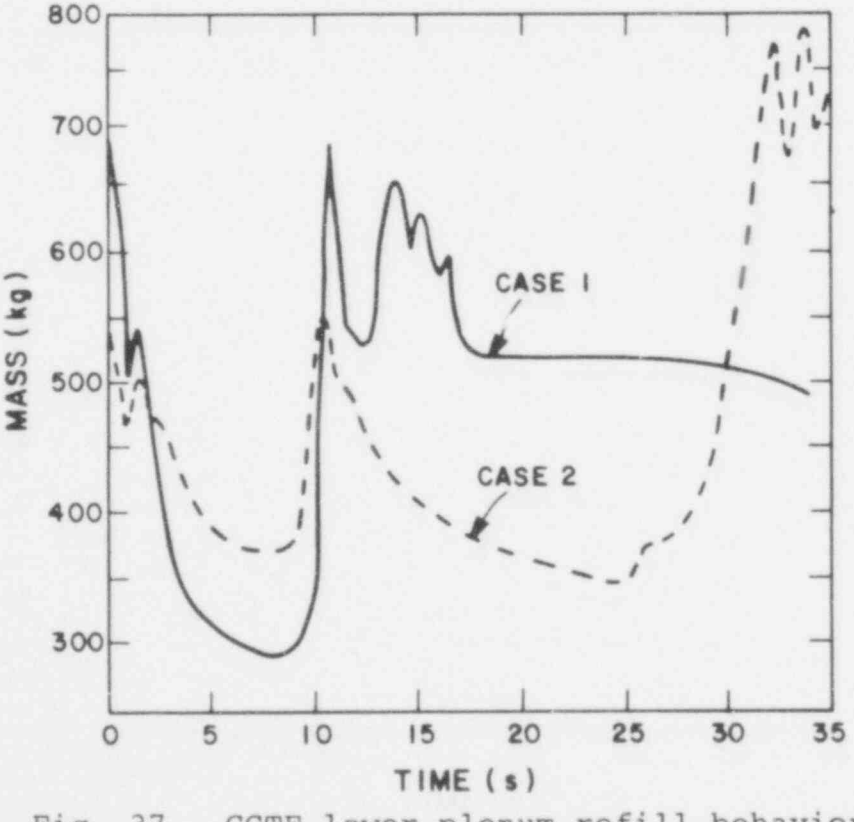

Fig. 37. CCTF lower plenum refill behavior.

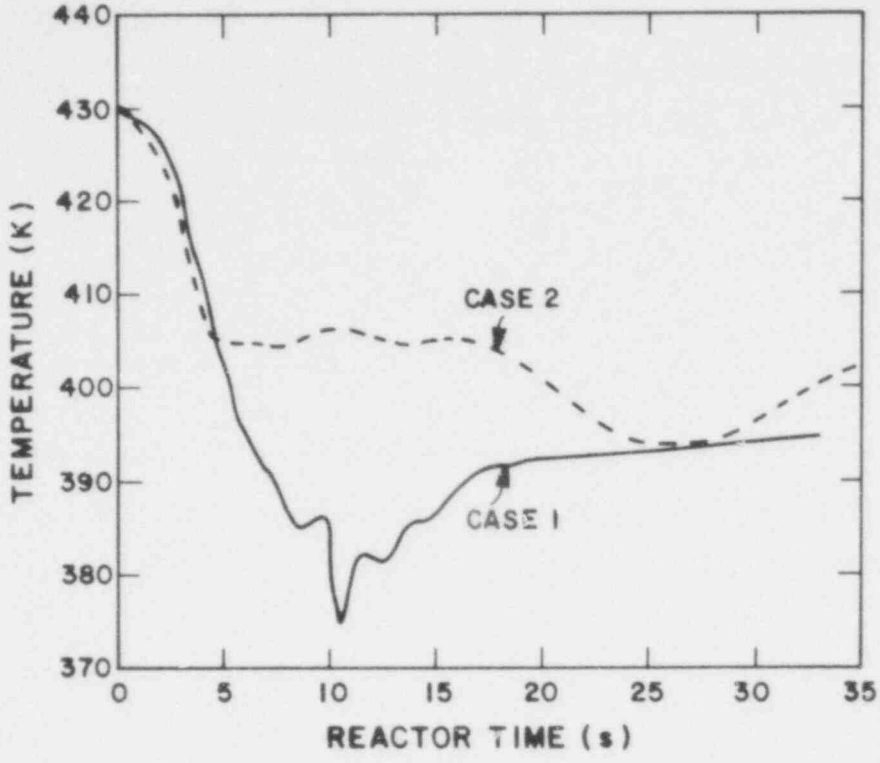

Fig. 38. CCTF lower plenum liquid temperature response during refill.

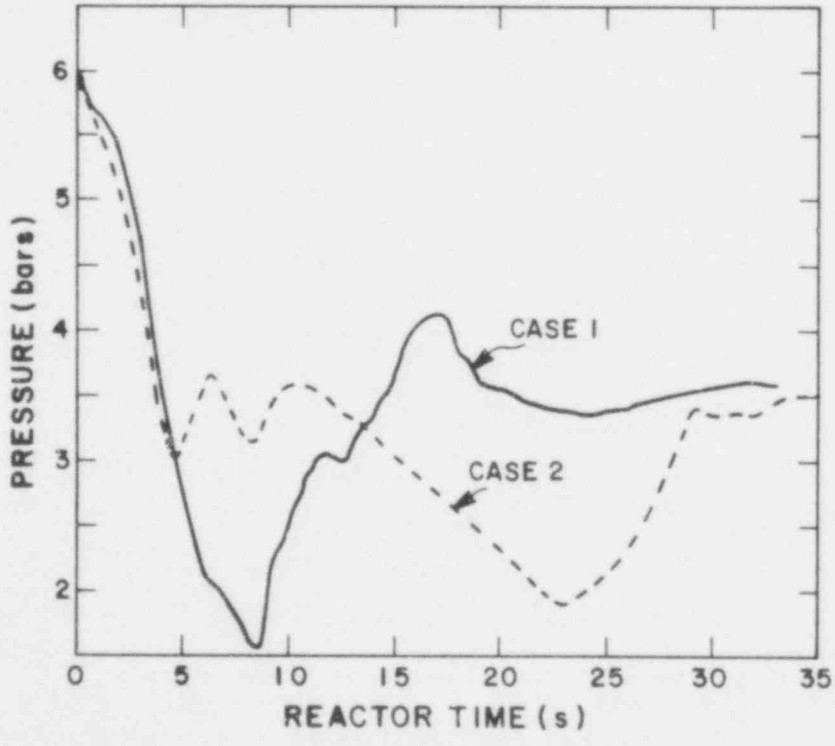

Fig. 39. CCTF lower plenum pressure response during refill.

experimental data. In contrast to this, the objective of the TRAC Independent Assessment Program is the independent testing of the TRAC models and scaling capability by performing blind pretest and posttest predictions for a variety of facilities. The assessment is independent in that the pretest predictions are performed by individuals different from those involved in the code development program.

Blind pretest predictions are referred to as "double blind" predictions because the analyst does not have access to either the initial test conditions or the transient test results. The usefulness of this type of calculation with respect to code testing is compromised if the actual initial test conditions differ significantly from those anticipated by the experimenters. In the blind posttest prediction, the analyst has access to the actual initial test conditions but the transient test results are not available until after the posttest prediction has been submitted.

Experiments selected for independent assessment of TRAC include either the first tests on new experimental facilities (e.g., nuclear LOFT) or tests on newly modified facilities (e.g., Semiscale Mod 3), which are substantially different from previous tests. In general, all of the independent assessment tests are required to be different from those used in the developmental assessment process.

In addition to the blind test predictions, the scope of the Independent Assessment Program includes posttest analyses to resolve any discrepancies between the code predictions and the test results. Participation in the NRC standard problem exercises as appropriate is also included.

The major activity during the quarter involved both a blind pretest prediction and a posttest prediction of LOFT nuclear test L2-2. Results of these calculations pointed out the importance of using the actual initial test conditions in the transient calculation. TRAC results are in good agreement with most of the data except that early quenching of the entire core is not predicted. TRAC calculations of LOFT isothermal test, L1-5, are also presented.

Although these were not blind predictions, they are reported here because they aid in the interpretation of the L2-2 results.

Noding of the LOBI facility at ISPRA is in progress in preparation for a pretest calculation. Additional design information has been requested for this facility. Calculation of Semiscale Mode 3 Test S-07-6, which exhibited long-term (100 s period) oscillations in the downcomer and vessel liquid masses, is in progress. The TRAC input deck for Test S-07-6 will be modified for a pretest prediction in the Mod 3 facility.

1. Pretest and Posttest Predictions of LOFT Nuclear Test L2-2

(K. A. Williams, Q-9)

TRAC has been used for a posttest calculation of LOFT test L1-5, as well as for a pretest ("double-blind") prediction and posttest analysis of the first nuclear test, L2-2. Exactly the same system noding was used to represent the LOFT facility for all three calculations.

Figure 40 shows schematically the arrangement of TRAC components. This model contains 27 components with a total of 300 fluid mesh cells. The entire reactor vessel is modeled using the three-dimensional, two-fluid VESSEL module, while all other components are modeled using one-dimensional modules. Figure 41 shows the vessel axial noding in relationship to the LOFT vessel; there are a total of 12 axial levels including 5 axial levels within the core region. Figure 42 shows the radial and azimuthal noding for the axial levels. As shown, each level contains 12 fluid cells within the core radius and 4 fluid cells within each downcomer level. Thus, there are a total of 192 fluid cells within the vessel, including 60 within the core itself. Figure 43 shows the detailed relation between the LOFT fuel pin location and the TRAC radial noding. Figure 44 gives the dimensions of the five axial levels of the core itself, with the cell numbers being the CORE LEVEL. Thus, CORE LEVEL 1 corresponds to axial level 4 (see Fig. 41). The dimensions are given in inches to facilitate comparison with LOFT thermocouple measurements whose axial location is given in inches above the bottom of the core. TRAC fuel rod temperatures correspond to the location at the axial center of each fluid cell; this

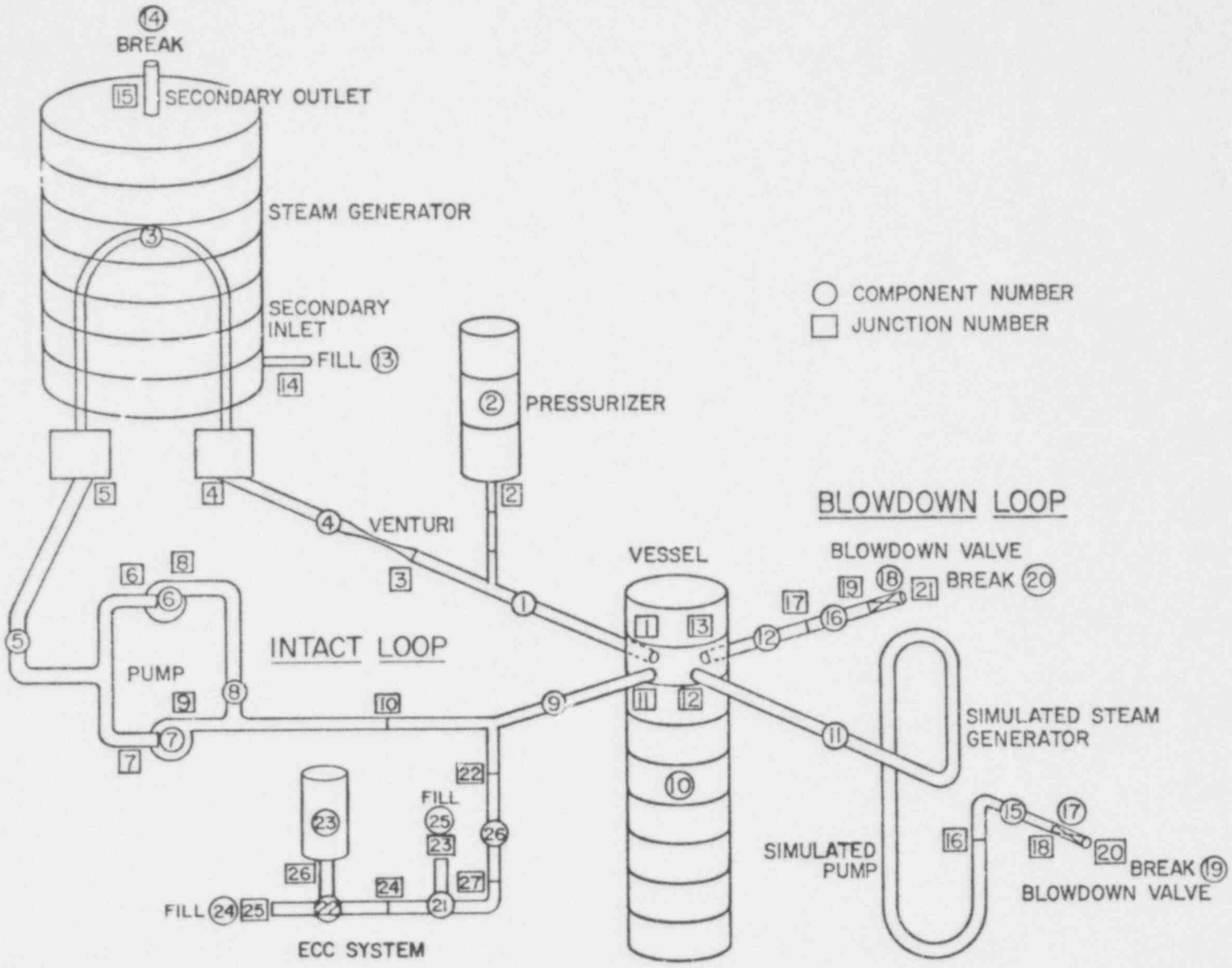

Fig. 40. TRAC model of LOFT facility for tests L1-5 and L2-2.

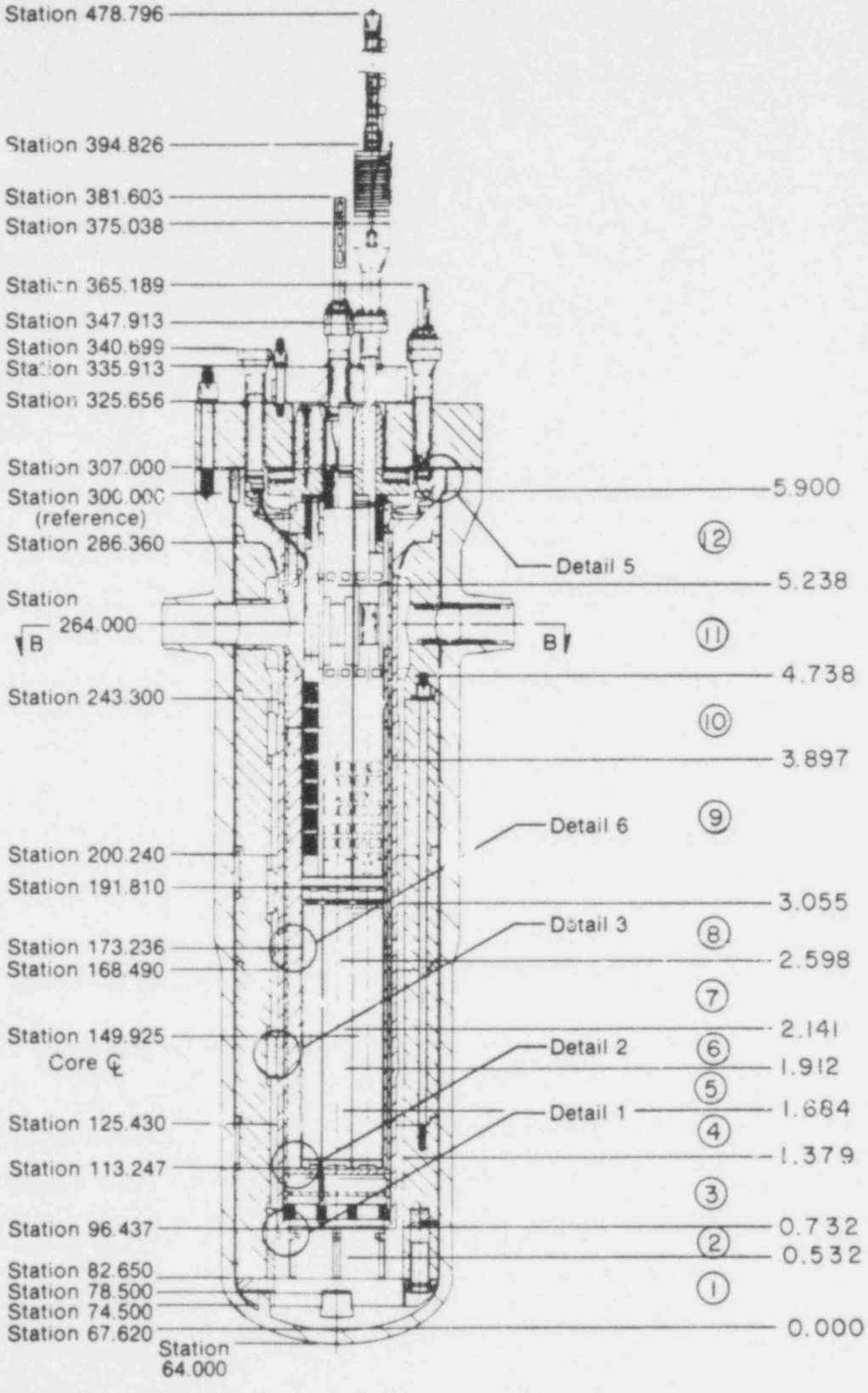

Fig. 41. Axial vessel noding for LOFT test L1-5 and L2-2.

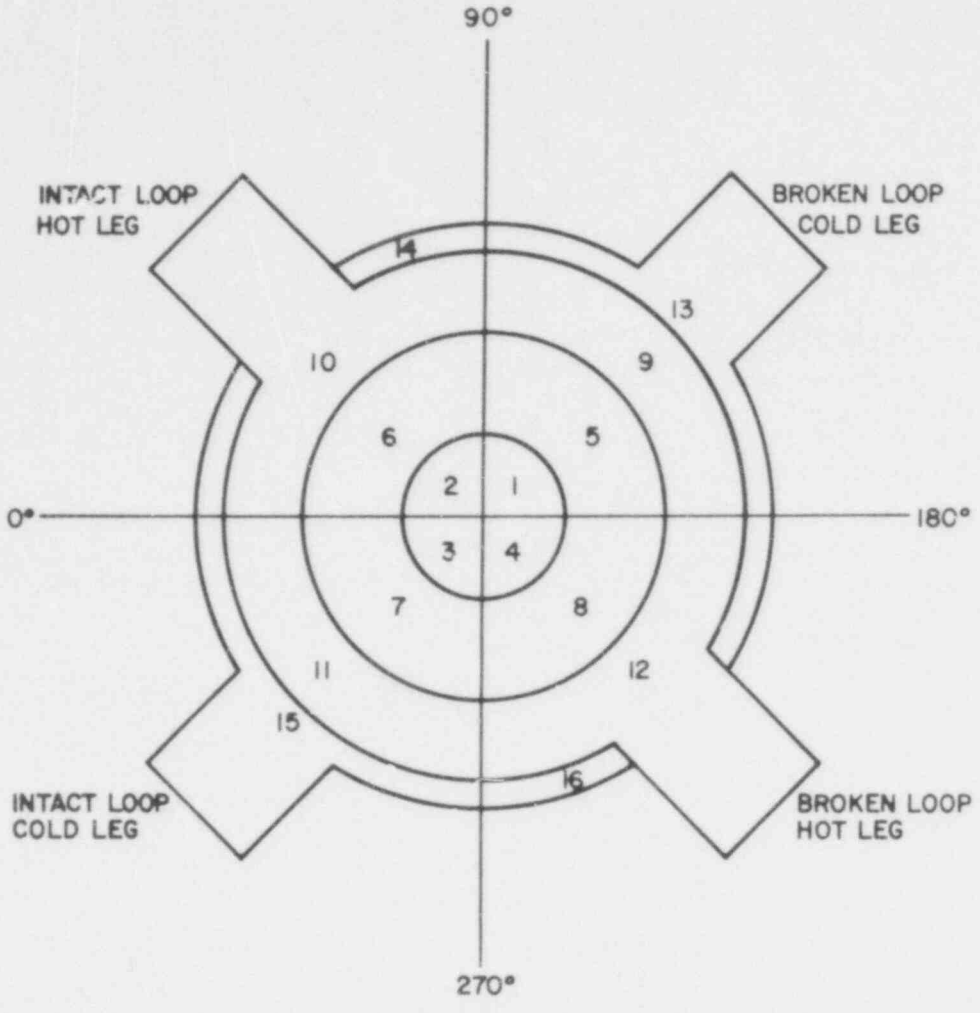

Fig. 42. LOFT vessel level noding.

height is also shown in Fig. 44. The reflood fine mesh is tripped 10 s after accumulator injection is initiated. There are 5 uniform fine-mesh intervals for each axial level giving a total of 25 fine meshes. Again, the TRAC fine-mesh temperatures correspond to the axial center of each fine mesh. This information, in conjunction with a LOFT core map[15] allows for comparison between TRAC cladding temperatures and LOFT thermocouple measurements.

a. Calculation of LOFT Test L1-5

LOFT test L1-5 was the last in a series of isothermal tests and was the only isothermal test conducted with the nuclear core installed. The test was initiated from an initial isothermal

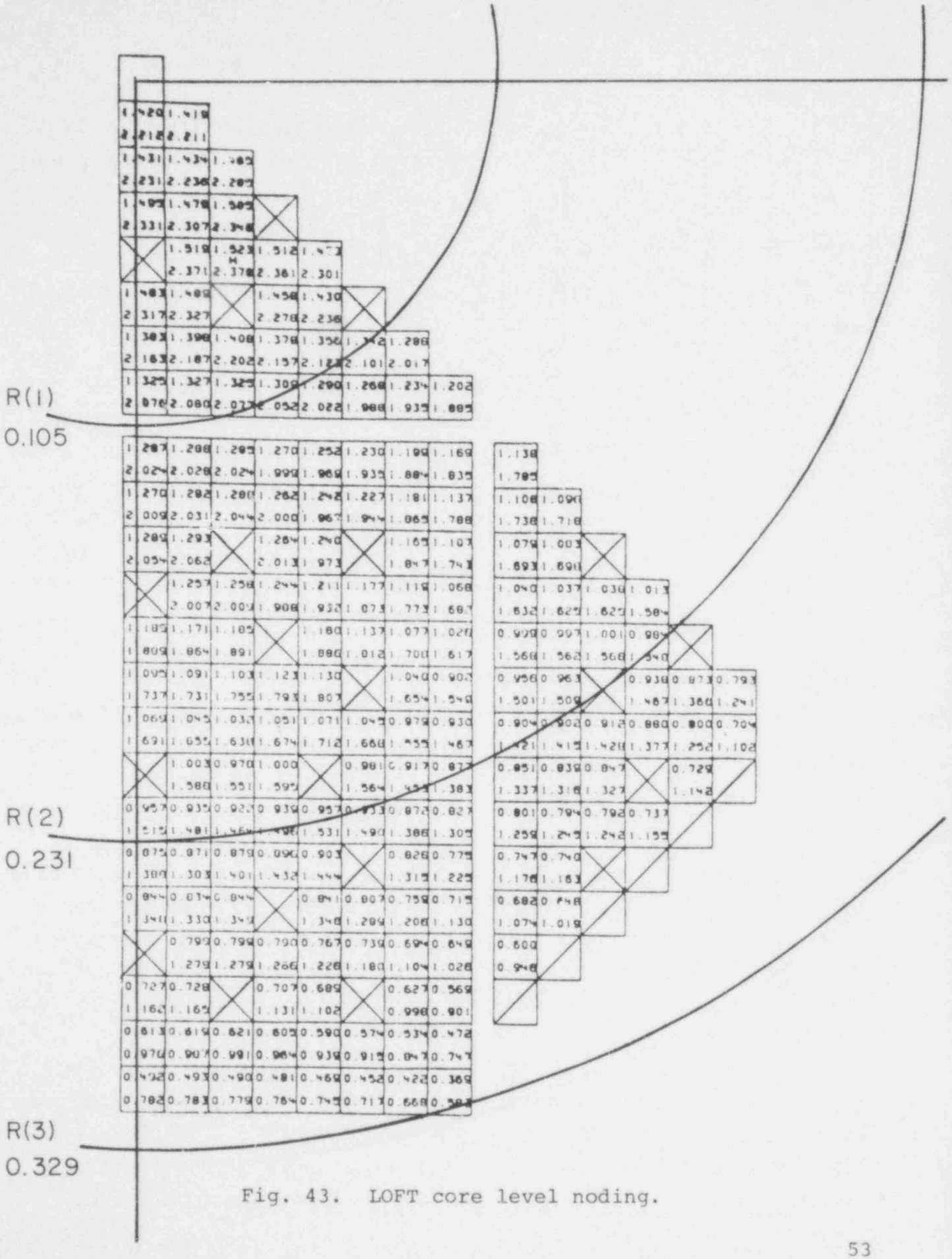

Fig. 43. LOFT core level noding.

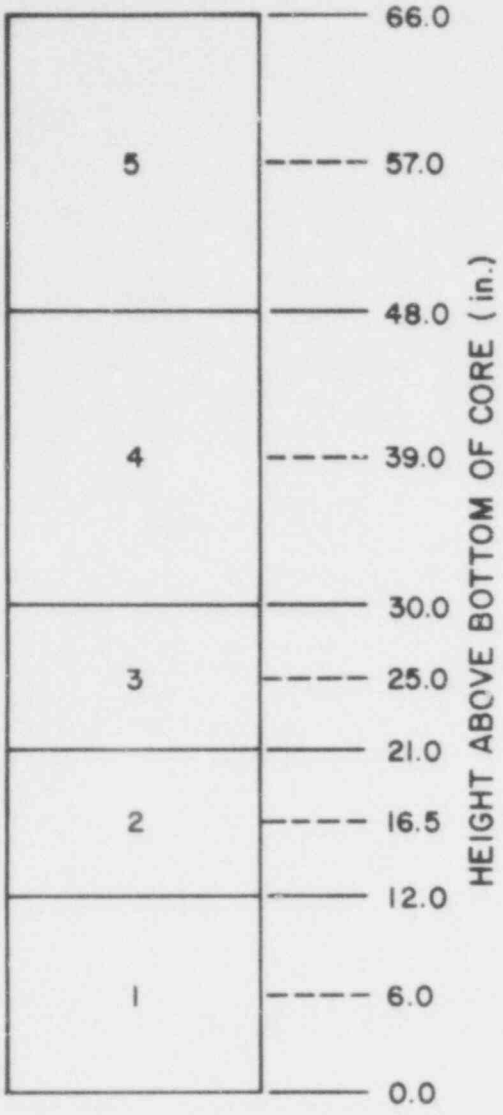

Fig. 44. LOFT core axial noding.

condition of 555 K and an intact loop flow rate of 171.4 kg/s. The test simulates a 200% double-ended shear break in a cold leg of a large PWR (LPWR) operating loop with cold-leg ECC injection. Further information on system initial conditions and experimental data can be found in Ref. 15.

The TRAC transient calculation was carried out to 60 s after blowdown initiation. The results indicate that the code is giving excellent results for the fluid thermal-hydraulics in both the intact and broken loops as well as for the ECC system.

The broken loop hot-leg contains orifice plates to simulate the hydraulic resistance of a steam generator and a pump. Figure 45 shows that the code is accurately representing the two-phase pressure drop through these resistances. In this figure, PE-BL-2 is near the vessel connection, PE-BL-6 is downstream of the simulated steam generator while PE-BL-3 is downstream of the simulated pump. The calculated discharge flow rate from this leg is likewise in good agreement as shown by Figs. 46 and 47.

Experimental data for fluid density in the broken cold leg shows some ECC bypass occurring during the entire period of accumulator discharge. Figure 48 compares the fluid density data with the TRAC calculation and shows that the code is also predicting bypass and is in relatively good agreement with the data. The mass

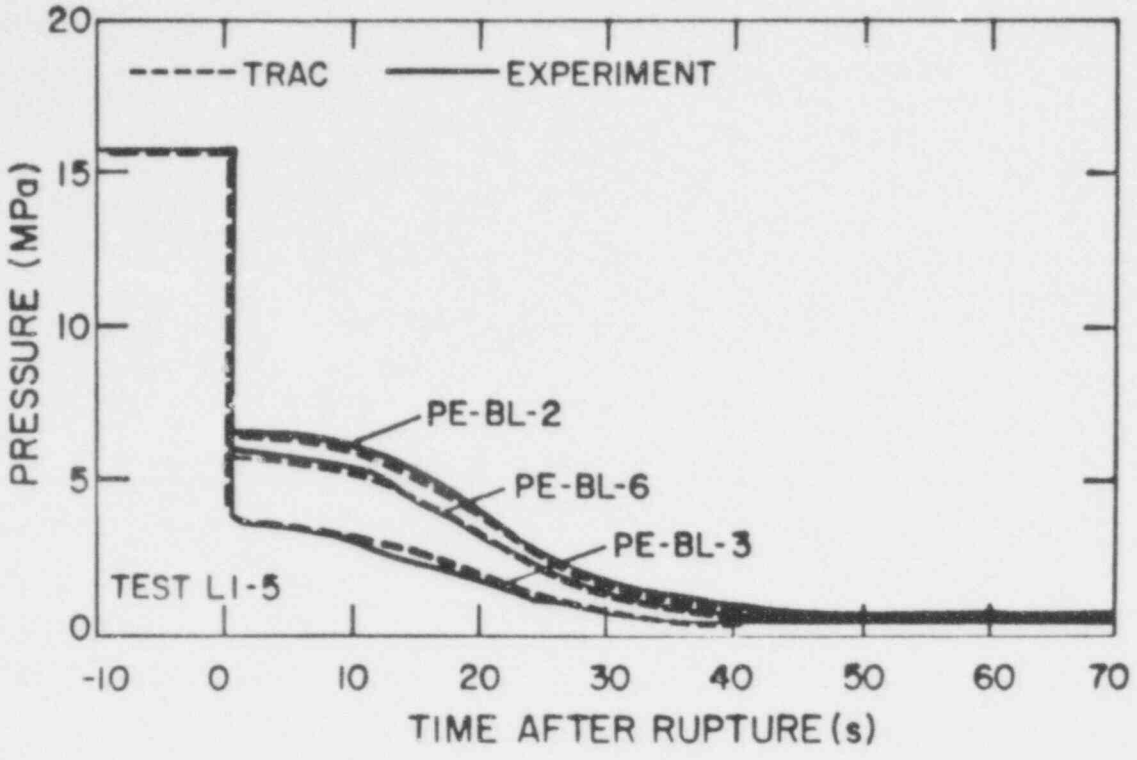

Fig. 45. LOFT Test L1-5: Pressure in broken loop hot leg.

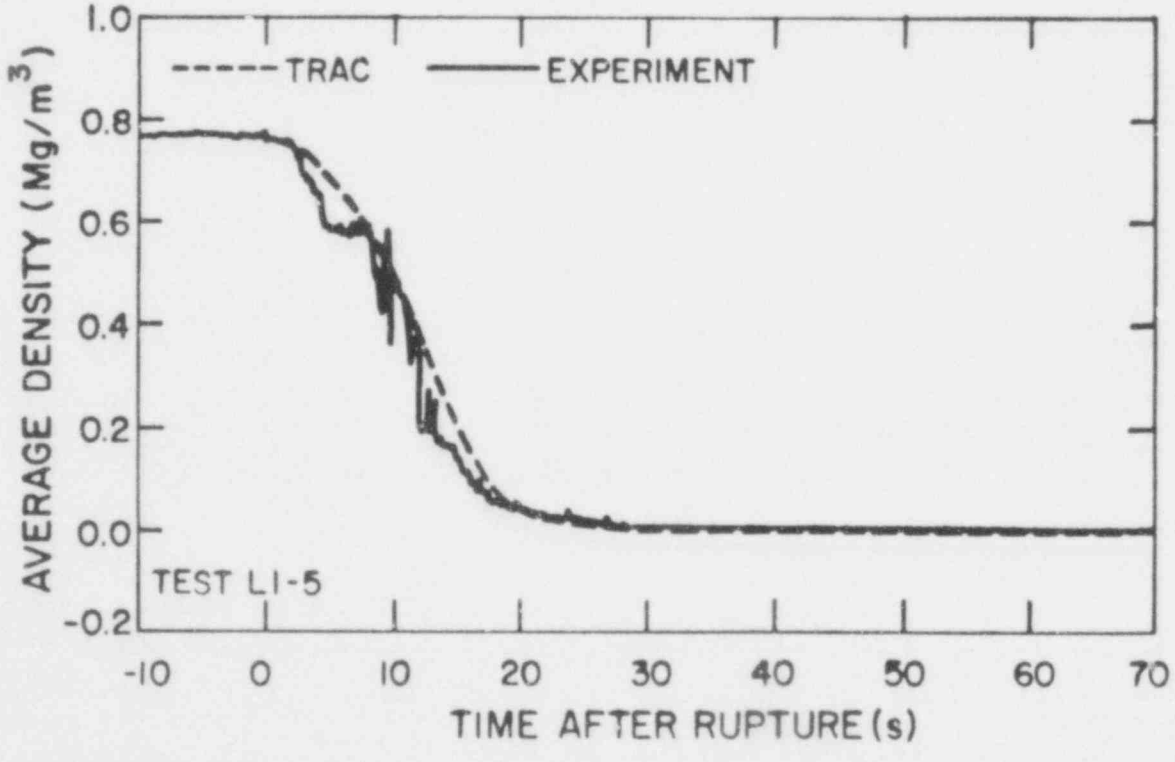

Fig. 46. LOFT Test L1-5: Average density in broken loop hot leg (DE-BL-2).

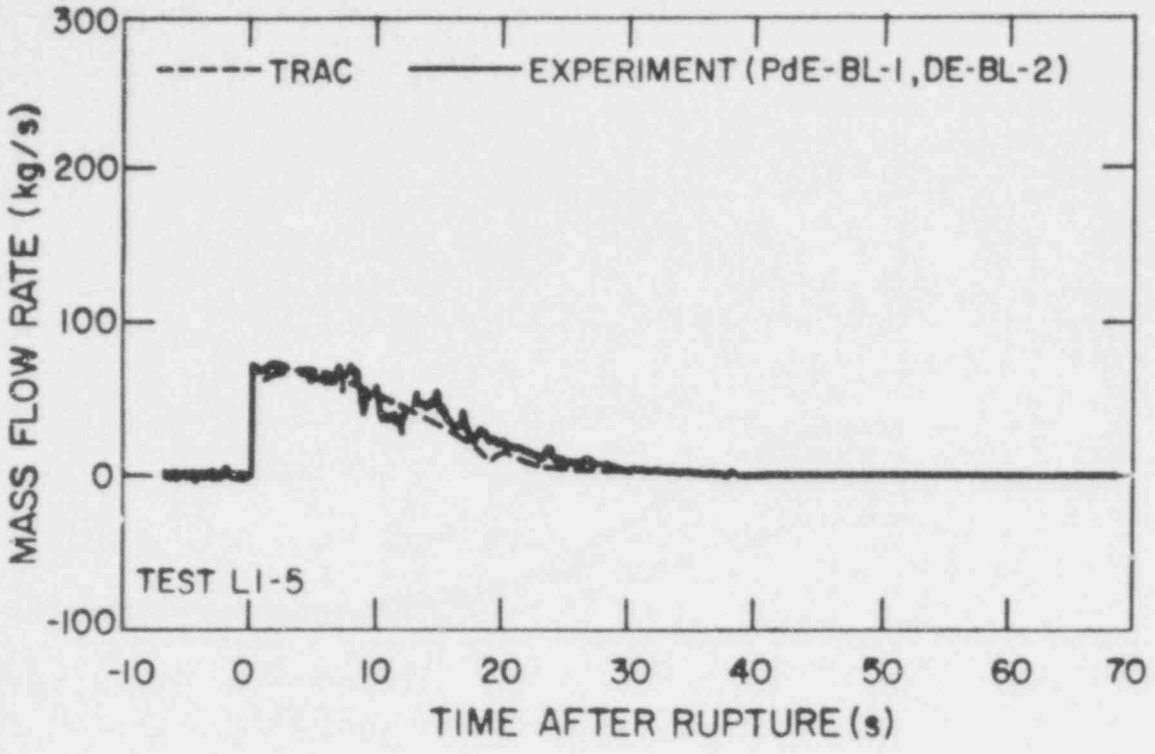

Fig. 47. LOFT Test L1-5: Mass flow rate in broken loop hot leg.

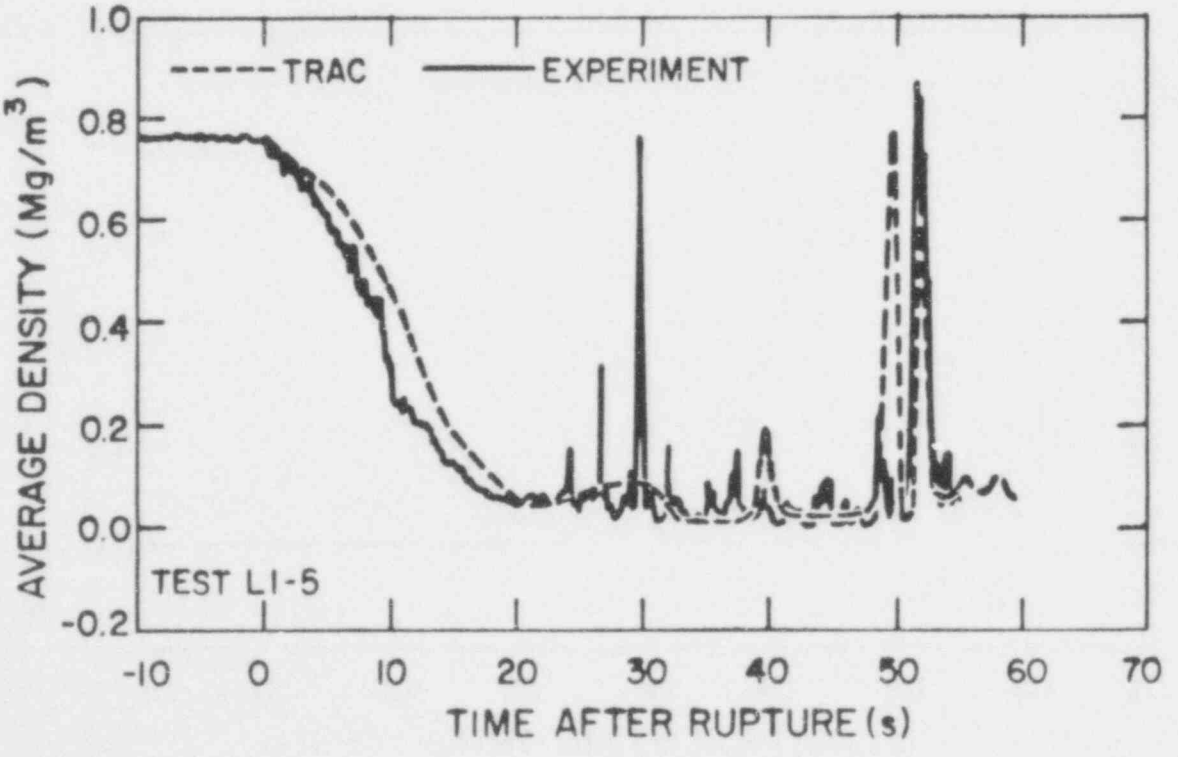

Fig. 48. LOFT Test L1-5: Average density in broken loop cold leg (DE-BL-1).

flow rate from this leg is given in Fig. 49. With this agreement between the measured and calculated discharge mass flow rates, it would be expected that the system pressure response would also be in good agreement. This is shown to be the case in Fig. 50.

Comparison with the fuel cladding temperature at the core midplane is given for two fuel assemblies. Figure 51 compares clad temperatures for assembly 1, which is a "triangular" assembly located at the outer core periphery and under the broken cold leg. Figure 52 compares clad temperatures for assembly 5, which is the center assembly. The experimental data show that for this nonnuclear test the clad temperature response is very similar for all locations. Namely, the clad temperatures follow saturation during roughly the first 30 s of blowdown, enter a dryout period during which the clad temperature increases due to stored energy in the fuel, and finally, rewet roughly 15 s after dryout. From these two figures it is obvious that the code is predicting dryout earlier than indicated by the exterior thermocouples. This calculated result appears to be due to the hydrodynamics modeling in TRAC and not to the heat transfer correlations. The calculated void fraction at the core midplane is given in Fig. 53, where it is seen that the core liquid fraction drops to essentially zero at the time of dryout. However, this void fraction result is in agreement with liquid level ("bubble plots") for fuel assemblies 1 and 5 as given in the experimental data report.[15] These plots show that the liquid level is below the core entrance after approximately 20 s. It is therefore not clear why the thermocouples show the clad to be at saturation until well after this time (about 30 s). Further investigation, both experimentally and computationally, is needed to resolve the question as to whether this apparent discrepancy is a result of the exterior mounted thermocouples ("fin effect"). The consequences of such an effect are extremely important in interpreting results from the nuclear test L2-2.

Figures 51 and 52 show that the rewet time is accurately predicted by TRAC. Since the rewet occurs when the injected ECC begins to "reflood" the core, it appears that the code is doing a satisfactory job of predicting the bypass/refill behavior. This

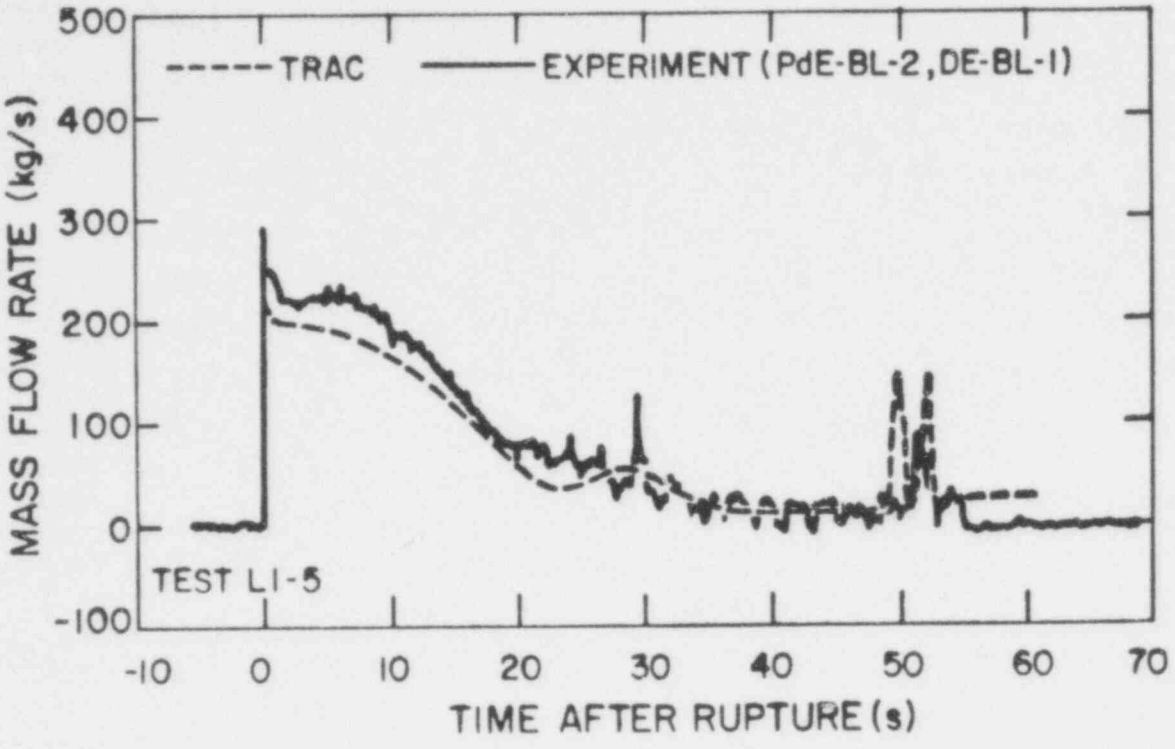

Fig. 49. LOFT Test L1-5: Mass flow rate in broken loop cold leg.

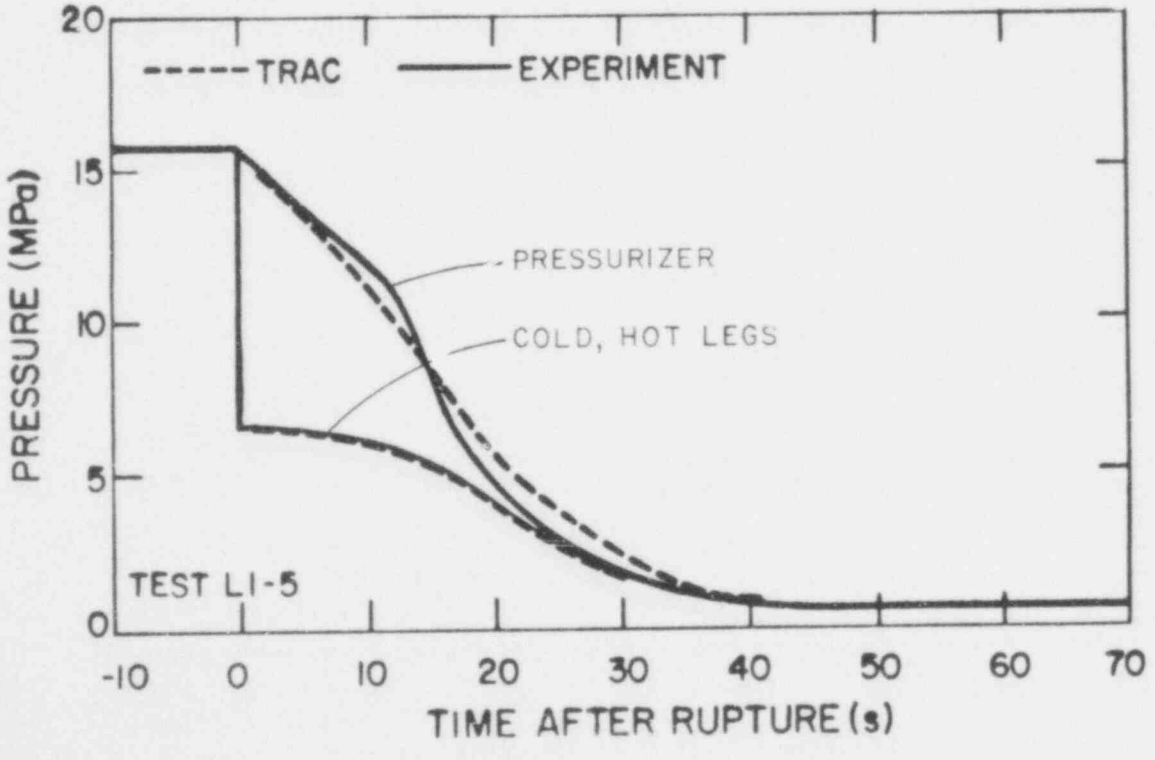

Fig. 50. LOFT Test L1-5: Pressure in intact loop cold leg, hot leg, and pressurizer.

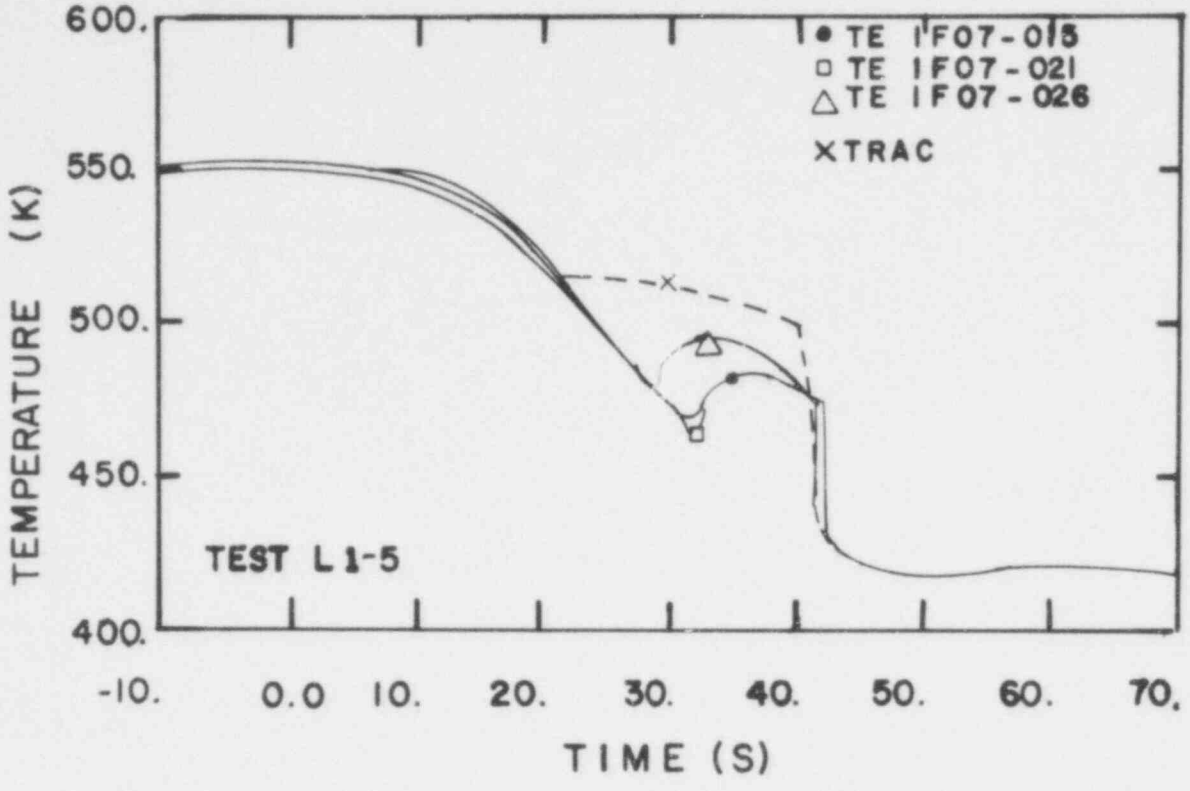

Fig. 51. LOFT Test L1-5: Temperature of cladding on fuel assembly 1, rod F7.

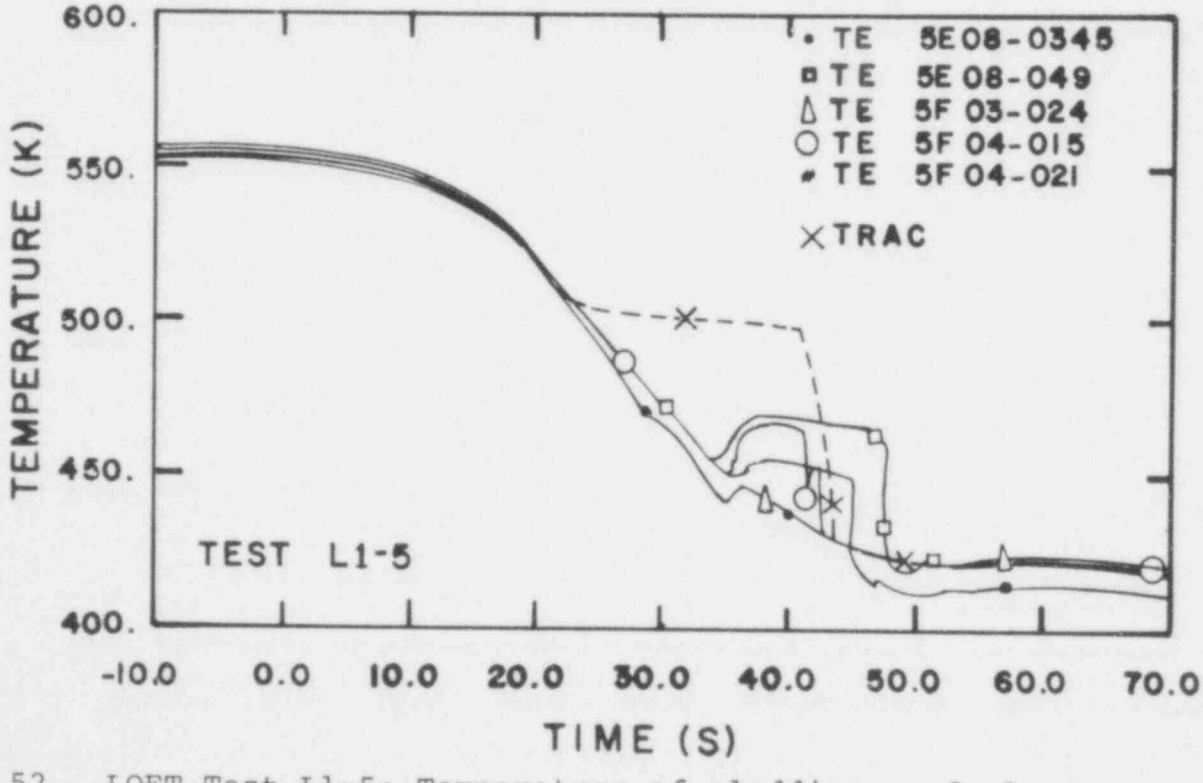

Fig. 52. LOFT Test L1-5: Temperature of cladding on fuel assembly 5, rods E8, F3, and F4.

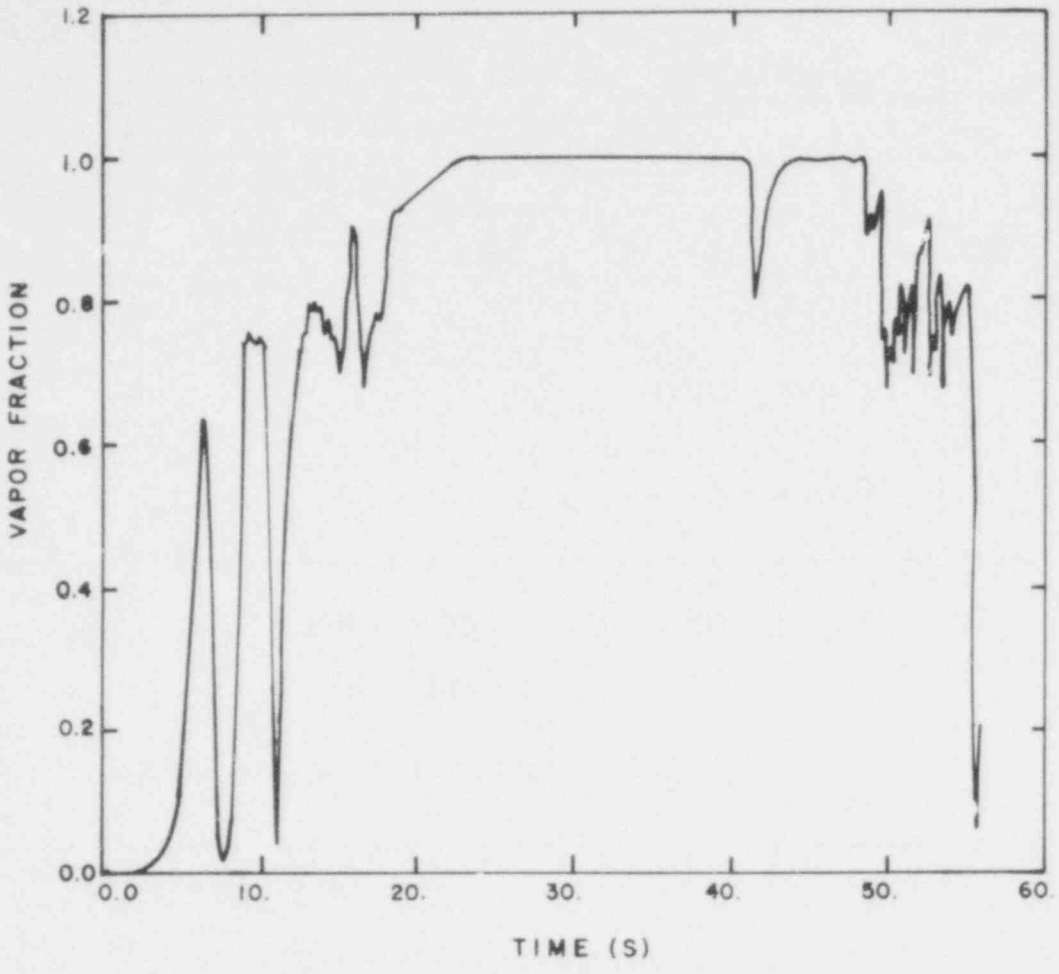

Fig. 53. LOFT Test L1-5: Calculated vapor fraction at core midplane.

is in agreement with the results of previous downcomer bypass/refill calculations.[16]

b. Calculation of LOFT Test L2-2

A pretest, "double-blind" TRAC calculation of the first LOFT Nuclear Test, L2-2, was performed by LASL. Test L2-2 was a 200% cold-leg break experiment run from a 50% power level of 25 MWt and an intact hot-leg temperature of 580 K.[17] Subsequent to this test, a posttest calculation was performed using the actual experimental initial conditions. Both calculations used exactly the same system noding. The only changes made were to the steam generator tube

area to achieve the measured fluid conditions and the use of the measured containment pressure as a boundary condition. The conclusions from these two calculations are that TRAC is, in general, satisfactorily representing the two-phase thermal hydraulics during blowdown, refill, and reflood. However, the experimentally measured peak clad temperature of 790 K was lower than both the pretest predicted value of 923 K and the posttest value of 880 K. It is also concluded that variations from the expected initial conditions used in a double-blind calculation can produce significant differences in the actual transient, especially in the core flow rate for a cold-leg break experiment.

The experimental initial conditions actually achieved for test L2-2 were somewhat different than the target values given in the Experimental Operating Specification (EOS).[18] The major differences were

1. the intact loop hot-leg temperature was 580 K rather than the EOS value of 587 K, and
2. the broken hot-leg temperature was 543 K rather than the expected 582 K.

These discrepancies produced a different system depressurization rate, and more importantly, a different core flow rate history in the "double-blind" pretest prediction than in the posttest analysis. This effect was further pronounced since the TRAC calculated pretest hot-leg temperature was 593 K. This difference is due to apparent inaccuracy of the published steam generator heat transfer area.

The calculated vessel upper plenum pressure history is shown in Fig. 54. The effect of the high hot-leg temperature in the pretest calculation is seen during the first 10 s. The posttest calculation is in excellent agreement with the experimental data during the entire transient, including the period of ECC injection. The RELAP4 pretest prediction has been included for comparison. Comparisons with measured accumulator LPIS and HPIS discharge flow rates show very good agreement with the data as presented in Figs. 55-57.

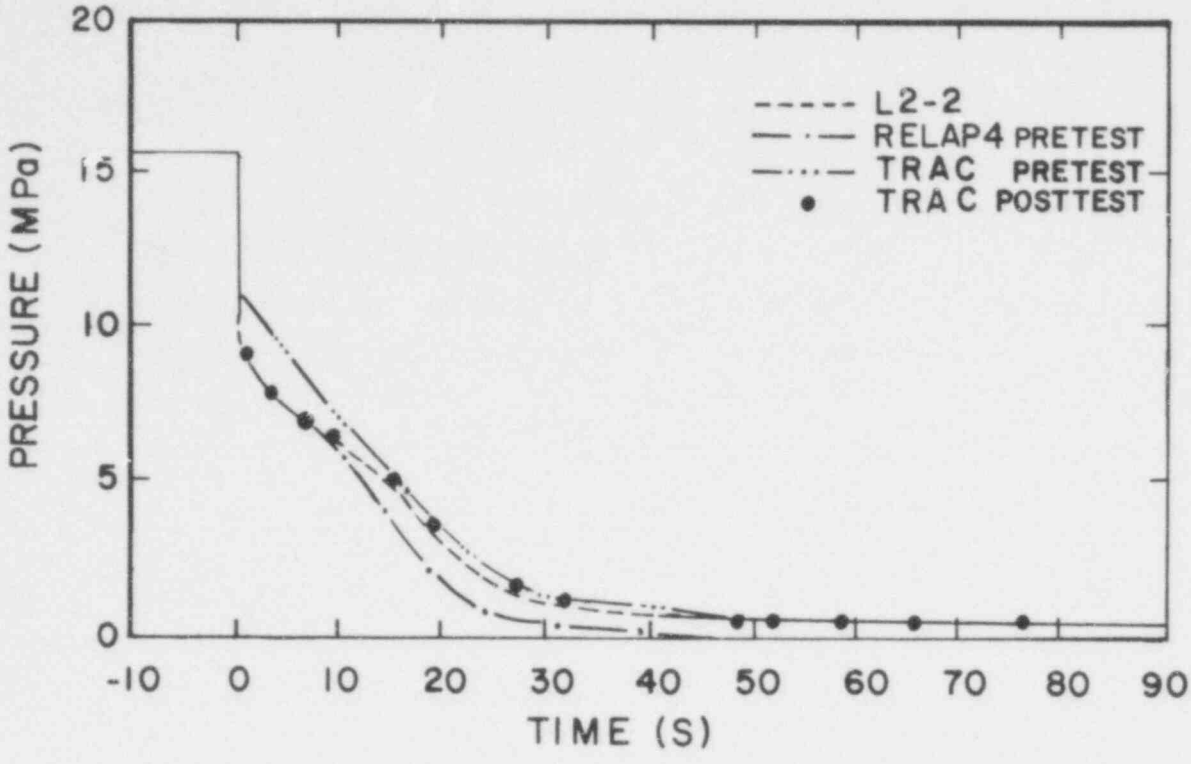

Fig. 54. LOFT Test L2-2: Pressure in upper plenum.

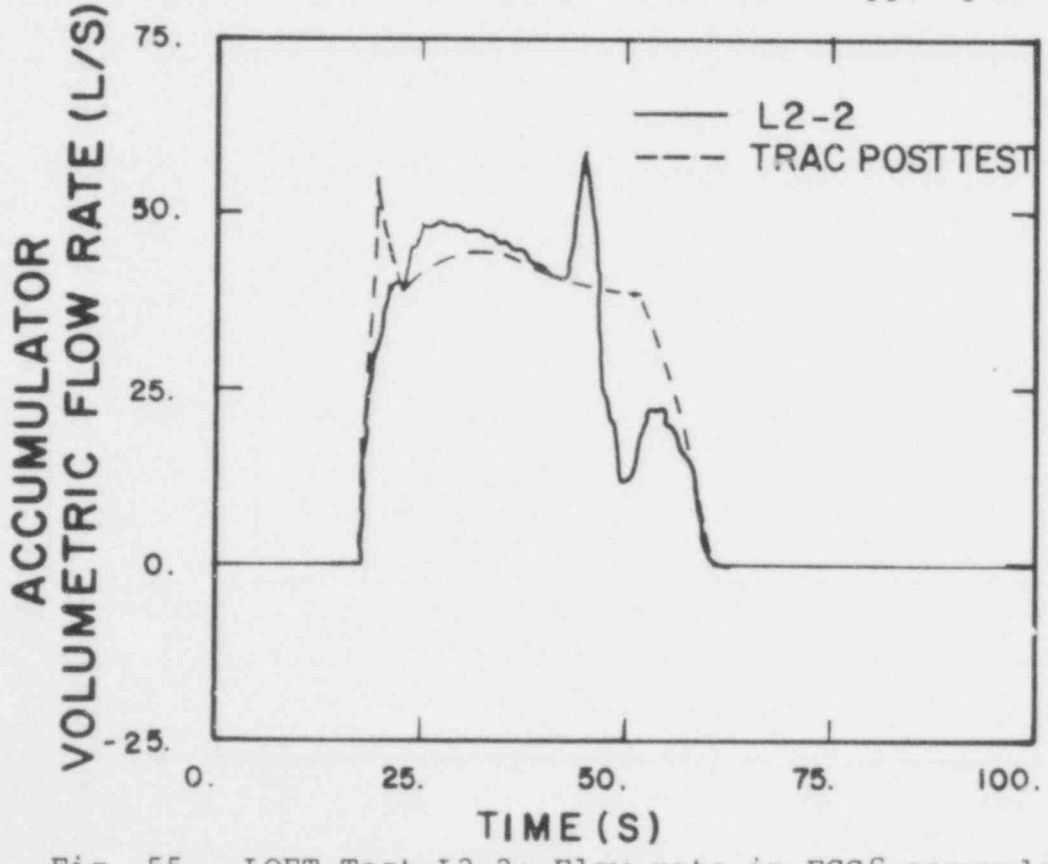

Fig. 55. LOFT Test L2-2: Flow rate in ECCS accumulator.

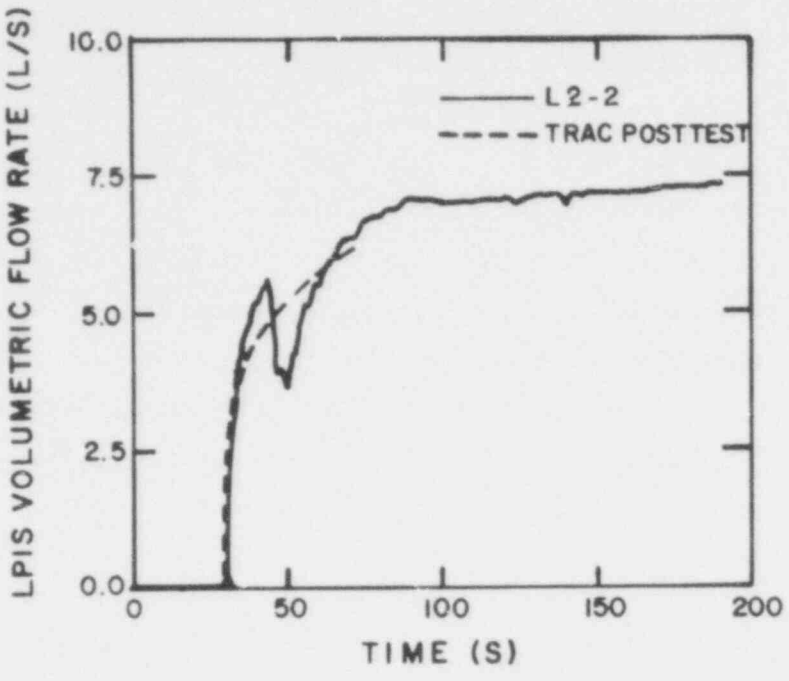

Fig. 56. LOFT Test L2-2: Flow rate in ECCS LPIS pump.

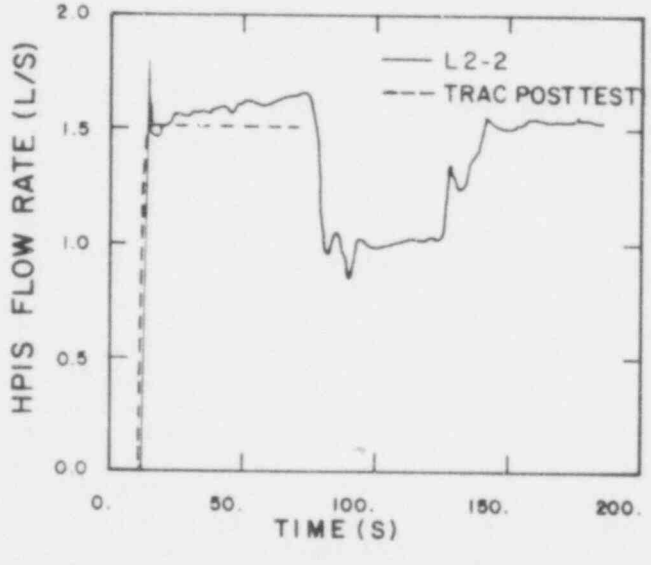

Fig. 57. LOFT Test L2-2: Flow rate in ECCS HPIS pump.

Figure 58 compares calculated peak clad temperature of the highest powered rod at the core midplane. As shown, the code overpredicted the measured peak clad temperature by 90 K and did not predict the sequence of rewets/dryouts that occurred between 6 and 30 s. There is, however, some concern that this unexpected rewet/dryout phenomena may be a result of the LOFT exterior thermocouples themselves. Moreover, comparisons at this location represent the largest disagreement between data and the calculation. Calculated times to quench for locations below the core midplane, even for high-power rods, are in good agreement with the data.

The calculated clad temperatures for lower power rods at the core outer periphery are also in very good agreement with data as shown by Fig. 59. This is true of all axial positions. This figure shows that the posttest calculation predicted the departure from nucleate boiling (DNB)/rewet result at 5-7 s, the dryout at 20 s when accumulator water enters the vessel, and the quench at 40 s. In general, the predicted time to DNB was very good for all the rods.

The major difference between the pretest prediction and posttest calculation was the core flow rate and the resulting clad temperature response. The core flow direction is determined by the relative balance between the broken loop cold-leg and hot-leg flow rates and as such is strongly affected by any deviation between expected and actual initial fluid conditions. The posttest calculation was able to predict the core flow reversal (return to positive) at 5 s that produced the clad rewets. Any further conclusions will have to await publication of the experimental data report and comparison with other calculated quantities.

D. Thermal-Hydraulic Research for Reactor Safety Analysis

(W. C. Rivard, T-3)

The research reported in this section focuses on several different areas in thermal hydraulics and on fluid-structure interactions.

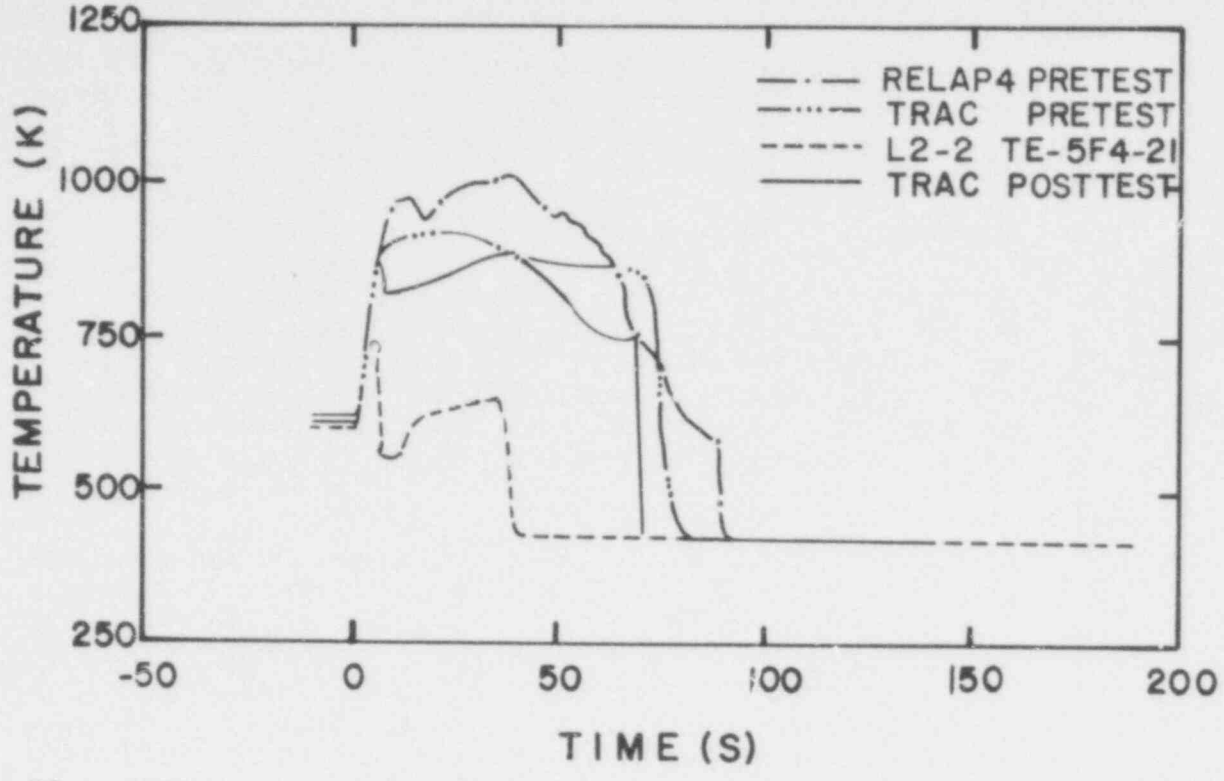

Fig. 58. LOFT Test L2-2: Temperature of cladding of fuel assembly 5, rod F4.

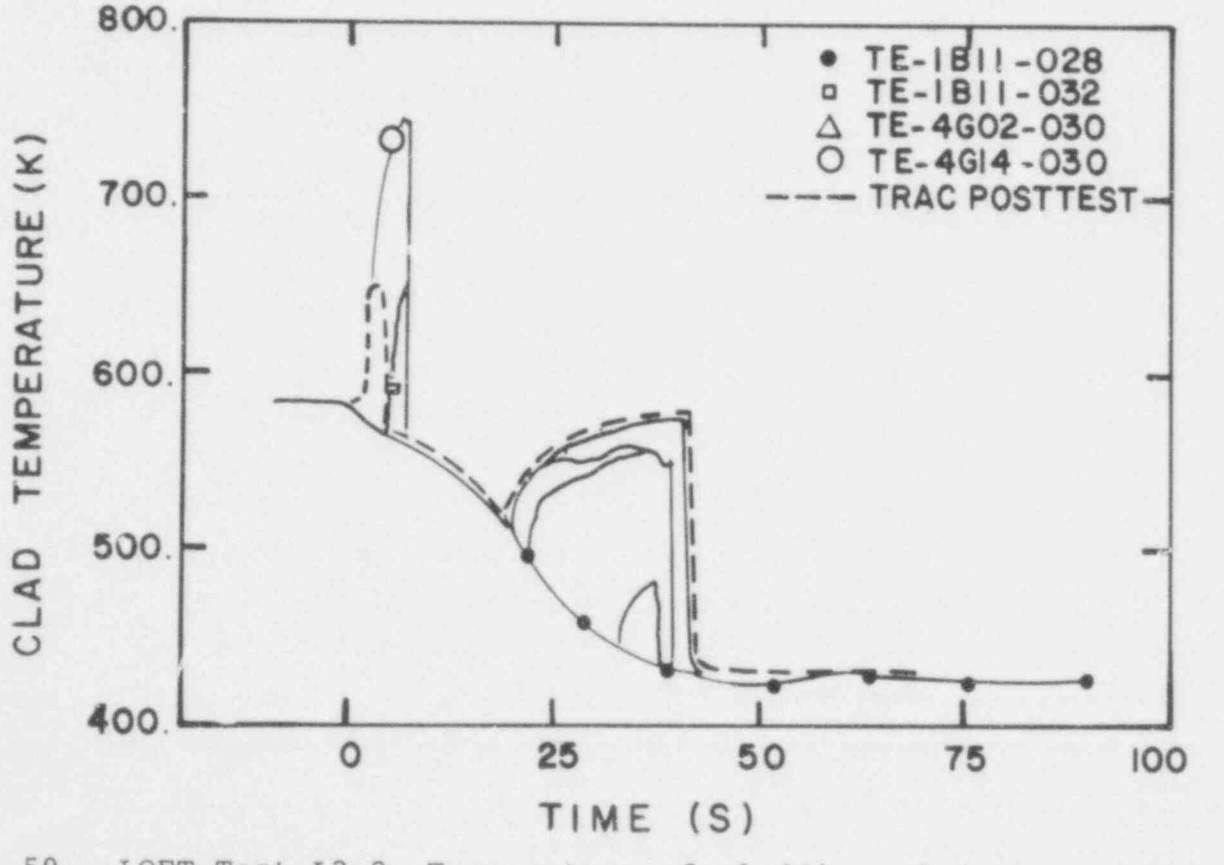

Fig. 59. LOFT Test L2-2: Temperature of cladding of fuel assembly 1, rod B11, and fuel assembly 4, rods G2 and G14.

1. Two reports have been written that describe the results of scaling and sensitivity studies in downcomer modeling. Calculations of selected CREARE experiments have been redone with a new momentum exchange formulation. The calculated delivery times are now in good agreement with data.

2. Two reports have been written that describe the coupled, fluid-structure, calculational results and solution methodology for the HDR reactor vessel. A third report describes the three-dimensional extension of the K-FIX code that was used in conjunction with the elastic shell code FLX to perform the calculations.

3. A computer-generated, self-contained movie has been produced through the MAPPER program that displays the HDR snapback calculated results in three-dimensional color perspective. Enhanced data displays such as this provide valuable assistance in understanding the vast amounts of data that are generated and provide an easily understandable medium for presentation of results.

4. A new project has been started to study the mechanics of droplet removal and re-entrainment in the upper plenum with a computational technique that follows the dynamics of individual droplets. The goal of this project is to describe the phenomena within the context of a two- or three-field treatment.

5. A milestone has been met for the addition of a seismic capability to SOLA-FLX.

1. Downcomer Dynamics

a. Scaling and Constitutive Relationships in Downcomer Modeling

(B. J. Daly and F. H. Harlow, T-3)

The transfer of momentum between phases in the interpenetrating flow of two materials has been examined by means of an "available-momentum" concept.[19] A transformation of coordinates is made to a system in which the two materials have equal momentum flux into a control volume, and the fraction of lost momentum in that volume is related to the interaction area per unit volume between the materials, f/r, in which f is a dimensionless quantity and r is a measure of local flow scale. The result of the analysis

is a drag coefficient between materials,

$$K = \frac{\rho_1 \rho_2 \alpha_1 \alpha_2 \, f|\vec{u}_2 - \vec{u}_1|}{r(\rho_1 \alpha_1 + \rho_2 \alpha_2)} . \qquad (9)$$

The subscripts number the two phases; ρ is density; α is volume fraction; and $\vec{u}$ is velocity.

The transfer of mass between phases is described in terms of a phase transition rate that is limited by the rate at which heat can be transferred to or from the region of evaporation or condensation. Heat transfer by turbulence plays a central role in the derivation.

Both of these constitutive relationships are examined in certain limiting cases where their relationship to previously derived forms can be ascertained. Some consequences of this new form for momentum exchange are described elsewhere in this report. The new form for mass transfer will be tested in circumstances for which phase transitions are thought to be more important than in the downcomer, namely in the NRC-sponsored experiments being performed at Northwestern University.

This study has also included a detailed investigation of the scaling properties of multiphase flow with various forms of constitutive relationships. The requirements for precise similarity among experiments at different scales are derived and shown not to exist in nature. Approximate similarity among experiments, however, can be achieved in circumstances that are described in detail. These results lead to suggestions for a series of experiments to verify the value of the scaling laws for extrapolation to full-scale PWR configurations.

b. Sensitivity of ECC Bypass and Lower Plenum Refill to Apparatus Scale Size

(B. J. Daly, T-3)

We have performed a numerical study using the K-TIF code to determine the effect of apparatus scale size on ECC bypass and

lower plenum refill in a PWR during a hypothetical LOCA. The principle conclusions of this study are the following.

1. The necessary conditions proposed in Ref. 19 for flow similarity at all scales under certain idealized flow conditions are verified.

2. ECC bypass and the delay time for lower plenum refill are sensitive to lower plenum pressure, when that pressure is greater than approximately 100 psia.

3. If one assumes a characteristic entity size for interfacial drag at full scale equal to that used in small-scale comparisons with experiment, then the importance of momentum exchange on ECC bypass and the timing of lower plenum refill becomes greater with increasing scale size.

4. The effect of mass exchange (and therefore ECC subcooling) on ECC bypass and lower plenum refill diminishes with increasing scale size.

5. ECC bypass and lower plenum refill are less sensitive to wall heat flux at large scale than at small scale.

6. During the refill process, the pressure in the downcomer may be less than the containment pressure. When this occurs, gas will flow from the containment vessel into the downcomer through the broken ECC injection port. In small-scale experiments, this gas is primarily air, while in the full-scale reactor the incoming gas should be primarily steam. The effect of injecting steam, rather than air, is to decrease the rate of refill of the lower plenum.

These results are described in Ref. 20.

c. Downcomer Calculations Using a Modified Drag Formulation

(B. J. Daly, T-3)

We performed a series of numerical calculations with the K-TIF code to compare with selected CREARF experiments[21] to test the accuracy of the momentum exchange function, Eq. (9), in predicting the time delay and rate of lower plenum refill for various ECC injection rates and subcoolings. The data for these

experiments are summarized in Table VI. Good agreement with experiment in regard to the time delay for lower plenum refill was obtained in all cases except the comparison with run H81. This good agreement is in contrast to previous calculations in which the calculated delivery time was consistently early by about 2 s. A typical comparison is shown in Fig. 60. However, as can be seen in that figure, the rate of refill is much greater in the calculations than in the experiment. This discrepancy seems to be related to the fact that the calculational lower plenum is modeled as a two-dimensional extension of the downcomer with the appropriate volume. Therefore, the lower plenum in the calculations is much deeper than in the scaled experiment, so refill proceeds at a rate more typical of a deep lower plenum, as can be seen in Fig. 61.

The lack of agreement with CREARE run H81 resulted from the fact that during the calculated refill process, water was reentrained by the steam and carried up into the downcomer. In this particular experiment, the steam flow was not ramped to zero, but to $J^*_{g,c} = 0.05$. Nevertheless, in plenum filling tests, Rothe and Crowley[22] show that, for saturated water, essentially complete delivery is obtained when $J^*_{g,c} = 0.05$ (constant). Therefore, to

TABLE VI

CREARE EXPERIMENTS FOR WHICH NUMERICAL COMPARISONS ARE MADE

CREARE ID	$J^*_{f,in}$	$J^*_{g,c}$ (t=0)	Subcooling (t=0)
H1	0.116	0.309	163°F
H15[a]	0.116	0.251	191°F
H23	0.058	0.308	167°F
H42	0.231	0.346	160°F
H81	0.058	0.167	14°F
H85	0.116	0.198	11°F
H97	0.232	0.271	39°F

[a]Deep Lower Plenum.

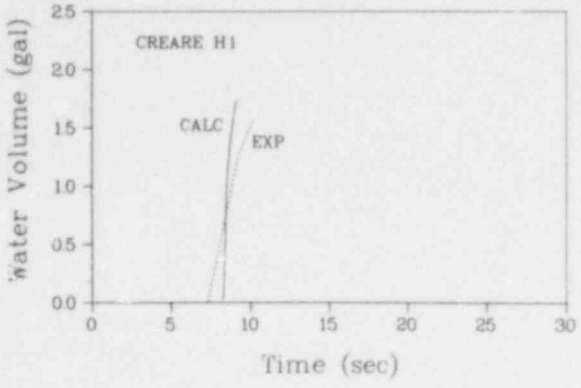

Fig. 60. A comparison of calculated and experimental refill curves for 60-gpm ECC injection and a scaled experimental lower plenum.

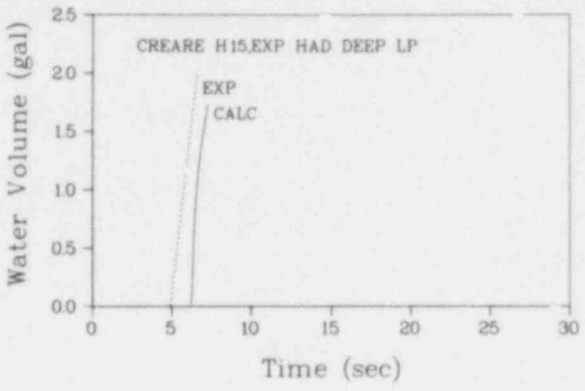

Fig. 61. A comparison of calculated and experimental refill curves for 60-gpm ECC injection and a deep experimental lower plenum.

test the effect of steam ramping on delivery, the calculation was repeated with $J^*_{g,c} = 0.05$ (constant). The results were as before, a very small amount delivered, with most of the water re-entrained into the downcomer. Several other variations in parameters were made to investigate the reasons for this failure to deliver water to the lower plenum. The ratio f/r was reduced from 35 (the value used in the above-described calculations) to 23; the wall temperature was reduced to the ECC temperature to prevent boiling in the falling water stream; and the calculation was repeated using a finer mesh resolution and including the hot legs as obstacles. None of these changes had any appreciable effect on refill history. Finally, the calculation was repeated with a much larger characteristic entity size, r. This calculation did result in lower plenum refill, with a time delay that was in fairly good agreement with experiment. We intend to repeat the calculations of the experiments listed in Table VI using a Weber number formulation for r.

2. Reports on Fluid-Structure Application

(W. C. Rivard and M. D. Torrey, T-3)

Several reports have been completed that describe coupled, fluid-structure calculations for the HDR reactor vessel and the code K-FIX(3D,FLX) that was used. Reference 23 describes the results of a series of calculations for blowdown that display

1. the importance of the coupled interaction on the core barrel dynamics and stress,
2. the utility of a two-dimensional fluid description for performing these calculations,
3. the influence of the bottom mass ring on the dynamics and stress, and
4. the sensitivity of the results to various structural nodings.

A second paper[24] focuses on the numerical methodology for coupling the three-dimensional, two-fluid code K-FIX(3D) to the three-dimensional elastic shell code FLX. In this paper, criteria are established for the numerical stability of the individual and coupled solution algorithms. Solution accuracy is also considered through a simple illustrative example. A user's manual that describes the extension of the K-FIX code[25] to three dimensions[26] has also been completed. K-FIX(3D) has been distributed to several users and will be sent to the NESC in January 1979.

3. Information Transfer Through Computer-Generated Films

(R. Griego and C. W. Hirt, T-3)

The NRC-RSR advanced code development program is producing a large variety of computational results relating to the safety of nuclear reactors. Intelligent presentation and interpretation of these results is fast becoming a serious problem. Consider, for example, the output from a one-dimensional code using a modest 100 node points. When run for 100 time steps there are 10 000 numerical values generated for each dependent variable. Fortunately, it is often sufficient to present only a portion of the computed results in the form of graphs showing the relationship of variable values

in space at a few select times, or the values at selected space points for all time. Clearly, graphs are more easily interpreted than long lists of numerical values. In some instances, however, such as those involving the propagation and interaction of waves or the superposition of several normal mode oscillations, the proper cause-effect or phasing relationships are not readily revealed by graphs. In these cases, it is advantageous to present the computational results in the form of a movie. That is, by plotting the data from each time cycle as a frame in a movie. This method not only provides a means of presenting all of the computed data, but also allows it to be viewed in its correct evolutionary sequence.

Computer-generated films of this type have been in use for approximately the last 15 years. Many of these films have increased their effectiveness by using a variety of sophisticated techniques such as color, three-dimensional perspective displays, hidden line removal, and shading algorithms. Nearly everyone would agree that a well-made, computer-generated film can rapidly deliver a large amount of useful information in an easily digestible form. However, this advantage is often lost when the viewer has not been properly oriented to the geometric arrangement, initial conditions, or other pertinent data that defines the specific problem to be presented. Thus, a serious limitation of these films is that they cannot be distributed or otherwise used without some form of explanation. Unfortunately, to include such descriptive material in a film typically requires the services of artists, animators, narrators, or other professionals, which can be time consuming and expensive.

Recognizing the need for an efficient and inexpensive alternative, we recently explored the possibility of generating self-contained films using only computer graphic material. For this purpose a computer graphics software package, MAPPER, recently implemented at LASL, seemed ideal.[27] The MAPPER program provides a simple-to-use tool for making computer-generated color slides and report quality figures. Its principal advantage over other software schemes is its use of many automated features and its easy-to-learn commands. At our request, the originator of MAPPER modified

the code to contain a set of additional commands essential for making movies (Fig. 62). For example, the STORE, COPY, and REPEAT commands permit the repetition of computed graphic data on successive movie frames. Furthermore, with simple FORTRAN additions, MAPPER can also generate dissolves, fades, zooms, animation, and other effects that previously were available only through expensive photographic processes. As a result, it is now possible for titles, graphs, diagrams, and other informative material needed in computer-generated movies (Fig. 63) to be effectively generated by anyone with a rudimentary knowledge of computer programming. With slightly more experience, the user can do simple animation to emphasize key features of a problem and to maintain viewer interest. Included in this category are zooms to selected regions of a figure, title roll-ups, shuttered windows, flashing symbols, moving arrows, etc. (Fig. 64).

To illustrate many of the basic movie capabilities of MAPPER, a short film was made showing the results from several calculations performed in support of the German HDR Blowdown Experiments.[28] This film, which is silent and in color, includes attractive titles, a description of the HDR facility, explanation of the display technique used to show the computed results, and specifications for each calculational sequence. Some animation was employed to emphasize selected portions of drawings and to show how three-dimensional perspective plots are used to display the computed results (Fig. 64).

MAPPER MOVIE COMMANDS

STORE

STOP STORE

RECALL

REPEAT

COPY

Fig. 62. Additional commands added to MAPPER program to allow the generation of movie frames.

At this time, the principal limitation of MAPPER is that it has no automatic features to generate three-dimensional drawings with hidden lines removed or with shading. Consequently, it is necessary to carefully select line drawings or to use

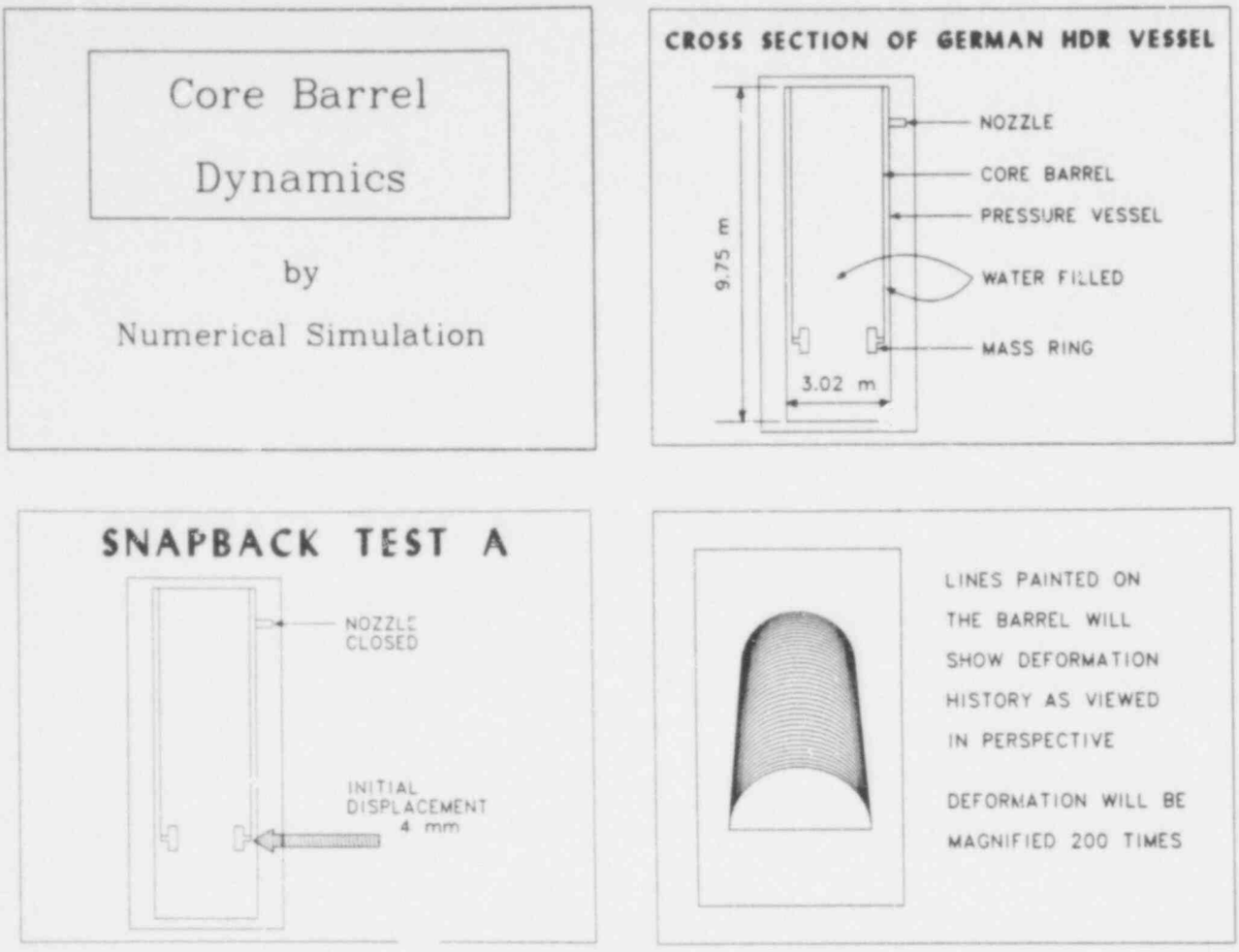

Fig. 63. Typical examples of informative material that can be added to movies using the MAPPEP program.

cross-sectional views to represent three-dimensional systems. In some cases, this limitation can be overcome by using a graphics tablet or other interactive technique to generate and digitize the desired drawings.

4. Droplet Spray Modeling

a. Droplet Removal and Re-Entrainment in the Upper Plenum

(H. M. Ruppel, A. A. Amsden, and F. H. Harlow, T-3)

A wind of steam carrying entrained water droplets passes through an array of vertical circular cylinders. The question of interest is to determine how much water is removed from the steam in comparison with the amount that is able to pass through the array. Two closely coupled processes are involved.

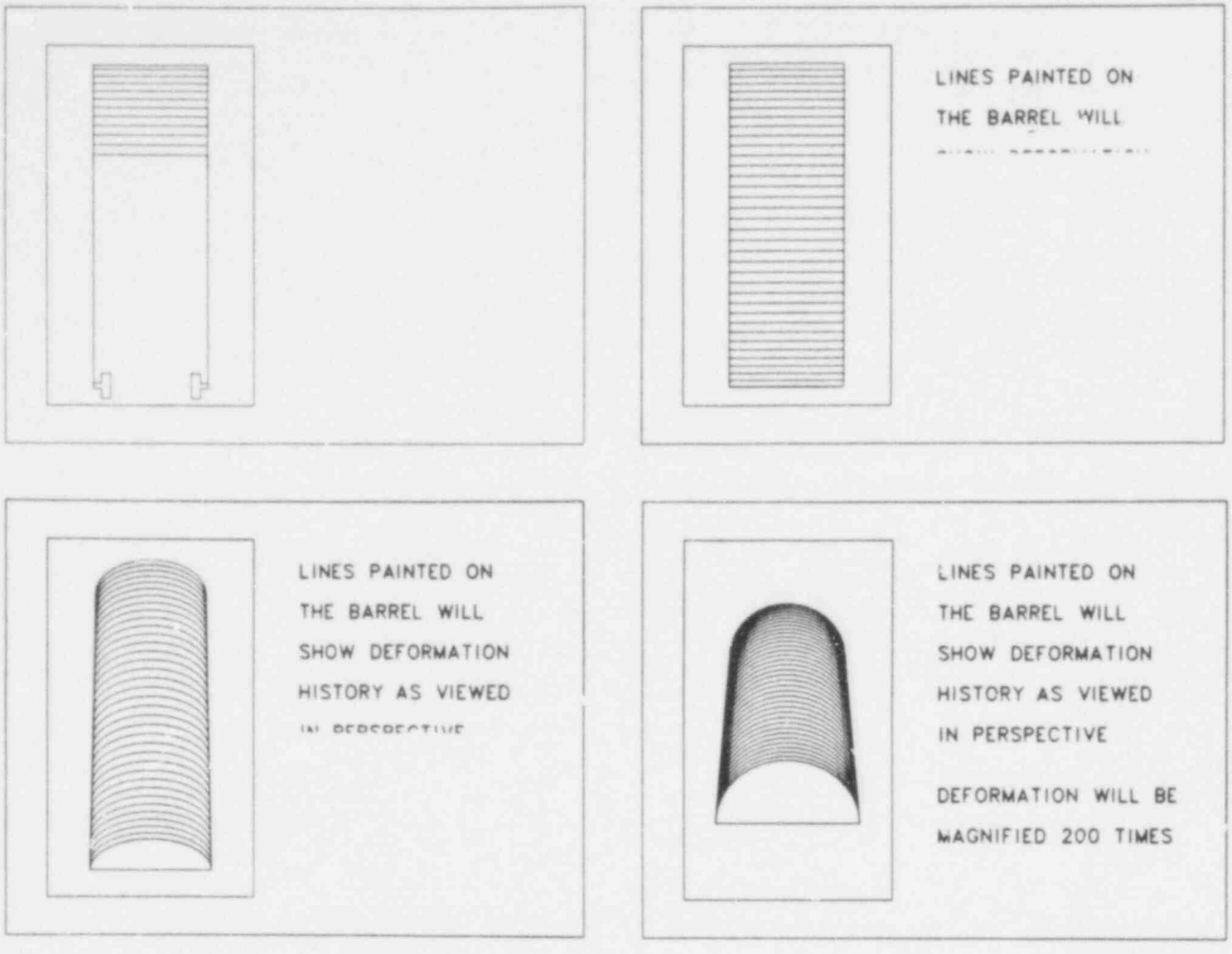

Fig. 64. Selected frames from an animated sequence showing how calculational results are to be presented in subsequent portions of a film.

1. Water drops collide with cylinders with a frequency that depends on the size of the drops, the size and placement of the cylinders, the mean flow speed, and various other factors.

2. Water that has collided with a cylinder may subsequently be removed by splash effects, re-entrainment from the film, or transport to the base of the cylinder as a result of gravity flow. The last is the net amount of water lost from the stream and is accordingly the quantity to be determined.

The first process has been investigated both theoretically and experimentally at other laboratories.[29-31] Theoretical studies follow droplet trajectories in the known flow field around a single

cylinder, and yield collection efficiency, defined as the ratio of water volume flux hitting the cylinder to the flux that would pass through the cylinder's position in its absence. Among other effects, it is found that smaller drops, which are more securely tied to the stream lines of gas flow, exhibit smaller collection efficiences, whereas the larger drops depart more readily from the curving stream lines and impinge with larger collection efficiencies. Experimental studies have been performed for a single cylinder with results that confirm the predictions and are being extended to arrays of cylinders for which analytical descriptions have not been accomplished.

The second process has received no theoretical investigation, but is the subject of experimental work at both Harwell[32] and LASL.[33]

The coupling between the two processes is especially important for an array of cylinders. Collection efficiency determines the water flux to the cylinder, impact influences the stability of the film, while re-entrainment from splash or shear stress on the film influences the number and size spectrum of droplets to be collected farther downstream.

Numerical studies for the first process have been carried out with considerable success for a spectrum of droplet sizes moving past two rectangular cylinders, using a computer technique developed by Dukowicz and Butler.[34] We are now in the process of using this technique to study the capture efficiency of a spectrum of drop sizes moving through several different arrays of circular cylinders. As a check, we have the analytic results for the single-cylinder capture efficiency to compare with the results from the full two-dimensional studies.

For the second process, the ZIA code, developed for three-dimensional downcomer studies, can be used to calculate the build-up of water film on a single circular cylinder, together with re-entrainment from the film back into the steam flow and the transport of water through the film to the base of the cylinder.

b. Droplet Spray Model with Phase Change

(J. K. Dukowicz and T. D. Butler, T-3)

In the last quarterly report,[34] we described a new numerical technique (embodied in the SOLA-SPRAY code), to calculate the dynamics of dispersed droplets in a gaseous environment. This methodology consists of a fully interacting combination of an Eulerian representation for the continuous phase and a Lagrangian particle representation for the droplets. The Lagrangian description avoids numerical diffusion of the droplets while permitting individual attributes such as droplet size, temperature, and composition to be statistically assigned for each particle.

The capability to calculate the dynamics of dispersed droplets with a spectrum of sizes will likely prove important in the analysis of current entrainment/de-entrainment experiments. In addition, it may prove useful in developing models for incorporation into TRAC.

The work previously reported dealt with problems in incompressible two-phase flow without phase change. We extended that methodology to include the effects of compressibility and phase change. In this report, we list the governing equations for this technique and outline the numerical procedure used in SOLA-SPRAY for their solution.

The current model permits the gaseous phase to have two species, the vapor and a noncondensible gas. The particles interact with the continuum phase by exchanging mass, momentum, and energy, as well as by volume displacement of the gas. The implicit numerical formalism used in our technique permits computation of the strong coupling between the droplets and gas which frequently occurs in fine sprays.

There are certain limitations in this technique. We assume that droplets are spherical and we neglect small effects such as the Basset force, virtual mass contributions, and nonuniform temperature within each droplet. In addition, collective effects between droplets and the effects of internal droplet circulation are neglected.

(1) Governing Equations

Omitting chemical reactions, the continuity equation for species α is

$$\frac{\partial\ \theta\ \rho_\alpha}{\partial t} + \underset{\sim}{\nabla} \cdot (\theta\ \rho_\alpha\ \underset{\sim}{u}) = \underset{\sim}{\nabla} \cdot\ \theta\ \rho D\ \underset{\sim}{\nabla} \left(\frac{\rho_\alpha}{\rho}\right) + (\dot{\rho}_\alpha)_p\ , \tag{10}$$

where θ is the void fraction, or the fraction of the volume occupied by the gas. The presence of the void fraction in this and the following equations accounts for the displacement effect of the particles. The last term $(\dot{\rho}_\alpha)_p$ is the source term giving the rate of change of density of species α due to change of phase of the particles. We assume that the droplets are composed of a single component so that

$$(\dot{\rho}_\alpha)_p = 0;\ \alpha \neq v$$

$$(\dot{\rho}_v)_p = -\ 1/V \sum_k \frac{dm_k}{dt}\ , \tag{11}$$

where the subscript v represents the vapor. The indicated summation is over all the particles in a subvolume V, which is taken to be the volume of a computational cell in the finite difference solution; m_k is the mass of particle k.

The fluid momentum equation is given by

$$\frac{\partial\ \theta\ \rho\ \underset{\sim}{u}}{\partial t} + \underset{\sim}{\nabla} \cdot\ (\theta\ \rho\ \underset{\sim}{u}\ \underset{\sim}{u}) = -\ \theta\ \underset{\sim}{\nabla}\ p + \underset{\sim}{\nabla} \cdot\ \theta(\mu\ \underset{\approx}{e} + \lambda\ \underset{\approx}{I}\ \underset{\sim}{\nabla} \cdot\ \underset{\sim}{u})$$

$$- \frac{1}{V} \sum_k D_k (\underset{\sim}{u} - \underset{\sim}{u}_{pk})\ , \tag{12}$$

in which $\underset{\sim}{u}_{pk}$ is the velocity of particle k and D_k is the particle drag function given by

$$D_k = 6\ \pi\ \mu r_k + 1/2\ \pi\ r_k^{\,2}\ \rho\ C_D |\underset{\sim}{u} - \underset{\sim}{u}_{pk}|\ , \tag{13}$$

where r_k is the particle radius and C_D is the drag coefficient. This form of the drag function assumes that the drag force is the sum of the Stokes' drag and the form drag.

The fluid internal energy equation is written as

$$\theta\rho\left[\frac{\partial I}{\partial t} + \underset{\sim}{u} \cdot \underset{\sim}{\nabla} I\right] = \frac{\theta p}{\rho}\left[\frac{\partial \rho}{\partial t} + \underset{\sim}{u} \cdot \underset{\sim}{\nabla}\rho\right]$$

$$+ \underset{\sim}{\nabla} \cdot \theta\left[K\underset{\sim}{\nabla}T + \rho D \sum_{\alpha} h_\alpha \underset{\sim}{\nabla}\left(\frac{\rho_\alpha}{\rho}\right)\right]$$

$$+ \theta\left[\frac{\mu}{2}\,\underset{\approx}{e} : \underset{\approx}{e} + \lambda(\underset{\sim}{\nabla} \cdot \underset{\sim}{u})^2\right]$$

$$+ \frac{1}{\forall}\sum_{k}\left[\left(D_k - \frac{1}{2}\frac{dm_k}{dt}\right)|\underset{\sim}{u} - \underset{\sim}{u}_{pk}| - q_k + (h - h_v)\frac{dm_k}{dt}\right] \tag{14}$$

in which q_k is the heat transfer rate from the gas to particle k, and h_α is the specific enthalpy of species α. The total gas enthalpy h is defined by

$$h = \frac{1}{\rho}\sum_{\alpha} \rho_\alpha h_\alpha \,. \tag{15}$$

The first term on the right-hand side of Eq. (14) represents the work due to the compression of the gas. The following terms take into account thermal conduction, enthalpy diffusion, and viscous dissipation within the gas. The remaining terms account for the rate of energy change due to the presence of particles. The first part of the term involving the relative velocity between the particles and the gas accounts for particle friction. The second part of this term accounts for the fact that vapor comes off at particle velocity and must be accelerated to gas velocity. The last term in the particle contribution is the enthalpy change due to the mixing of the vapor whose enthalpy must be brought from its initial enthalpy at evaporation to the local gas enthalpy.

The particle equations are

$$\frac{d}{dt} \underset{\sim}{x}_k = \underset{\sim}{u}_{pk} \, , \tag{16}$$

$$\frac{d}{dt} m_k \underset{\sim}{u}_{pk} = - \frac{m_k}{\rho_p} \underset{\sim}{\nabla} p + D_k (\underset{\sim}{u} - \underset{\sim}{u}_{pk}) \, , \tag{17}$$

and

$$m_k \frac{d\, h_{pk}}{dt} = q_k + (h_v - h_{pk}) \frac{dm_k}{dt} \, , \tag{18}$$

where p_k is the particle density and h_{pk} is the specific enthalpy of particle k. The pressure gradient term in the momentum equation is usually small but it is retained for consistency with the corresponding term in the two-fluid equations.[38] The last term in the energy equation represents the energy required for phase change (the latent heat).

To complete this set of equations we need a model to specify the phase change rate. We start from the assumption that in thermal equilibrium the droplet is at its wet-bulb temperature T_{WB}. The equilibrium is a balance between heat transfer to the droplet and the latent heat carried away by the vapor or absorbed by the droplet

$$(h_v - h_{pk}) \frac{dm_k}{dt} = - q_k \, . \tag{19}$$

It can be expected that a large portion of the droplet lifetime is spent while in this equilibrium. However, the droplet temperature will go through a transient whenever its temperature differs from T_{WB}. For this portion of its lifetime we assume that

$$m_k \frac{d}{dt} (C_{pk} T_k) = \eta (T_{WB} - T_k) , \tag{20}$$

and

$$(h_v - h_{pk}) \frac{dm_k}{dt} = - q_k + \eta(T_{WB} - T_k) \ , \tag{21}$$

where T_k is the droplet temperature, assumed to be uniform within the droplet, and C_{pk} is its specific heat, and η defines a characteristic time constant for droplet temperature change. The heat transfer q_k is obtained from an empirical correlation;[39] it can be expressed in the form

$$q_k = h^*(T - T_k) \ , \tag{22}$$

where T is the local gas temperature. The parameter η is then deduced from Eq. (21):

$$\eta = h^* \left(\frac{T_{SAT} - T}{T_{SAT} - T_{WB}} \right) , \tag{23}$$

where T_{SAT} is the saturation temperature.

(2) Method of Solution

Briefly, the solution procedure through one time cycle in SOLA-SPRAY is accomplished in the following way.

1. Intermediate values of specific internal energy are obtained from Eq. (14) omitting the conduction, enthalpy diffusion, and particle contributions.

2. New particles are injected into the computing region.

3. Characteristic evaporation temperatures T_{SAT} and T_{WB}, together with the rate of change of T_{WB} with gas temperature ($\partial T_{WB}/\partial T$) are computed.

4. Phase change is calculated using a predictor-corrector scheme to allow accurate calculation for cases with strong phase change. In the predictor phase, phase change is calculated using previous values of T and T_{WB} and this is used to predict new values of T and T_{WB}.

5. In the corrector phase, final values for the particle radii, temperatures, and phase change contributions to mass and energy are calculated.

6. The specific internal energy is then updated for conduction, enthalpy diffusion, and all contributions due to the presence of particles, such as phase change, heat transfer between phases, enthalpy of mixing between the vapor and the gas, and particle friction.

7. Equation (16) is used to update particle positions using velocities from the previous time step. The new void fraction is then computed.

8. Again, using a predictor-corrector method, the particle drag function is evaluated and intermediate particle and gas velocities are obtained using a linearly implicit technique.

9. The final advanced time velocities, pressures, and total densities are obtained by iteration using a technique similar to that used in RICE.[40]

10. The species densities are then obtained using Eq. (10).

11. Finally, the particle velocities are updated to account for changes in gas velocities and pressures obtained in the iteration.

In the coming months, we plan to refine the phase change models and incorporate the droplet algorithm into an ICED-ALE code to permit calculations that include arbitrarily shaped geometries.

5. Hydroelastic Response of a PWR Core Barrel to Seismic Accelerations

(C. W. Hirt and L. R. Stein, T-3)

The internals of a PWR would be subject to highly transient, asymmetric loads in the event of a LOCA. To quantitatively assess the consequences of such loads, we are developing two numerical methods for computing coupled fluid-structure dynamics. In one method, SOLA-FLX, the downcomer or annulus region surrounding the core support barrel is treated as a two-dimensional region whose thickness (the radial direction) may change as a consequence of core barrel deformations.[35] The barrel dynamics are computed by finite-difference approximations to a set of three-dimensional shell equations.

In the second method, fully three-dimensional fluid and structure equations are solved. For this purpose, a three-dimensional

version of the K-FIX code[25] has been coupled to the solution method for the elastic shell equations.[26] Unfortunately, the full three-dimensional method is considerably more expensive to operate so that it has been primarily used as a check on the accuracy of the two-dimensional method.[23]

A variety of SOLA-FLX calculations illustrating the dynamics of model core barrels subjected to LOCA and mechanical loads have been previously reported.[12]

For PWR safety analysis, however, current licensing practice requires the consideration of possible earthquake-induced loads. In particular, it is of interest to have a means of predicting the response of pressure vessel internals to seismic disturbances. Because an earthquake is a potential source of a LOCA, it is desirable to have the seismic load capability in SOLA-FLX where the combined effects of an earthquake and LOCA may be simultaneously evaluated.

A seismic disturbance is assumed to be given in the form of time histories for horizontal (SX,SY) accelerations. Vertical (SZ) accelerations could also be incorporated but are not expected to significantly influence core barrel dynamics, which is currently our primary concern. Specifically, these accelerations are those felt by the pressure vessel, which is assumed to be a rigid structure. The equations of motion for the internal structure (e.g., the core support barrel) and fluid in the vessel are transformed to a coordinate system moving with the vessel. This coordinate system is not an inertial one and therefore the transformed equations have body accelerations appearing in them that are equal and opposite to the vessel accelerations. In this coordinate system all boundary conditions, including those describing the fluid-structure coupling, remain unchanged. Thus, the use of the transformed coordinate system provides a relatively easy way to account for seismic effects.

To illustrate the seismic capability of SOLA-FLX we have performed several calculations using a rectilinear, harmonic acceleration, $SX = g \cos \Omega t$. The amplitude was taken to be one g (g =

acceleration of gravity) in accordance with the maximum acceleration required for a reactor to still be safely shut down. The frequency of shaking was 5 cycles/s, which is in the range of typical earthquake frequencies responsible for damage to large structures.[36] In addition, the acceleration was assumed to start impulsively at its maximum value to ensure an extreme case for test purposes. For this illustration, the vessel and core barrel dimensions used were those of the German HDR facility being prepared for large-scale blowdown tests and eventually for some simulated seismic tests.[37] The cylindrical vessel has an internal radius of 1.484 m, in which a cylindrical barrel 1.318 m in radius is hung from the top end plate. The barrel is 0.023 m thick and 7.47 m long. In the HDR tests, a mass ring weighing 12 tons will be attached to the bottom of the barrel to represent the influence of fuel rod bundles and other components that would be attached to a core barrel in a real reactor. For calculations described here the mass ring has been omitted from all calculations in order to simplify the analysis. Its presence or absence does not affect the basic seismic capability that we wish to illustrate.

Because the seismic acceleration in these tests is rectilinear, the fluid and structural responses are symmetric about a diameter parallel to the acceleration. For this reason we need only compute one of the symmetric halves. Furthermore, we have simplified the problem by neglecting the lower plenum. In its place we assume a flat rigid cap across which the end of the core barrel is free to slide. This is done because the two-dimensional SOLA-FLX code cannot exactly account for the three-dimensional effects arising from the lower plenum or core regions. However, the fluid in the downcomer annulus, which is well represented in the code, is responsible for an overwhelming portion of the coupled fluid dynamics. Therefore, the two-dimensional model used in SOLA-FLX should be a relatively good approximation. Nevertheless, a three-dimensional calculation with the K-FIX(3D,FLX) code will be performed to check the two-dimensional results.

In the first example problem, the cylindrical barrel is shaken in air. This calculation provides a check on the elastic shell

dynamics in the absence of any fluid dynamics. Figure 65 shows the radial displacement history of a point near the free end of the barrel. The barrel is executing beam-like oscillations with period 28 ms (35.71 cycle/s) added to a sinusoidal displacement having the 200-ms period (5 cycles/s) of the driving acceleration. This result for the fundamental beam-like frequency is in excellent agreement with earlier calculations that investigated the response of the barrel to locally applied lateral loads.[12]

Seismic shaking appears to be an excellent means of generating the fundamental beam-like mode. This should not be surprising, because the reaction acceleration felt by the barrel is axially uniform and is therefore most likely to excite this mode.

Further confidence in the computed results may be obtained from a simple analytical model. Let us assume the barrel is a simple harmonic system with frequency ω (the beam frequency). Application of a driving acceleration proportional to cos Ωt leads to a displacement history proportional to $(\cos \omega t - \cos \Omega t)/(\omega^2 - \Omega^2)$. This is the type of behavior observed in Fig. 65.

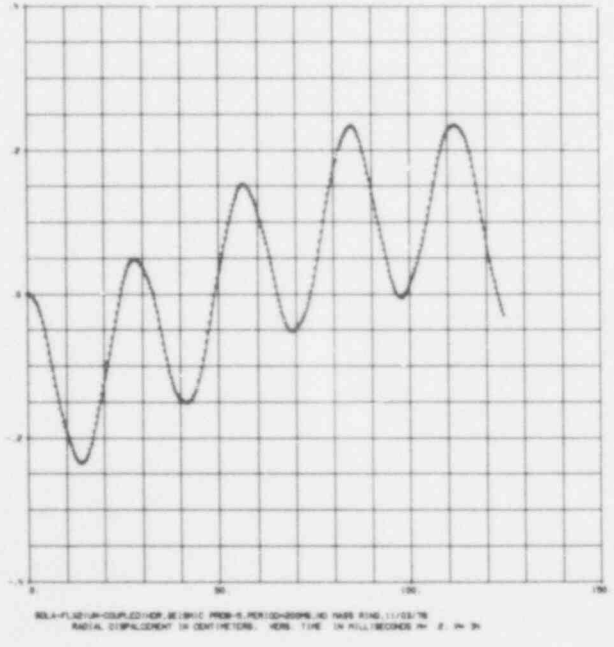

Fig. 65. Radial displacement at bottom of barrel, when shaken in air.

To check the hydrodynamics without structural influence, a calculation was performed in which the core barrel was held rigid. In this case, we expect pressure waves to bounce back and forth around the downcomer annulus, with period $2\pi R/c$ = 5.8 ms. Figure 66 shows this to be the case. We also note from this figure that the oscillations initially have a mean value of -0.13 bars, which is the value expected for a hydrostatic pressure field generated by a constant acceleration of magnitude g. Of course, in the present case, the acceleration

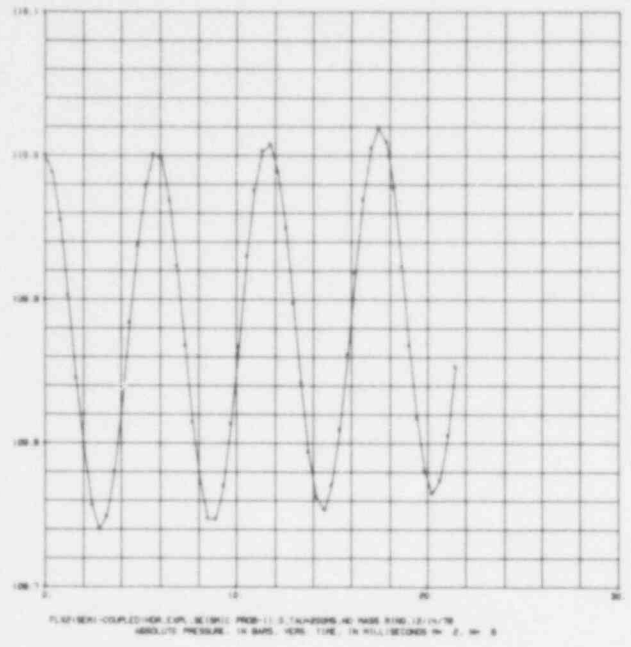

Fig. 66. Pressure history in annulus with rigid barrel.

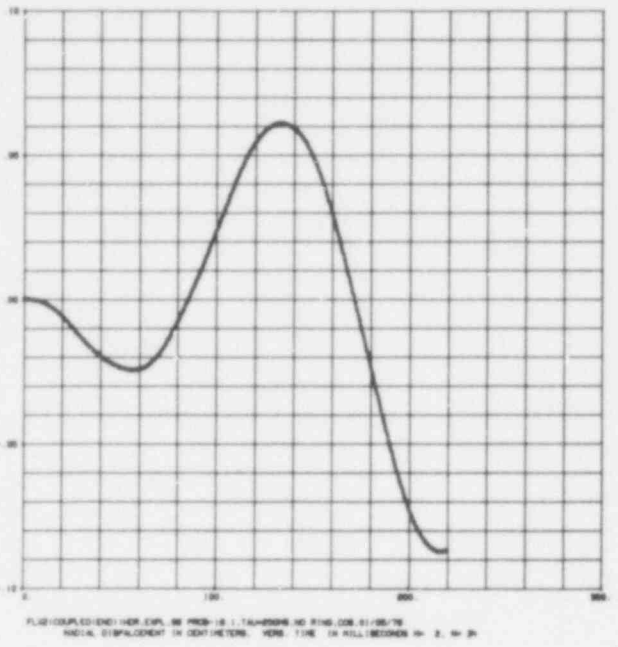

Fig. 67. Radial displacement at bottom of barrel, when shaken in water.

magnitude is changing according to g cos Ωt and Fig. 66 shows that the mean value of the oscillations is following this behavior.

Finally, Fig. 67 shows the displacement history for a point near the bottom of the barrel when full fluid-structure coupling is included. The barrel motion again appears to be primarily in the beam-like mode, but the presence of the water significantly reduces the frequency of this oscillation. The displacement history has the general time dependence observed in the air test, cos ωt - cos Ωt, except that now ω is much closer to Ω, which produces a more pronounced beating as the phase difference (ω - Ω)t runs between even and odd multiples of π. A crude hand calculation shows that a frequency of 6.45 cycles/s (period 155 ms) when used in (cos ωt - cos Ωt) produces a reasonably good approximation to the observed time dependence in Fig. 67. Using this value we estimate the maximum displacement at the bottom of the barrel will be 0.1 cm.

Pressure histories obtained in the coupled calculation exhibit a high-frequency oscillation superimposed on the variations expected from the mean dynamics of the system. These oscillations are clearly shown in the expanded scale of Fig. 68 for the first few milliseconds of the calculation. The origin of these oscillations is easily traced to horizontal oscillation of the barrel axis about the axis of the pressure vessel. If the barrel were treated as a rigid cylinder that is not clamped at the top, we would expect to see this type of oscillation arising from the compressibility of the water in the surrounding annulus. The water acts like a pair of springs resisting the barrel motion as schematically shown in Fig. 69. A simple calculation gives the period of this oscillation as 1.03 ms. From Fig. 68 the observed period is computed to be 0.64 ms. The shorter period observed is associated with the additional elastic stiffness of the barrel that is rigidly clamped at its upper end.

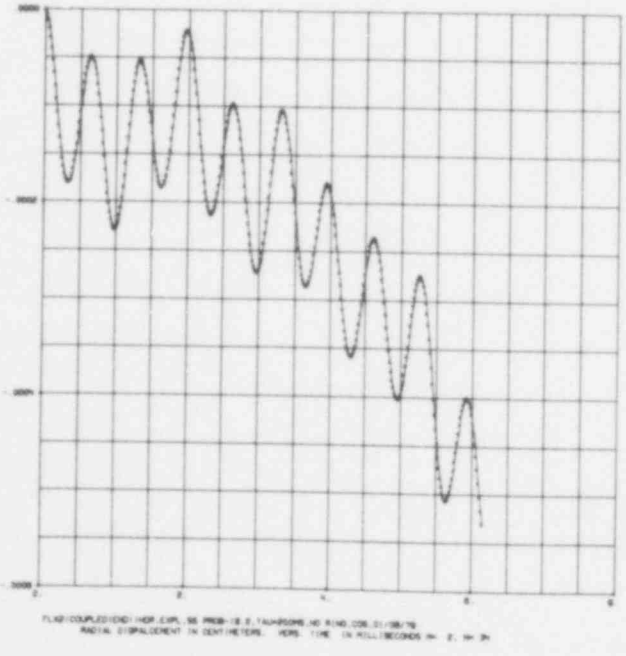

Fig. 68. Radial displacement at bottom of barrel when shaken in water, showing high-frequency oscillations.

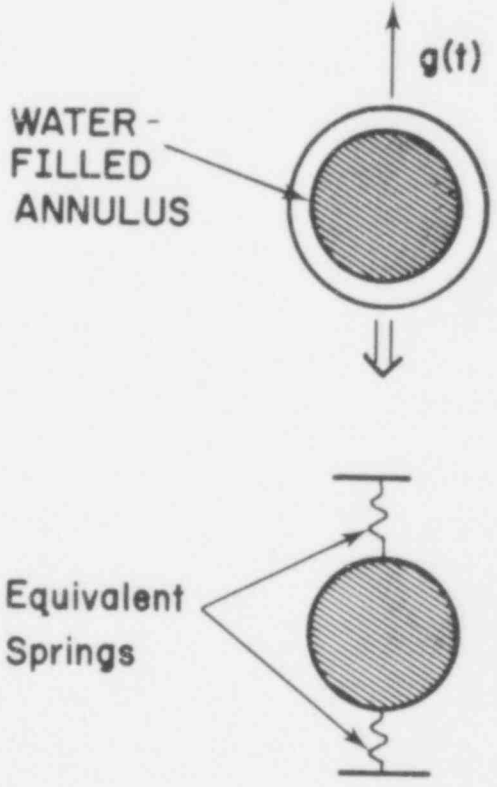

Fig. 69. Schematic of equivalent mechanical problem responsible for high-frequency oscillations.

E. LWR Experiments

(H. H. Helmick and W. L. Kirchner, Q-8)

The objectives of LASL's LWR Safety Experiments Program remain to provide experimental support for model development activities and to develop advanced instrumentation techniques. This program is conducted in close coordination with code and model development efforts at LASL and the multinational 2D/3D refill/reflood program for which advanced instrumentation is being developed.

The stereo lens system to be used at the PKL facility in Germany is mechanically complete; however, adjustments of optical components are being made prior to shipment to Germany in an effort to improve image quality. Fabrication of the heat pipe for the optical probe to be used at the Japanese Atomic Energy Research Institute (JAERI) is complete. Assembly of the optical components is in progress. The steam loop for testing each probe is now equipped for remote control operation and is available for use as the probes are completed.

Droplet de-entrainment studies are continuing in an existing wind tunnel, while assembly of a larger tunne is under way. The evaluation of a laser droplet velocity and sizing instrument is nearing completion. Development of a uniform drop generator has also been undertaken. Expansion of the PDP-11/34 computer data acquisition system continues as well as software development for video image analysis.

1. Video Stereogrammetry

(C. R. Mansfield, J. F. Spalding, D. B. Jensen, and P. F. Bird, Q-8)

a. Probe Development

The prototype stereo lens for use at PKL has been completely assembled. Testing has begun on the optical bench and in the de-entrainment facility to quantify the optical performance of the lens.

The initial results indicate that the constrast in the image is significantly lowered on the large number of lens elements required. The curvature of field also increased with the number of

elements. In addition, the illumination provided by the fiber optics was lower than expected. Each of these problems can be delt with to some degree, however. For example, illumination is being improved by using a larger fiber optics bundle and a brighter lamp.

Heat conduction and temperature tests have been run on a prototype heat pipe 3.5 m in length which simulates the JAERI probe. These tests are discussed in detail in the next section of the report. The heat pipe is capable of operating with a heat load of 1 100 W using methanol as the working fluid and more than 2 400 W using water as the working fluid. When methanol is used, the heat pipe performs isothermally at a heat load of 150 W and maintains the optical channel at a temperature of about 20 K above the inlet water temperature. Heat loads expected at PKL and JAERI are 50 W and 150 W, respectively.

The first JAERI probe is being fabricated and is currently about 70% complete.

b. Development of the Annular Heat Pipe Cooling System

(F. C. Prenger, J. E. Kemme, and M. G. Elder, Q-13)

During the quarter a performance test was conducted on a heat pipe typical of the one proposed for use in the JAERI stereographic lens system. The test article was a 3.5-m annular heat pipe with a 2.6-m evaporator, a 70-cm adiabatic section, and a 20-cm condenser. The cross-sectional geometry of the heat pipe is similar to the PKL design;[41] however, the length of the JAERI probe is three times longer. The additional length poses startup difficulties since the heat pipe is operated in the gravity assist mode. The objectives of the performance tests were to determine the most suitable working fluids, the quantity of working fluid, the capacity, and the temperature gradients during startup of the heat pipe.

Because of the length of the heat pipe, the wick will not be full of liquid initially and the liquid inventory will form a pool at the bottom of the evaporator. The depth of this pool will influence the amount of superheat required to vaporize the liquid

during startup. Due to the static pressure of the liquid, a vertical temperature gradient will result. However, the liquid inventory must be sufficient to fill the wick during steady-state operation. Since the test article has a large length-to-diameter ratio, the required amount of liquid results in a pool depth of approximately 45 cm.

In addition, a graded wick composed of three layers of screen was used. The three layers were 60, 100, and 250 mesh. The fine screen was placed next to the wall to facilitate circumferential distribution of the liquid. The coarser layers interface with the vapor passage. As the power transported by the heat pipe increases, the coarse screens fill last providing a return passage for the liquid with a correspondingly low pressure drop. The test results show that the graded wick design works well in this application since excessive hot spots in the heat pipe wall were avoided during startup, yet power levels in excess of 1 000 W were achieved.

Tests were run using water and methanol as the working fluid. The quantity of working fluid was varied between 50 and 100 cm^3. A methanol working fluid of 100 cm^3 resulted in a heat pipe capacity of 1 100 W whereas with a 100 cm^3 charge of water the heat pipe capacity exceeded the input power capability of the heaters, which was 2 400 W. As expected, the use of water as the working fluid resulted in a higher capacity heat pipe.

Figure 70 shows the heat pipe operating temperature as a function of power. The water-filled heat pipe has a lower operating temperature than the methanol filled unit for the same power. The reason being that water's high latent heat results in a thinner liquid film in the condenser and correspondingly lower thermal resistance. Thus, a smaller temperature difference between the coolant and the heat pipe working fluid results.

Maximum axial temperature differences during startup are shown as a function of power in Fig. 71. The solid lines represent an approximate fit of the data for methanol and water. The maximum axial temperature difference observed for methanol was less than 293 K, whereas for water, the maximum change was 308 K. For this

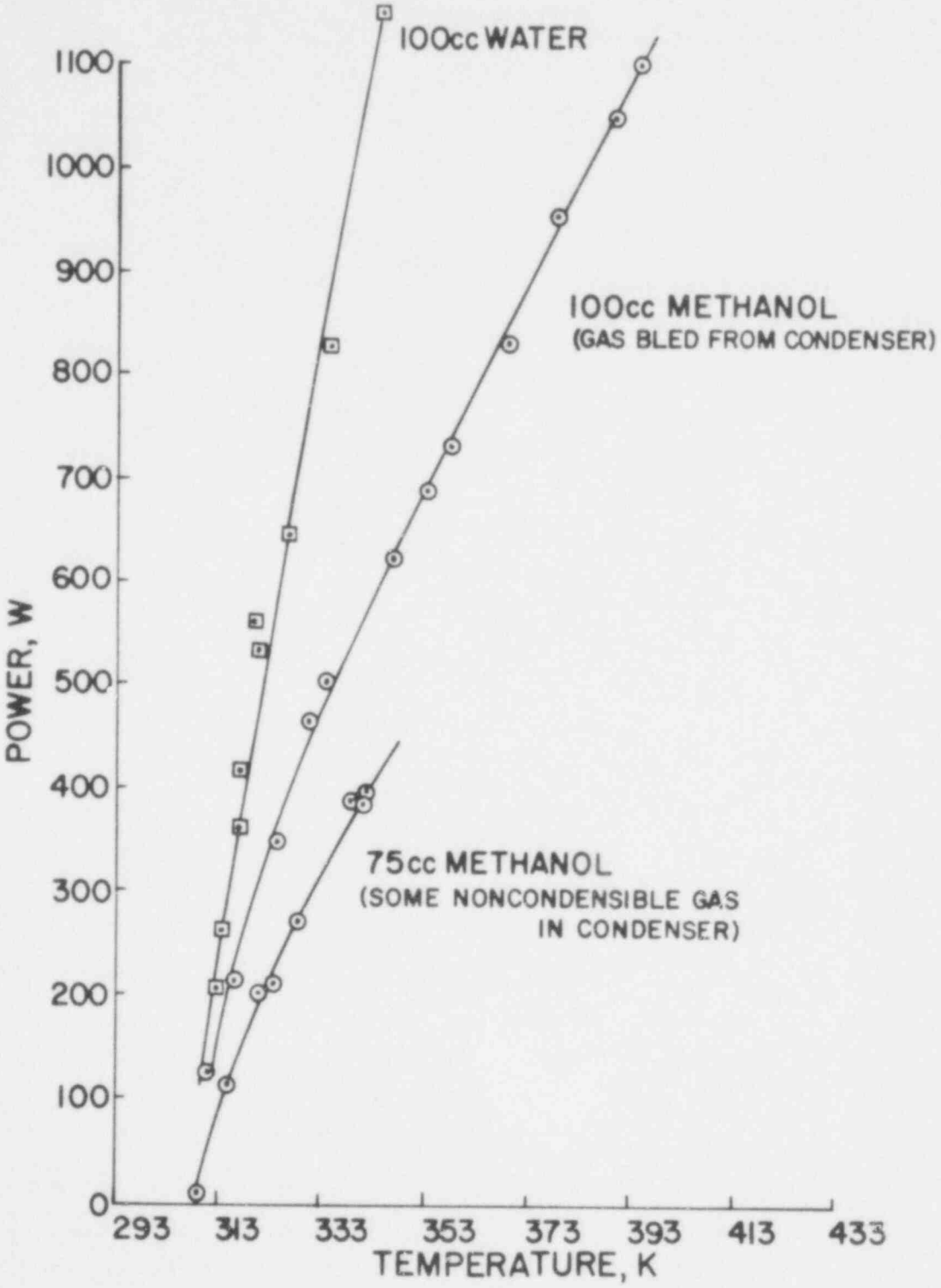

Fig. 70. Heat pipe operating temperature.

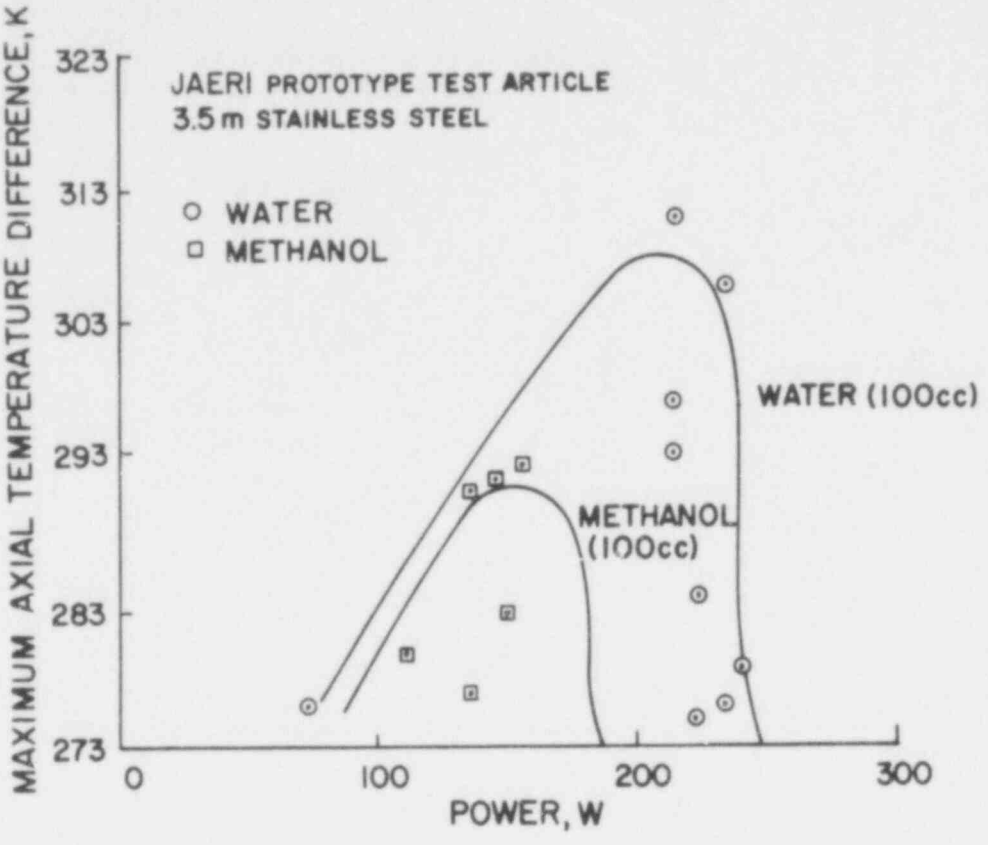

Fig. 71. Heat pipe axial temperature differences.

reason methanol was chosen as the working fluid. Since the total heat load[42] on the heat pipe is expected to be only 150 W, the improved startup characteristics at lower power of methanol is an advantage. Figure 72 shows an axial temperature profile during startup for the methanol-filled heat pipe. The data show that the maximum temperature occurs in the evaporator just above the liquid pool. Presumably, this results from insufficient liquid in the wick at this location. Apparently the return liquid flow is not fully established. Eventually, the axial temperature gradeints decay to less than 1.0 K which indicates complete filling of the inner screen. The heat pipe then performs isothermally.

The test results show that with 100 cc of water, the heat pipe capacity exceeds 2.4 kW; whereas, with 100 cc of methanol the capacity is 1.1 kW. Both working fluids have adequate capacity since the predicted heat load is only 150 W. Startup tests show that the methanol-filled pipe starts at lower power with smaller

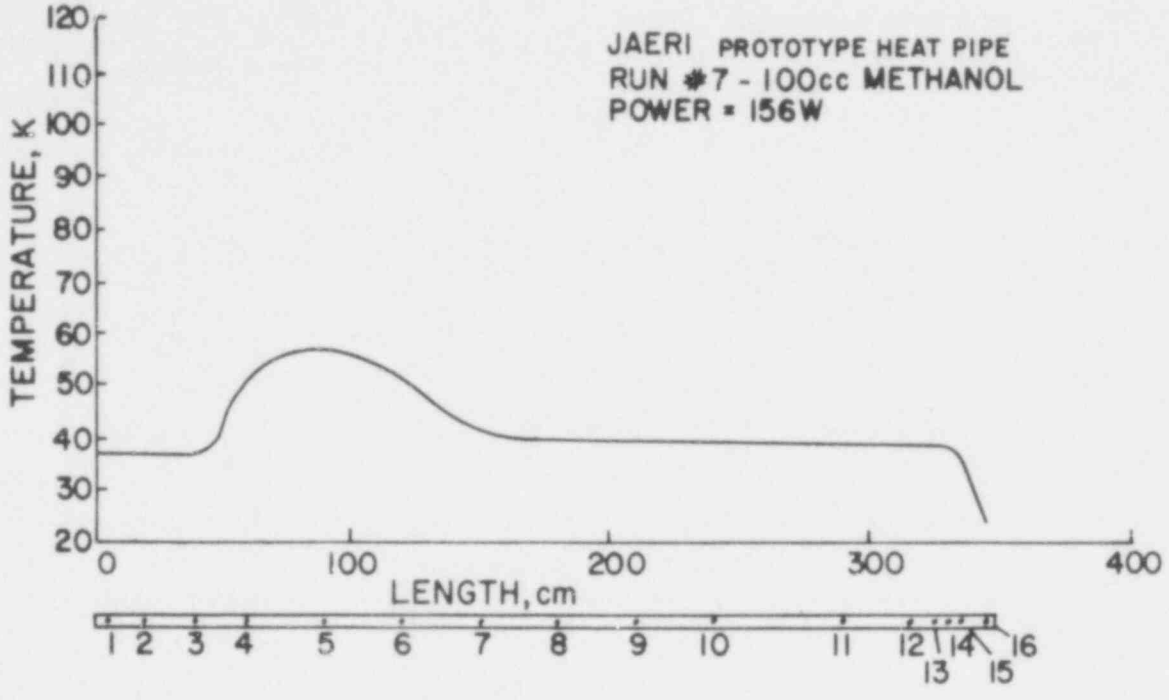

Fig. 72. Heat pipe axial temperature distribution.

axial temperature gradients and for this reason was chosen as the working fluid. The operating temperature of the methanol-filled pipe is 313 K with a coolant inlet temperature of 293 K.

c. Steam Test Loop

The remotely operated steam test loop (Fig. 73) was used to test the 1.0-m-long video stereogrammetry probe to be used in PKL. The purpose of the test was to investigate the probe's resistance to thermal shock. The portion of the probe containing a synthetic sapphire observation window (nominally 57.15 mm in diameter and 3.175 mm thick) withstood a series of 13 tests. The most violent test consisted of surrounding the probe with superheated steam at 689.48 kPa (100 psig) and 548 K, allowing the window to reach thermal equilibrium, and then injecting water at 1 034.22 kPa (150 psig) and 294 K directly onto the window.

A fourteenth test occurred after insulation on the steam test vessel was increased and superheated steam at 689.48 kPa (100 psig)

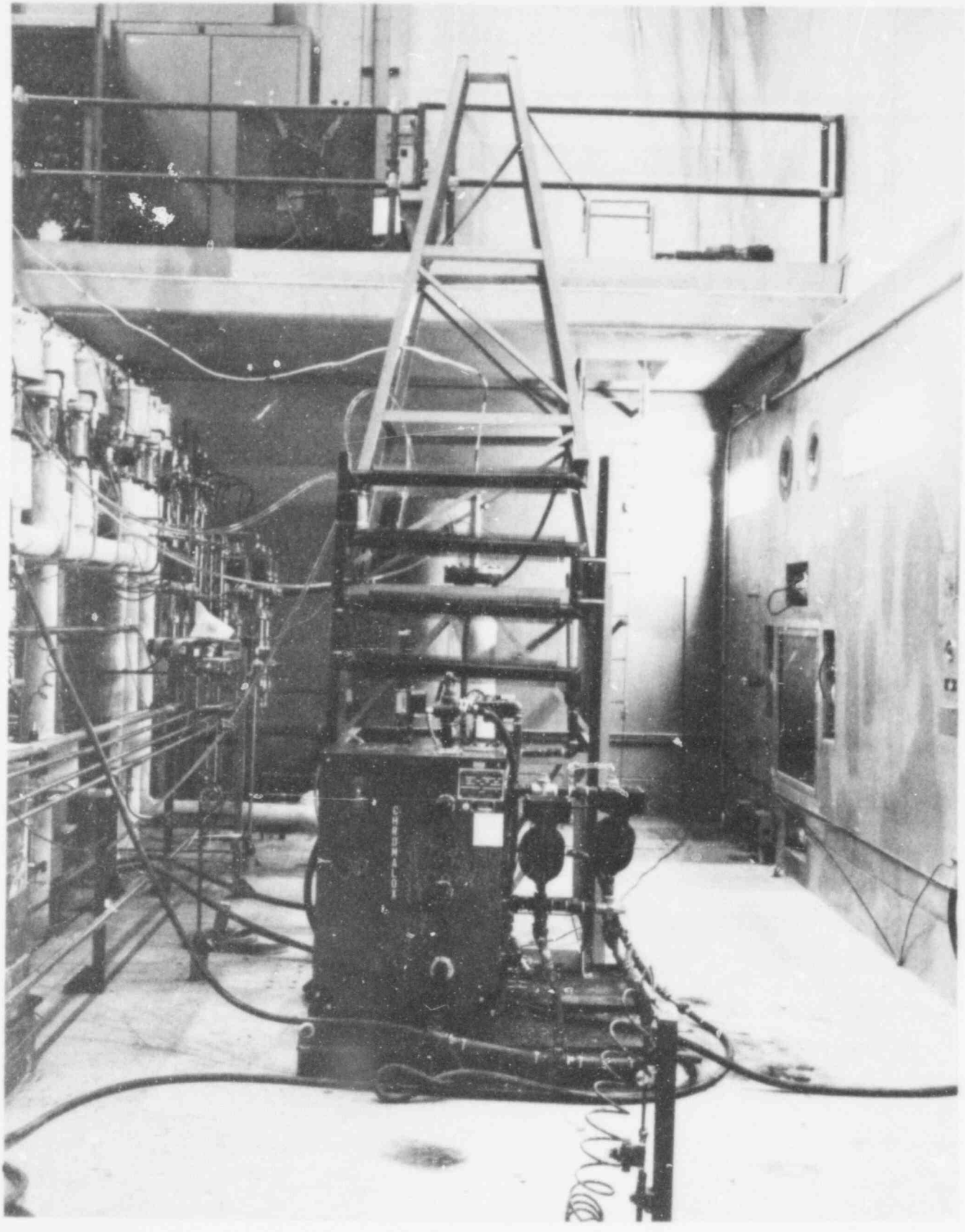

Fig. 73. Remotely operated steam test loop.

and 603 K was produced. At this temperature, injecting 21°C water directly onto the window caused it to shatter; however, it maintained pressure barrier integrity. An improved design will be used in future windows.

2. Data Acquisition System

An initial evaluation of the video data acquisition system was performed. A few minutes each of different views of a test target and electronically generated video test signals were recorded on magnetic tape. The tape was subsequently played back through the time base corrector and a single frame from each different set of views or test signals was digitized. The digital images were recorded on digital magnetic tape and subsequently processed in the Central Computing Facility (CCF) and displayed on image processing equipment. Photographs were taken of each of the displayed images.

The primary conclusion is that we can record video data and transform it into a format suitable for analysis in our CCF. Secondary conclusions are that we need to carefully check out our analog equipment to ensure correct performance and to modify our sampling frequency generator both to increase image resolution and to further simplify postdigitization data processing.

Our Computer Automated Measurement and Control (CAMAC)-based data acquisition and control system is functional at a level which requires that signals and control lines be proximate to our DEC PDP-11/34 minicomputer system. This imposes severe requirements on the quality of single lines in order to minimize the effects of noise on our measurements. We are proceeding with development and implementation of a system which will provide a data acquisition and control station proximate to each in-house experiment, but retaining the capability of communicating with the PDP-11/34 system.

3. Upper Plenum De-Entrainment Experiment

(J. C. Dallman and V. Starkovich, Q-8)

Initial measurements of single-structure de-entrainment have been completed using 101.6-, 63.5-, and 25.4-mm-diam right circular cylinders as well as a 76.2-mm-square pin. All structures were 560 mm long. These measurements were done with superficial gas

velocities of 0, 7, and 14 m/s and water spray rates up to 45 kg/min. in a 560-by 560-mm flow area test section. Representative results are presented in Figs. 74a, b, and c for the 101.6- and 63.5-mm pins. These results were reported at the American Nuclear Society (ANS)[33] Winter Meeting. The spray capture efficiency is the ratio of the liquid mass de-entrained to the total liquid mass intercepted by the cylinder. These results indicate that over the range of conditions examined, there is a strong dependence of the superficial gas velocity and the liquid mass flow rate; however, the effect of cylinder diameter appears to be rather weak for this range of sizes. These measurements are being rechecked as improvements to the liquid injection system are implemented and will be checked again in the new wind tunnel facility.

Continuing studies in the small wind tunnel facility include single- and multiple-pin (limited to 3 pins due to fan capacity) de-entrainment measurements, a strong effort to improve droplet

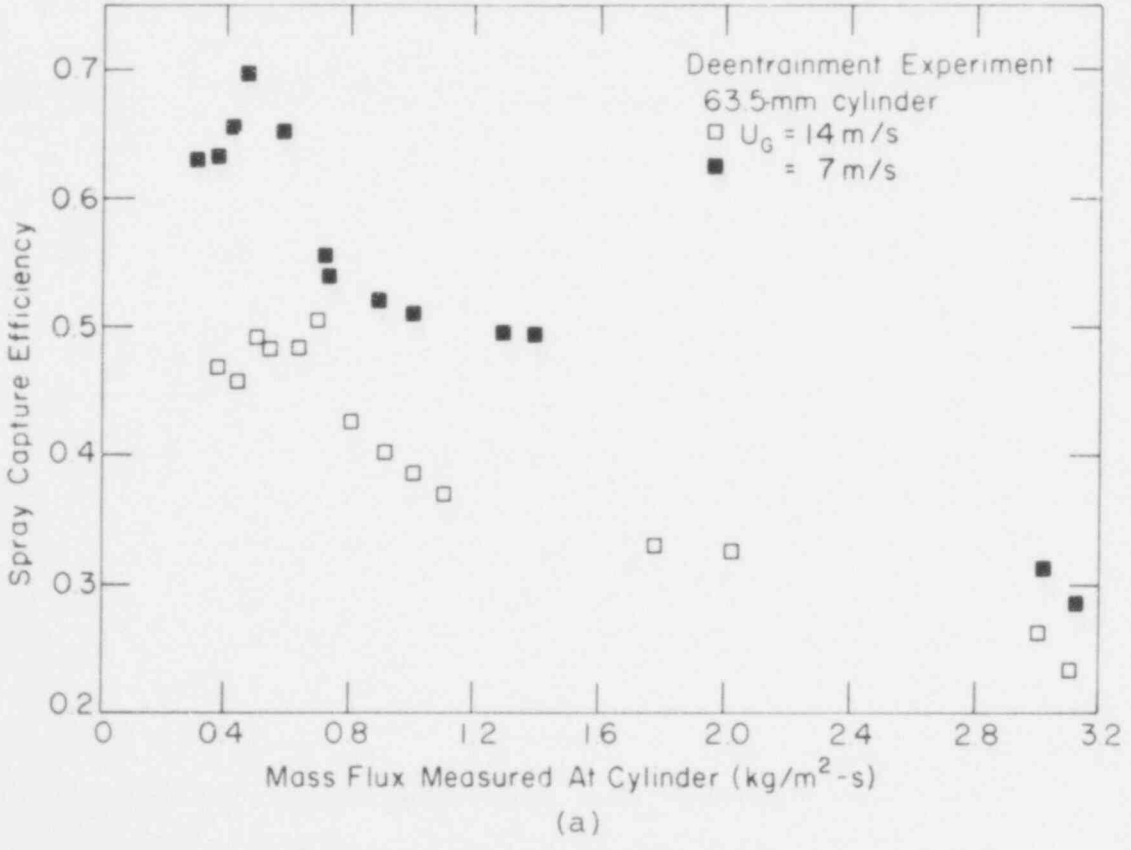

(a)

Fig. 74. Single-structure de-entrainment measurement.

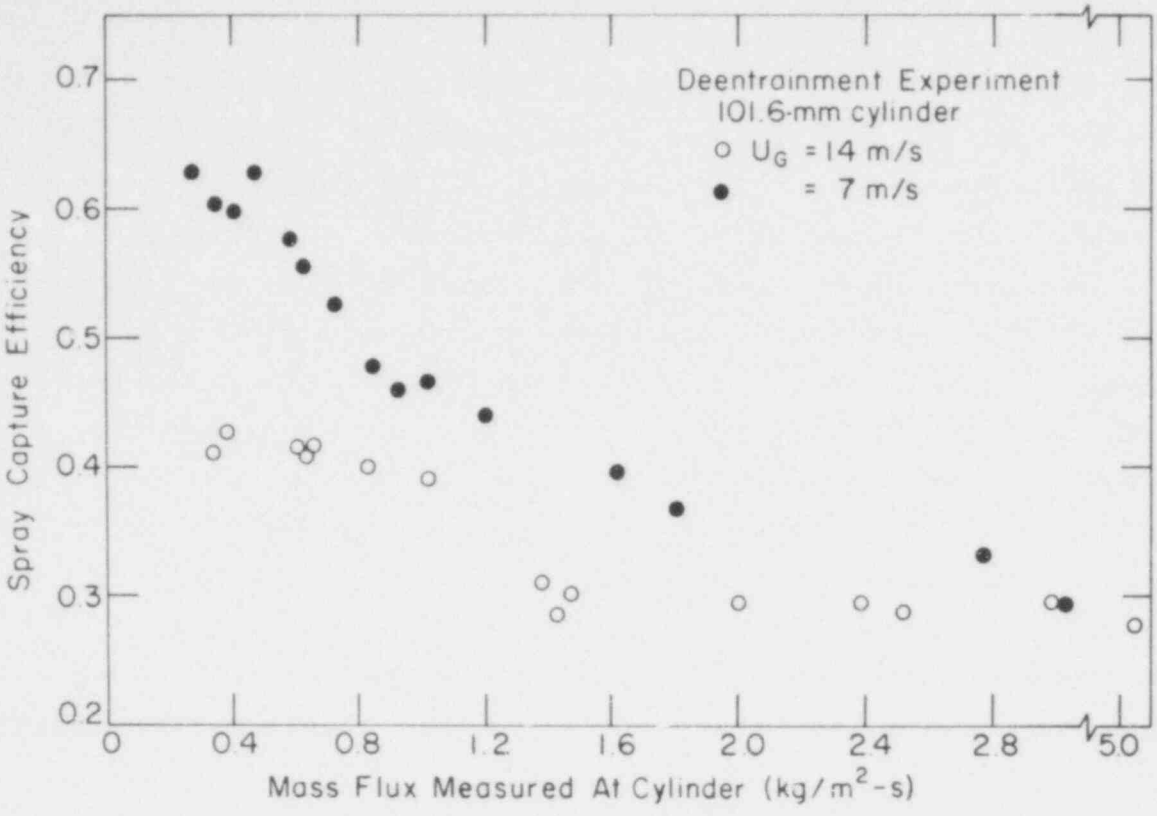

(b)

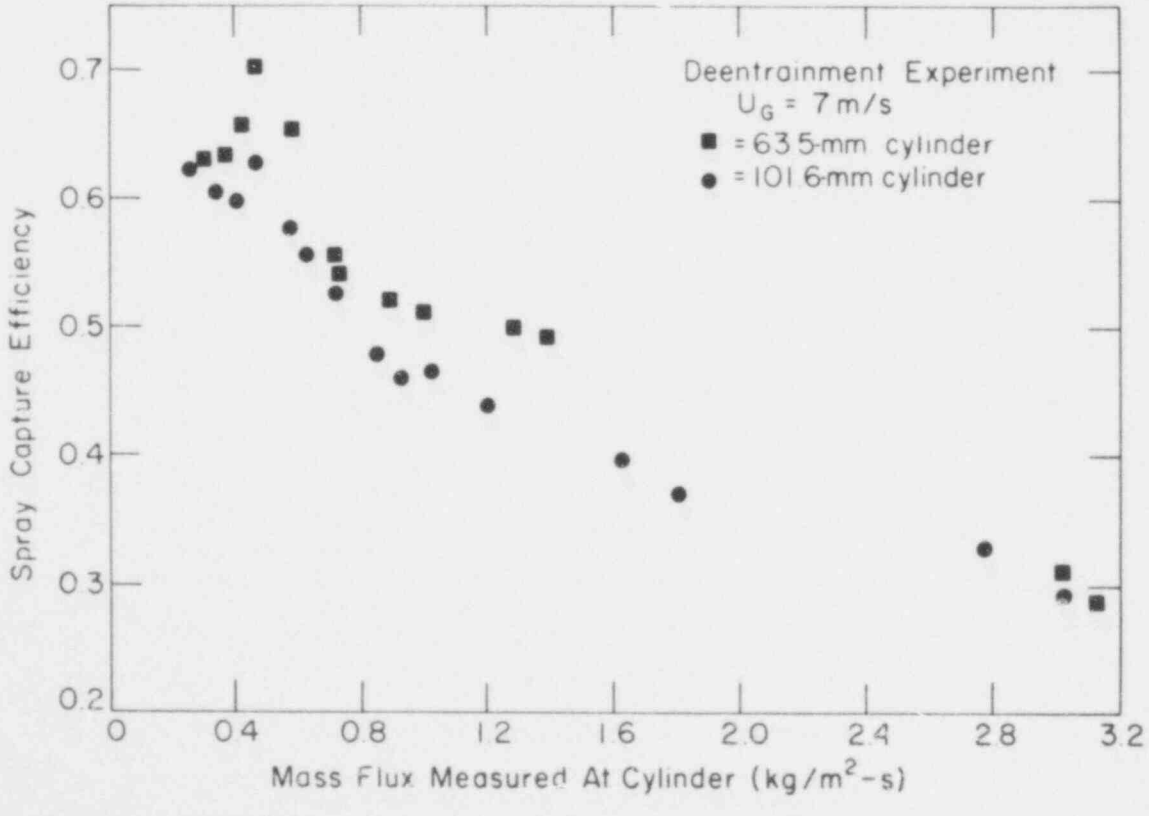

(c)

Fig. 74. (cont).

spray uniformity and reproducibility, and testing of a 17-pin "infinite" array of 101.6-mm-diam pins.

In order to quantify such parameters as the spray droplet size distribution and the droplet velocities, an investigation of various nonintrusive two-phase velocimetry and droplet sizing systems was undertaken The desired design capabilities of such a system would include velocity measurements up to the velocity of sound, with simultaneous sizing measurements from a few μm to about 5 mm.

Components for a larger wind tunnel have been received and assembly of the components is under way. Designs for the liquid supply and air draft systems are complete and awaiting construction.

In order to advance our understanding of droplet/film dynamics, the design of a uniform drop generator, capable of large-size drops, is continuing. This system, combined with high-speed photography and a laser velocimetry/droplet sizing system, will improve our ability to investigate the effect of drop size on the coalescence of a droplet with a liquid film. The droplet generator could also be used to check the calibration of a laser velocimetry/drop sizing system or a hot-film anemometer.

4. Instrumentation Development

(P. F. Bird, Q-8)

Void Fraction Meter

Modifications were made to the electronics which take the output signal from the hot-film anemometer and convert it into a number representative of void fraction. This number is displayed for viewing and can also be entered into a data acquisition system. The modifications were twofold: first, to simplify adjustment of the detector used to determine the edge of a droplet and second, to conform the signal processing to our understanding of quantitative stereology as presented by Underwood.[43]

We have re-evaluated some of the data and the results are very encouraging in the sense that the measured void fraction is what we expect it to be. More careful experiments are essential, both to prove that the instrument is measuring void fraction correctly and to characterize the range of conditions over which the measurements are valid. These investigations are continuing.

III. LMFBR SAFETY RESEARCH

(M. G. Stevenson, Q-DO; and J. E. Boudreau, Q-7)

The LMFBR safety research effort at LASL consists of several programs. In the first of these, the SIMMER code is being developed and applied to core disruptive accident (CDA) analysis with support from the Division of Reactor Safety Research (RSR) of NRC. SIMMER is a two-dimensional, coupled neutronics-fluid dynamics code intended for transition phase, core disassembly, and extended fuel motion analysis. The second version of the code, SIMMER-II, has been completed and is now being used in the analysis of CDA problems.

In a separate, but closely related, program funded by the U.S. DOE, models are being developed for phenomena important to the progression and consequences of CDAs. Some of this work is basic research on phenomena, but in most cases the developed models will be included directly in accident analysis codes and, particularly, in SIMMER. Another part of this DOE program is focused on the application of the accident codes, particularly the SIMMER code, to the study of specific aspects of accident sequences. The work in the SIMMER code development and application area is reported in Sec. III.A.

Experimental investigation, including confirmation of reactor safety analysis methods, is an important part of safety research. Section III.B provides a summary of recent analytical and experimental work in a program funded by NRC/RSR in support of SIMMER model development and testing.

A. SIMMER Code Development and Applications

(L. L. Smith and C. R. Bell, Q-7)

The first three topics in this section describe areas of code development that have been completed or are in progress. The first topic concerns analytic equation-of-state (EOS) modifications in SIMMER-II to permit a more realistic and functional treatment of materials at their critical points. The difficulty with the previous

critical point treatment was particularly evident in analyses involving rapid and extensive heating of relatively volatile materials such as water and sodium. The second section gives a summary of pressure and component density iteration improvements made in the solution technique in SIMMER-II. The third section describes work being performed to improve the tabular EOS of UO_2 fuel.

The final two sections describe progress in various ongoing analyses. The first of these describes mechanistic calculations of transition phase dynamics. The results of three SIMMER-II calculations are summarized, major phenomena are identified, and some important questions are noted. The second section summarizes the analysis of the structural behavior of the above-core structure (upper subassembly and upper pins) during the postdisassembly expansion phase of energetic CDAs. Core pressure thresholds are identified for upper subassembly motion, entire upper core motion, and pin buckling and jamming.

1. Analytic Equation-of-State Improvements for SIMMER-II Analyses

(W. R. Bohl, Q-7)

The use of the AEOS as described in the SIMMER-II manual[44] has led to significant difficulties in some code applications. Some of the AEOS properties which cause problems are

1. the internal energy for a component at the critical point is generally too low,

2. the vapor density at high pressure may be more than an order of magnitude low, and

3. in calculations where vapor properties are significantly pressure dependent (for example, in analysis of experiments using simulant materials such as water), the AEOS results strongly depend on an initial, but possibly erroneous, cell pressure estimate.

These AEOS properties not only result in unrealistic effects for some calculations but also require the coding of special cases in other models, increasing code complexity and running times.

To obtain a more reasonable value for the critical point internal energy, an analogy to a suggestion applied by Padilla[45] to obtain sodium properties is used. Padilla assumed that beyond 1 644 K the sodium average enthalpy could be extrapolated linearly to the assumed critical temperature. The liquid and vapor enthalpies were then obtained by subtracting and adding one-half of the heat of vaporization from the average enthalpy. This suggests that beyond a temperature of about two-thirds of the critical temperature, the equations for the liquid energies utilized in the SIMMER-II AEOS should include a term related to the heat of vaporization. The form chosen for the saturated liquid internal energy, $e_{Con,M}$, for each material was

$$e_{Con,M} = e_{Liq,M} + c_{vLM}\left[T_{Sat,M} - T_{Melt,M}\right], \quad T_{Sat,M} \leq \frac{2}{3} T_{Crit,M}, \tag{24}$$

$$e_{Con,M} = e_{Liq,M} + c'_{vLM}\left[T_{SAT,M} - \frac{2}{3} T_{Crit,M}\right] + a_{L,M} - \frac{1}{2} h_{\ell g,M}, \quad T_{Sat,M} > \frac{2}{3} T_{Crit,M} \tag{25}$$

$M = 1, \ldots, NMAT,$

where

$e_{Liq,M}$ is the liquidus energy of material M,

$h_{\ell g,M}$ is the enthalpy of vaporization of material M,

c_{vLM} is the constant volume specific heat for the liquid phase for material M,

$T_{Sat,M}$ is the saturation temperature for material M,

$T_{Crit,M}$ is the critical temperature for material M,

$T_{Melt,M}$ is the melting temperature for material M,

$a_{L,M}$ is defined to obtain continuity in $e_{Con,M}$ at $T_{Sat,M} = \frac{2}{3} T_{Crit,M}$, and

c'_{vLM} is defined such that the correct (input) critical point energy, $e_{Crit,M}$, is obtained. This means that

$$a_{L,M} = \frac{1}{2} h^*_{\ell g,M} \left[\frac{1}{3}\right]^{\zeta_M} + c_{vL,M} \left[\frac{2}{3} T_{Crit,M} - T_{Melt,M}\right], \quad (26)$$

and

$$c'_{vL,M} = 3\left[e_{Crit,M} - e_{Liq,M} - a_{L,M}\right]/T_{Crit,M}, \quad (27)$$

$M = 1, \ldots, NMAT$

where

$h^*_{\ell g,M}$ and ζ_M are input parameters for material M.

The vapor internal energy, $e_{G,M}$, is now obtained by the standard AEOS relationship

$$e_{G,M} = e_{Con,M} + h_{\ell g,M} - p\Delta v_M + c_{vGM}\left[T_G - T_{Sat,M}\right], \quad (28)$$

$M = 1, \ldots, NMAT$

where

$p\Delta v_M$ is the pressure volume work term for material M,

c_{vGM} is the constant volume specific heat of the vapor phase of material M, and

T_G is the vapor temperature.

However, the use of the new saturated liquid internal energy will significantly improve the calculated va ues.

The equations for the liquid component internal energies are modified in a similar fashion. They become

$$e_{LM} = e_{Liq,M} + c_{vLM}\left[T_{LM} - T_{Melt,M}\right], \quad T_{LM} \le \frac{2}{3} T_{Crit,M}, \quad (29)$$

$$e_{LM} = e_{Liq,M} + c'_{vLM}\left[T_{LM} - \frac{2}{3}\,T_{Crit,M}\right] + a_{L,M} - \frac{1}{2}\,h^{+}_{\ell g,M},$$

$$T_{Lm} > \frac{2}{3}\,T_{Crit,M} \qquad (30)$$

$M = 1, \ldots, 4$

where

$$h^{+}_{\ell g,M} = h^{*}_{\ell g,M}\left[1 - \frac{T_{Lm}}{T_{Crit,M}}\right]^{2}_{M}, \qquad T_{LM} < T_{Crit,M}, \qquad (31)$$

$$h^{+}_{\ell g,M} = 0, \qquad T_{LM} \geq T_{Crit,M}. \qquad (32)$$

T_{Lm} is the temperature of liquid field energy component m. This completes the changes in the definitions of the AEOS internal energies.

To obtain a better calculation of the vapor density at high pressures, the ideal gas law relationship must be modified. For simplicity, it was decided to maintain the same equation format and just require that a component gas constant R_M vary as a function of local conditions. Further, in the analysis of LMFBR hypothetical core disruptive accident (HCDA) situations, high vapor densities and significant deviations from nonideal behavior are generally calculated with vapor very close to saturated conditions. For example, it would appear very difficult to obtain highly superheated sodium vapor except at low density and pressure. Therefore, it was assumed that variations in R_M could be based on saturated conditions. Now, it is possible to derive thermodynamic expressions for the vapor heat capacity at constant pressure minus the heat capacity at constant volume under saturated conditions and, hence, define the R_M terms. Unfortunately, these expressions are quite complex (see Rowlinson[46]). Consequently, a simple empirical fit to R_M as a function of the vapor density temperature product, $\rho_{GM}\,T_G$, was selected, assuming that each component can be fit independently using saturated vapor conditions. The formulation chosen was

$$R_M = R_{Mi}, \qquad \rho_{GM}\, T_G < \text{ROGCUT}, \tag{33}$$

$$\ell n\, R_M = a_{M10} + a_{M20}\, \ell n(\rho_{GM}\, T_G) + a_{M30} \sqrt{\rho_{GM}\, T_G},$$

$$\text{ROGCUT} \le \rho_{GM}\, T_G \le (\rho_{GM}\, T_G)_o, \tag{34}$$

$$\ell n\, R_M = a_{M11} + a_{M21} \sqrt{\rho_{GM}\, T_G} + a_{M31}\, \rho_{GM}\, T_G,$$

$$(\rho_{GM}\, T_G)_o < \rho_{GM}\, T_G \le (\rho_{GM}\, T_G)_{Crit}, \tag{35}$$

$$R_M = R_{Crit,M}, \qquad (\rho_{GM}\, T_G) > (\rho_{GM}\, T_G)_{Crit}, \tag{36}$$

where

R_{Mi} = $(\gamma_M - 1)\, c_{vGM}$,

$R_{Crit,M}$ = $P_{Crit,M}/[\rho_{Crit,M}\, T_{Crit,M}]$,

$(\rho_{GM}\, T_G)_{Crit}$ = $\rho_{Crit,M}\, T_{Crit,M}$,

$(\rho_{GM}\, T_G)_o$ = the product of the vapor density and temperature at $T_{Sat,M} = 0.95\, T_{Crit,M}$,

a_{M10}, a_{M20}, a_{M30}, a_{M11}, a_{M21}, and a_{M31} are fitting constants,

γ_M = the ratio of vapor specific heats at infinite dilution for material M,

$P_{Crit,M}$ = the critical pressure for material M,

$\rho_{Crit,M}$ = the critical density for material M, and

ROGCUT = a SIMMER input variable.

The six fitting constants are determined from the following conditions.

1. For continuity, $R_M = R_{Mi}$ at $\rho_{GM}\, T_G$ = ROGCUT.

2. At infinite dilution, R_M should be constant; therefore,

$$\frac{d(R_M)}{d(\rho_{GM}\ T_G)} = 0 \qquad \text{at } \rho_{GM}\ T_G = \text{ROGCUT} .$$

3. At $T_{Sat,M} = 0.95\ T_{Crit,M}$, $R_M = R_{Mo}$ where R_{Mo} is defined using the vapor pressure relationship and $(\rho_{GM}\ T_G)_o$.

4. Values for R_M must be continuous at $(\rho_{GM}\ T_G)_o$.

5. For continuity, $R_M = R_{Crit,M}$ at $(\rho_{GM}\ T_G)_{Crit}$.

6. When a component's partial pressure equals the critical pressure, infinite compressibility is assumed; therefore,

$$\frac{\partial(\rho_{GM}\ R_M\ T_G)}{\partial \rho_{GM}} = 0 \text{ when } \rho_{GM}\ T_G = (\rho_{GM}\ T_G)_{Crit}.$$

Using the above modifications for the vapor energy and density, the vapor temperature is obtained by the implicit relationship

$$F(T_G) = \frac{e_G - \sum_{M=1}^{NMAT} x_M\ e^*_{G,M}}{\sum_{M=1}^{NMAT} x_M\ c_{vGM}} - T_G = 0 , \qquad (37)$$

where

$e^*_{G,M} = e_{G,M} - c_{vGM}\ T_G$,

e_G = total vapor mixture internal energy, and

x_M = the mass fraction of vapor material M in the vapor mixture.

The pressure is then obtained for two-phase cells from

$$p = \sum_{M=1}^{NMAT} \rho_{GM}\ R_M\ T_G. \qquad (38)$$

557 122

There are three aspects involved in solving the above relations. Initial conditions must be setup; Eq. (37) must be solved for the vapor temperature during the transient calculation; and an iteration is required for Eq. (30) if $\frac{2}{3} T_{Crit,M} < T_{Lm} < T_{Crit,M}$.

First, it is assumed that values of $e_{Crit,M}$ and $\rho_{Crit,M}$ can be input. The fitting conditions then allow the constants in Eqs. (34) and (35) to be determined by solution of the resulting simultaneous linear equations using Gauss elimination. In two-phase cells with the vapor density and temperature known, direct substitution into Eqs. (37) and (38) gives the vapor internal energy and cell pressure. In two-phase cells that have one component in saturated equilibrium, the component form of Eq. (38) is solved by a Newton-Raphson iteration for the microscopic vapor density. The macroscopic density is then determined using the principle of mass conservation, i.e., the sum of the macroscopic vapor and liquid densities must equal the initial input liquid density. The vapor internal energy then comes directly from Eq. (37).

For single-phase cells, the procedure chosen was selected on the basis of two criteria:

1. maintaining vapor conditions close to saturated equilibrium and
2. maintaining pressure continuity at the single-phase to two-phase transition.

To satisfy the first criterion e_G is determined by mass-averaging the component saturated specific internal energy, or

$$e_G = \sum_{M=1}^{NMAT} \rho_{GM}\left[e_{Con,M} + h_{\ell g,M} - p\Delta v_M\right] \Big/ \sum_{M=1}^{NMAT} \rho_{GM}. \qquad (39)$$

From Eq. (37) this implies that for a single-phase cell

$$T_G = \sum_{M=1}^{NMAT} \left[\rho_{GM}\, c_{vGM}\, T_{Sat,M}\right] \Big/ \sum_{M=1}^{NMAT} \rho_{GM}\, c_{vGM} \cdot \qquad (40)$$

Now, the saturation temperature for each component can be assumed to be at the corresponding liquid temperature minus any superheat. At these saturation temperatures, the vapor partial pressures, p_{vM}, are calculated from the vapor pressure relationships. The second condition can now be satisfied if

$$p_{vM} = \rho_{GM}\, R_M\, T_G \cdot \qquad (41)$$

Due to the form of R_M, Eq. (41) can be solved by a Newton-Raphson iteration for the vapor density temperature product, and R_M can thus be defined. Substitution of Eq. (41) into Eq. (40) then defines T_G as

$$T_G = \sum_{M=1}^{NMAT} \left[p_{vM}\, c_{vGM}\, T_{Sat,M}/R_M\right] \Big/ \sum_{M=1}^{NMAT} p_{vM}\, c_{vGM}/R_M \cdot \qquad (42)$$

All quantities in Eq. (42) are known; therefore, the ρ_{GM} can be determined by Eq. (41) and a consistent e_G can be calculated from Eq. (39).

Second, during the transient calculation, Eq. (37) is solved for T_G by a Newton-Raphson iteration, assuming that e_G and ρ_{GM} are known for any EOS call. This is straightforward except for one difficulty. If the vapor density is high, $F(T_G)$ may possess a second zero at a low value of T_G because $e_{Crit,M}$ may be less than $h^*_{\ell g,M}$ (the specific vapor internal energy decreases with increasing density at high pressure). Hence, obtaining the correct solution requires a respectable initial estimate for T_G. This is accomplished by saving the previous vapor temperature of the cell. Therefore, the initial T_G estimate for any EOS cell is furnished by the converged solution from the previous call. This appears to suffice for placing the iteration on a path leading to convergence.

Third, a final Newton-Raphson iteration is used for the T_{Lm} calculation when it is to be determined from Eq. (30) and $e_{Lm} < e_{Crit,M}$. Unfortunately, a good initial estimate is not available. The maximum of $T_{Sat,M}$ and $\frac{2}{3} T_{Crit,M}$ is used; however, if the final converged solution is close to $T_{Crit,M}$, the iteration may immediately start to oscillate by prediction of $T_{Lm} > T_{Crit,m}$ followed by a $T_{Lm} < \frac{2}{3} T_{Crit,M}$. The solution here is to use the formula

$$T_{Lm}^{N+1} = \frac{1}{2}(T_{Lm}^{N} + T_{Crit,M}) \quad , \tag{43}$$

for the n^{th} iteration if the estimated T_{Lm}^{N+1} is greater than $T_{Crit,M}$. Once T_{Lm} is close to the solution, convergence is rapid.

Test calculations indicate that reasonable agreement with saturated vapor properties can now be obtained with the SIMMER-II AEOS. Figure 75 shows a comparison with the sodium vapor enthalpy. Figure 76 illustrates a comparison to the sodium vapor density. Results from SIMMER-II using the new formulation are still preliminary; however, they are encouraging. The SIMMER-II energy

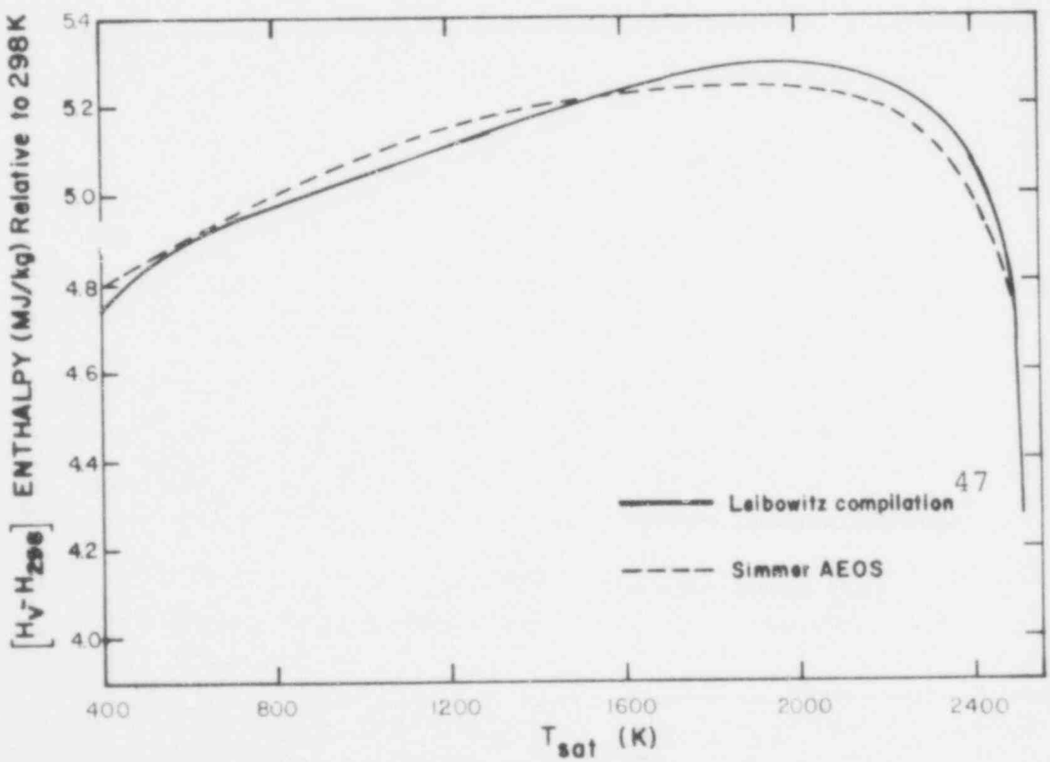

Fig. 75. Sodium vapor enthalpy vs temperature.

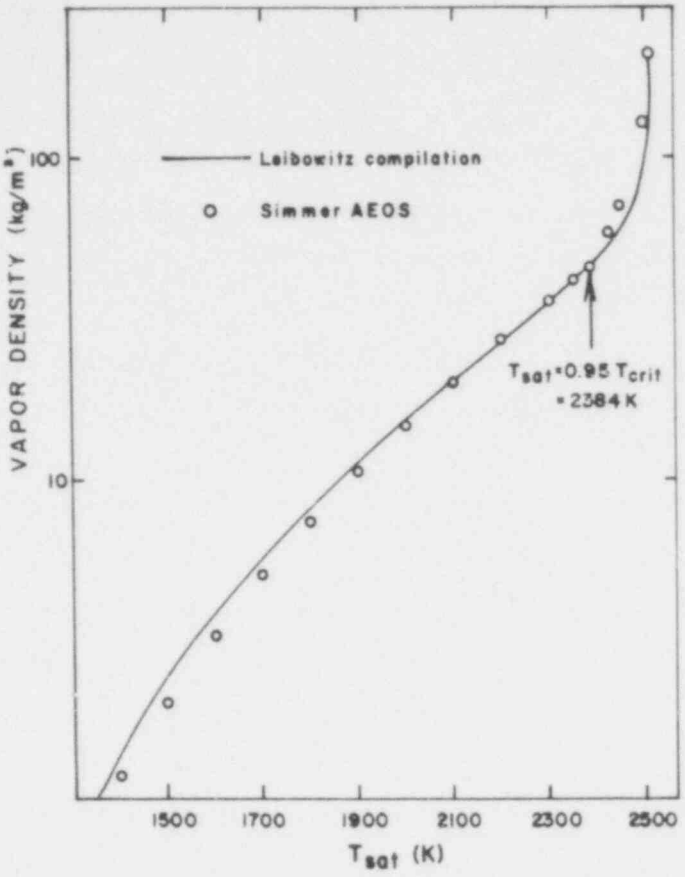

Fig 76. Saturated sodium vapor densities vs temperature.

partition test problem[44] involves a core with molten fuel at 5 966 K accelerating into a sodium-filled fission gas plenum. With the new AEOS, results not only appeared to be smoother and more plausible, but also, less computer time was consumed despite the iterations involved for the vapor and some liquid temperatures. The improved calculational speed is related to the faster convergence character of the phase transition model with the revised AEOS. It will be interesting to discover what improvements can be obtained in prevous comparisons of SIMMER calculations to experiments. The results of further testing of these improvements will be discussed in subsequent reports.

2. Matrix Inversion Methods

(R. G. Steinke and L. B. Luck, Q-7)

The implicit equations in SIMMER-II have been restructured to evaluate a simultaneous solution of spatial coupling.[12] This was done to reduce the number of iterations required and to enhance

numerical stability. Larger time steps and shorter running times result. To achieve this, an efficient matrix inversion method is needed. Two different methods have been selected: Successive Line Overrelaxation (SLOR)[48,49] and a new algorithm called Approximate Inverstion Method (AIM). A description of each method and its application in SIMMER-II as well as a comparison of their efficiencies will now be given.

The equations to be solved are the matrix equations[12] for the k^{th} iteration pressure change.*

$$\underline{\underline{\beta}}^k \cdot \underline{\Delta p}^k = \underline{-\tilde{D}}^k \tag{44}$$

and the matrix equation for the advanced time (n+1 time point) liquid field (f = ℓ) and vapor field (f = g) component densities for each component m,

$$\underline{\underline{A}}_f^{n+1} \cdot \underline{\bar{\rho}}_{fm}^{n+1} = \left[\underline{\bar{\rho}}_{fm}^{n} + \Delta t\ \underline{\Gamma}_{fm}^{n}\right] \quad . \tag{45}$$

$\underline{\underline{\beta}}^k$ and $\underline{\underline{A}}_f^{n+1}$ are sparse matrices with five diagonals of nonzero elements coupling each spatial node to its four adjacent nodes in two-dimensional rectilinear geometry. The general form

$$\underline{\underline{M}} \cdot \underline{F} = \underline{Q} \tag{46}$$

for the above matrix equations will be used in the following discussion. The matrix $\underline{\underline{M}}$ and the vector $\underline{Q}$ are known; the vector $\underline{F}$ is the unknown to be determined.

SLOR is a popular method for solving this matrix equation because it is simple and efficient. Because extensive documentation of the method exists in the literature,[48,49] a detailed description will not be given here. However, for completeness, a summary of the working equations and a discussion of unique features in their application is given.

---

*Our notation will use a single underline to indicate a vector and a double underline to indicate a matrix.

The method is based on partitioning the block tridiagonal matrix $\underline{\underline{M}}$ into the sum of the three matrices representing the block diagonals, $\underline{\underline{M}} = \underline{\underline{L}} + \underline{\underline{D}} + \underline{\underline{U}}$. Matrix $\underline{\underline{D}}$ has tridiagonal element submatrix blocks accounting for the spatial coupling of a line of nodes. Matrices $\underline{\underline{L}}$ and $\underline{\underline{U}}$ have diagonal element submatrix blocks accounting for spatial coupling to the neighboring node in the previous line and next line, respectively. Rearranging the matrix equation as an iterative equation and extrapolating each i^{th} iteration estimate of the solution with a relaxation parameter ω gives the SLOR iterative algorithm,

$$\underline{F}^{i} = \underline{F}^{i-1} + \omega\{-\underline{\underline{D}}^{-1} \cdot [\underline{\underline{L}} \cdot \underline{F}^{i} + \underline{\underline{U}} \cdot \underline{F}^{i-1} + \underline{Q}] - \underline{F}^{i-1}\}$$

$$\text{for } i = 1, 2, 3, \ldots \quad . \tag{47}$$

Starting with an initial estimate of the solution $\underline{F}^{o}$, the iterative evaluation continues until the convergence criterion

$$\frac{(\underline{F}^{i} - \underline{F}^{i-1}, \underline{F}^{i} - \underline{F}^{i-1})}{(\underline{F}^{i}, \underline{F}^{i})} < \varepsilon \ , \tag{48}$$

is satisfied for some small number ε, defined by the user. The user also defines the number of iterations between updating the relaxation parameter ω based on[48,49]

$$\omega = \frac{2}{1 + \sqrt{1 - \mu_o^2}} \ , \tag{49}$$

where

$$\mu_o = \frac{\mu + \omega_{previous} - 1}{\omega_{previous} \sqrt{\mu}}$$

and

μ = the iteration matrix spectral radius

$$\mu \cong \sqrt{\frac{(\underline{F}^{i} - \underline{F}^{i-1}, \underline{F}^{i} - \underline{F}^{i-1})}{(\underline{F}^{i-1} - \underline{F}^{i-2}, \underline{F}^{i-1} - \underline{F}^{i-2})}} \quad .$$

The initial value of ω is set to unity. Infrequently, the update value of ω can cause the iterative solution to diverge. This occurs when the L2 norm error ratio overestimates μ and causes ω to be too large. This condition is corrected by setting ω to unity for the next update cycle. At the end of the cycle, the maximum of the current Euclidean norm error ratio and 90% of its value before divergence occurred is used to evaluate the next ω.

AIM is a second method which is based on modifying $\underline{\underline{M}}$ to achieve an efficient direct inversion. Error in the solution from modifying $\underline{\underline{M}}$ is removed iteratively. The existing error at iteration i is

$$\underline{\Delta Q}^{i} = \underline{Q} - \underline{\underline{M}} \cdot \underline{F}^{i} \quad . \tag{50}$$

The change in $\underline{F}^{i}$ to remove this error is defined by the matrix equation

$$\underline{\underline{M}} \cdot \underline{\Delta F}^{i} = \underline{\Delta Q}^{i} \quad . \tag{51}$$

Modifying $\underline{\underline{M}}$ during its inversion results in the approximate solution:

$$\underline{\Delta F}^{i} \cong (\underline{\underline{M}}^{approx})^{-1} \cdot \underline{\Delta Q}^{i} \quad . \tag{52}$$

Because $\underline{\Delta F}^{i}$ is approximate, combining it with $\underline{F}^{i}$ defines only the next iteration estimate of $\underline{F}$, i.e., $\underline{F}^{i+1}$. To accelerate convergence of $\underline{F}^{i+1}$ to $\underline{F}$, a diagonal element relaxation matrix $\underline{\underline{\omega}}$ is applied to $\underline{\Delta F}^{i}$.

$$\underline{F}^{i+1} = \underline{F}^{i} + \underline{\underline{W}} \cdot \underline{\Delta F}^{i} \quad . \tag{53}$$

Three definitions of $\underline{\underline{W}}$ are used in SIMMER-II:

1. $\omega_{\ell\ell} = 1$, no relaxation;
2. $\omega_{\ell\ell} = \omega$, a global rebalance relaxation; and
3. $\omega_{\ell\ell} = \omega_j$, a line rebalance relaxation where $j = 1 + (\ell-1)/I$ and I is the number of nodes in a line.

No relaxation is applied the first NITSRU iterations; the global rebalance relaxation is applied the next NITSRU iterations and line rebalance relaxation is applied thereafter. NITSRU is specified by the user through input. The rebalance parameters ω and ω_j are defined to minimize the remaining Euclidean norm error in $\underline{Q}$.

$$\begin{aligned} \text{Error} &= (\underline{\Delta Q}^{i+1}, \underline{\Delta Q}^{i+1}) \\ &= \sum_{\ell}^{I*J} (\Delta Q_\ell^{i+1})^2 \\ &= \sum_{\ell}^{I*J} (\Delta Q_\ell^{i} - \omega_{\ell\ell}\, \Delta^2 Q_\ell^{i})^2 , \end{aligned} \tag{54}$$

where

$\underline{\Delta}^2 Q^i = \underline{\underline{M}} \cdot \underline{\Delta F}^i$ and J is the number of node lines.

Requiring that $d(\text{Error})/d\omega = 0$ or $\partial(\text{Error})/\partial\omega_j = 0$ for $j = 1,2, \ldots J$ minimizes the Error with respect to ω or ω_j, respectively. Solving the $d(\text{Error})/d\omega = 0$ equation for ω defines

$$\omega = \frac{\sum_{\ell}^{I*J} \Delta Q_\ell^i\, \Delta^2 Q_\ell^i}{\sum_{\ell}^{I*J} (\Delta^2 Q_\ell^i)^2} . \tag{55}$$

The J equations of the type $\partial(\text{Error})/\partial\omega_j = 0$ give a five diagonal element coefficient matrix equation with spatial coupling to the

four nearest node lines. This matrix equation is solved for ω_j by forward elimination of the two lower diagonals and backward substitution into the two modified upper diagonals. Having relaxed $\underline{F}^{i+1}$ by one of the above definitions of $\underline{\underline{W}}$, the iterative evaluation continues until the convergence criterion

$$\frac{(\underline{\Delta Q}^{i+1}, \underline{\Delta Q}^{i+1})}{(\underline{Q}, \underline{Q})} < \varepsilon \ , \tag{56}$$

is satisfied for some small number ε defined by the user.

The AIM algorithm for modifying and inverting $\underline{\underline{M}}$ is the familiar Crout-Cholesky forward elimination and backward substitution method.[48] Rather than operating on individual elements, AIM operates on submatrix blocks. The block tridiagonal matrix $\underline{\underline{M}} = \underline{\underline{L}} + \underline{\underline{D}} + \underline{\underline{U}}$ is inverted by forward elimination of the lower block diagonal $\underline{\underline{L}}$ and backward substitution into the modified upper block diagonal $\underline{\underline{U}}^*$. This procedure is made efficient by a submatrix collapsing approximation. To describe this in more detail, first consider the forward elimination of $\underline{\underline{L}}$. The procedure involves stepping along the $j = 1,2, \ldots, J-1$ node lines eliminating the $(j+1)^{th}$ line submatrix $\underline{\underline{L}}_{j+1}$. One starts by setting

$$\underline{\underline{D}}_1^* = \underline{\underline{D}}_1 \quad \text{and} \tag{57}$$

$$\underline{\Delta Q}_1^{*i} = \underline{\Delta Q}_1^i \tag{58}$$

for the first node line. Then, for each j^{th} node line, starting with $j = 1$, the tridiagonal element submatrix $\underline{\underline{D}}_j^*$ is directly inverted by the Crout-Cholesky forward elimination and backward substitution method. $\underline{\underline{U}}_j$ becomes $(\underline{\underline{D}}_j^*)^{-1}$. $\underline{\underline{U}}_j$, a full element submatrix, and $\underline{\Delta Q}_j^{*i}$ become

$$\underline{\Delta Q}_j^{*i} = (\underline{\underline{D}}_j^*)^{-1} \cdot \underline{\Delta Q}_j^{*i} \ . \tag{59}$$

An element collapsing approximation is now made on $(\underline{\underline{D}}_j^*)^{-1} \cdot \underline{\underline{U}}_j$. Row elements to the left and right of the submatrix diagonal

element are collapsed (summed) to the adjacent left and right elements, respectively,

$$(\underline{\underline{D}}_j^*)^{-1} \cdot \underline{\underline{U}}_j \xrightarrow[\text{approximation}]{\text{collapse}} \underline{\underline{U}}_j^* \ . \tag{60}$$

$(\underline{\underline{D}}_j^*)^{-1} \cdot \underline{\underline{U}}_j$ becomes the tridiagonal element submatrix $\underline{\underline{U}}_j^*$. Thus far our purpose has been to convert the tridiagonal submatrix $\underline{\underline{D}}_j^*$ to an identity matrix. $\underline{\underline{L}}_{j+1}$ can now be eliminated from the $(j+1)^{th}$ row submatrix equation by multiplying the modified j^{th} row submatrix equation by the diagonal element submatrix $\underline{\underline{L}}_{j+1}$ and then subtracting it from the $(j+1)^{th}$ row equation giving

$$\underline{\underline{D}}_{j+1}^* = \underline{\underline{D}}_{j+1} - \underline{\underline{L}}_{j+1} \cdot \underline{\underline{U}}_j^* \ , \tag{61}$$

$$\underline{\Delta Q}_{j+1}^{+i} = \underline{\Delta Q}_{j+1}^{i} - \underline{\underline{L}}_{j+1} \cdot \underline{\Delta Q}_j^{*i} \ . \tag{62}$$

At this point the reason for collapsing $(\underline{\underline{D}}_j^*)^{-1} \cdot \underline{\underline{U}}_j$ to the tridiagonal element submatrix $\underline{\underline{U}}_j^*$ becomes evident. The tridiagonal element form of $\underline{\underline{D}}_{j+1}$ is maintained during its modification to $\underline{\underline{D}}_{j+1}^*$. Without the collapsing approximation $\underline{\underline{D}}_{j+1}^*$ would be a full element submatrix. Inverting $\underline{\underline{D}}_{j+1}^*$ in the next step can now be done efficiently by the Crout-Cholesky method rather than by a full element submatrix inversion.

After stepping forward with the above procedure for each j = 1,2, ..., J-1 line, the solution estimate in the J^{th} (last) node line is defined by

$$\underline{\Delta F}_J^i = (\underline{\underline{D}}_J^*)^{-1} \cdot \underline{\Delta Q}_J^{+i} \ . \tag{63}$$

At this point $\underline{\underline{L}}$ has been eliminated, $\underline{\underline{D}}$ has become the identity matrix $\underline{\underline{I}}$, and $\underline{\underline{U}}$ has been modified to $\underline{\underline{U}}^*$ having tridiagonal element submatrix blocks. The solution is completed by backwards substitution into the $\underline{\underline{I}}+\underline{\underline{U}}^*$ upper triangular matrix to obtain

$$\underline{\Delta F}_j^i = \underline{\Delta Q}_j^{*i} - \underline{\underline{U}}_j^* \cdot \underline{\Delta F}_{j+1}^i \ , \tag{64}$$

for j = J-1, J-2, ..., 1.

In the process of implementing the SLOR and AIM algorithms in SIMMER-II, several common features have been introduced. To improve their efficiency, the coefficient matrix is only inverted during the first iteration. Subsequent iterations apply the inverted matrix to the right-hand side vector. This reduces calculational effort per iteration by 40%. An automatic procedure is used to select the best node line direction. The best direction is that with strongest spatial coupling. Effects such as flow blockage and can wall failure can cause the best line direction to change as problem time evolves. SIMMER-II periodically determines the best line direction by evaluating the pressure change matrix equation for both directions. The best line direction is that for which the method converges fastest. This line direction is used until the next test is made. The frequency of this evaluation is user controlled through input. Another common feature of both programmed algorithms is the use of the direct Crout-Cholesky method for solving one-dimensional problems.

Both the SLOR and the AIM methods are used in SIMMER-II. AIM requires twice the variable storage of SLOR. Using LCM to relax SMC requirements avoids any penalty for extra AIM storage.

A numerical study to compare the efficiency of both methods has been performed for their application in SIMMER-II and in a neutron diffusion equation program.[50] The SIMMER-II evaluations were based on the postdisassembly and transition phase test problems in the SIMMER-II manual. SLOR required four times as many iterations and twice the calculational effort of AIM with no rebalance relaxation to solve the pressure change matrix equation. Equal calculation times were required for the component density matrix equations because SLOR converged in two iterations and AIM in one iteration. Applying global and line rebalance relaxation in AIM increased calculational effort per iteration by 20 and 30%, respectively. For these small test problems, not using rebalance relaxation was more efficient. However, for large problems with strong spatial coupling, the rebalance options become more efficient when their ability to enhance convergence and to reduce

the number of iterations overcomes their additional calculational effort per iteration.

The SLOR and AIM algorithms have also been applied to the few group neutron diffusion equation. The existence of such a program[44] employing the Strongly Implicit Procedure (SIP) method provided a convenient means for comparing all three algorithms.[51] The four energy group SNR-300 LMFBR benchmark problem[52] and the two energy group IAEA LWR benchmark problem[53] were evaluated. A comparison of convergence behavior differed among the energy groups of the above problems. In all cases, however, AIM with global and line rebalance required 40-60% less calculational effort than SIP with an optimum acceleration parameter. Nonoptimum parameters reduced the convergence rate of SIP significantly. AIM with rebalance required 50-80% less calculational effort than SLOR. The relative efficiency of AIM with no rebalance relaxation varied among the energy groups based on their strength of spatial coupling. AIM with no rebalance was the most efficient method in the loosely coupled LWR problem. On the other hand, it was just slightly better than SLOR in the strongly coupled first energy group of the LMFBR problem. In all cases, however, AIM with no rebalance gave a similar level of error reduction during the first few iterations as when rebalance was applied. Based on this, applying AIM (as in SIMMER-II) with no relaxation during the initial iterations and with global and line rebalance optimum relaxation thereafter will be more efficient than SIP and SLOR for the neutron diffusion equation.

3. Equation of State for UO_2

(J. D. Johnson, T-4)

We have continued gathering data for refining the tabular EOS for uranium dioxide (UO_2) suitable for reactor safety studies. The data that are available and needed are vapor pressures, liquid and solid densities, heat of fusion, melting temperature, and liquid and solid enthalpies. Some considerable effort to understand the data has been necessary to produce a comprehensive EOS. A study of an anomaly in enthalpy data is discussed below.

The constant pressure specific heat c_p for solid and liquid UO_2 (as derived from enthalpy data[54,55] and direct measurements of c_p)[56] has always appeared anomalously high for the measured temperature range 1 000 K $\leq$ T $\leq$ 3 500 K. No data exist for higher temperatures but the anomaly probably persists higher in T. One could expect at most a 279 J/kg-K contribution to c_p from vibration excitations, but the data strongly imply c_p to be at least 465 J/kg-K or higher. Because several good experiments all give the same results, one hesitates to point to experimental errors as the problem.

The initial explanation[56,57] used defect formation as the source of the anomalous contribution to c_p. However, this is not at all reasonable because one cannot obtain a large enough contribution from defects.[58] More recent calculations[58] have focused on electronic excitations as the source. MacInnes has used a crude band model that encompasses some band data on UO_2 to estimate the electronic part of c_p. We consider his work to be a success. His numbers are in sufficient agreement with the data to show that electronic excitations are the probable explanation of the specific heat anomaly.

To lend further credence to the above explanation, we have pursued the following approach. We are looking at the specific heat of the gaseous phase of UO_2 and metallic uranium (U) with models of the Saha type.[59] In the density ranges of interest, i.e., low density, such models should be good approximations to our system. We use the Clausius-Clapeyron relation

$$\frac{dp_v}{dT} = \frac{h_g - h_c}{T(v_g - v_c)} , \tag{65}$$

to relate the enthalpy of the gas h_g to that of the condensed phase h_c, p_v is the vapor pressure at temperature T, v_g is the specific volume of the gas, and v_c is the specific volume of the condensed phase. Using Eq. (65) and the experimental vapor pressures, one finds that if there is a large electron contribution to the specific heat of the gas there should be one also to c_p of

the condensed UO_2, supporting our above interpretation of MacInnes' work. Furthermore, if we can find a model that reproduces the h_g for $T \leq 3\ 500$ K, as obtained from h_c using Eq. (65), we will use the model to extend the h_c beyond the data, again by using Eq. (65).

The preliminary results of our study are very encouraging. There is more data for U vapor than UO_2. Therefore, we first looked at that substance. In the neighborhood of T = 3 000 K, we obtained an electronic contribution to c_p of 140 J/kg-K for U. The UO_2 molecules should have even denser energy levels than U and should have a larger electronic c_p.

In summary, we believe that for $T \geq 2\ 000$ K, the electronic contribution to the enthalpy of both gaseous UO_2 and condensed UO_2 is significant. Experiments on the condensed UO_2 show that the electron excitations could double c_p. Our preliminary theoretical investigations indicate that the same is happening in gaseous UO_2. These electronic contributions will be included in the tabular EOS.

4. Whole-Core Transition Phase Analysis with Space-Time Neutronics

(S. T. Smith, Q-6)

The SIMMER-II[44] code has been used to extend a SAS3A calculation of an unprotected loss-of-flow accident (ULOF) for the end-of-equilibrium-cycle (EOEC) Clinch River Breeder Reactor (CRBR) core.[60] The SAS3A transient was terminated following a mild power burst at 16 s. Three SIMMER-II calculations [a power-vs-time (as input) calculation and two space-time neutronics calculations with an initial reactivity of \$0.76[61]] were begun at this point with an initial power of 12.65 GW, about 13 times nominal power. A previous report[14] described the results both for the power-vs-time calculation, whose purpose was to examine the fluid dynamics behavior without neutronics effects, and for the first few seconds of the first space-time neutron diffusion calculation, whose purpose was to include neutronics feedback and to study material motion. The gross overall trends for both of these calculations included a rapid decrease in power, a highly incoherent redistribution of

fuel and steel strongly affected by the can wall failure sequence, a quenching of the molten fuel by the liquid steel, and a stabilization of the neutronics at a fairly subcritical level for the case with space-time neutronics. (The power-vs-time case assumed a nominal full-power level.)

The second space-time neutronics calculation was similar to the first in several respects: it used the same computing mesh, as shown in Fig. 77, initial reactivity, initial power, and initial distributions of total fuel, total steel, and liquid steel, as shown in Figs. 78a-c. To determine whether the behavior developed in the first case would be similar to that developed when the core materials started at higher energies, the initial energy level of the second case was increased by 20%. This increase was achieved

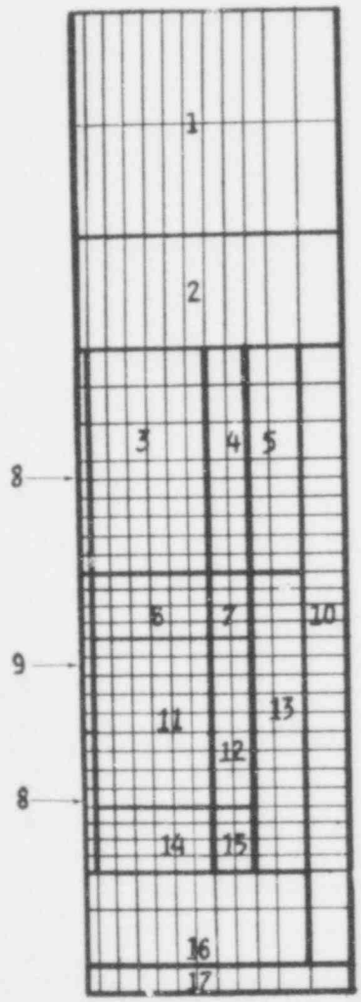

1 - Above-core structure
2 - Sodium pool
3 - Inner core fission gas plenum
4 - Outer core fission gas plenum
5 - Radial blanket fission gas plenum
6 - Inner upper axial blanket (UAB)
7 - Outer UAB
8 - Control rod (plenum region)
9 - Control rod (B4C region)
10 - Radial shield
11 - Inner core
12 - Outer core
13 - Radial blanket
14 - Inner core lower axial blanket (LAB)
15 - Outer core LAB
16 - Lower shield
17 - Orifice region

Fig. 77. SIMMER-II geometrical mesh for whole-core transition phase analysis with space-time neutronics.

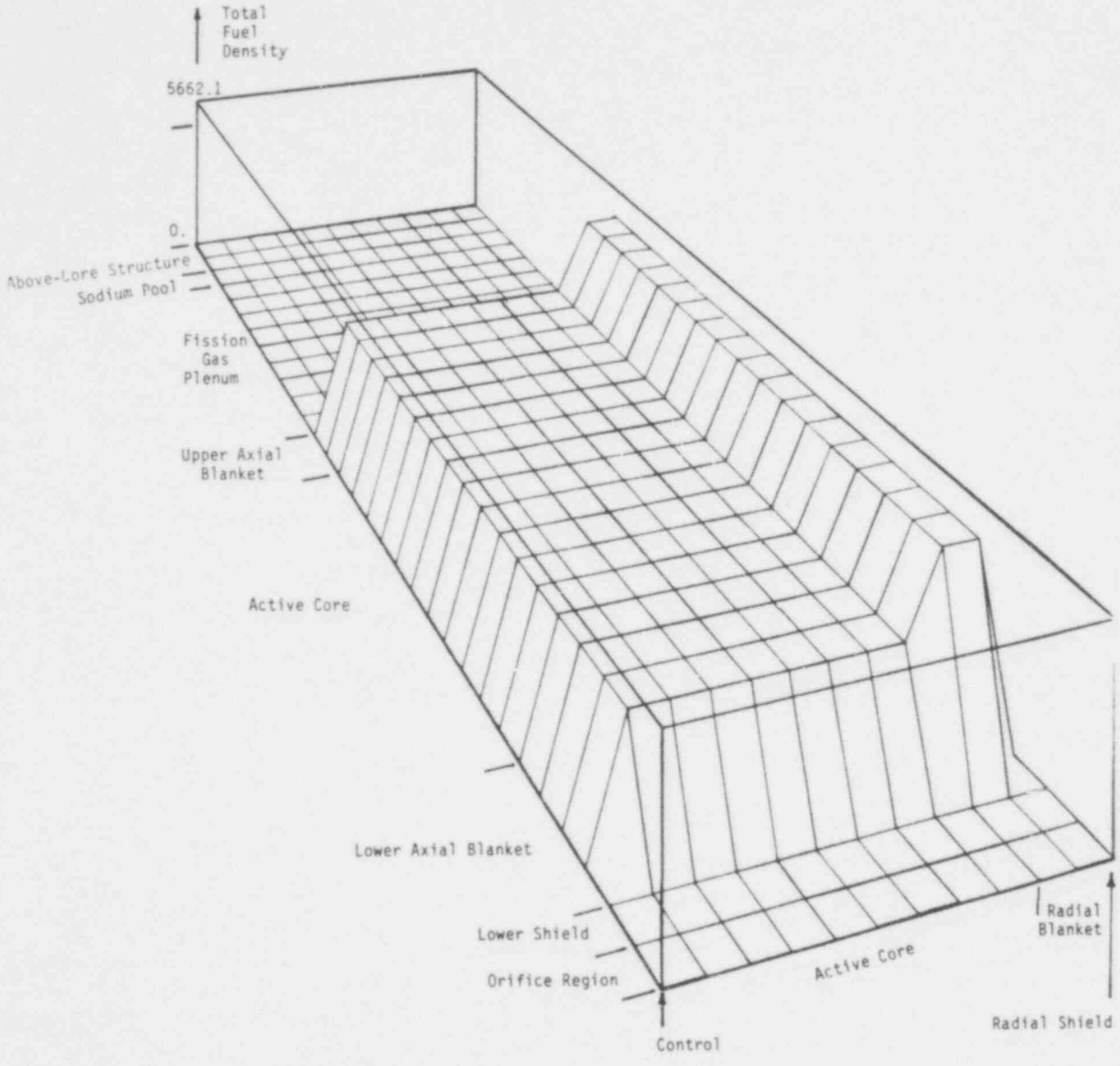

Fig. 78a. Initial total fuel distribution for both full neutronics cases.

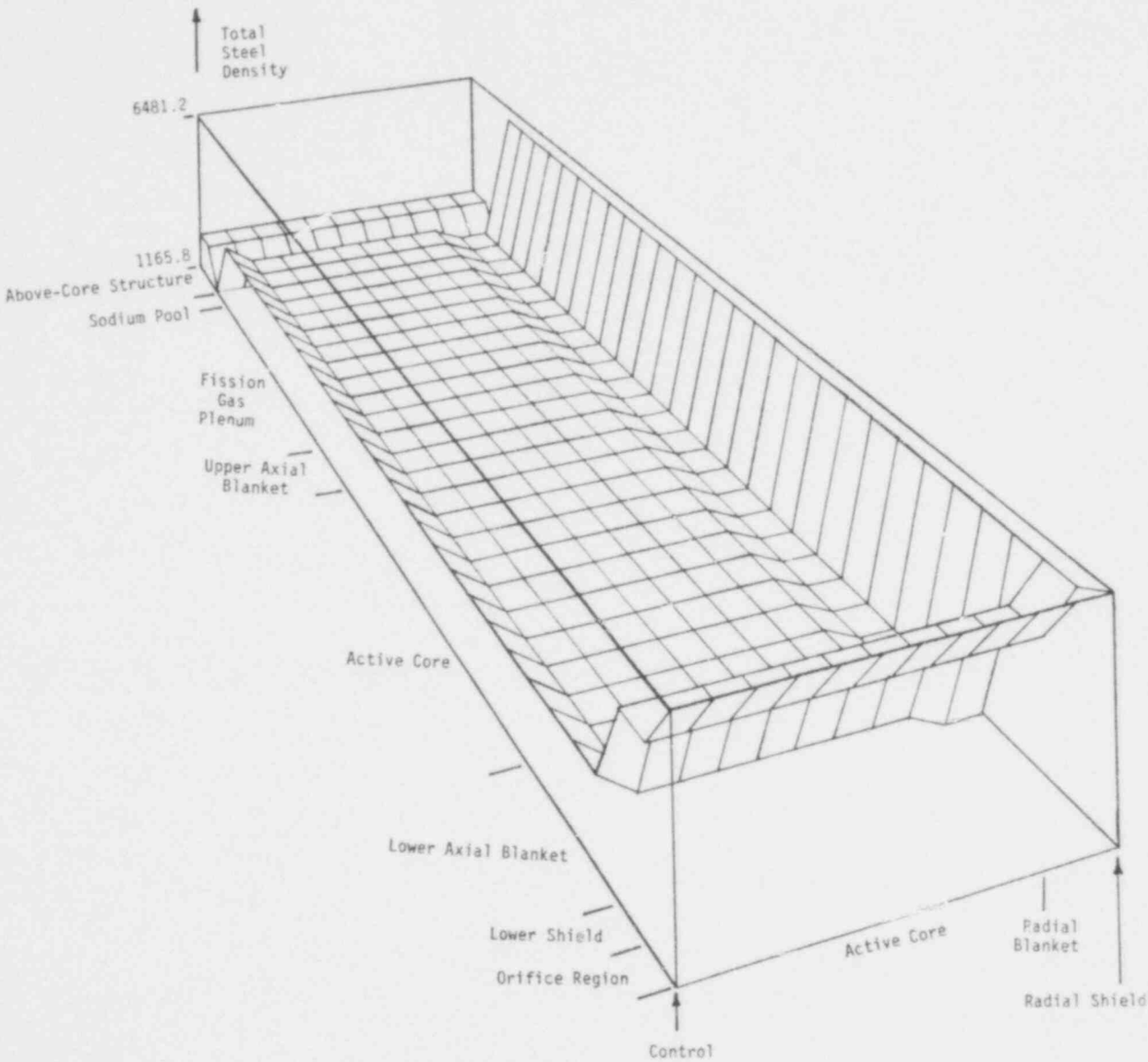

Fig. 78b. Initial total steel distribution for both full neutronics cases.

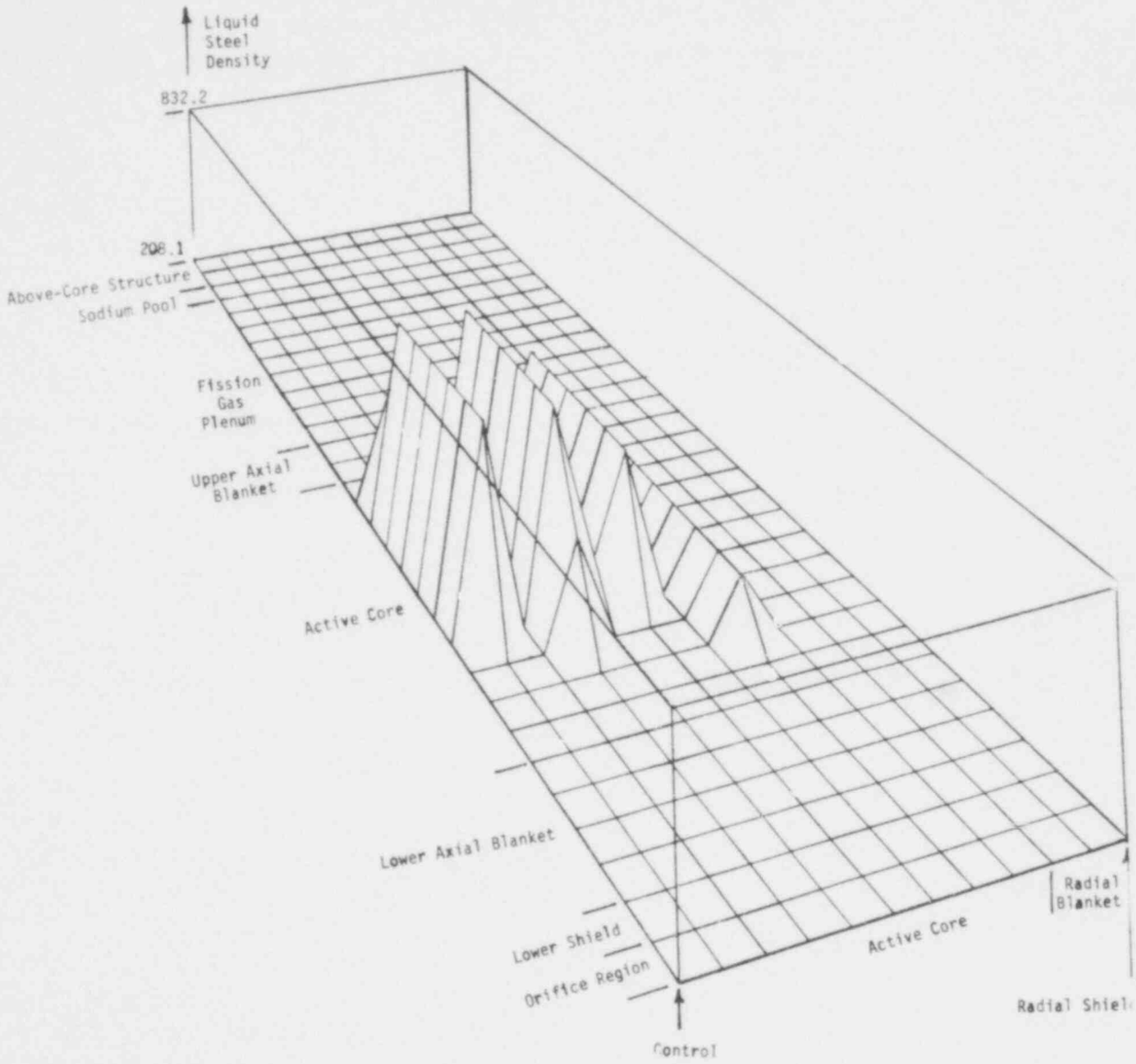

Fig. 78c. Initial liquid steel distribution for both full neutronics cases.

by raising the fuel specific energy in each cell in both enrichment zones of the active core in proportion to the normalized power distribution and calculating the corresponding liquid and solid densities and temperatures for the fuel. A peak initial liquid fuel temperature of approximately 3 700 K was obtained for the second space-time case, as compared with 3 101 K for the first. Hence, considerably more molten material was present in the second case (approximately 5 times more) with the result that liquid fuel was generated in some cells where there previously was none. The sodium in those cells was removed to obviate any unphysical fuel-coolant interactions. Figures 79a-d show the initial solid fabricated fuel distributions and the initial liquid fuel distributions for both cases.

The higher energy resulted in a more vigorous dispersal (driven by sodium vaporization at the lower sodium interface where liquid-liquid heat transfer occurs) of the liquid fuel and steel than in the first case, with molten core material pushed both upwards into the fission gas plenum and the above-core structure and downwards into the lower shield and orifice region. As a result, in a few hundred milliseconds the reactivity plummeted from the initial \$0.76 to about -\$40.00, compared with the drop to only -\$7.00 in the first case. The reactivity continued to decrease more slowly until it reached about -\$60.00 at 2.9 s. The duration of both calculations was 5 s, during which time the reactivity in the first case oscillated by a few dollars around -\$9.00, whereas in the second case it oscillated by a few cents around -\$55.00. In the first case, the oscillations were caused by fuel draining into the core under the influence of gravity from its dispersed position in the upper axial blanket and subsequently being pushed out again by liquid-liquid heat transfer at the lower sodium interface. In the second case, the liquid fuel initially was pushed so far above the active core that it took much longer to drain back. As a result, it had both a longer time and a longer distance to transfer heat to the cold solid structure and the cooler liquid steel and subsequently to freeze onto structure or to form solid particles.

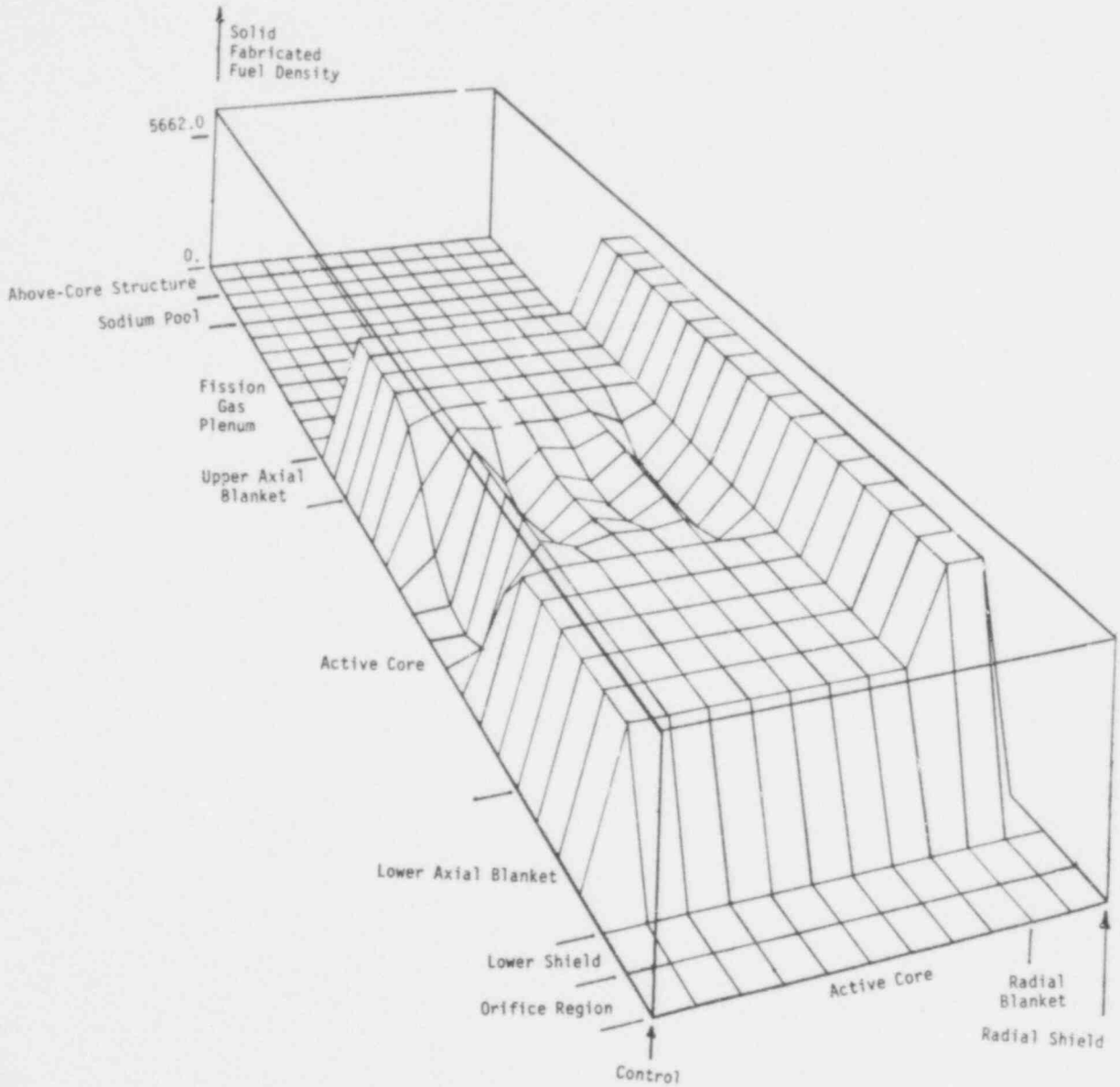

Fig. 79a. Initial solid fabricated fuel distribution for first case.

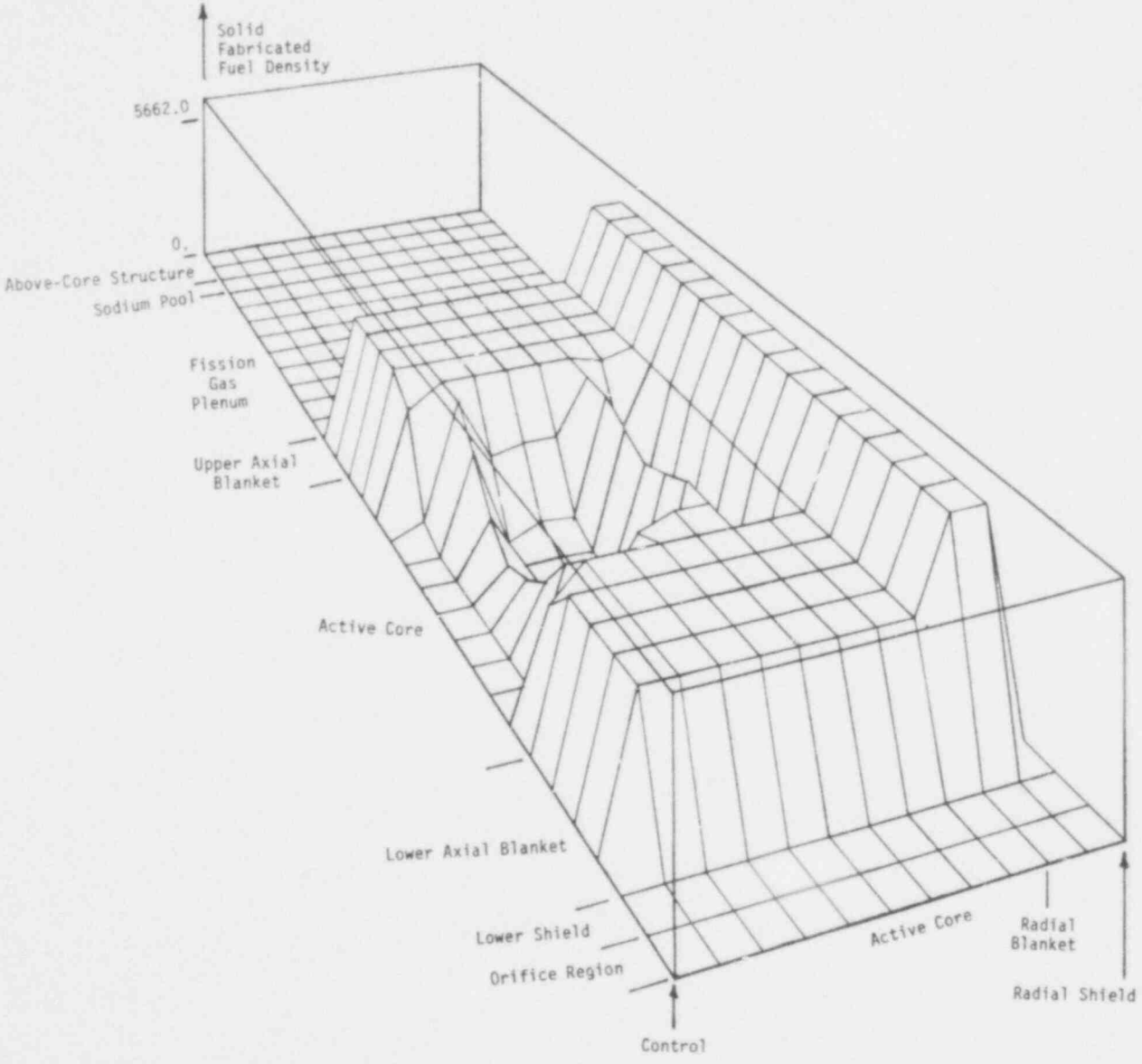

Fig. 79b. Initial solid fabricated fuel distribution for second case.

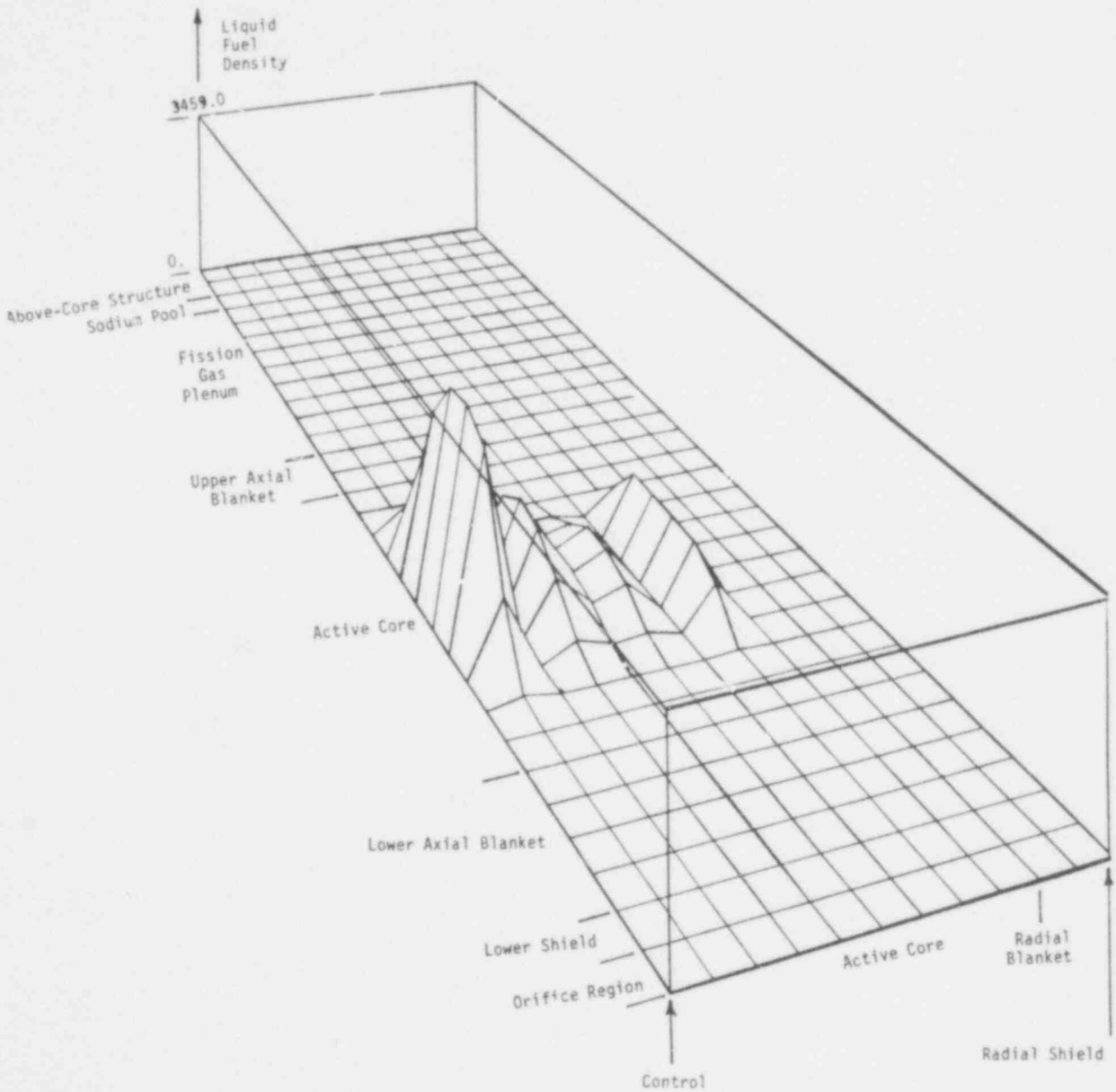

Fig. 79c. Initial liquid fuel distribution for first case.

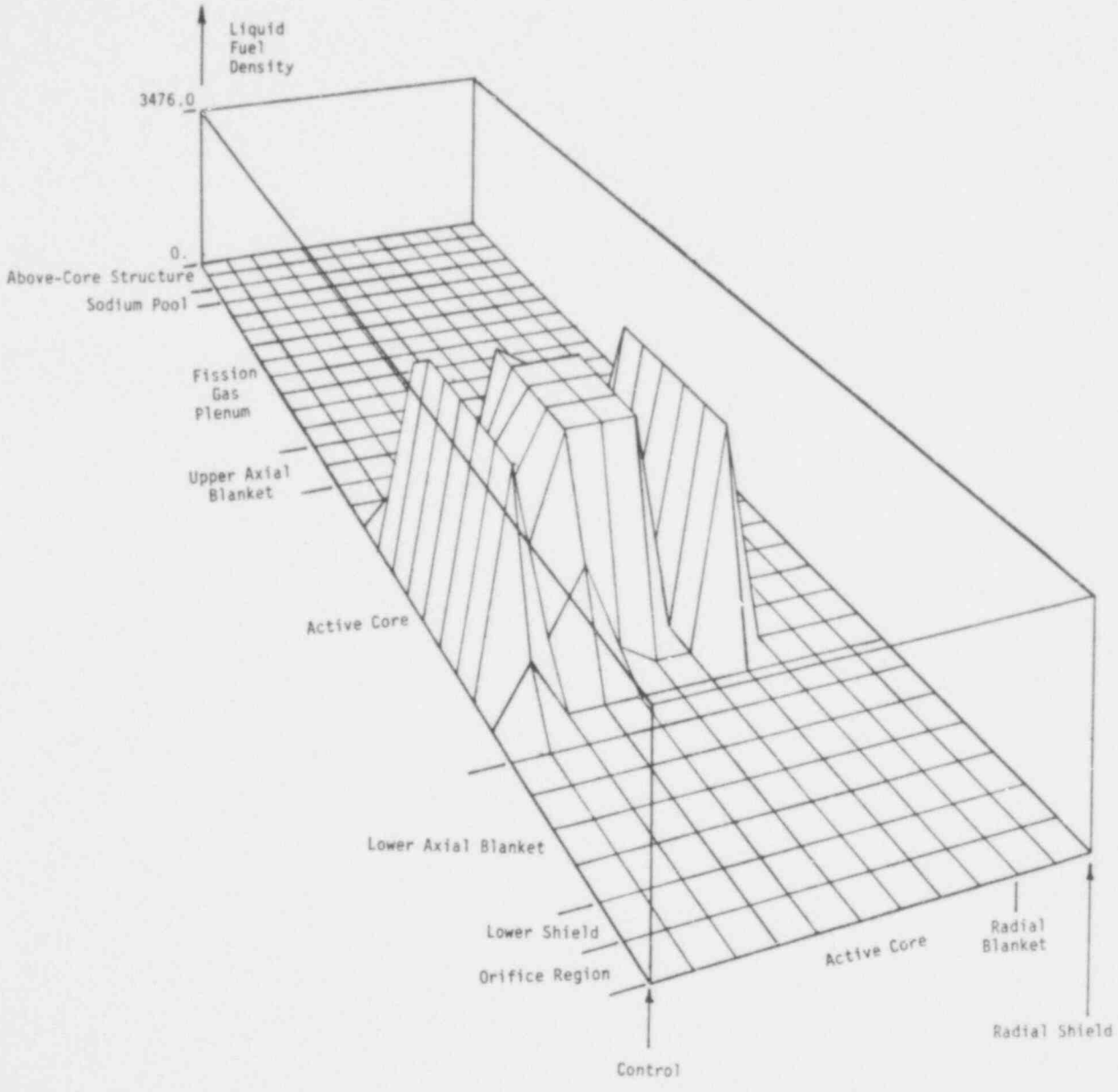

Fig. 79d. Initial liquid fuel distribution for second case.

The slight (10%) upper blockage formation of the first case did not occur in the second case because the frozen fuel was distributed throughout the entire upper structure instead of being concentrated in the upper axial blanket. Further, the initial fuel temperatures were higher. Partially molten can walls pervaded the core in less than 1 s in the second case, as compared with about 3 s in the first case.

Only small amounts of fuel and steel (about 40 kg and 300 kg, respectively) were lost from the system in the first case, whereas the larger initial quantity of molten material in the second case resulted in a much larger mass loss: 800 kg of fuel (10%) and 2 000 kg of steel (50%). Most of the mass loss was in the form of a slurry of liquid steel and solid fuel particles which drained or was pushed downward through the inlet orifice region. Figures 80a-h show the distribution of total fuel, solid fabricated fuel, frozen fuel, and mobile solid fuel particles for both cases at 5 s; by this time there was no liquid fuel remaining. Figures 81a-f show the distribution of total steel, liquid steel, and mobile steel particles for both cases at 5 s.

There was no massive voiding of sodium from the sodium pool in the second case as was seen in the first case, due to the rapid can wall failure enabling the formation of a molten pool which effectively prevented the channeled flow of sodium vapor through the core region. In addition, the vigorous radial sloshing back and forth that occurred in the first case did not happen in the second case because the strong initial liquid-liquid interactions that dispersed the fuel and steel upward also ejected the sodium downward, thereby voiding the lower portion of the subassemblies. Hence, the sodium was unavailable at the bottom of the molten pool as a pressure source to drive sloshing.

These first mechanistic calculations of transition phase dynamics have highlighted the influence of several phenomena on the overall problem behavior and have raised several significant questions which can be used to focus further analyses. The early behavior is strongly influenced by the strength of the heat transfer from the liquid core material to the liquid sodium at the lower sodium interface.

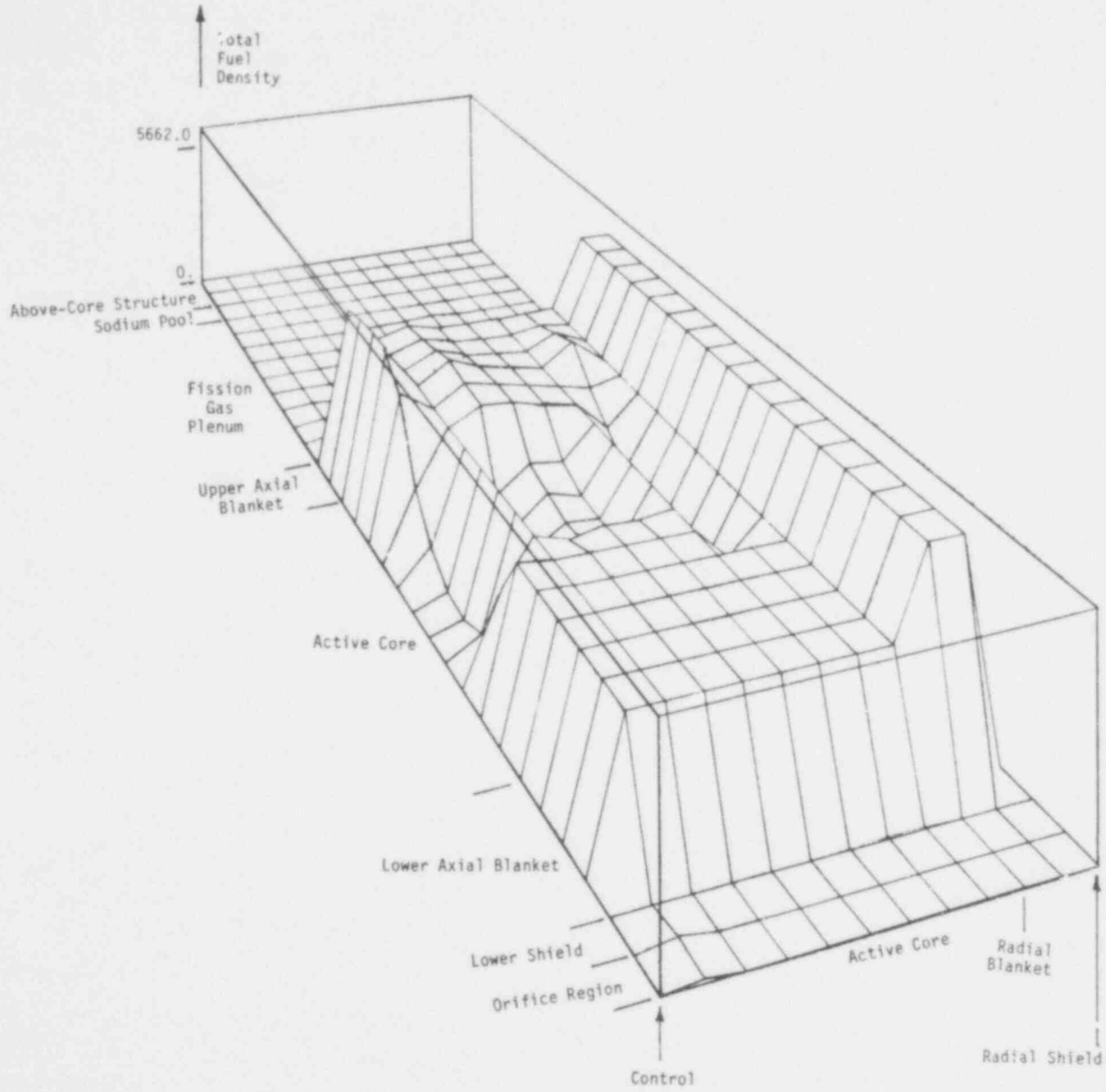

Fig. 80a. Total fuel distribution for first case at t = 5 s.

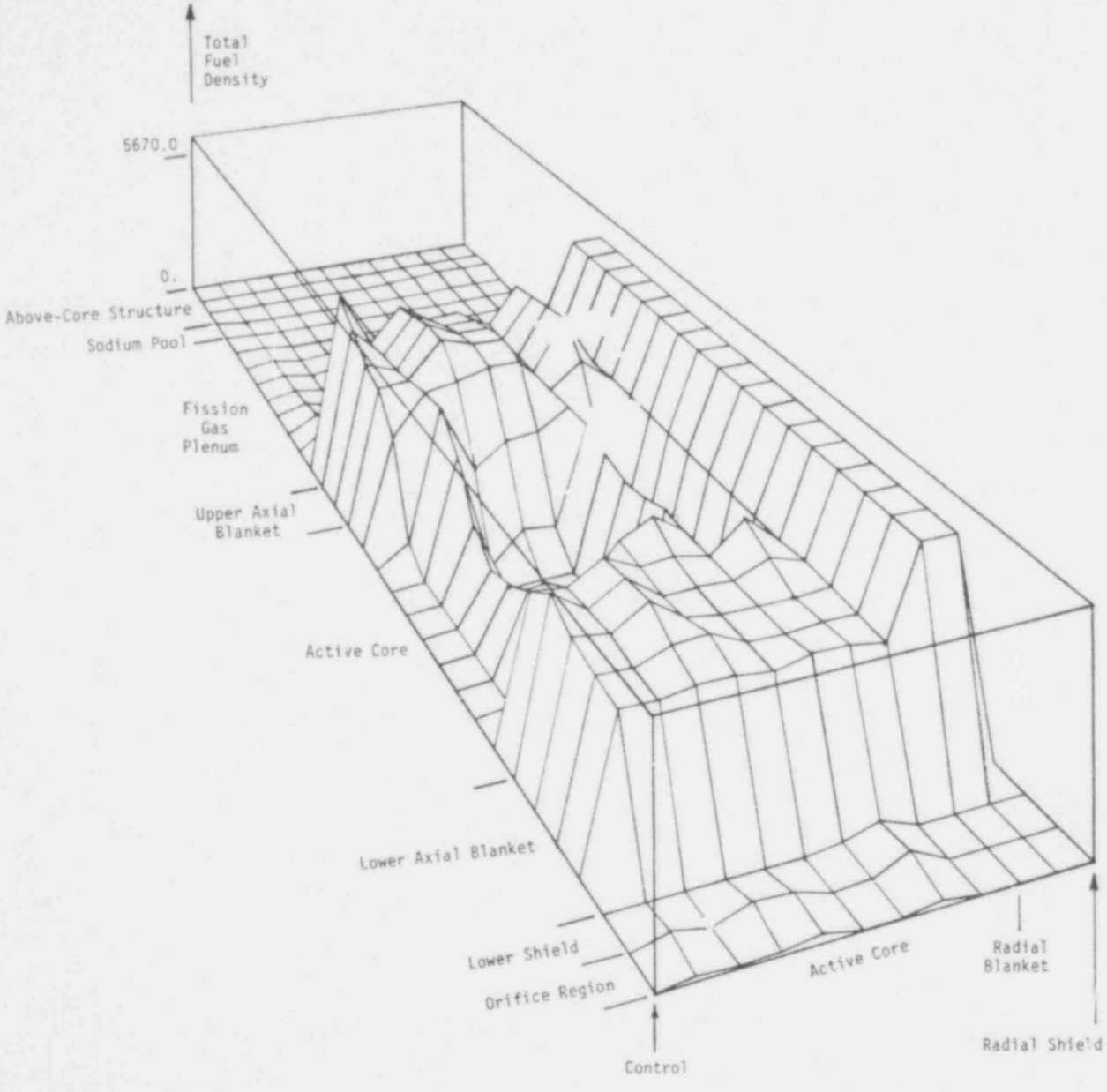

Fig. 80b. Total fuel distribution for second case at t = 5 s.

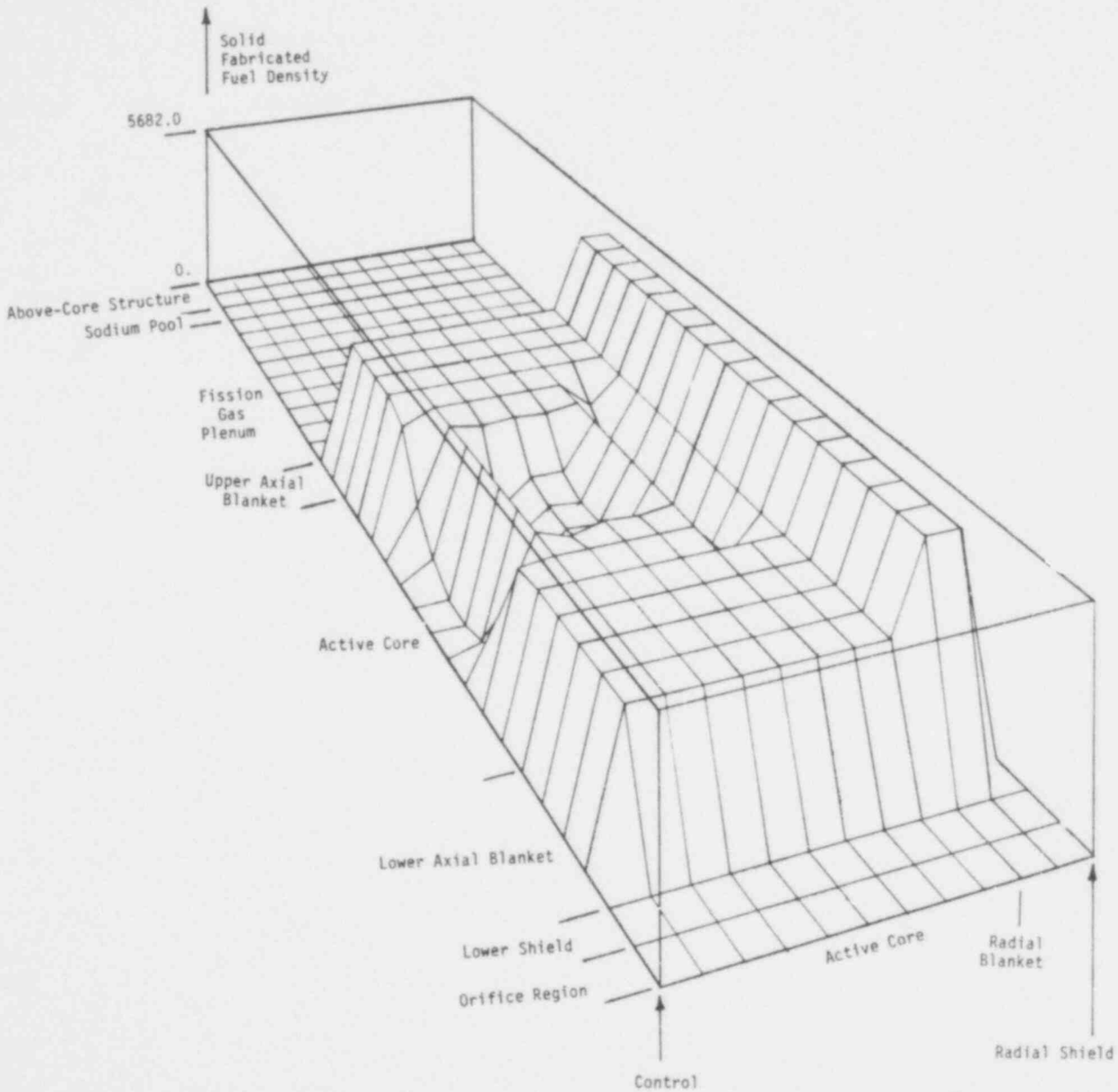

Fig. 80c. Solid fabricated fuel distribution at t = 5 s for first case.

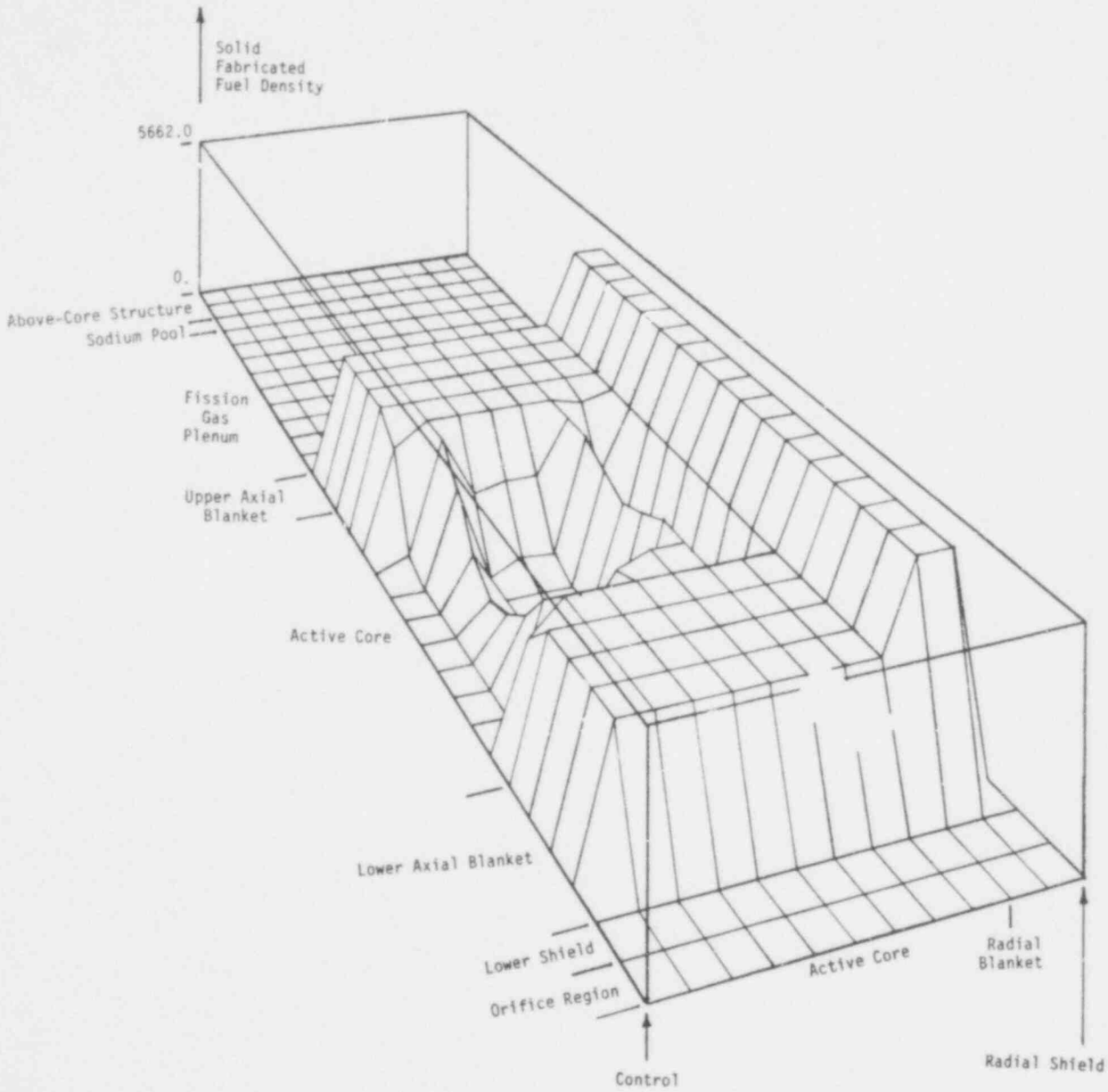

Fig. 80d. Solid fabricated fuel distribution at t = 5 s for second case.

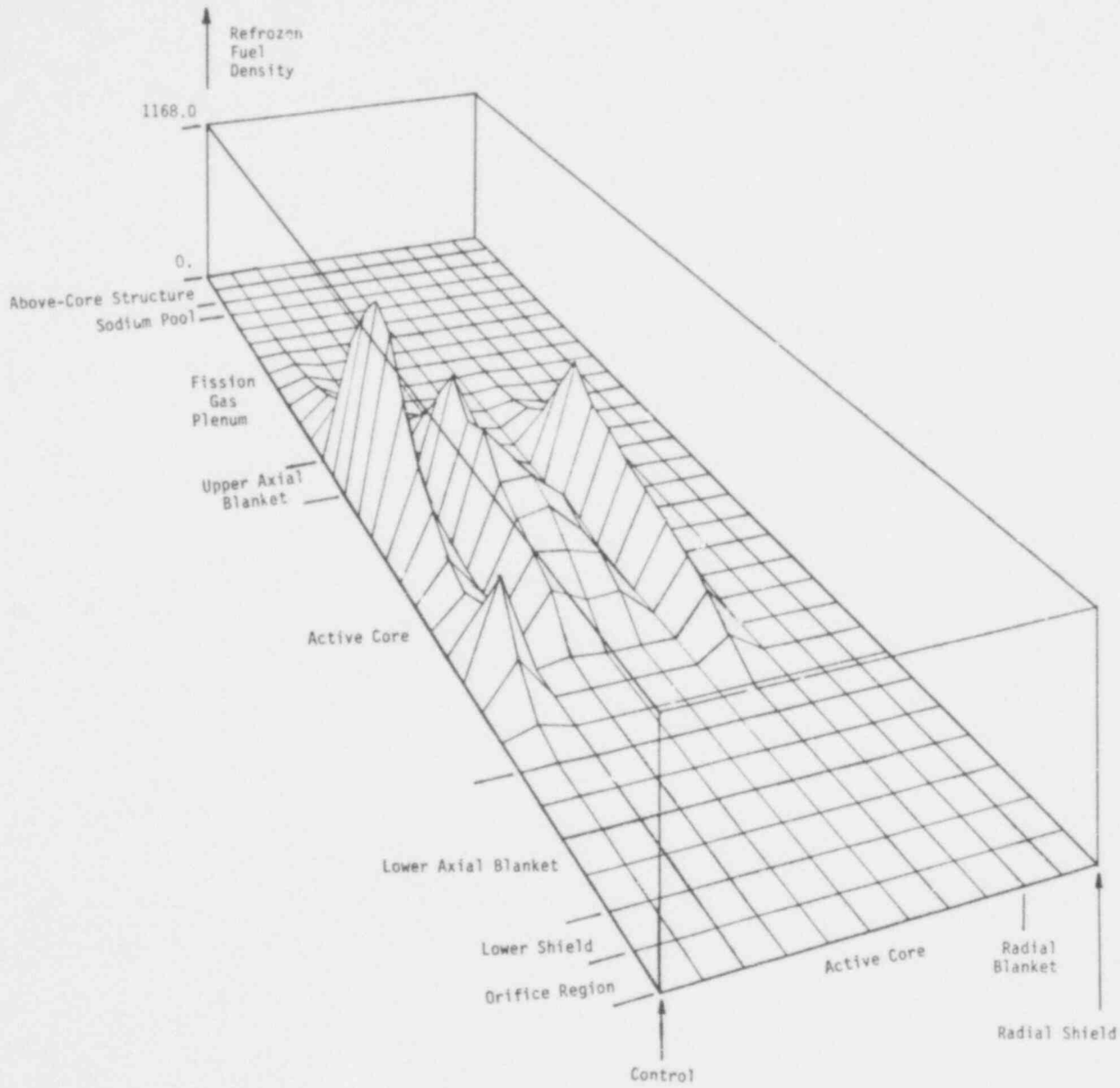

Fig. 80e. Refrozen fuel distribution at t = 5 s for first case.

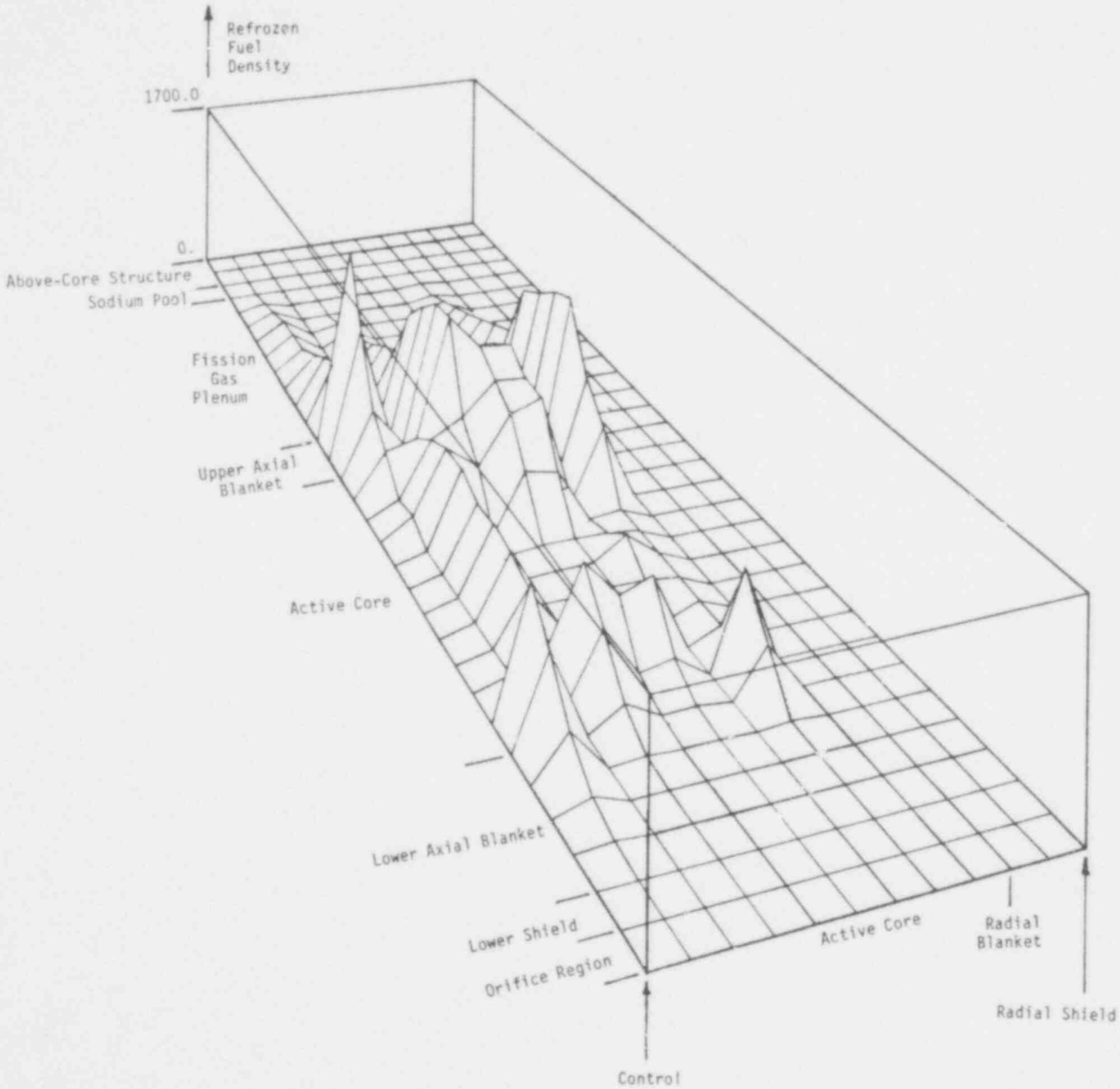

Fig. 80f. Refrozen fuel distribution at t = 5 s for second case.

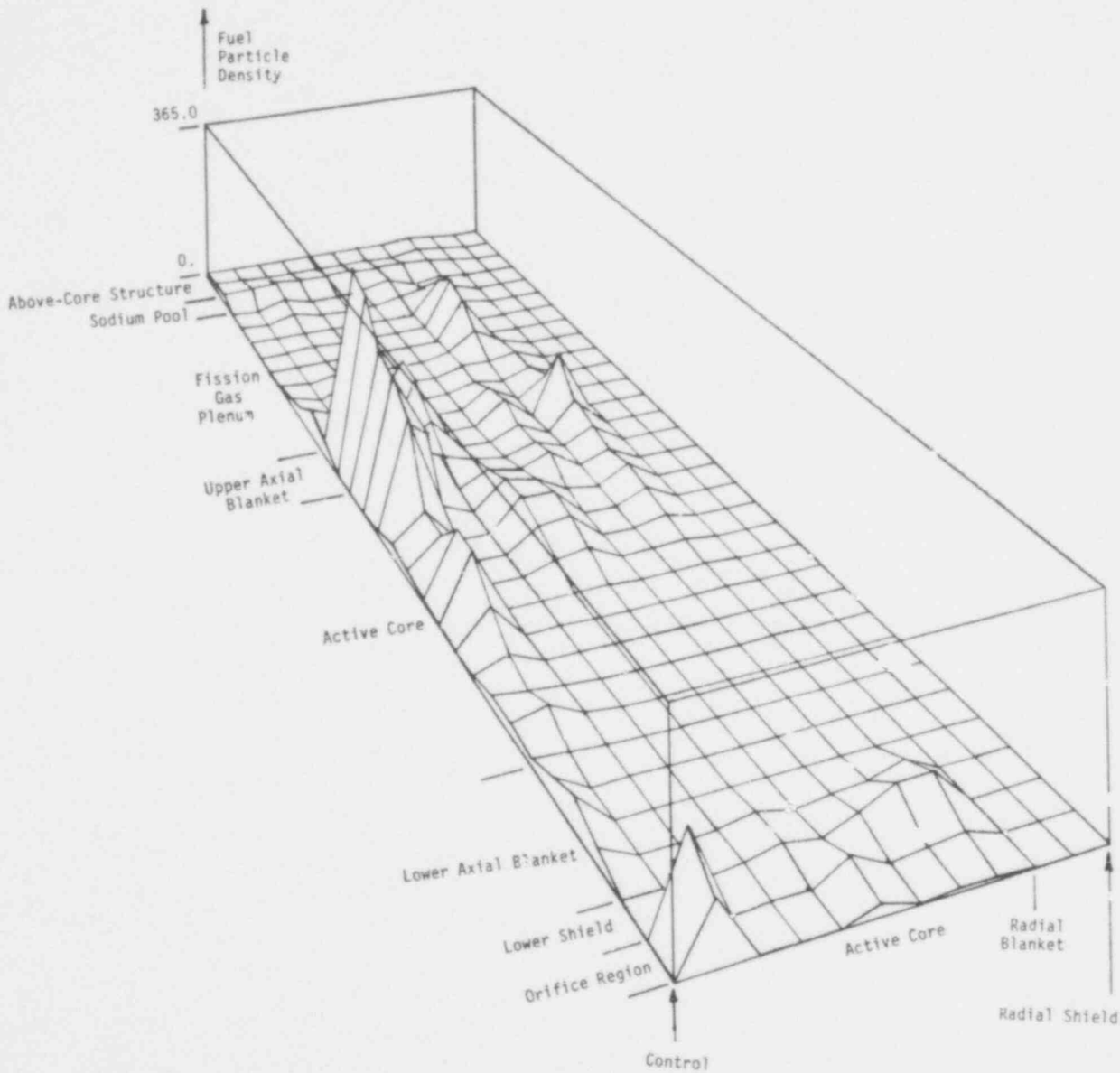

Fig. 80g. Distribution of mobile solid fuel particles at t = 5 s for first case.

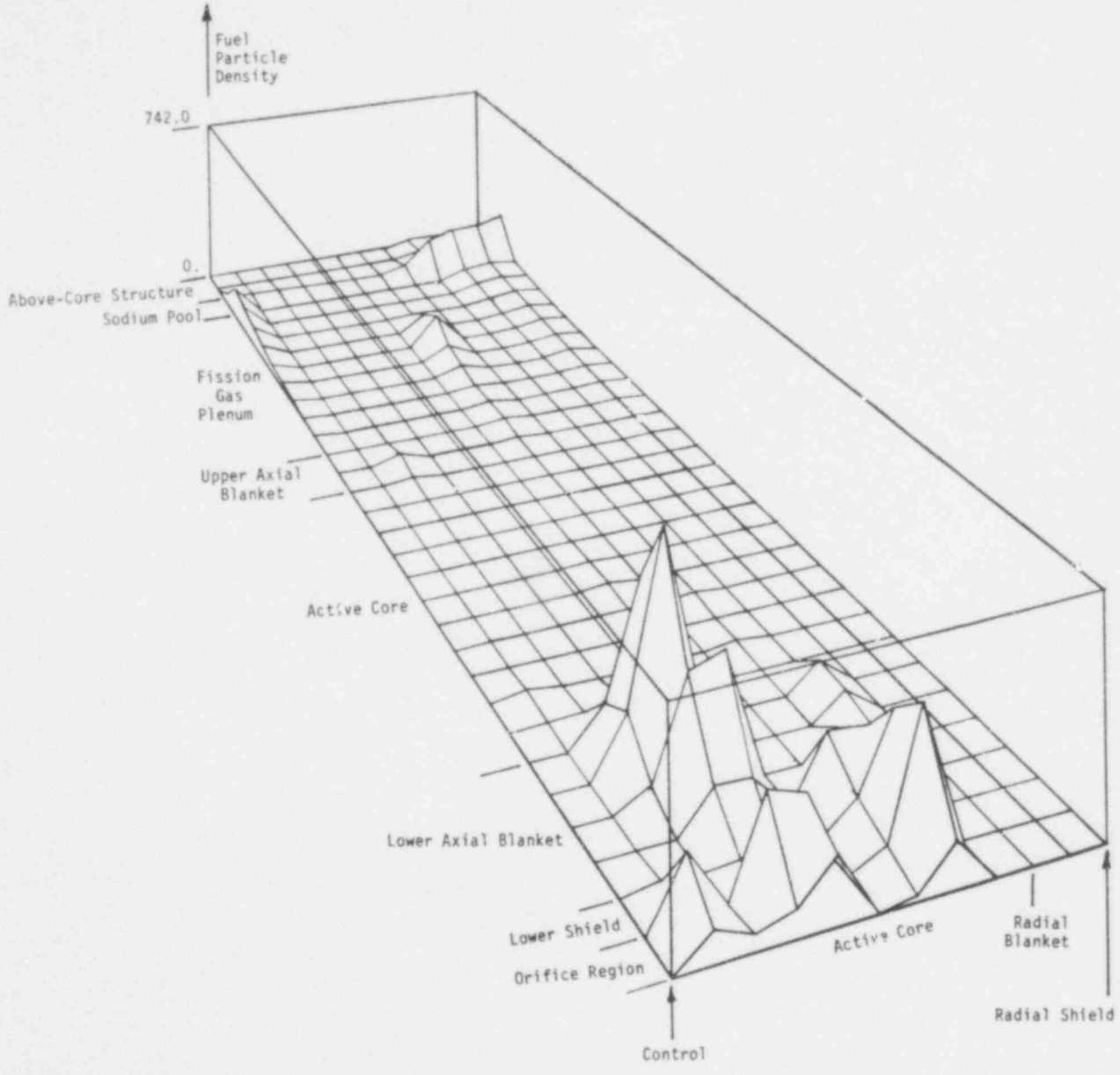

Fig. 80h. Distribution of mobile solid fuel particles at t = 5 s for second case.

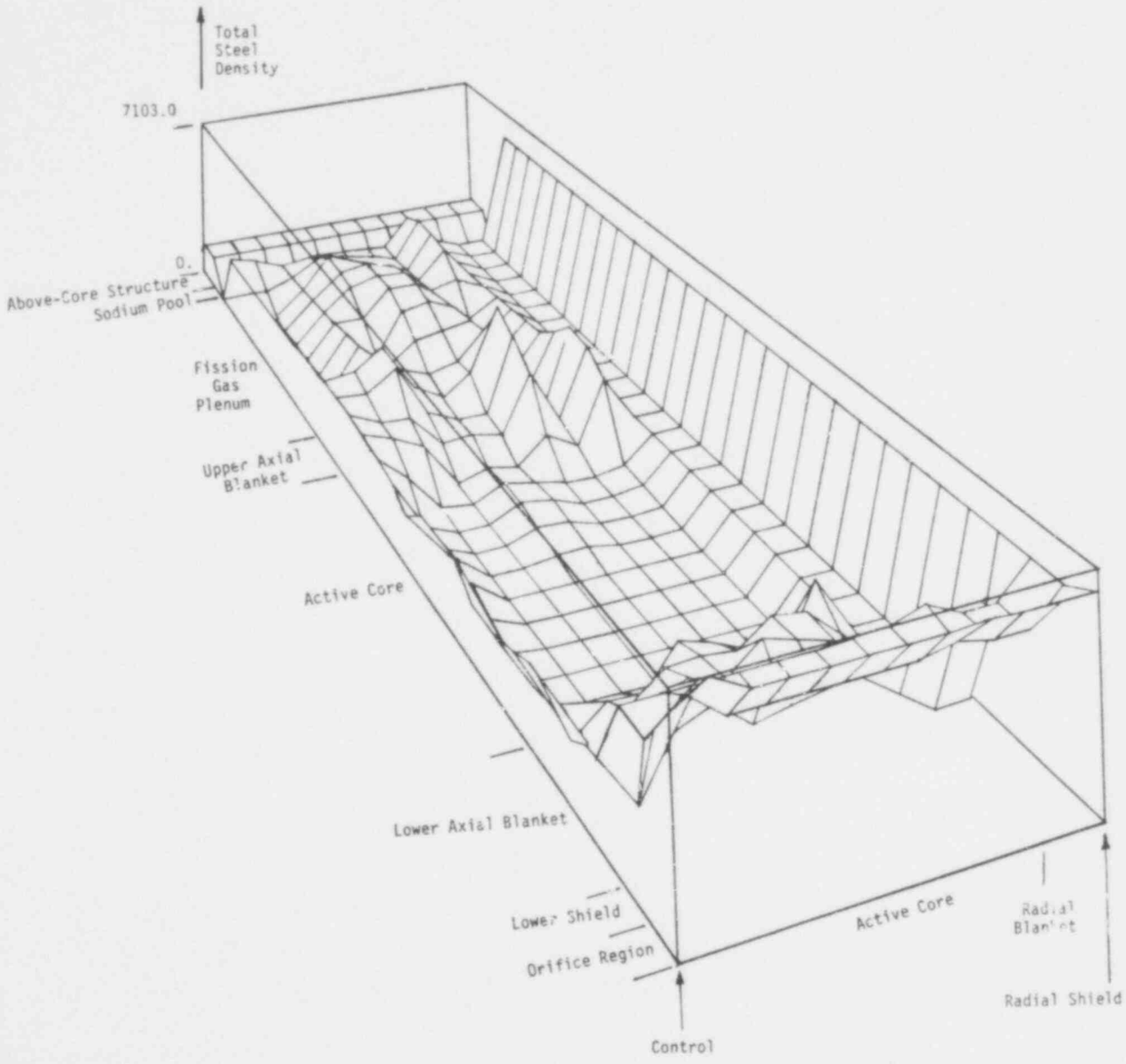

Fig. 81a. Total steel redistribution at t = 5 s for first case.

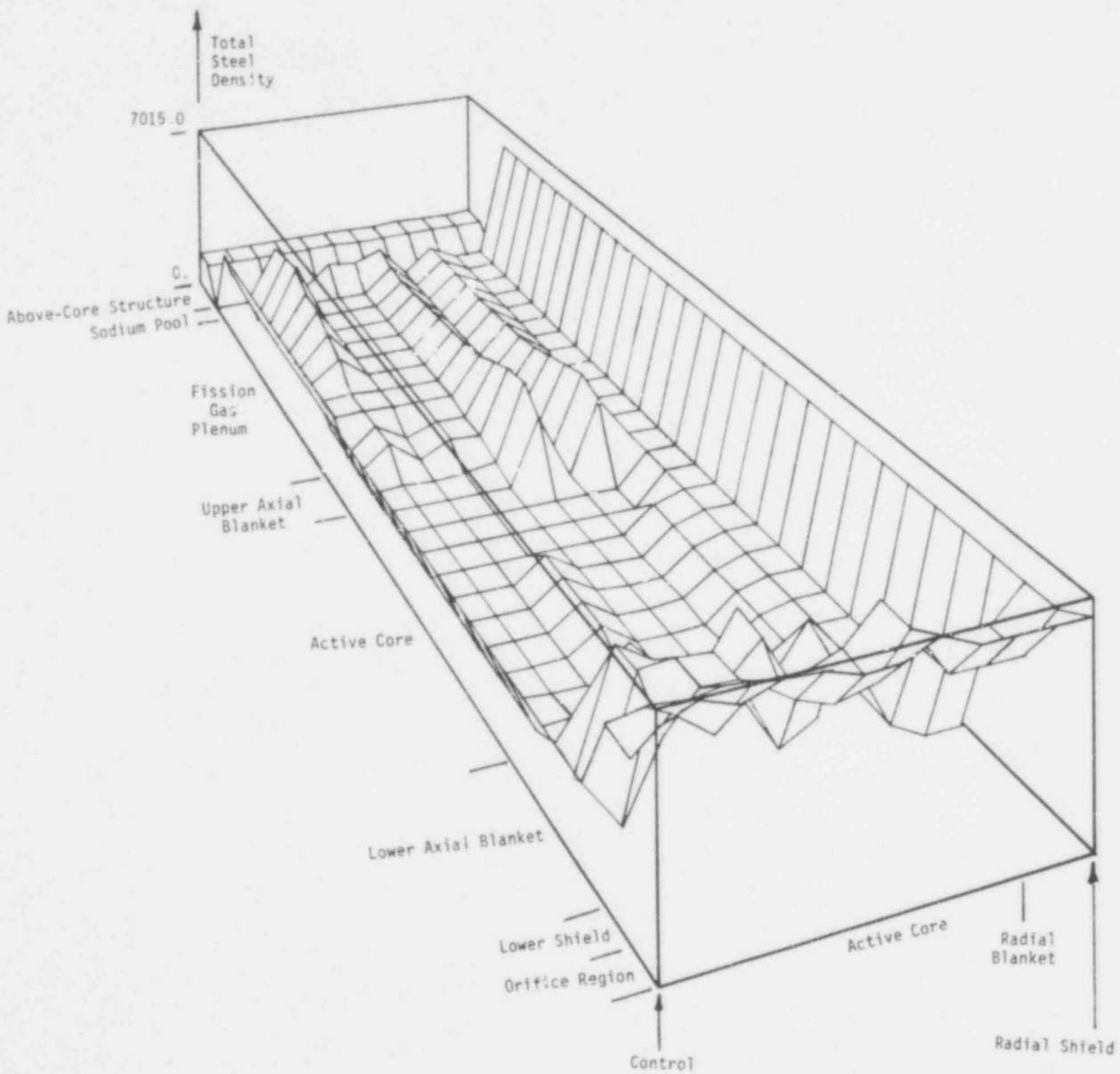

Fig. 81b. Total steel redistribution at t = 5 s for second case.

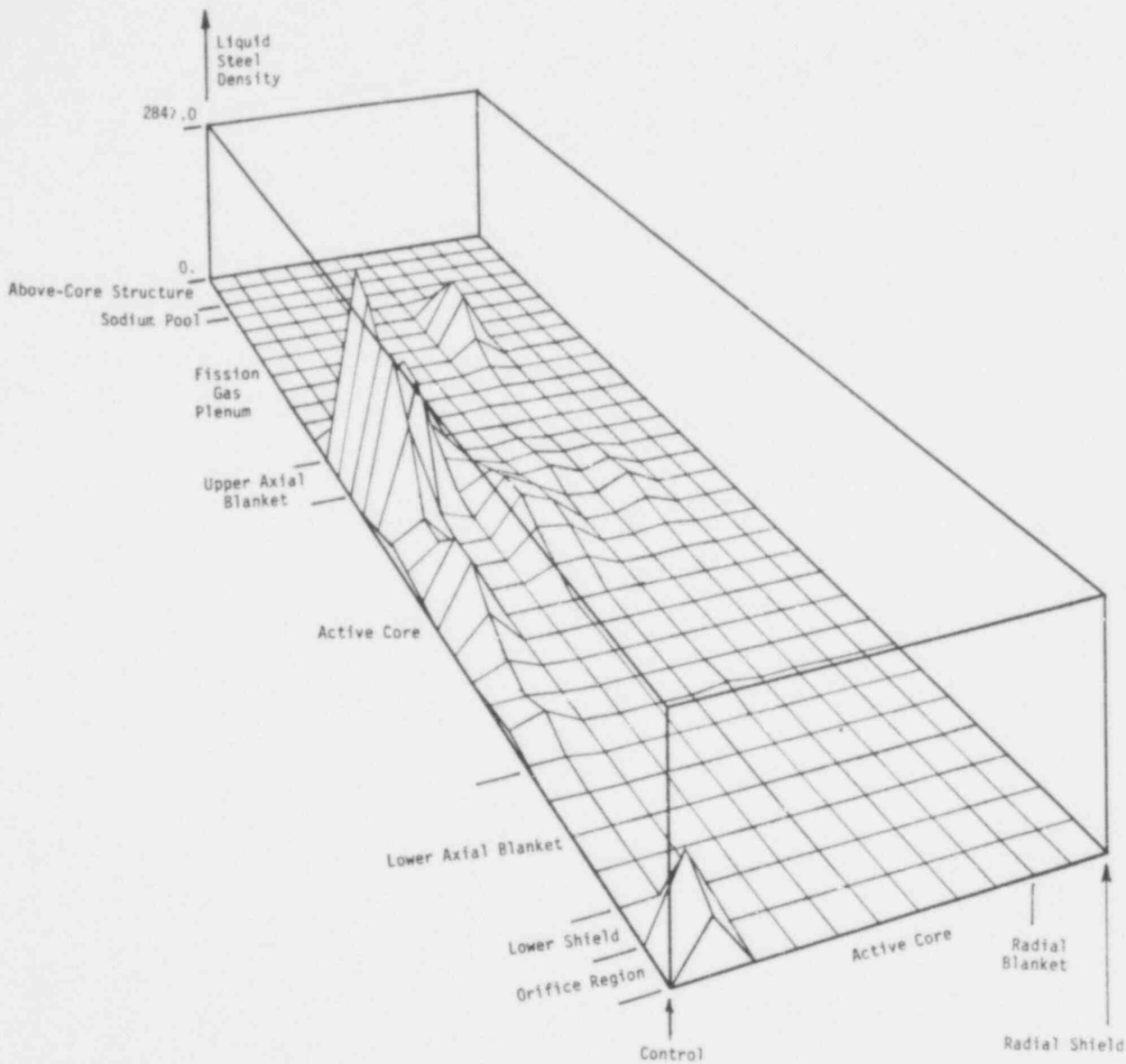

Fig. 81c. Liquid steel distribution at t = 5 s for first case.

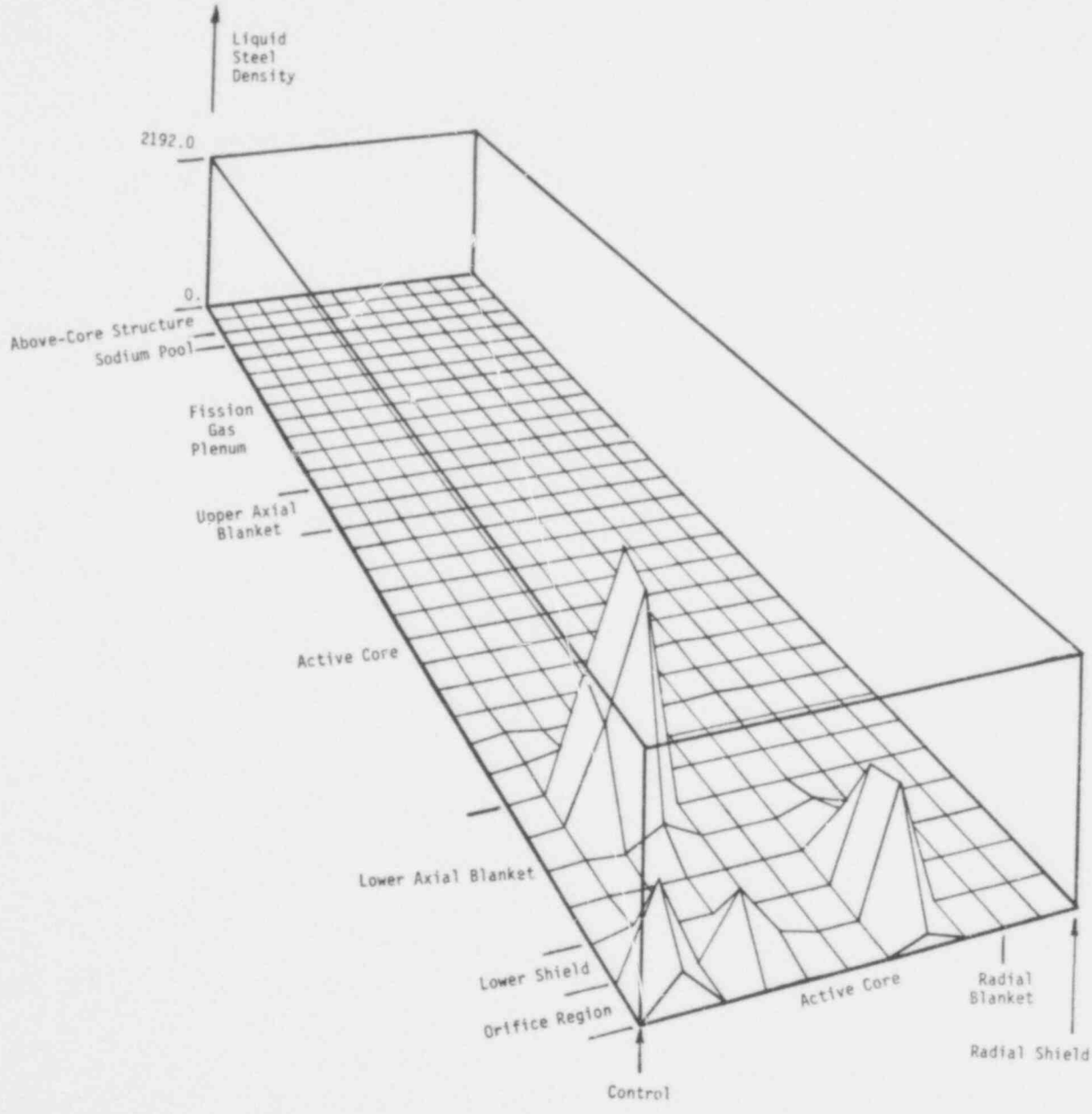

Fig. 81d. Liquid steel distribution at t = 5 s for second case.

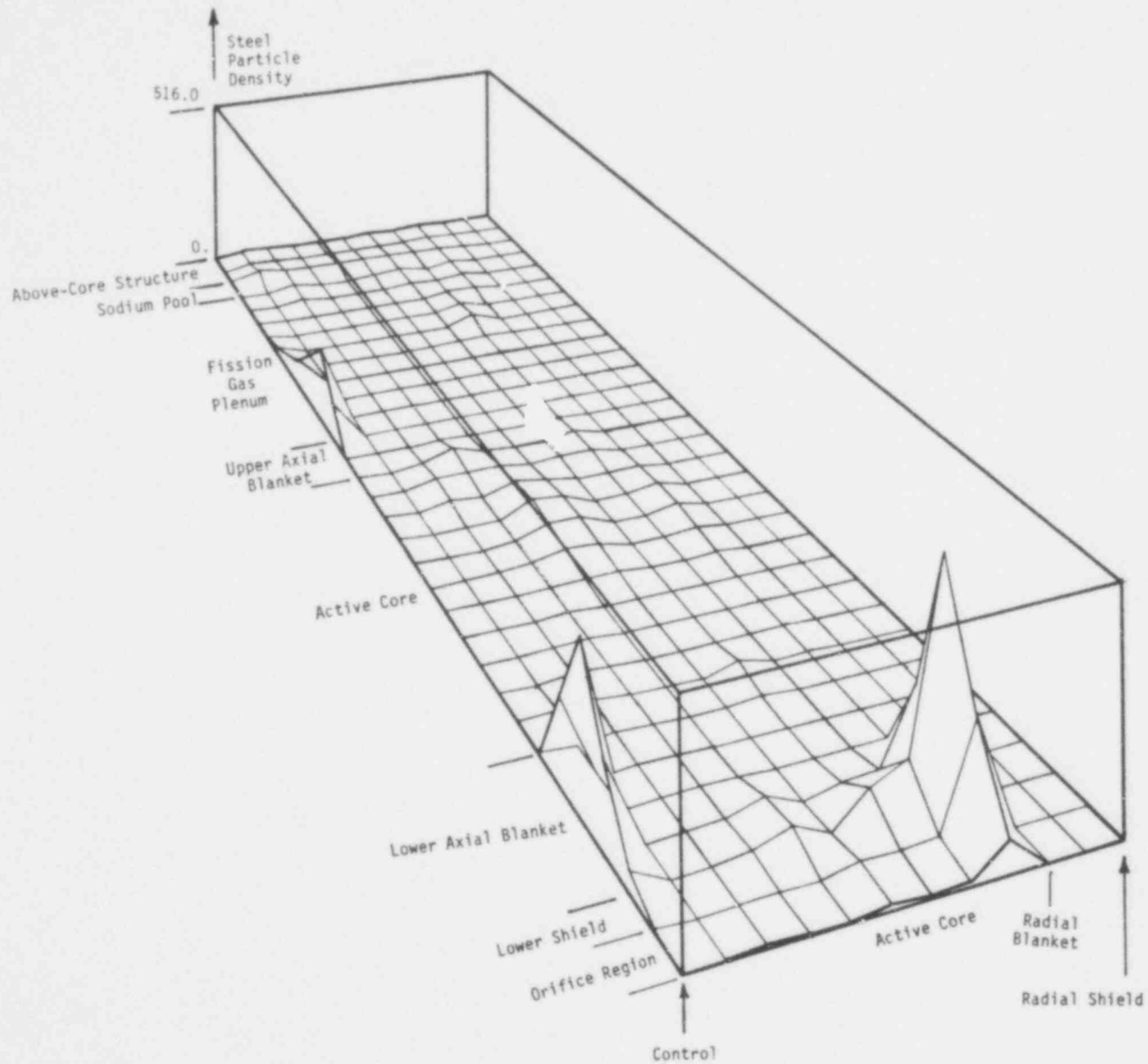

Fig. 8le. Distribution of mobile solid steel particles at t = 5 s for first case.

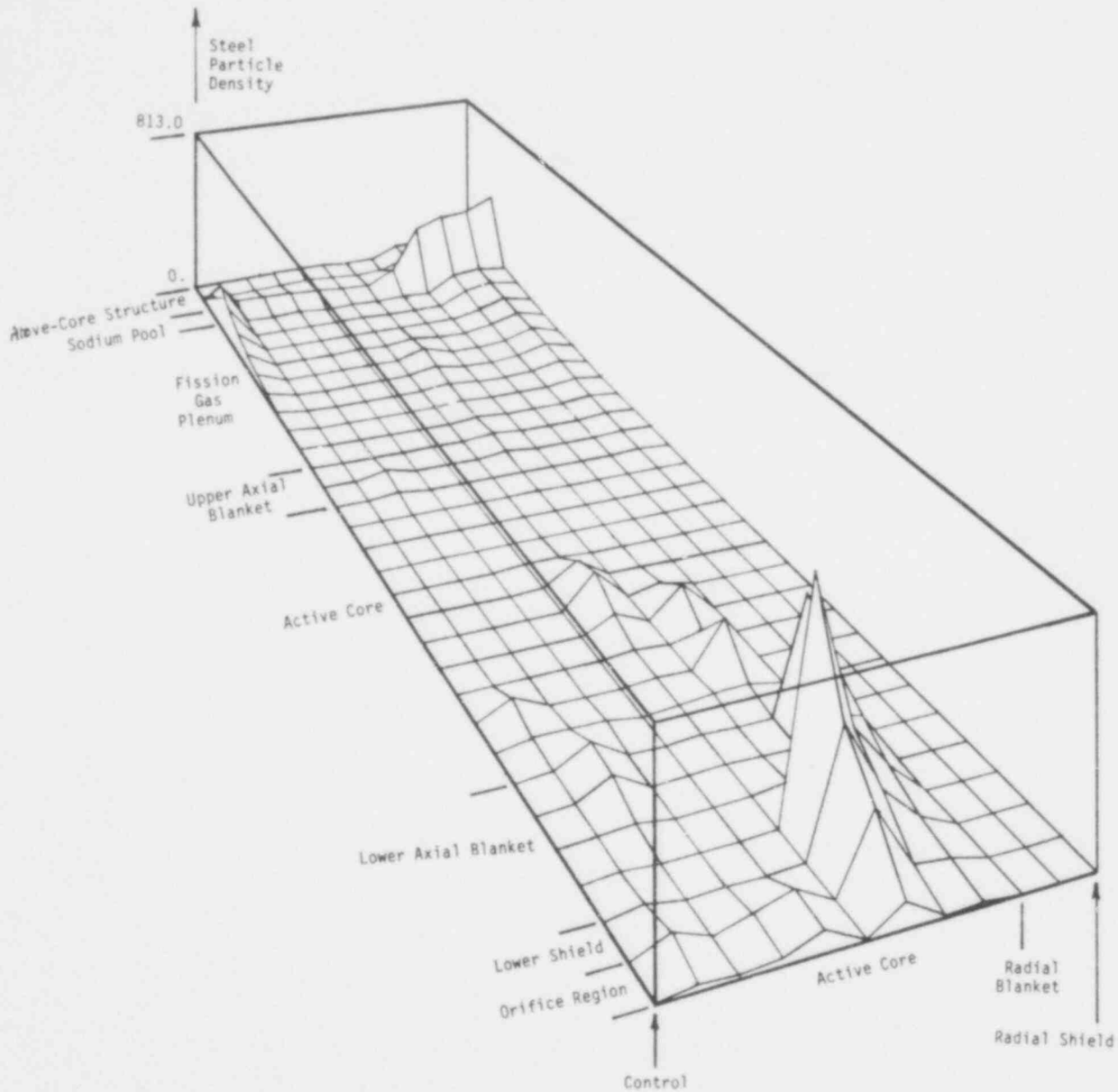

Fig. 81f. Distribution of mobile solid steel particles at t = 5 s for second case.

Strong interactions of this sort are highly dispersive axially, leading to a rapid drop in reactivity. In addition, the downward ejection of sodium reduces or eliminates opposition (from sodium vapor production) to molten core material draining into the lower axial blanket and the lower shield.

A second important phenomenon is the freezing of the mixture of fuel and steel. The bulk cooling of the fuel by the entrained steel may cause early plugging of the escape paths for the molten fuel. If this were to happen, the larger fuel loss predicted in the second full neutronics case might not occur, thus significantly altering the character of the subsequent behavior.

The most significant questions related to generic transition phase behavior are

1. Will incoherent fuel motion always (to a high probability) prevent significant reactivity insertion rates (> 50 $/s) from developing during the early part of the transition phase when most can walls are still intact? If so, then the necessity for great detail and accuracy in establishing initial conditions may be relaxed. Also, the requirement for detailed and verified early transition phase models (such as heat transfer to can walls, etc.) may be relaxed substantially.

2. Is there a range of transition phase initial conditions in which boilup dispersal will not moderate or prevent recriticality events while the molten pool is forming? In the first full neutronics case, the energy content of the fuel was insufficient to bring the molten steel to its boiling point. Hence, boilup dispersal could not occur without additional heating, such as long-term decay heating or recriticality.

3. Are there modes for locally perturbing the molten pool with resulting significant neutronics effects? An example of such a perturbation observed in the first full neutronics case is the series of local fuel-coolant interactions at the lower unblocked boundary, with the resulting reactivity oscillations, albeit while far subcritical in this case.

These initial explorations of the transition phase have been helpful in providing a better perspective on the various physical processes that may occur and in illustrating the feasibility of the

mechanistic approach. Further efforts will be directed toward the above generic questions and toward resolution of the treatment of those processes identified as key phenomena in the overall results.

5. Structural Analysis of the Upper Core Structure Under Postdisassembly Expansion

(F. Ju and J. G. Bennett, Q-13)

The mechanistic analysis[62] of the postdisassembly expansion phase of a hypothetical core disruptive accident (HCDA) has indicated the importance of the upper core structure in mitigating the damage potential of the accident. It is thus important to determine the conditions under which this mitigating effect may deteriorate because of pressure driven motion of the upper core structure and/or crushing of the pins, thereby blocking the flow channels. Both of these structural dynamics effects could lead to reduced heat absorption in the upper core structure and loss of the throttled ejection of core material into the sodium pool.

Two aspects of the integrity of the above core structures are discussed below. The total ejection of the upper core structure can occur only if the upper internal structure (flow guide structure) is effectively loaded by the high core pressure and driven upward to open a large flow path between the core and the pool. This pressure loading can occur if the upper core structure is driven from the core barrel region and up against the upper internal structure. The threshold for this to occur is estimated below. The pin crushing threshold is also estimated.

It is assumed that the restraining structures at the Top Load Plane (TLP) and at the Above Core Load Plane (ACLP) are essentially at normal operating temperatures and the upper core structure is near the sodium saturation temperature during the core voiding transient. While details of the models are not presented here, the results of the analysis are discussed. Figures 82 and 83 show schematically the regions of concern and the model used to estimate the threshold for core uplift. Using the available data for the CRBR core, the total frictional force generated

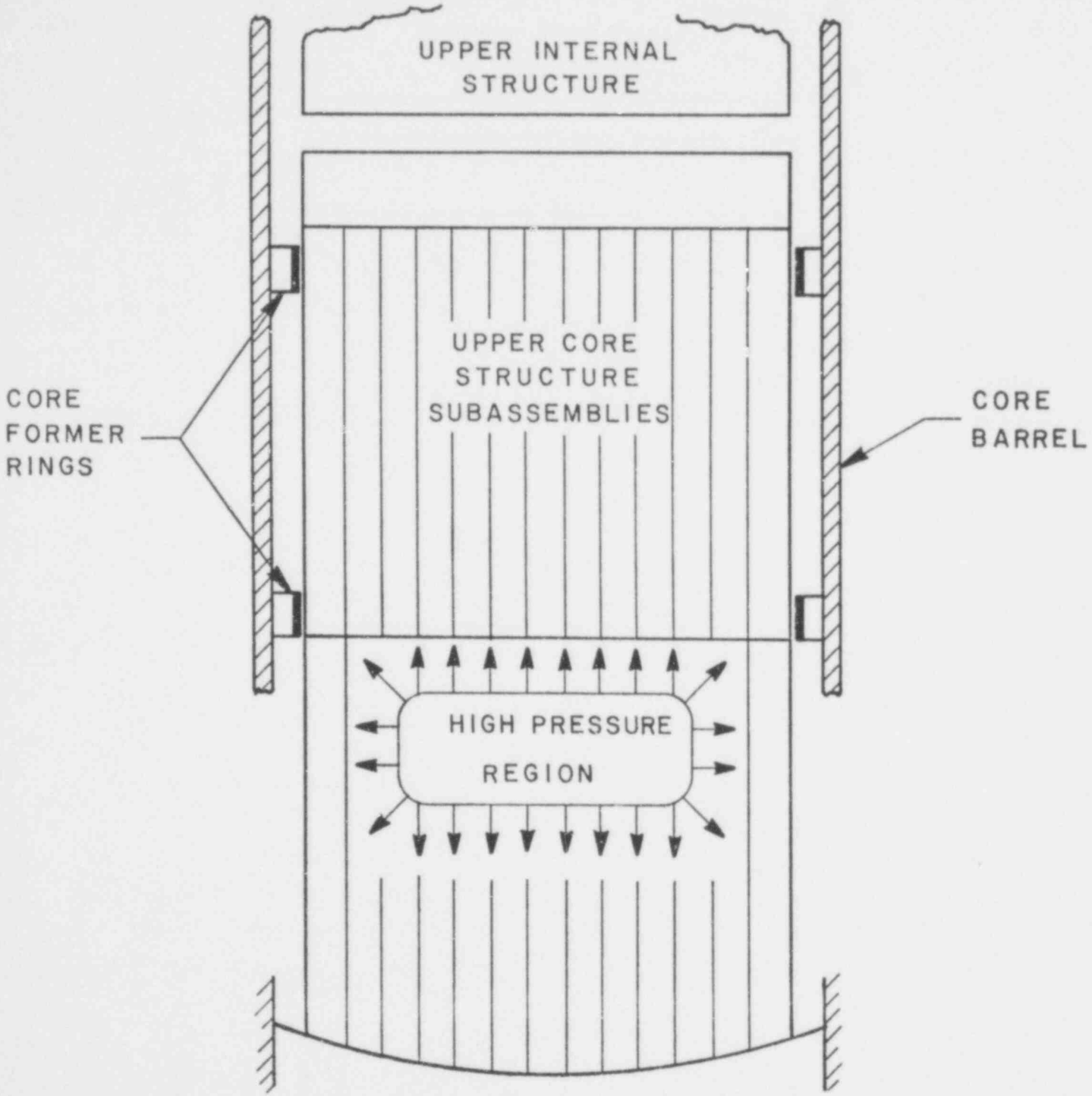

Fig. 82. Schematic section of the core illustrating the modeling used for uplift calculations.

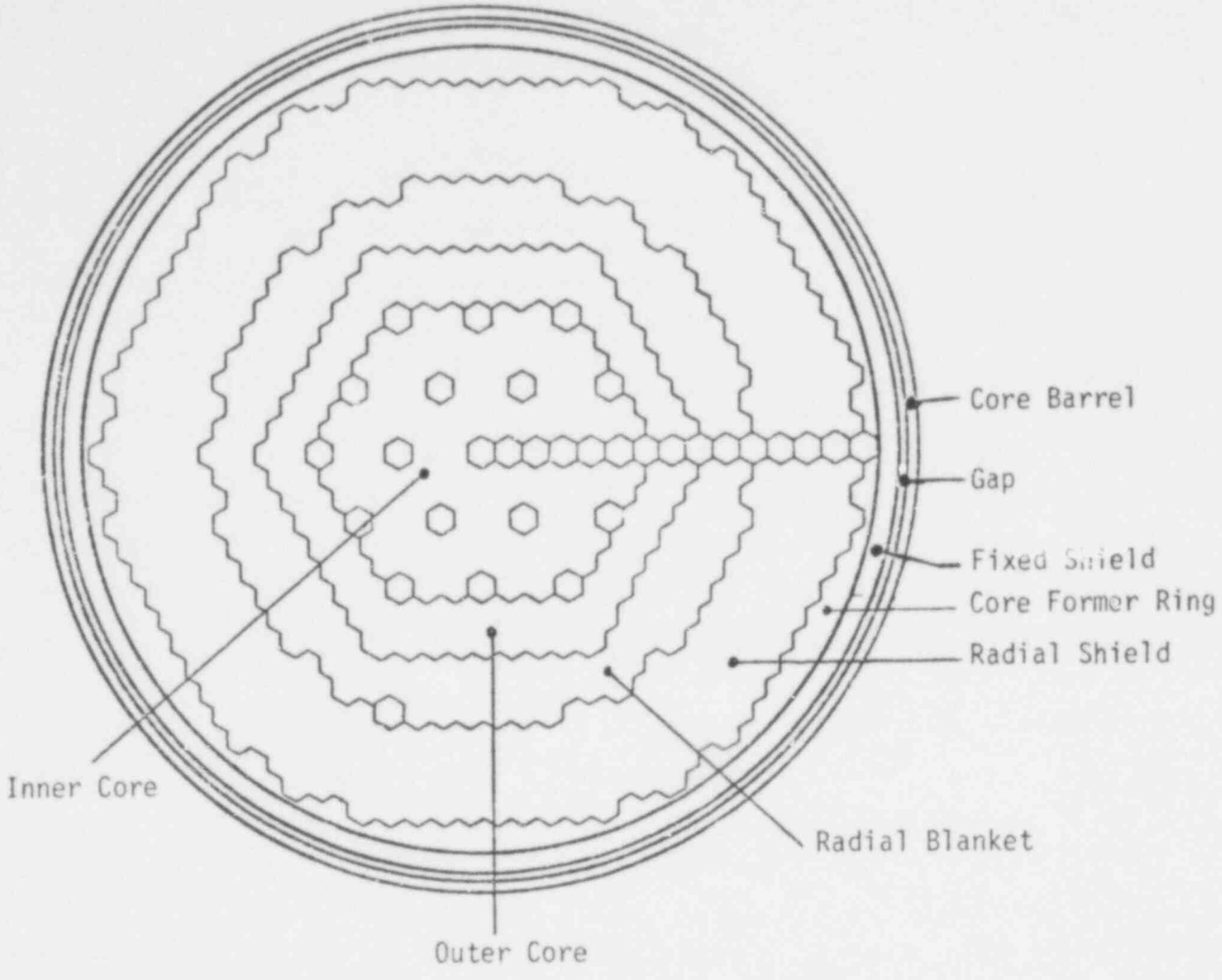

Fig. 83. Schematic cross section of the core showing regions considered for uplift.

at the core former rings to resist an uplifting pressure is estimated to be

$$F(\text{Breakaway}) = 82 \text{ MN } (18.29 \times 10^6 \text{ lb})$$

$$F(\text{Kinematic}) = 35 \text{ MN } (7.68 \times 10^6 \text{ lb}).$$

This frictional force is the result of differential thermal expansion between the upper core structure and the core barrel. The effect of core-pressure-induced core-barrel-strain, which could relieve to some extent the normal forces at the former rings, has been neglected. If the core pressure were applied over the active

core and radial blanket regions only, which have a combined cross-sectional area of 4.646 m^2, we estimate the uniform threshold uplifting pressures as

p(Breakaway) = 17.65 MPa (2 540 psi)

p(Kinematic) = 7.53 MPa (1 065 psi).

The kinematic value is that pressure required to sustain the uplift once it has been initiated.

The pressure required to lift a single hex can from the upper core structure can also be estimated from the geometric configuration and material property data. The breakaway and the kinematic lifting vapor pressures for a single hex can are respectively,

p(Breakaway) = 208.4 MPa (30 105 psi)

p(Kinematic) = 88.9 MPa (12 690 psi).

We can conclude that the lifting of any individual can is most unlikely, unless there is a bridging situation in the hex arrangement.

If we consider the slip plane to be at the interface between the radial blanket and the radial shield region, the resisting frictional force is esimated to be

F(Breakaway) = 60.5 MN (13.6×10^6 · lb)

F(Kinematic) = 25.5 MN (5.7×10^6 · lb).

If the pressure is applied uniformly to the entire cross-sectional area of the active core and radial blanket (4.646 m^2), then we have the following values:

p(Breakaway) = 13.0 MPa (1 890 psi)

p(Kinematic) = 5.5 MPa (800 psi).

We conclude that under the assumed conditions, large portions of the upper core structure would likely be ejected upward rather than single subassemblies or small groups of subassemblies. It would also appear likely that the upper core structure would begin to move toward the upper internal structure for core pressures on the order of 13 MPa (this would occur at about a 100 $/s reactivity insertion rate in a voided core LOF transient).

The second aspect of the problem of assessing the structural dynamics behavior of the upper core structure involves the local failures of fuel pins that can lead to closure of the flow channels through the upper core structure. Under high core pressure, the fuel pins may be pushed up against the upper hex can cap. If the local deformation or the bulk warpage of the pins becomes so severe as to block the passage of core material, the large mitigating effect of the upper core structure may be partially lost and the core pressure will tend to act directly on the upper internal structure in the case of CRBR. This analysis assumes that any core pressure that initiates warpage is the critical pressure above which the pin will continue its deformation and culminate in the total blockage of the passage.

The deformation of the fuel pin is assumed to be in the nature of either overall or local buckling of the pin. The critical load has been computed for both cases and the lower value is used for the failure pressure.

It is assumed that the limiting structural resistance is that of the fission gas plenum part of the pin. The plenum is modeled by a long hollow cylinder, subjected to an axial load from the core pressure acting over its full cross-sectional area.

Local buckling threshold stresses computed for the pin fission gas plenum walls vary from about 5.8 GPa to 9.9 GPa, which are well over the ultimate strength of the material. Therefore, local buckling will not occur, and it is more meaningful to examine the plenum buckling behavior as a column.

When the pins are all pushed up against the hex can cap, the shape of the cap is such that the top ends of the pins will all be held without displacement or rotation. The fission gas plenum

section of the individual pins can be displaced laterally except at points and directions where their lateral motion is constrained by the wire wrap. The model for this deformation mode is shown in Fig. 84. The plenum section then is modeled by a column, clamped at one end and pivoted at the other. There are lateral constraints at the discrete locations that represent the effect of the wire wrap.

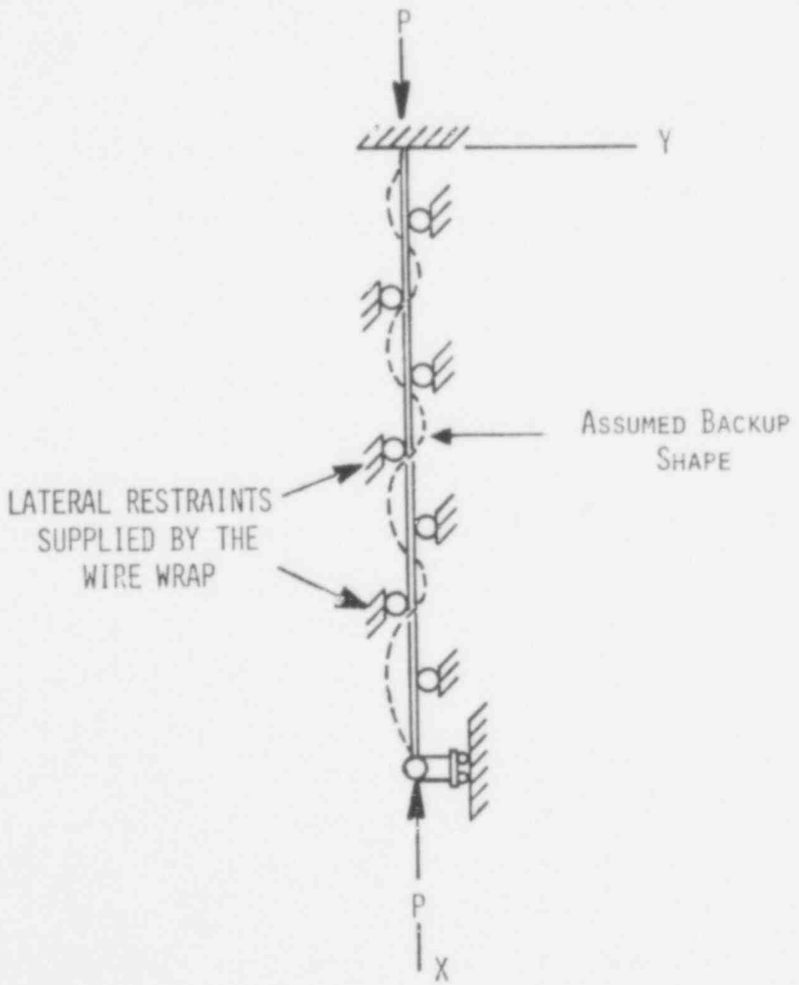

Fig. 84. Assumed deformation mode and model for buckling of the fission gas plenum of the fuel pin.

The critical stress computed from this model is about 58 MPa, far lower than critical stresses computed for local buckling. The core pressure necessary to produce this critical stress is estimated to be about 14 MPa. We conclude then, that the pins will buckle at about the same core pressure required to eject the entire upper core structure out of the core barrel region.

The models for these analyses are undergoing further study and improvement. At this point, the values given represent our best estimates of critical pressures for very complex thermal and structural interaction situations.

B. SIMMER Testing and Verification

(J. H. Scott, Q-7; and H. H. Helmick, Q-8)

SIMMER model development, testing, and verification tasks at LASL include both analytical and experimental efforts, as reported in this section.

The experiment analysis and planning activity is concentrated in two areas: testing of the SIMMER-II accident analysis code and development of the Los Alamos Fuel Model (LAFM) transient fuel pin behavior code. SIMMER-II testing is currently concentrated on verification of the postdisassembly energetics calculations.[44] The reduction in system kinetic energy seen in these calculations is attributable to two effects: purely fluid dynamics mitigation and mitigation through rate-controlled processes. Experiment analysis using SIMMER-II has in the past been nearly exclusively devoted to testing fluid dynamics modeling using primarily SRI International test data. The reason for limited involvement in testing the modeling of rate controlled processes is the limited quantity of relevant data. The CRI-III/FAST experiments of Oak Ridge National Laboratory (ORNL) are notable exceptions.

During the past quarter we have begun an investigation of the UKAEA COVA experiments. We expect these experiments to contribute significantly to the SIMMER testing program, particularly in the area of fluid dynamics modeling. We are also investigating the

Sandia Laboratory PBE carbide fuel tests in order to test SIMMER modeling of liquid-liquid heat transfer.

The development and application of the LAFM code continues. During the last quarter, a high-temperature fuel creep model was incorporated; work on a generalized fuel creep model continues. The impact of this modeling on running time is expected to be minimal. The LAFM code has been used to investigate nonprototypicalities in TOP TREAT tests. A potentially serious nonprototypical failure mechanism was discovered in the low ramp rate capsule tests.

1. COVA Experiment Analysis

(P. E. Rexroth, Q-7)

The UKAEA and the Joint Research Center of Euratom (ISPRA) are engaged in a series of small-scale, well-instrumented tests aimed at providing data for the stresses, strains, and loads occurring when an explosive source is released within a fluid in a containment vessel. The data are to be used in the COVA (Code Validation) program to validate computer codes employed in the study of the response of a fast reactor primary containment system to a hypothetical excursion involving a rapid release of energy. Tests are being carried out with various configurations of internal components within the vessel, some deformable, others rigid. Those experiments that do not include deformable structures are being analyzed at LASL using SIMMER. This analysis is intended to further test the hydrodynamic models in SIMMER as well as provide insight into the nature of the effects of structural components on expansion dynamics.

The test rig consists of a simple closed, rigid vessel, filled nearly to the top with water. The pressure source, a low-density PETN explosives, is detonated at the center of the tank. Twenty pressure gages are distributed about the vessel walls. Figure 85 shows the vessel and various pressure transducer locations.

A preliminary SIMMER calculation has been carried out for experiment FT4, one in which no internal structure was included. For the first analysis, the explosive charge was modeled as a high

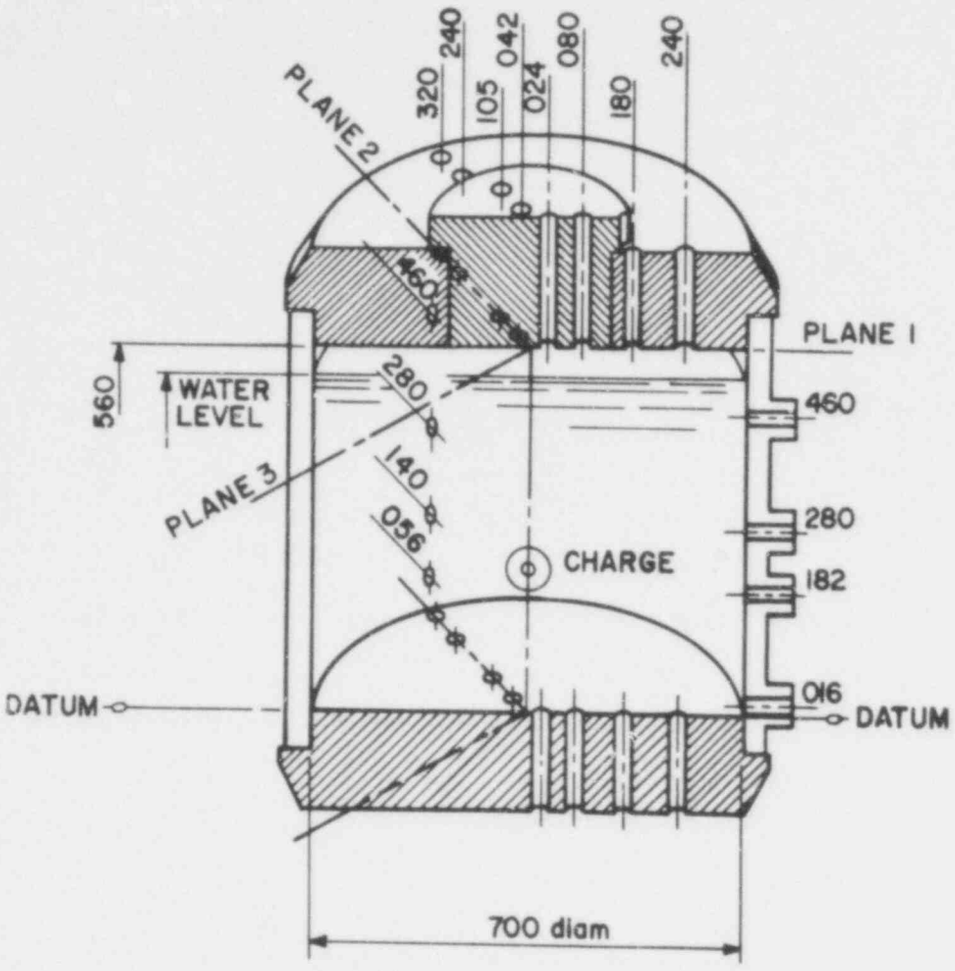

Fig. 85. COVA vessel showing pressure transducer locations.

density perfect gas; thus, the SIMMER analytical EOS was used. A comparison of the measured and calculated pressures at the vessel head is shown in Fig. 86. The calculated timing of the pressure events is in good agreement with the experimental results. The magnitude of the calculated pressure is in general less than that experimentally observed. Pressure differences may be due, in part, to the fact that pressures are calculated at node centers and are therefore offset somewhat from the vessel wall. Another effect that may contribute to a discrepancy is that the transducers are set in mounts, slightly recessed from the main tank. The effect of this geometry is being investigated.

In the future, tests incorporating internal structures will be calculated, and the effect of using an EOS more appropriate for explosives will be investigated.

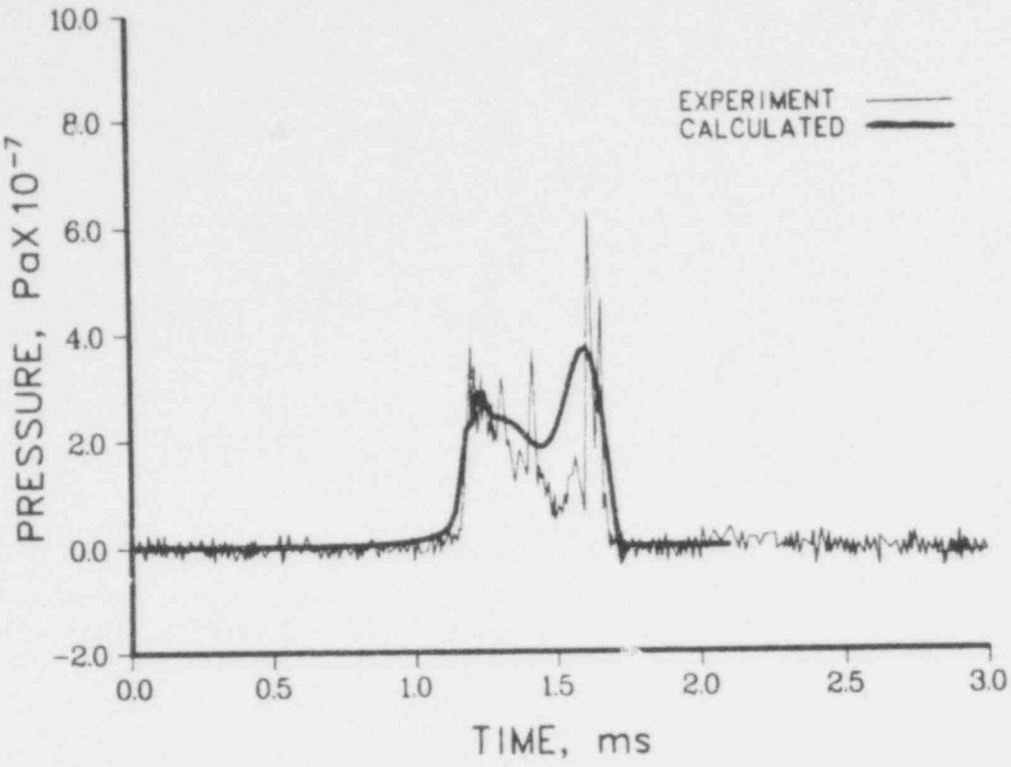

Fig. 86. Vessel head pressure for COVA experiment FT4.

2. Analysis of Postdisassembly Expansion Experiments

(A. J. Suo-Anttila, Q-7)

LASL, DOE, and the NRC have initiated a program to test the predictive capabilities of the SIMMER-II[44] computer code. As an initial part of this effort, analyses of experiments related to the fluid dynamics of postdisassembly expansions are being performed. A considerable body of such experimental data has come from the SRI International experiments in which high-pressure sources are discharged into a water pool. The geometry of the system is 1/30 scale CRBR; the high-pressure sources are either N_2 at 100 atm or saturated water at 80 atm. The results of the SIMMER-II calculations of the N_2 experiments have been reported elsewhere.[63] In this report, the results of the flashing water experiments will be discussed. The structureless experiment, E-001, will be discussed in detail; results of calculations for the experiments with

upper core and upper internal structures are preliminary at this time.

In the E-001 flashing water experiment conducted by SRI International, a 1/30 scale CRBR vessel is simulated. The geometry is shown in Fig. 87. Hot saturated water (570 K) is contained in a vessel below the sliding doors and is used to simulate the molten flashing core. Cold (290 K) water in the upper vessel is used to simulate the sodium pool. Upon opening the doors (opening time is about 250 μs) which separate the hot and cold water, the hot saturated water flashes, generating high-pressure vapor which pushes the cold water slug upward until it impacts the head of the experimental vessel. Pressure measurements were taken at various points in the system, and these can be compared directly with those computed numerically. These experiments are thus close simulations of the upward discharge of the HCDA bubble in CRBR and ideal for SIMMER-II testing. Upper core and upper internal structures can be included. During the SIMMER-II analysis it was found that the system behavior was very sensitive to the details of the flashing process. It was discovered that flashing could not be simulated with a dispersed flow treatment unless one had prior knowledge of an optimum (and not necessarily physically real) droplet size. Therefore, a bubbly flow regime model was implemented in SIMMER. A variety of bubbly flow models, as well as different heat transfer models, was tested. Each model has its own characteristic pressure decay curve, which may or may not agree well with the experimental data.

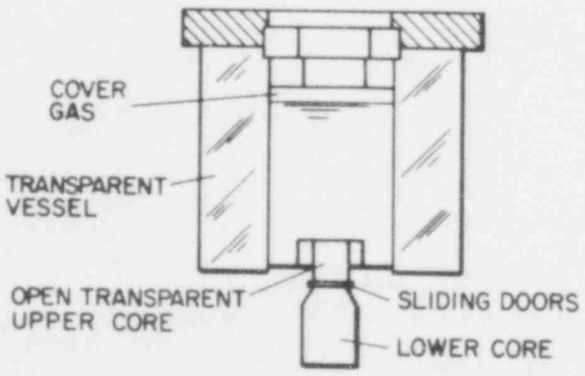

Fig. 87. Experiment E-001.

The results presented here are for a constant size bubble, bubbly flow regime model with transient and steady-state heat transfer coefficients. Figure 88

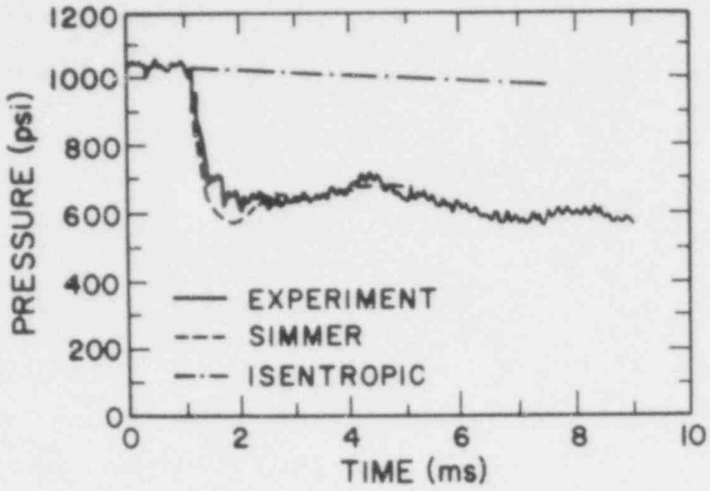

Fig. 88. Lower core pressure.

shows curves of the pressure in the lower core region below the sliding doors vs time for both the experiment and the SIMMER computation. The agreement is very good except for the initial transient. The large sudden drop in pressure with time corresponds to the high degree of thermodynamic nonequilibrium. The bulk liquid temperature remains near its initial saturation temperature, dropping only by about 3 K at the time of head impact. The vapor temperature, however, varies from 20 K colder than the liquid in the core to 100 K colder than the liquid out in the bubble. This large degree of thermal nonequilibrium causes the measured pressures to be considerably less than the corresponding bulk liquid saturation pressures. The driving force for phase change is precisely this temperature difference.

The time to head impact was 4.4 ms in the experiment vs 4.9 ms in the SIMMER calculation. The difference is due primarily to inadequate modeling in the expanding two-phase bubble which emerges from the core. This becomes evident in Fig. 89, where the experimental water level displacement curves are compared with those computed by SIMMER. The agreement is very good to 3-1/4 ms. At this time, the bubble has emerged from the upper core barrel and is beginning to grow spherically. The liquid in this two-phase

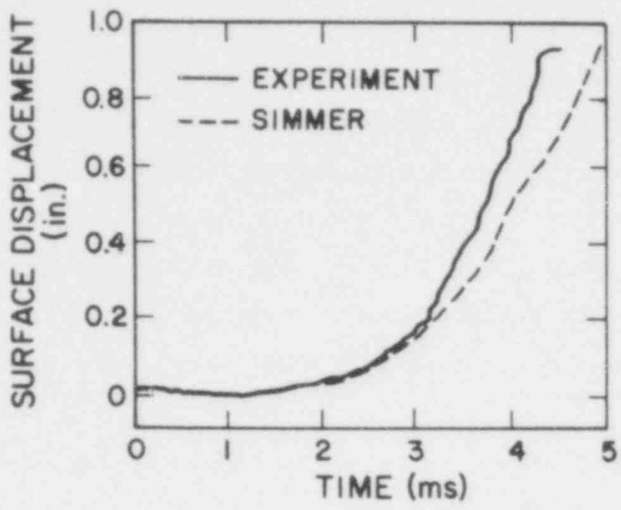

Fig. 89. Surface displacement

bubble vaporizes at a greater rate than that predicted by SIMMER, resulting in a slightly shorter impact time.

These calculated results show very good agreement with the experiment, but more importantly, show that the degree of departure from an ideal (isentropic) expansion predicted by SIMMER is real and substantial even without the dissipative effects of structures. Even in the absence of structures, the system kinetic energy developed is only 50% of isentropic, which agrees well with the SIMMER calculation. The inclusion of the upper core and upper internal structures in the flashing source experiments leads to significant reductions in kinetic energy in this case as it did in the N_2 cases previously reported.[63] The final kinetic energies, when structures are included, are of the order of 20% of isentropic. This is an important result since the N_2 cases were isothermal, purely fluid dynamic cases while the flashing source experiments include heat transfer and phase transition as well as fluid dynamic effects. We therefore conclude that the dissipative effects of structures and rate-controlled processes are real and large and, further, that SIMMER predicts these effects well. This lends considerable confidence to our treatment of the CRBR postdisassembly expansion, although some interesting questions remain. For example,

in experiment E-001, nonequilibrium effects were seen to dominate the calculation of the expansion. This was not the case with the CRBR calculations. It was believed that the scale of the experiment may have contributed to the nonequilibrium nature of the expansion, and calculations were initiated to investigate this effect. Several calculations were performed assuming the E-001 experiment was scaled to full CRBR size.

Whenever a model is scaled up to a larger size, one must be careful in making sure that the model is appropriate and that all the parameters used in the model will scale correctly. The model used here, when scaled, simply asserts that a large-scale system will flash in the same manner as a small-scale system.

Assuming for the moment that the flashing water in a small-scale experiment is representative of flashing water in a full-size CRBR vessel, a calculation indicates results quite different from those in the small-scale experiment. It is found that due to the longer time scale for the expansion, the rate processes tend to dominate and the flashing water remains closer to equilibrium. This results in a more energetic expansion and a shorter scaled impact time. The expansion for the full-size vessel still falls short of the theoretical isentropic limit because of pressure gradient effects. The results are shown in Fig. 90.

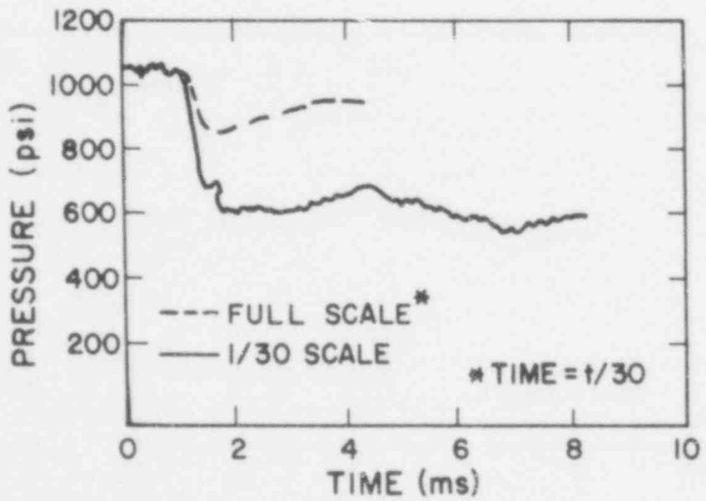

Fig. 90. Core pressures, 1/30 and full scale.

From this set of calculations, it appears that analysis of small-scale experiments requires greater sophistication in modeling when compared to full-size systems. However, to say this with any assurance, the experiment in question must be analyzed in sufficient detail such that scaling can be done with confidence.

Several conclusions can be drawn from these and previously reported[63] analyses.

1. Purely fluid dynamic dissipative effects can be significant. SIMMER models these effects extremely well.

2. The effects of heat transfer and phase transition, in the absence of explosive boiling, are large and dissipative and SIMMER predicts these effects well in small scale.

3. These calculations lend strong support to the SIMMER accident analyses where large dissipative effects were predicted.[64]

Thus, in the absence of explosive boiling, we conclude that it is reasonable to believe, for expanding systems, ideal expansions are extremely conservative and that real systems would have to sustain far less energetic expansions. (It should be noted that with a more volatile receiver fluid, the energies developed could be higher.)

3. Analysis of Prompt Burst Energetics (PBE) Experiment PBE-SG2

(J. L. Tomkins, Q-7)

The PBE[65,66] experiments are a series of in-pile tests conducted at Sandia Laboratories in the Annular Core Pulse Reactor (ACPR) and more recently in the Annular Core Research Reactor (ACRR). These experiments are designed to evaluate the pressure behavior of fuel and coolant as working fluids during a hypothetical prompt burst disassembly in an LMFBR. Herein, we present preliminary SIMMER-II analyses of PBE-SG2, a carbide fuel experiment. These preliminary calculations are, of necessity, mainly for

demonstration purposes although some information concerning separate mechanisms in the experiments can be derived. Complete SIMMER model testing requires additional calculations.

The initial series of PBE experiments used a single fuel pin in a fluted channel. Pressure transducers were mounted at the top and bottom of the channel. Also, at the top of the channel there was a linear motion transducer connected to a movable piston. For both experiments listed above, the channel was filled with sodium. A complete description of the initial series of PBE experiments can be found in Refs. 65 and 66. In the experiments, the pressure data recording locations were substantially removed from the pressure source. Therefore, to determine the effects of channel geometry, it is necessary to perform detailed hydrodynamic calculations. Also, particularly in the carbide experiments, measured pressures cannot be accounted for by fuel vapor pressure alone and, therefore, the effect of fuel-to-coolant heat transfer must be included in the analysis. Initial conditions are summarized in Table VII. The calculation was started at the point of pin failure with initial conditions obtained using the EXPAND pin failure code.[67] Figure 91 shows the SIMMER-II model constructed for the analysis of PBE experiment SG2. The model consists of a single fuel pin in a coolant channel. The ends of the fuel pin are plugged, and the failure is assumed to be a 10-mm-long circumferential break with an area of approximately 1.8×10^{-4} m^2. The break is located 195 mm from a rigid bottom boundary. Initially, the fuel pin is assumed to be filled with a uniform density of uranium carbide and the coolant channel with sodium. All materials except the fuel pin are assumed initially at 770 K and 0.28 MPa. The initial fuel temperature was assumed to be 6 942 K with a corresponding internal pin pressure of 20 MPa. Initial conditions are given in Table VII.

TABLE VII

SIMMER MODEL INITIAL CONDITIONS

Fuel type	UC
Fuel mass (kg)	8.0×10^{-2}
Fuel temperature (K)	uniform 6 942
Maximum radially averaged energy deposition (J/gm)	2 420
Fuel vapor pressure (MPa)	20.0
Sodium temperature (K)	770
Area of cladding break (m^2)	1.8×10^{-4}
Cladding temperature (K)	770
Top boundary	Rigid
Bottom boundary	Rigid

Experimental pressure traces for PBE-SG2 along with calculated results are shown in Fig. 92. A summary of experimental and calculated results is presented in Table VIII. At the bottom pressure transducer location, the measured peak pressure is approximately 190 MPa while the corresponding calculated pressure in Case 1 is about 160 MPa. At the top pressure transducer location, the measured experimental peak is about 170 MPa while the calculated peak pressure in Case 1 is approximately 175 MPa. These pressures are predominantly due to sodium vapor generation. While agreement in magnitude between experimental and calculated results is good for Case 1, there is a difference in that the ratio of top to bottom pressure peaks varies in direction. The discrepancy is most probably a result of the rigid top boundary condition assumed in Case 1.

4. Pretest Predictions for AX-1 Transient Test

(H. M. Forehand, Jr. and J. H. Scott, Q-7)

As an exercise to establish input values for the SIMMER-II analysis of the AX-1 transient test, the Sandia Laboratories static capsule carbide pin test, PBE-SG2, was analyzed as reported in the previous section. The calculated results are in reasonable agreement with the experimentally observed results with respect to pulse width, amplitude, and damping rate. In these results we

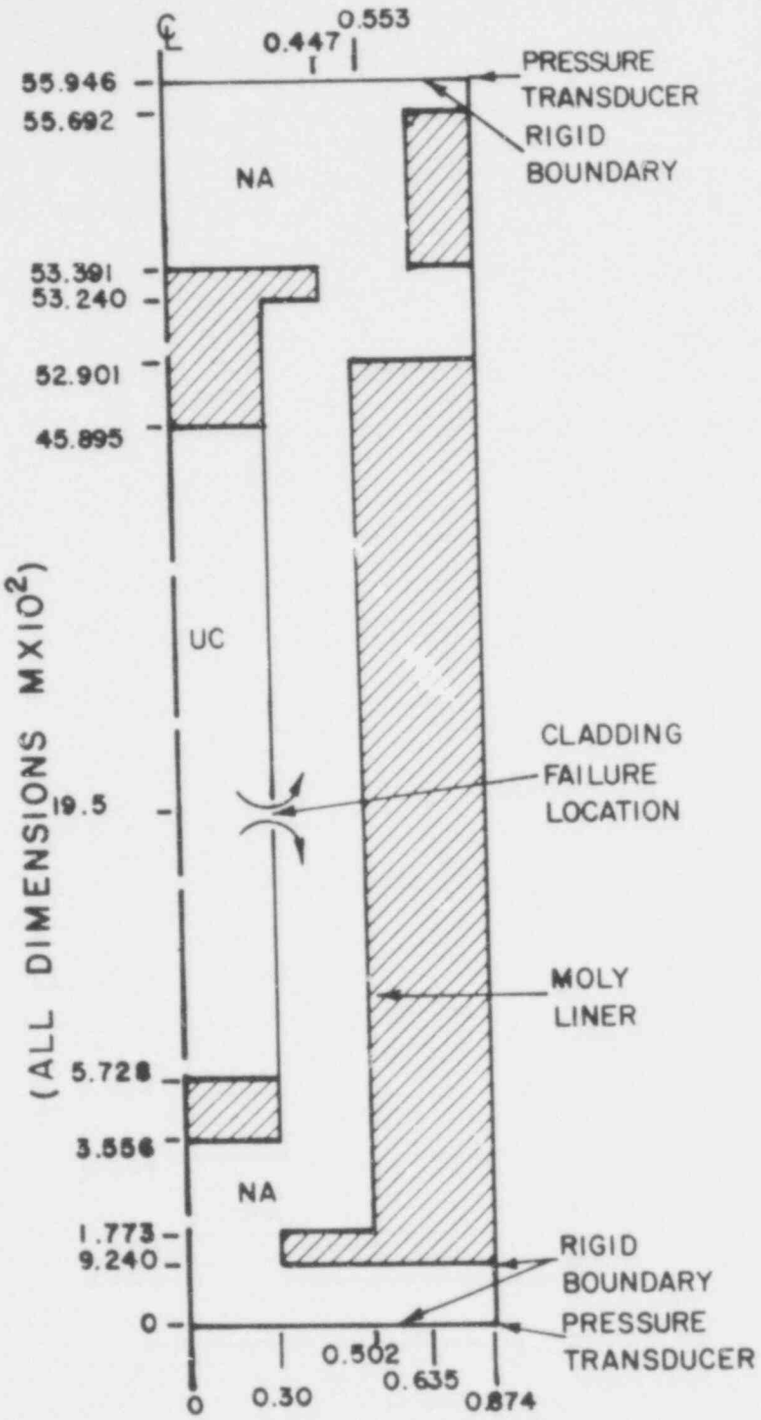

Fig. 91. SIMMER model of PBE-SG2.

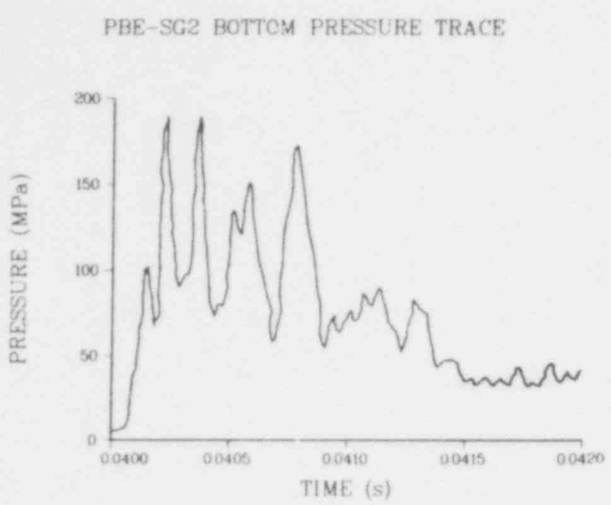

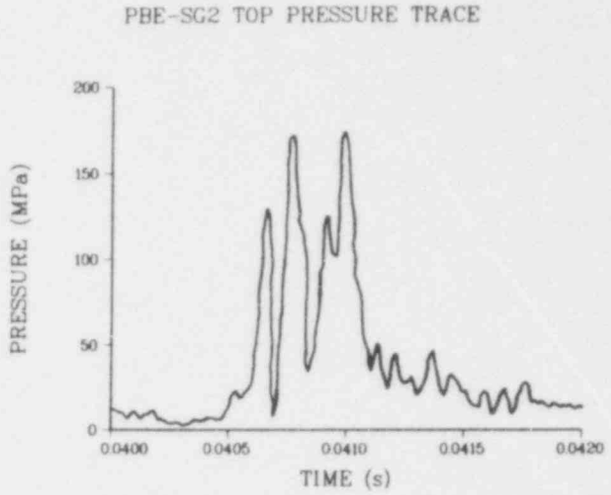

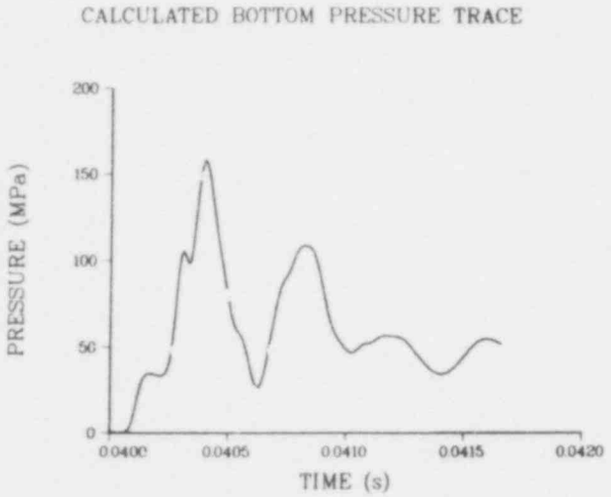

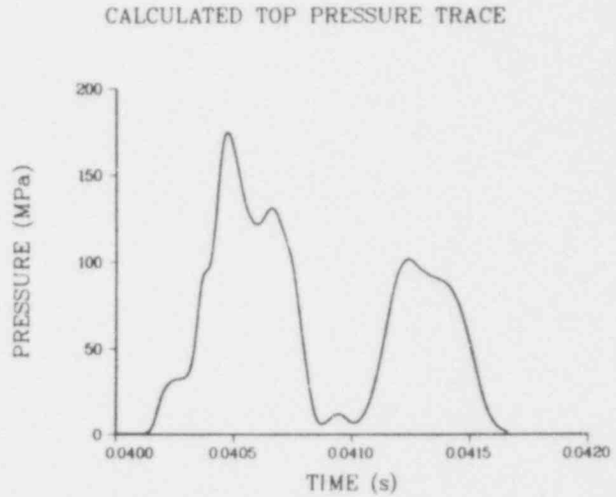

Fig. 92. Comparison of calculated and experimental pressures from PBE-SG2.

TABLE VIII

KEY RESULTS FROM TEST PBE-SG2

	Experiment	SIMMER-II Calculations
Peak pressure at bottom (MPa)	190	160
Peak pressure at top (MPa)	170	175
Peak pressure in interaction zone (MPa)	-	120
Pressure ratio top/bottom	0.89	1.09
Mass of fuel in coolant channel (kg)	-	3.5×10^{-3}

observed that the initially high pressures were attributable not to "single phase" peaks but rather to rapid heat transfer from the carbide fuel coupled with the fluid dynamics characteristics of the capsule. The initially high sodium vaporization rates (10^9 kg/m^3 m^2·s) cause production of a volume of vapor which expands to occupy all of the available capsule volume. Nonequilibrium effects then result in extremely high local pressures which act to suppress further vaporization. Vaporization is suppressed until the reflected shock reaches the interaction zone, but by that time the excellent conductivity of uranium carbide has caused the liquid sodium to be heated to near the critical point. Therefore, when vaporization again becomes possible, the large energy stored in the sodium leads to sustained boiling. This sequence of events is entirely different from UO_2, primarily because of its poor conductivity. Also, the sequence of events is strongly dependent on the geometry of the capsule. We therefore employed only the carbide and sodium thermophysical data and the mixing input parameters from this calculation for application in the AX-1 test analysis.

a. AX-1 Initial and Boundary Conditions

Because SIMMER is written for r-z geometry, it is difficult to model accurately a three-pin test. It was, therefore, decided to model the single fuel pin predicted to fail first. It

was argued that since the initial failure is likely to be outward, the mixing (interaction) zone will be defined by the near loop wall. Therefore, the flow area for the single pin was based on this near-wall radial dimension (approximately 38% of the test section flow area). Very shortly, however, three-dimensional effects will become important and subsequent failures will contribute to the uncertainty in system conditions. Therefore, we can regard the results presented here as being valid at most for about 2 ms beyond pin failure.

The geometry of the calculation is shown in Fig. 93. The test section is represented by 22 axial nodes of which 17 (3-19) are in the active fuel region. There are four radial nodes, two in the fuel and two in the coolant channel. Variable noding was used in this calculation; in order to accurately study the fluid and thermal dynamics at the break site, three small axial nodes (10-12) were used in the region of the break. The break itself was assumed to have a flow area of $\simeq 1.5 \times 10^{-5}$ m^2.

The time and location of initial failure were taken from Hanford Engineering Development Laboratory (HEDL) COBRA calculations. Since the power coupling factor and TREAT power transient (external test conditions) were revised from initial estimates, a two-case analysis was performed where the low internal pin pressure case represents the final external test condition variation. For the high internal pin pressure case, the failure time was 1.11 s into the transient at a relative pin height of 0.5. The conditions in the fuel pin at this time were

peak fuel temperature = 6 600 K
at.% molten fuel = 100
pin internal pressure = 11.4 MPa.

The failure time was 1.0 s into the transient for the low internal pin pressure case. The failure location was unchanged. Conditions at the time of fuel pin failure for this case are

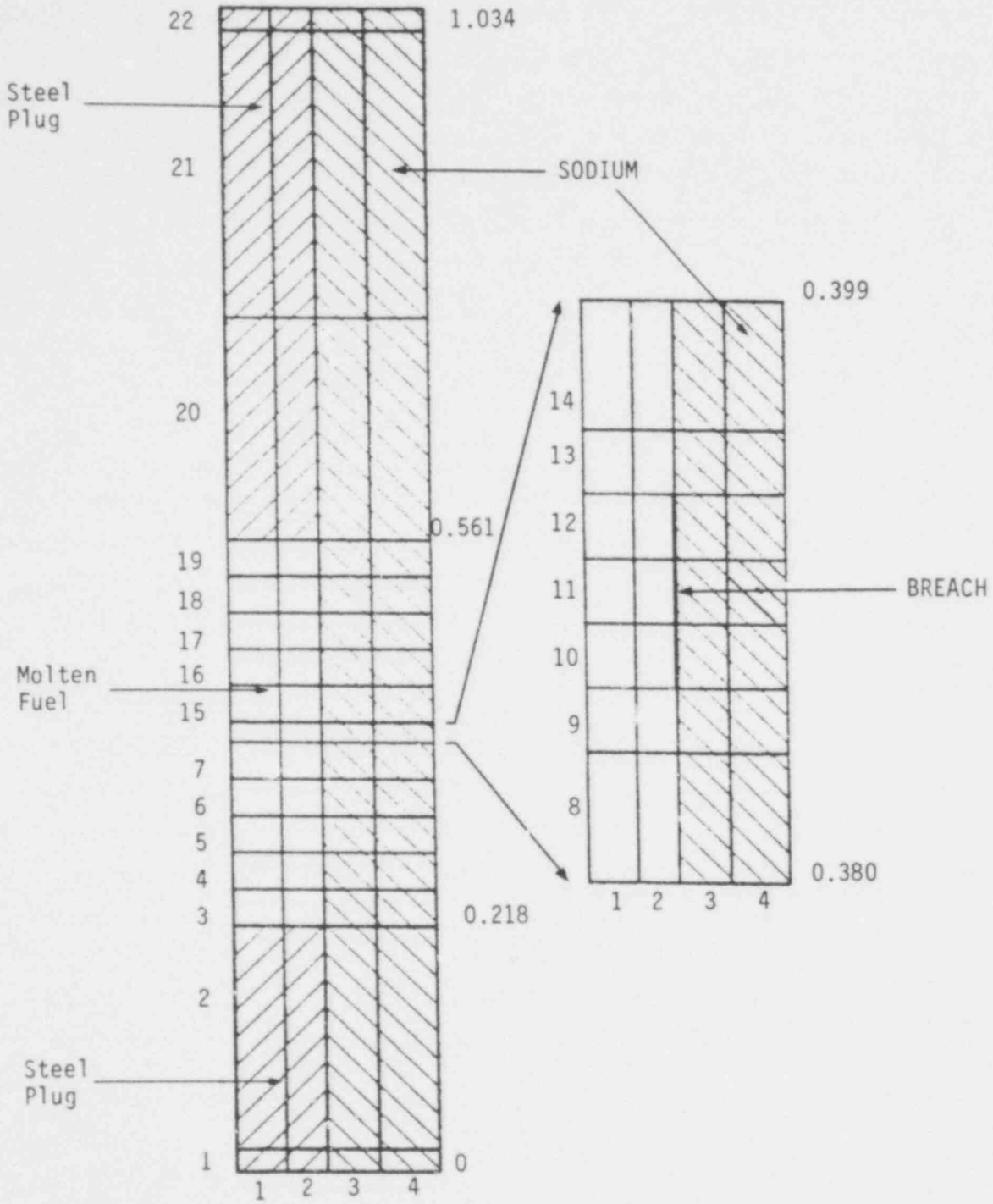

Fig. 93. SIMMER calculation geometry.

peak fuel temperature = 6 236 K
at.% molten fuel = 100
internal pin pressure = 5.9 MPa.

This case will be referred to as the low (internal) pressure case.

b. Calculational Results

(1) High Pressure

At the estimated time of failure, 1.11 s, the fuel is ejected into the coolant channel and the maximum ejection velocity over the first 0.15 ms is 11 m/s. The initial effect of this ejection is to cause rapid vaporizaton ($\simeq 10^9$ kg/m^3·s) of the sodium in the interaction zone with the attendant rapid production of very high pressure (~ 56 MPa). The pressure time history at the break center is shown in Fig. 94. The high pressure causes flow stoppage and inhibits further vaporization. Flow of fuel from the cladding break is also radically reduced during this period of high interaction zone pressure. However, heat transfer to the sodium continues during this time period and since further vaporization is suppressed, the liquid sodium becomes significantly superheated. At about 0.15 ms, the interaction zone confinement is terminated by arrival of a rarefaction wave and the pressure begins to drop rapidly. Figure 94 shows that the pressure decreases linearly until 0.2 ms at which time the superheated liquid sodium begins to vaporize. The broad dome between 0.2 and 0.6 ms is attributable to sustained boiling of the superheated liquid sodium and replenishment of sodium in the interaction zone. This mechanism for pressure production does not assume instantaneous contact temperatures or homogeneous nucleation but is instead controlled by heat transfer due to the high fuel conductivity and by the fluid dynamics constraints of the loop.

The sodium axial velocities at the break region and the top of the test section, as a function of time, are shown in Figs. 95 and 96. Observe that the sodium velocity at the top of the pin increases from 8 m/s to 43 m/s in 0.5 ms. This acceleration should appear on the upper flowmeter data.

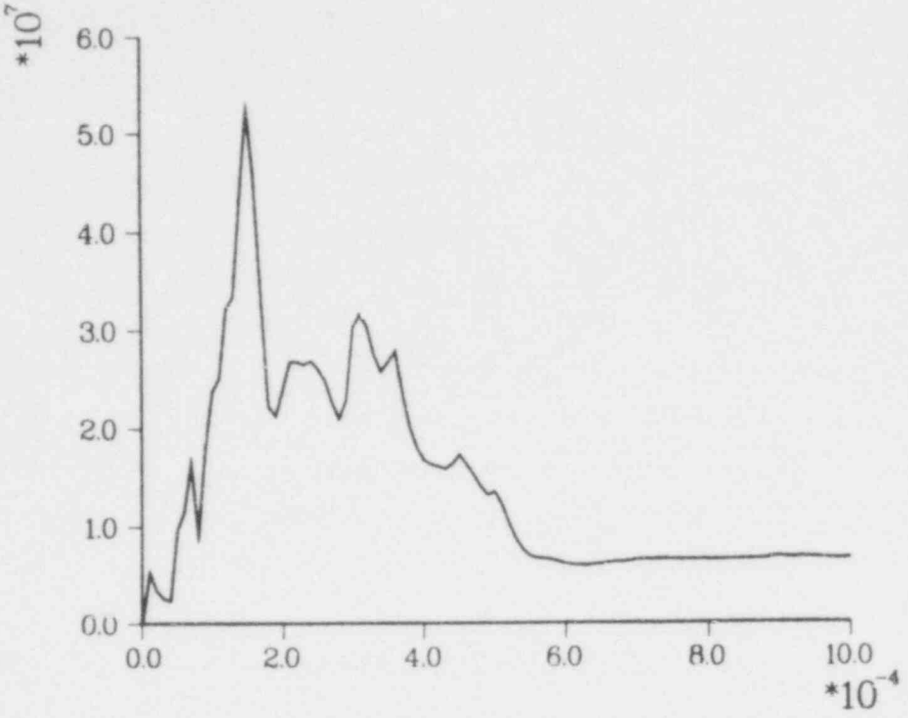

Fig. 94. Pressure time history for the high internal pin pressure case at the center of the break for the inner coolant node (3,11).

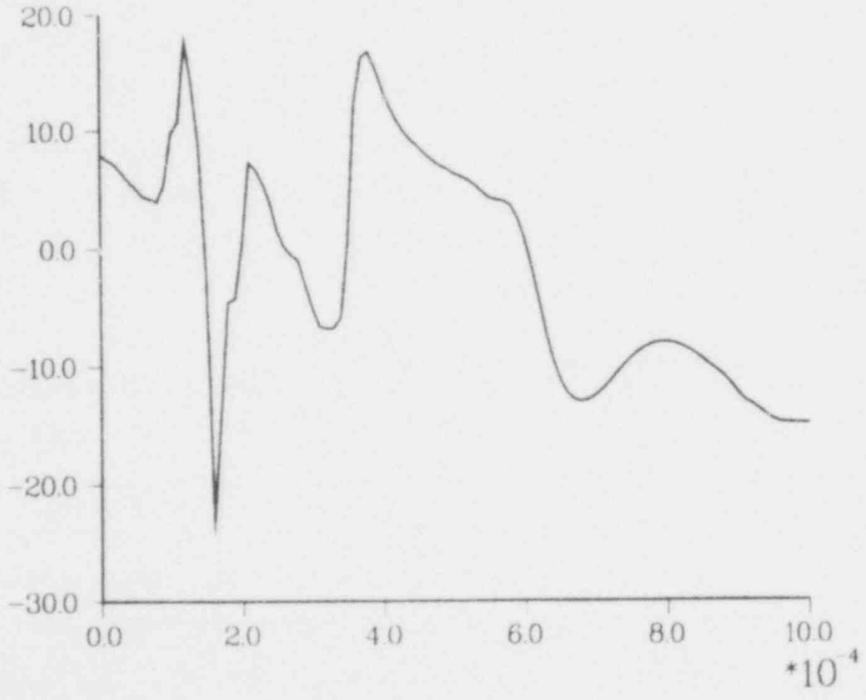

Fig. 95. Liquid sodium axial velocity time history for the high internal pin pressure case at the center of the break for the inner coolant node (3,11).

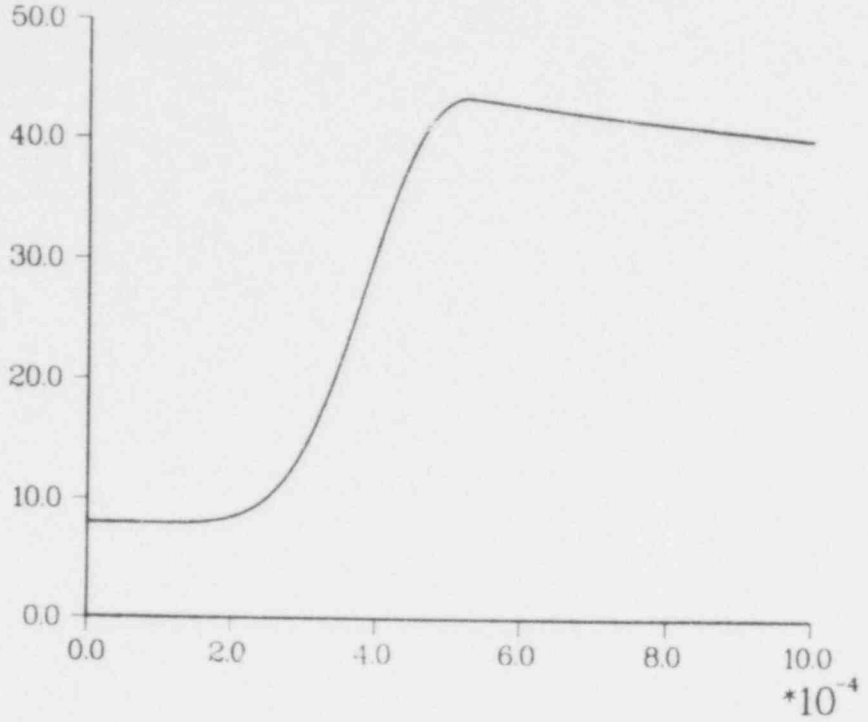

Fig. 96. Liquid sodium axial velocity time-history for the high internal pin pressure case at the top of the test section for the inner coolant node (3,22).

(2) Low Pressure Failure

Assuming the lower failure pressure, one obtains similar results in terms of the interaction zone phenomenology. Since the internal pin pressure is lower, the initial fuel ejection rate is considerably lower than in the previous case. As a consequence, the pressure generated in the interaction zone is somewhat lower, 46 MPa. Because a smaller volume of fuel is initially injected, less liquid sodium is superheated and, as a consequence, the sustained boiling in the period 0.2-0.6 ms is not prominent. No pressure dome exists in this case; pressure decreases linearly in this time regime. The pressure history is shown in Fig. 97.

c. Conclusions

We conclude that there is a significant possibility of interaction zone pressure of between 46 MPa (low-pressure failure) and 56 MPa (high-pressure failure) due to sodium vaporization. The

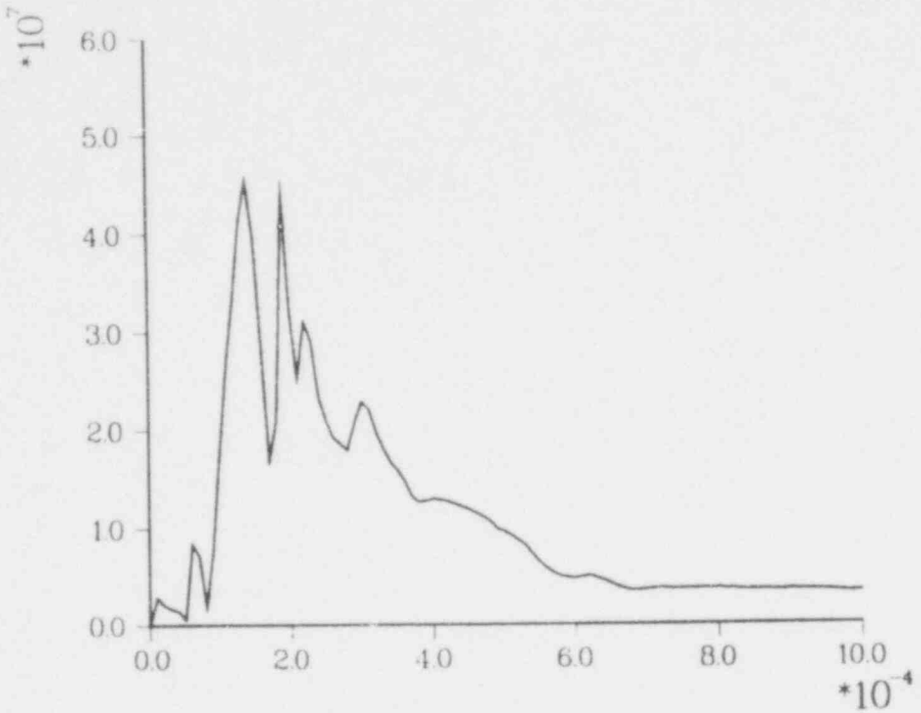

Fig. 97. Pressure time history for the low internal pin pressure core at the center of the break for the inner coolant node (3,11).

difference in pressures observed in the two cases is largely due to the differences in initial fuel expulsion rates. The total fuel removed from the pin, as a function of time, is shown for both cases in Fig. 98. Note the difference in initial slope of the curve and also that at any point in time, more fuel is removed from the high-pressure pin. No major phenomenological differences exist between the two cases.

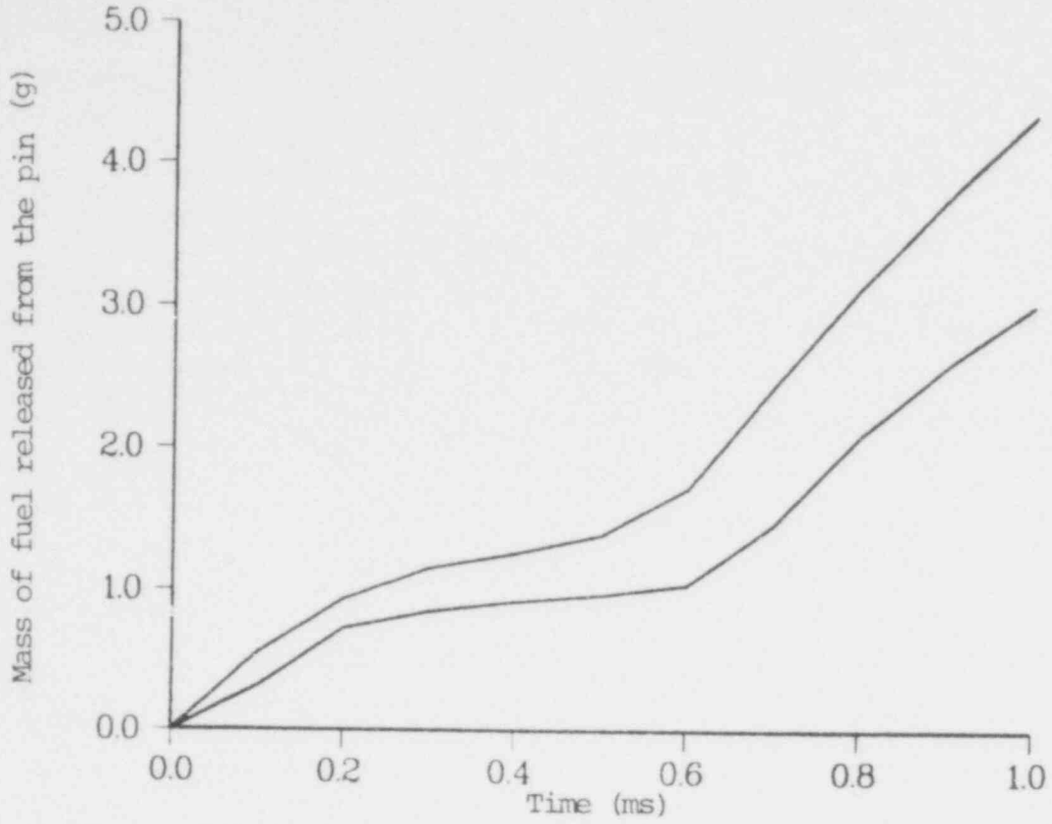

Fig. 98. Cumulative mass release.

5. The Influence of TREAT Nonprototypic Effects on Prediction of Pin Failure in LMFBRs

(P. K. Mast and J. H. Scott, Q-7)

There are a number of nonprototypicalities associated with the transient testing of EBR-II irradiated fuel pins in the TREAT facility. Some of these nonprototypic effects, such as the fluence-to-burnup ratio and axial fluence distribution are attributable to irradiation conditions in EBR-II. Other nonprototypic effects, such as the use in some tests of static rather than flowing cooling systems, are a direct consequence of the test conditions.

The LAFM[68] code has been used to compare fuel pin failure behavior in TREAT with the behavior in the Fast Test Reactor (FTR). The LAFM code employs a multinode hydrostatic-elastic fuel model and a single node elastic-plastic cladding treatment in conjunction with a life fraction failure criterion to predict the time and axial location of cladding failure. The life fraction failure

criterion is based upon the stress rupture lifetime data generated at HEDL.[69] The major failure mechanisms of fuel-cladding differential thermal expansion, fission gas release and pressurization, fission-gas-induced fuel swelling, and cladding thermal stress are modeled. Details of this treatment may be found in Ref. 68.

A variety of analyses have been performed with the LAFM code as part of the code testing effort. In general, agreement with experiment tends to be excellent; the results of these verification analyses to date are summarized in Table IX. Additional analyses to investigate the influence of unhealed shutdown cracks[70] and fluence-to-burnup ratio[71] have been previously reported. It was shown that these nonprototypic effects altered the calculated failure time but not the failure mechanism. The current analyses indicate that a more important nonprototypic effect may lie in the way some of the TREAT tests are performed, i.e., in a static capsule vs a flowing sodium loop.

In general, failure predicted by LAFM for irradiated fuel pins during a transient overpower (TOP) event is primarily attributable to either differential thermal expansion or internal pin pressurization (due to fission gas release coupled with molten fuel expansion); the nature of the failure being very sensitive to the particular mechanism that causes failure. Typically, differential thermal expansion favors failure near the axial midplane while internal pin pressurization favors failure above the midplane.

In the course of analyzing terminated and unterminated overpower transients in the FTR,[72] we have observed that the dominant failure mechanism and, hence, axial failure location are strongly dependent upon the reactivity ramp rate. In the analysis of very rapid \$3/s FTR transients, failure was calculated to occur near the top of the pin at a relative height of ~0.86 for a high-power pin and ~0.75 for an intermediate-power pin. Fission gas pressurization of the pin was calculated to be the dominant failure mechanism in both cases. In the slower \$0.50/s transients, however, failure was calculated to occur nearer the axial midplane at a relative height for ~0.64 for the high-power pin and ~0.58

TABLE IX

COMPARISON OF LAFM PREDICTIONS AND EXPERIMENTAL RESULTS FOR TOP TREAT TESTS

Test	Observed Failure Time (s)	Predicted Failure Time (s)	Observed Maximum Strain (%)	Predicted Maximum Strain (%)
E6	9.18	9.196	a	0.95
H4	6.69	6.68	a	0.46
HUT5-5A	-	-	0.068	0.072
HUT5-5B	11.00	11.08	a	0.44
HUT5-3A	8.95	8.80	a	0.12
HUT3-3A	-	-	0.51	0.57
HOP3-2A	-	-	0.13	0.15
HOP3-2B	-	-	0.30	0.26
HUT3-5A	-	-	0.08	0.06
HOP3-1A	-	-	0.00	0.03
HUT3-5B	9.74	9.675	a	0.74

[a]Strain could not be measured because of test pin destruction.

for the intermediate-power pin. In both of these cases, differential thermal expansion combined with fission gas pressurization to cause cladding failure. This can be seen quite clearly by calculating the cladding life fraction (failure being defined to occur when the cladding life fraction reached 1.0) at the nominal failure time while ignoring the presence of fission gas in the pin. For the \$3/s transients, the life fraction calculated in this manner is near zero indicating the lack of importance of differential thermal expansion. For the \$0.50/s transients, however, the life fraction calculated ignoring fission gas is sizable; 0.25 for the high-power pin and 0.60 for the intermediate-power pin. These calculations are summarized in Table X.

The importance of differential thermal expansion in the \$0.50/s FTR transients can also be seen by calculating pin failure

TABLE X

SUMMARY OF FTR UNTERMINATED TOP RESULTS

Transient	Failure Time	Axial Failure Location	Life Fraction Due to D.T.E.[a]
High-power pin $3/s	0.62 s	0.86	~ 0
Intermediate-power pin $3/s	0.61 s	0.75	~ 0
High-power pin $0.50/s	3.15 s	0.64	0.25
Intermediate-power pin $0.50/s	3.47 s	0.58	0.60

[a]Differential thermal expansion.

while ignoring the effects of differential thermal expansion. Given this assumption, failure in the $0.50/s transients is calculated to occur at 3.155 s at an axial height of ~0.81 for the high power pin and at 3.725 s at an axial height of ~0.81 for the intermediate power pin. These results, summarized in Table XI, clearly show that differential thermal expansion in the $0.50/s transients causes cladding failure to occur earlier in the transient and at a lower axial position than if only internal pin pressurization was assumed to drive failure.

TABLE XI

EFFECT OF IGNORING DIFFERENTIAL THERMAL EXPANSION IN CALCULATING FAILURE IN FTR TOP TRANSIENTS

Transient	Failure Time	Axial Failure Location
High-power pin $3/s	0.62 s	0.86
Intermediate-power pin $3/s	0.61 s	0.75
High-power pin $0.50/s	3.155 s	0.81
Intermediate-power pin $0.50/s	3.725 s	0.81

The reason for the difference in failure characteristics between the $3/s and $0.50/s FTR transients can be attributed to the higher cladding temperature (relative to the fuel temperature) in the $3/s transients. The time scale (time-to-failure) in the $3/s transient is about 5 times shorter than in the $0.50/s transient. The coolant velocity in each case is, however, the steady-state nominal value (~ 7 m/s). Thus, the excess heat generated during the transient is removed much more effectively during the slower $0.50/s transient. This effect shows up most clearly in the cladding temperature, which is much cooler (relative to the fuel temperature) in the $0.50/s transient. This relatively cooler cladding temperature leads to a higher potential for fuel cladding differential thermal expansion.

These results are in contrast to the results of the TREAT tests, in particular, the static capsule tests, in which all failures, regardless of ramp rate, are due primarily to fission gas pressurization of the molten fuel volume. This result is born out by a statistical analysis reported by Burns and Scott[73] in which it was found that the time of failure in the static capsule tests was strongly correlated to the combination of gas retention and melt fraction, implying fission gas-driven failure. The same conclusion could not be made for those tests performed in the Mark-II sodium loop. Thus, it appears that the simulated $0.50/s transients performed in the static capsule result in failures that are characterized by a nonprototypic (for that ramp rate) failure mechanism.

To investigate this nonprototypicality in failure mechanism, we have examined and compared the HUT5-3A[74] capsule test and H6[75] loop test. In both of these tests, an intermediate power (PNL-10) pin was subjected to a simulated $0.50/s transient. The primary difference between the two tests was that HUT5-3A was performed in a static NaK-filled capsule while H6 was performed in a flowing sodium environment. The coolant flow rate in the H6 test was 6.23 m/s (compared to ~ 7 m/s in the FTR) and provided the most prototypic coolant conditions achieved in any $0.50/s TREAT test.

Pin failure occurred at a TREAT transient time of 9.92 s in the H6 test and 8.95 s in the HUT5-3A test. In each case, failure was calculated by LAFM to occur at a relative axial height of ~ 0.67. This is consistent with the recorded thermocouple responses in the two tests. An axial failure location of 0.67 would seem to imply a differential thermal expansion induced failure in each case. However, it should be noted that in the HUT5-3A test, this axial location also corresponds to the peak in the axial cladding temperature distribution (a consequence of the static coolant).

As in the FTR transients, the importance of differential thermal expansion can be estimated by calculating the life fraction at the actual failure time while ignoring the effects of fission gas. For the H6 transient, a life fraction due only to differential thermal expansion of 0.80 is obtained; comparable to the life fraction of 0.60 that had been calculated for the intermediate-power pin FTR transient. A similar calculation for the HUT5-3A transient, however, shows that virtually no cladding life is consumed due to differential thermal expansion. Thus, these calculations, summarized in Table XII, confirm the expected result that the $0.50/s capsule tests are nonprototypic in that differential thermal expansion does not play a role in causing cladding failure.

This difference in the failure characteristics of the two TREAT tests can be attributed directly to the difference in the thermal characteristics of the two tests. The potential for differential thermal expansion at any axial position is largely determined by the ratio of the radially averaged solid fuel

TABLE XII

SUMMARY OF H6 AND HUT5-3A CALCULATIONS

Transient	Failure Time	Axial Failure Location	Life Fraction Due to D.T.E.
H6	9.92 s	0.67	0.80
HUT5-3A	8.95 s	0.67	~ 0

temperature (increase over steady-state value) to the radially averaged cladding temperature (increase over steady-state value); the higher this ratio, the higher the potential for differential thermal expansion. This comparison of fuel to cladding temperature is shown for the H6 and HUT5-3A transients (at the axial failure location) in Fig. 99. (Since the test pins were irradiated in EBR-II at similar operating conditions, the actual transient temperatures are compared.) It can be seen that for the same cladding temperature, the average fuel temperature is much higher in the H6 transient than in the HUT5-3A transient. The LAFM calculated differential thermal expansion strains resulting from these distributions are shown in Fig. 100. The differential thermal expansion strain calculated for the intermediate-power pin $0.50/s FTR transient is also included for comparison. As can be seen, the peak differential thermal expansion is comparable in the H6 and FTR transients and considerably lower in the HUT5-3A transient.

We therefore conclude that the particular design (both mechanical and neutronic) of the low ramp rate static capsule tests is such that a potentially serious nonprototypicality is introduced; the high temperature of the cladding relative to the fuel in these tests suppresses differential thermal expansion. In the FTR, differential thermal expansion is calculated to contribute to pin failure. If one were to apply the low ramp rate capsule test data directly to FTR, one would predict failure higher in the core and later in time than mechanistic calculations suggest. While there are certain limitations in the current LAFM code (such as the use of a very approximate fuel creep model), the mechanistic calculations are nonetheless supported by the results of the H6 loop test.

The low ramp rate static capsule tests are certainly useful for testing mechanistic codes such as LAFM. However, as a result

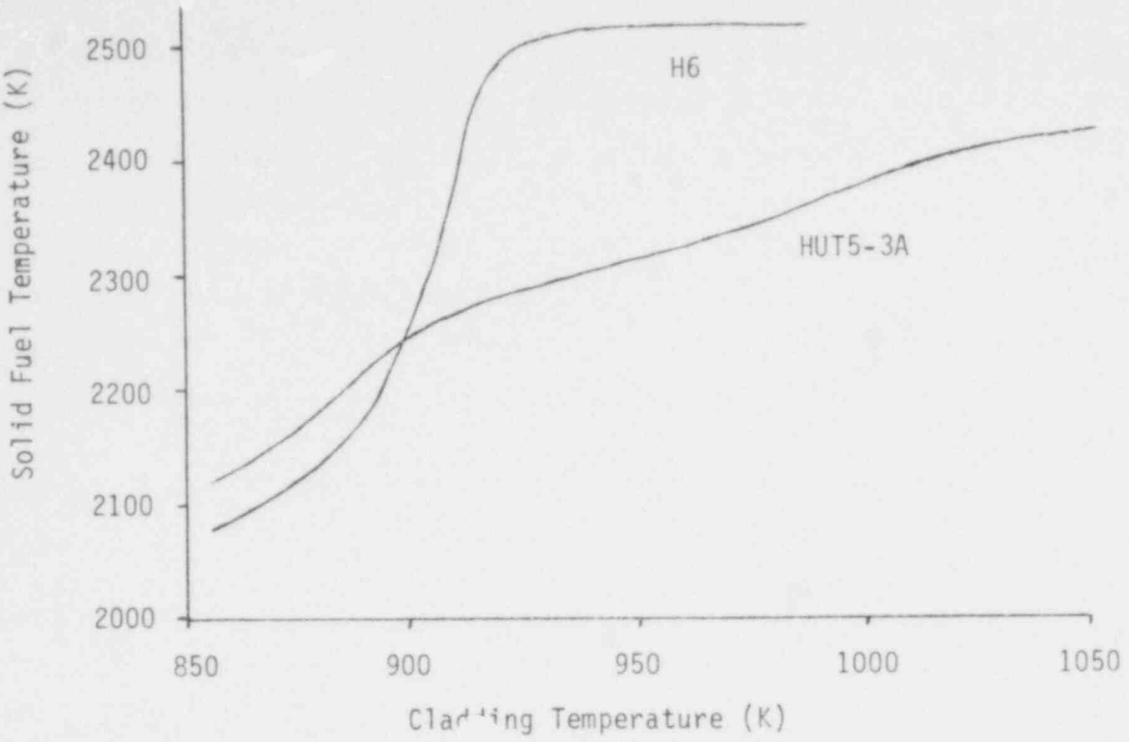

Fig. 99. Comparison of fuel and cladding temperatures in TREAT tests HUT-3A and H6.

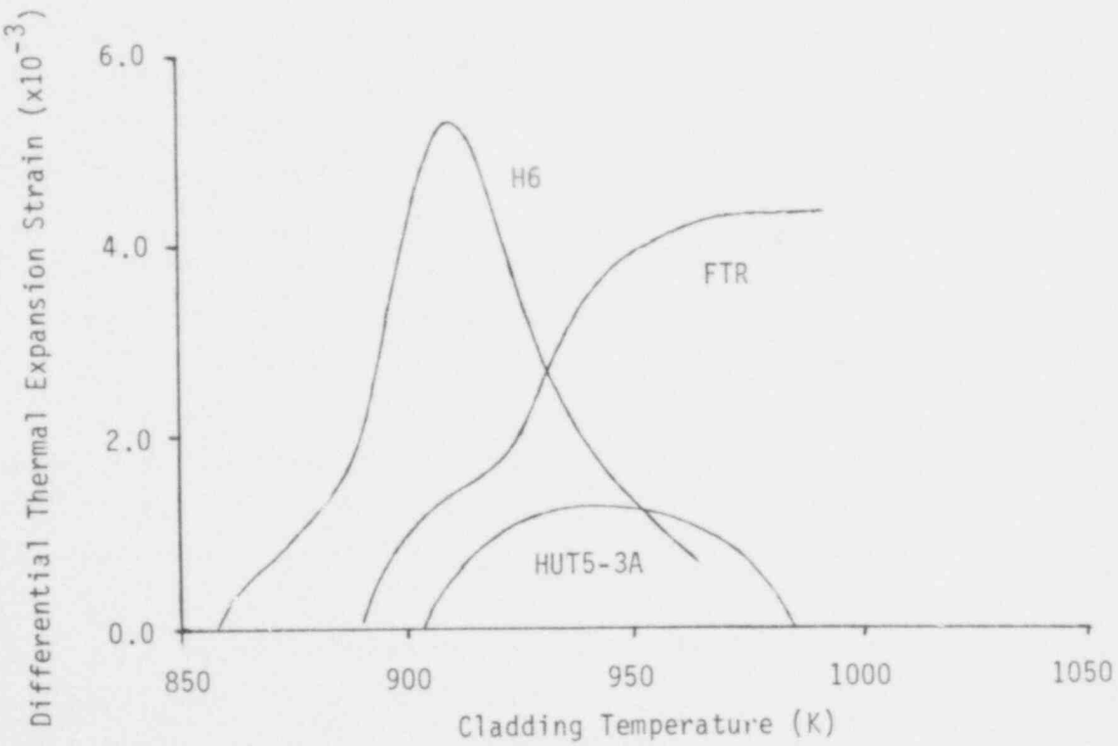

Fig. 100. Comparison transient differential expansion strains in TREAT tests H6 and HUT5-3A and FTR transient.

of the calculations presented above, their use in a data base for a direct experimental correlation appears not to be valid. To strengthen and make more prototypic the data base for both direct correlations and code testing, more prototypic low ramp rate tests are extremely desirable.

6. Evaluation of LMFBR Fuel Motion Diagnostics for SIMMER Verification Experiments

(A. E. Evans, A. R. Brown, L. R. Creel, A. E. Plassmann, M. Diaz, R. E. Malenfant, and B. Pena, Q-14)

With no current plans for building a new large Fast Reactor Safety Test Facility (STF), we have suspended our STF support program of fuel motion diagnostic studies. Instead, our work with the PARKA critical assembly has been re-oriented to provide fuel motion diagnostics evaluations for presently planned and future experiments at TREAT, ACRR, and other existing LMFBR test facilities. Thus, we have discontinued all tests on large multipin bundles and are now concentrating on fuel motion diagnostics for bundles of 37 pins or less with a particular intent of evaluating diagnostics techniques in terms of SIMMER verification needs.

Of considerable importance to experiment planning is a decision on the test capsule wall thickness for TREAT-type test assemblies. Since the steel test thimble will affect the resolution which can be obtained by nuclear self-imaging of its contents, a tradeoff will be necessary between safety considerations and the amount of image degradation which can be tolerated to meet experimental objectives. To study this problem, the no longer needed 127-pin test bundle in PARKA was replaced with a 37-pin assembly surrounded by a 21-mm-thick steel sleeve. The steel occupies the space between the 37-pin grid and the inside wall of the old 127-pin test chamber. This 15-cm-long sleeve is designed to be remotely raised from and lowered into the field of view of the hodoscope.

The results of scanning the 37-pin bundle across the flats, with and without the steel sleeve in position, are listed in

Table XIII. For these measurements, we used the stilbene scintillation detectors with pulse-shape discrimination to count gamma rays and neutrons simultaneously. In both cases, the fractional effect of a single-pin void was measured by withdrawing the central fuel pin. The results show that the steel sleeve causes a loss in total signal and background of ≈30% for fast neutrons and nearly 50% for gamma rays. More important is the fact that the signal-to-total ratio for removal of a single pin is approximately one-third less for fast neutrons and one-half less for gamma rays when imaging through the steel. Assuming that the reduction in mass-loss sensitivity will be exponential with capsule thickness, the table shows the mass-resolution losses to be expected for 25- and 50-mm-thick steel capsules.

Figure 101 displays the results of fast-neutron scans of the 37-pin bundle across corners, i.e., with the rows of fuel parallel to the direction of observation. For this orientation, as discussed in the last progress report,[13] a counting rate minimum occurs when the collimator is pointed directly at a row of fuel because the resolution of the collimator is slightly greater than the distance between rows of fuel. In the figure, scans with and without the steel sleeve are compared. The central and far corner pins were withdrawn in both cases to compare mass-loss resolutions. The degree to which the details of the scan are degraded by the presence of the steel sleeve is obvious. The results of similar gamma-ray scans with energy thresholds of 330 and 660 keV are plotted in Figs. 102 and 103. As expected, the degrading effect of the steel on these gamma-ray images, particularly for the lower energy threshold, is more pronounced than that observed with the neutron scans.

Preparations are under way to measure neutron and gamma-ray spectra emitted by test items in PARKA. A presentation on the technique to be used for neutron spectrometry (the gridded ^{3}He ion chamber of Cuttler and Shalev[76]) with pulse-shape discrimination was made in November at the Fifth Conference on the Use of Small Accelerators in Research and Industrial Applications.

TABLE XIII

EFFECT OF A 21-mm-THICK STEEL CASING ON HODOSCOPE IMAGES OF A 37-PIN BUNDLE IN PARKA

	Counts/J/g-^{235}U			
	E_γ > 0.66 MeV	E_γ > 0.33 MeV	E_n > 2.2 MeV	E_n > 1.3 MeV
37 pins across flats, no casing:	38 150	63 200	9 500	19 000
Single-pin void, no casing:	38 500	59 600	8 900	17 900
Single-pin void, fraction of total:	0.061 ± 0.003	0.056 ± 0.002	0.065 ± 0.006	0.058 ± 0.005
37 pins across fats, 21 mm casing:	20 250	34 400	6 300	13 900
Single-pin void, 21-mm casing:	19 600	33 400	61 000	13 300
Single-pin void, fraction of total:	0.032 ± 0.005	0.029 ± 0.003	0.040 ± 0.007	0.042 ± 0.005
Fractional count rate loss due to casing:	0.47	0.46	0.34	0.27
Loss in mass sensitivity for:				
21-mm steel casing:	48 ± 8%	48 ± 5%	38 ± 8%	28 ± 4%
25-mm steel casing:	54%	54%	43%	32%
50-mm steel casing:	78%	78%	68%	54%

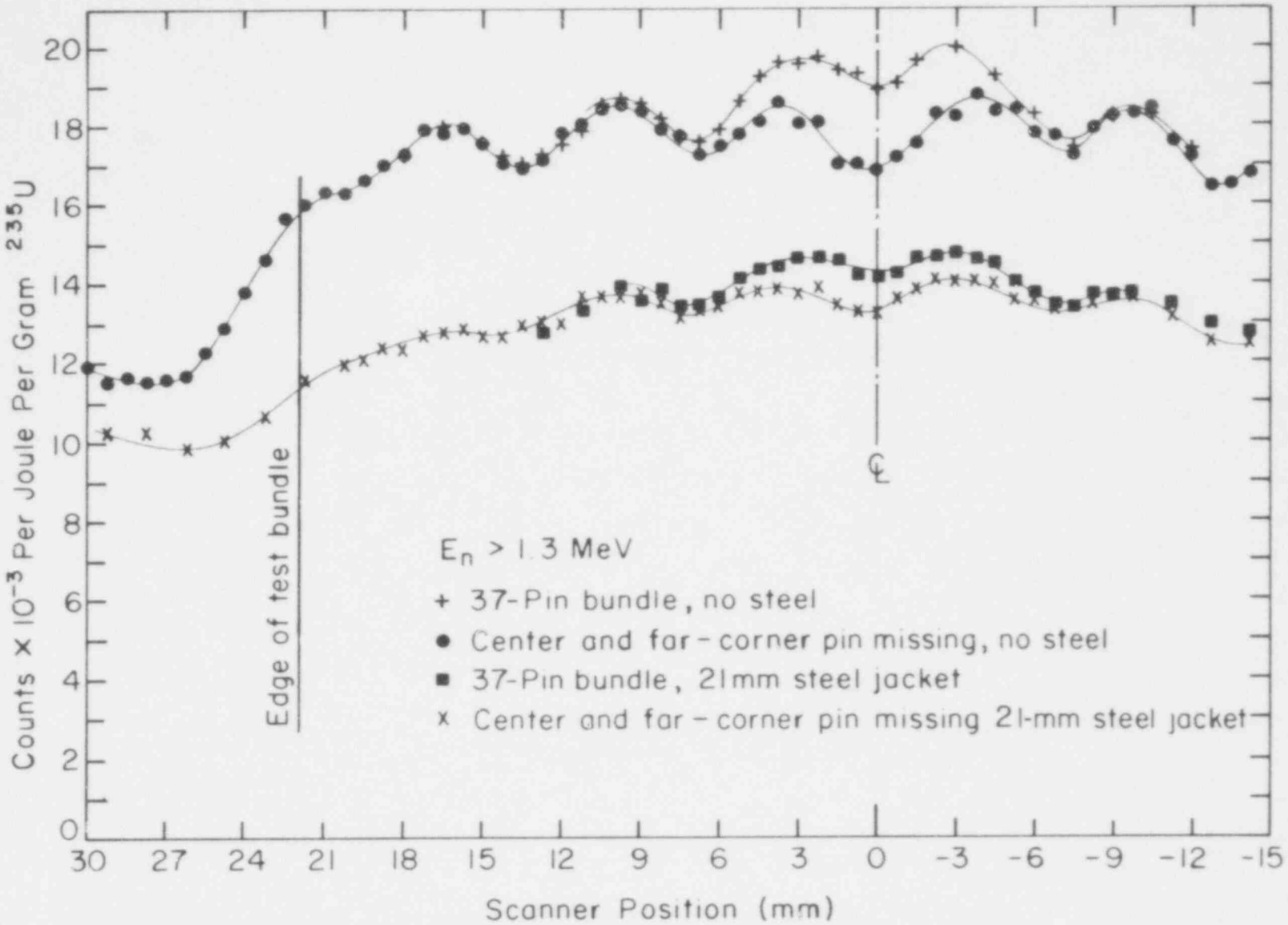

Fig. 101. Effect of a 21-mm-thick steel sleeve on fast-neutron hodoscope scans across corners of a 37-pin FTR fuel bundle.

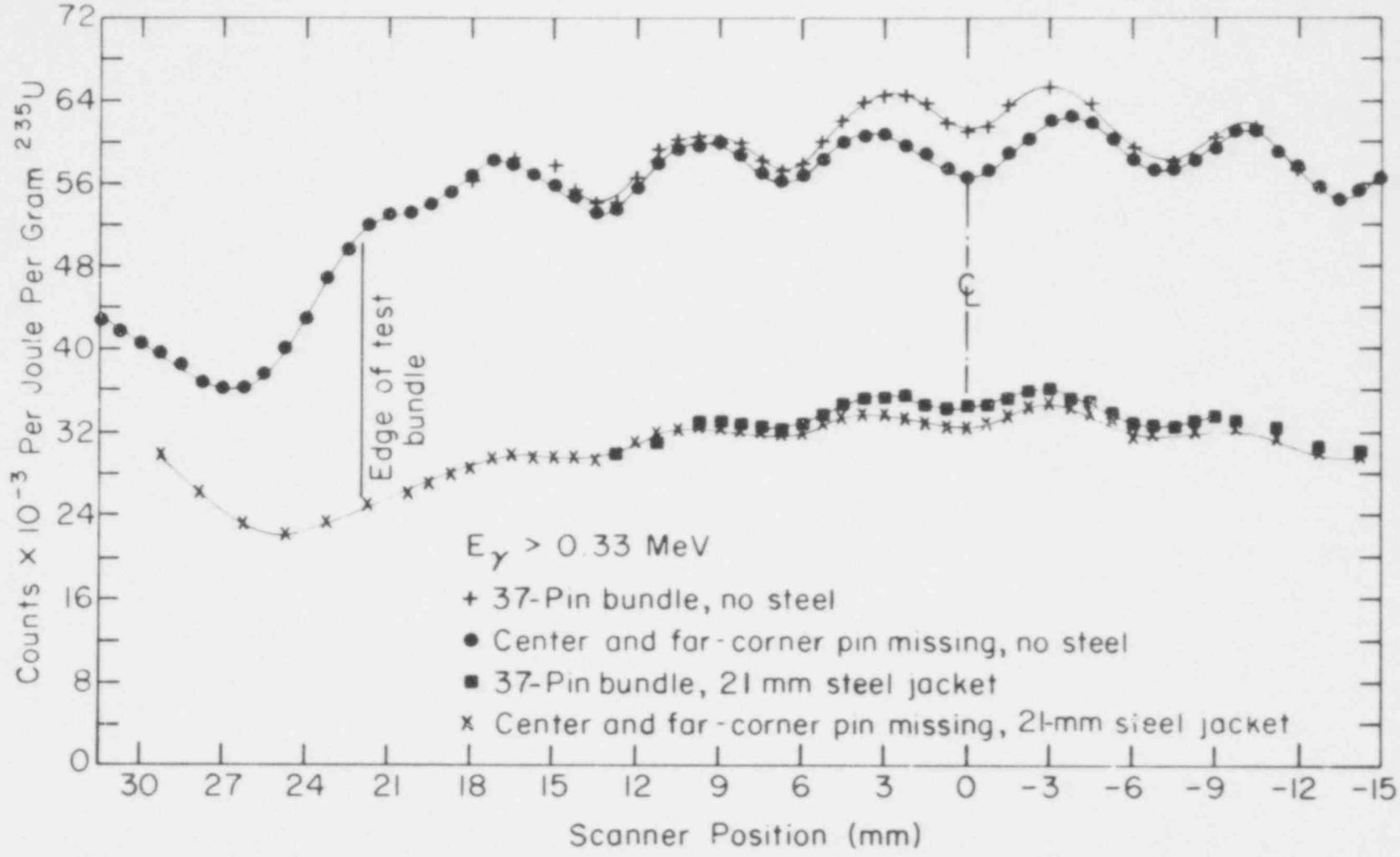

Fig. 102. Effect of a 21-mm-thick steel sleeve on hodoscope scans for gamma rays of 0.33 MeV, across corners of a 37-pin fuel bundle.

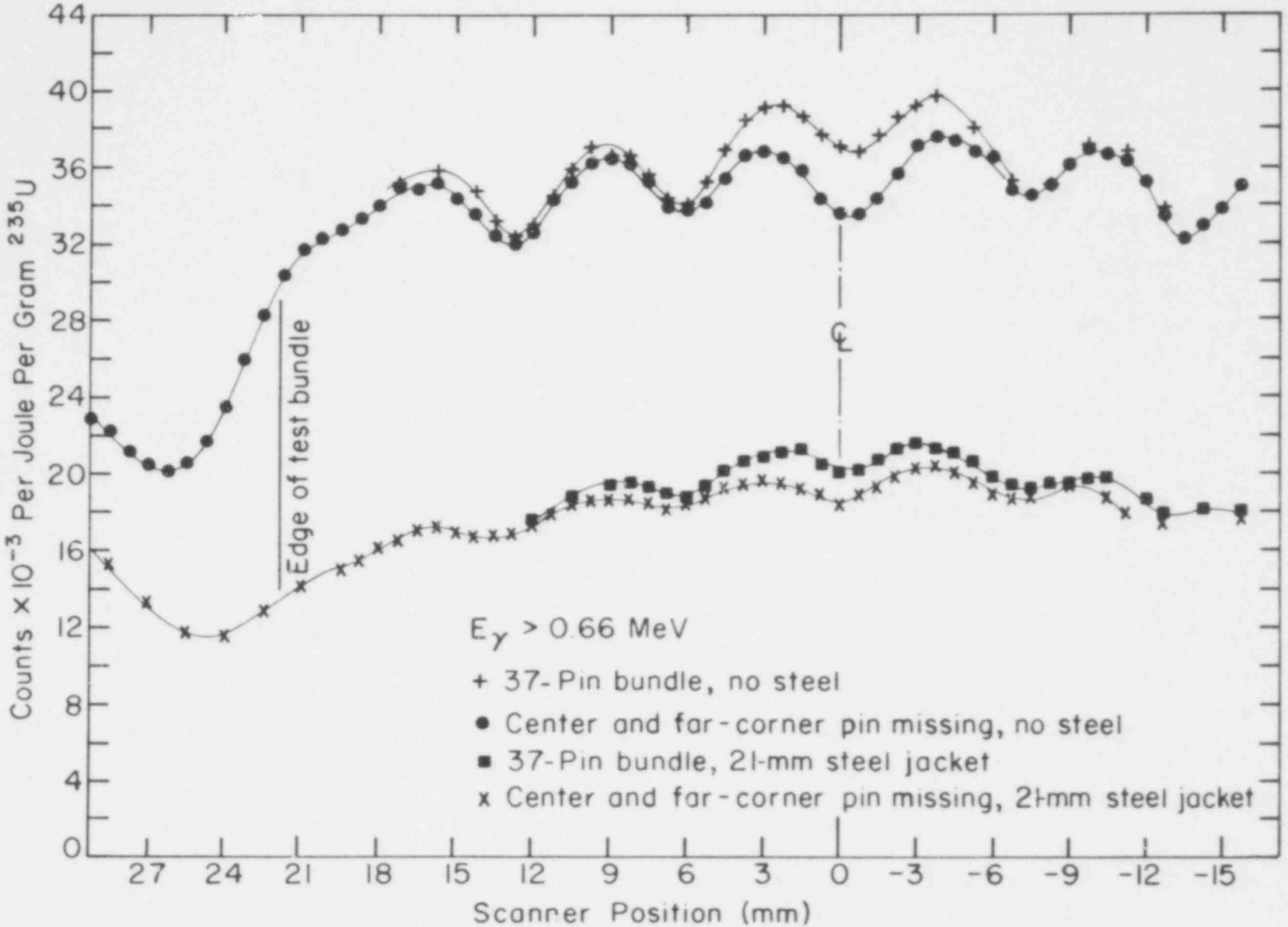

Fig. 103. Effect of a 21-mm-thick steel sleeve on hodoscope scans for gamma rays 0.66 MeV, across corners of a 37-pin fuel bundle.

IV. HTGR SAFETY RESEARCH

(M. G. Stevenson, Q-DO)

Under the sponsorship of the NRC/RSR, LASL is conducting a program of research in HTGR safety technology structural investigations and phenomena modeling, systems analysis, and accident delineation. Progress for this quarter in these areas is reported below.

A. Structural Investigations

(C. A. Anderson, Q-13)

Activities in this program during the past quarter have continued to focus on the seismic modeling and prestressed concrete reactor vessel (PCRV) analysis efforts. In the former task, we have completed the last in a series of tests of one-dimensional models to further investigate the effect of Coulomb friction on the system response. In particular, results are reported below on how to correct a distorted (graphite) model by adjustment of the coefficient of friction. During the past quarter, R. C. Dove visited the JAERI Tokai Establishment to confer and work with personnel concerned with seismic problems as they relate to the Japanese development of the very high-temperature, gas-cooled, graphite-moderated reactor (VHTR). A trip report has been prepared and is being distributed.

In the PCRV analysis effort, a major milestone was achieved with the publication of the NONSAP-C code manual and release of the final version of the code to the Brookhaven and Argonne code libraries. Results are also reported below on a simplified elastic-plastic model to represent concrete behavior.

1. Seismic Experimental Program

(R. C. Dove and W. E. Dunwoody, Q-13)

During this quarter, the one-dimensional, four block core model systems were again tested on the servohydraulic shaker at

the White Sands Missile Range (WSMR). The purpose of these final tests on the one-dimensional system was to investigate further the effect of Coulomb friction on the system response.

Previous tests on the graphite model (a distorted model, since the friction forces were known to be improperly scaled) had shown that, when subjected to seismic excitation, the strains predicted by the graphite model were too large.[77] In the current series of tests the graphite prototype system was subjected to five identical simulated earthquake events. Peak strains produced by block impacts were recorded and are given in Table XIV. The graphite model was also subjected to five identical earthquake events which were appropriately scaled relative to the prototype pulse. During posttest examination of these pulses, it was discovered that the acceleration amplitude of the scaled pulses was slightly higher than desired. However, it was invariant during all model tests (with and without increased friction); hence, the results presented here are not affected. The results of these tests are also shown in Table XIV. The graphite model system was disassembled and friction disks* were bonded to the base of each model block. Following this modification to increase the static (μ_s) and kinetic (μ_k) coefficients of friction of the model, the model was again subjected to the same earthquake events to which it had previously been subjected. The results of these tests are also shown in Table XIV.

These tests, which used a somewhat different earthquake signal than had been used in previous tests, reaffirm the findings previously reported, i.e., the graphite model is distorted with frictional effects too small, and, as a result, it predicts strains that are too large.[77] In addition, these tests show that for this

---

*1/4-in.-diam disks of 120 grit SiC. This produced a static coefficient (μ_s) of 0.61, and a kinetic coefficient (μ_k) of 0.39.

TABLE XIV

MAXIMUM STRAIN PRODUCED IN FOUR-BLOCK SYSTEMS
DURING SIMULATED EARTHQUAKE TESTS

Test No.	Max. Strain in Prototype x 10^6	Max. Strain in Graphite Model x 10^6	Max. Strain in Friction Corrected Graphite Model x 10^6
1	150	231	208
2	173	254	162
3	173	266	162
4	185	266	162
5	185	266	127
Average of 5 Tests	173	257	164
Deviation from Avg. (%)	-13 + 6	-10 + 4	-22 + 27
Error in Prediction of Avg. Max. (%)		+48%	-5%

one-dimensional system, it is possible to "correct" the distorted model by adjustment of the coefficient of friction. This method of compensating "distortion" has been discussed in a previous report.[78]

These tests also indicate that distortion due to too low a value of friction force has effects in addition to increased impact forces. With the distorted model, the impact sequence begins when the first significant acceleration peak of the earthquake event is reached, and during the remainder of the event the impact pulses are more numerous as well as more intense.

"Distortion compensation" by increasing friction not only reduces the magnitude of the block impacts to the level actually experienced by the prototype, but, in addition, it corrects the impact sequence starting point and number of contacts. These conclusions are drawn from the test data presented in Fig. 104 and Table XV.

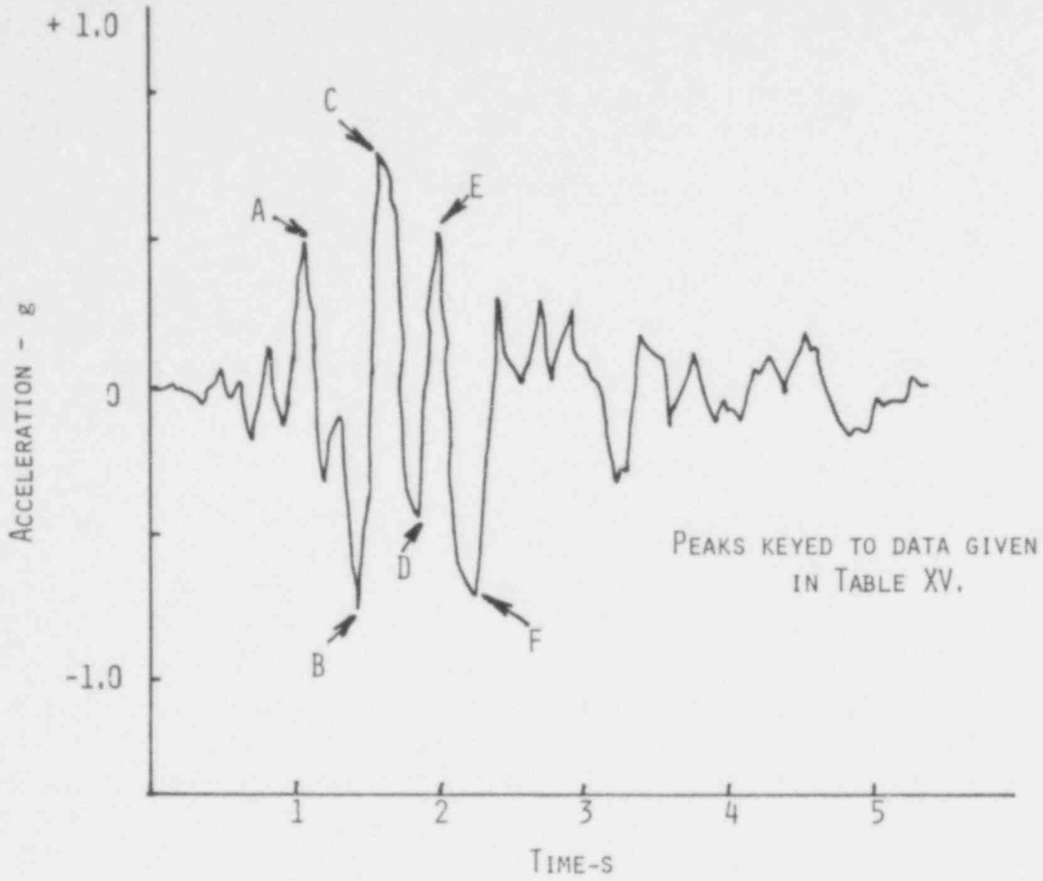

Fig. 104. Acceleration time history of simulated earthquake.

TABLE XV

NUMBER OF IMPACTS IN FOUR-BLOCK SYSTEMS
DURING FIVE SIMULATED EARTHQUAKE TESTS ON EACH SYSTEM

	Number of Impacts		
Pulse Point[a]	Prototype	Distorted Model	Friction Corrected Model
A	0	18	0
B	20	20	20
C	20	20	20
D	0	20	0
E	14	20	14
F	20	20	20

[a]See Fig. 104.

It is interesting to note that if a distorted model (low friction forces) were tested to a low acceleration level earthquake (say, all peaks equal to or less than point A on Fig. 104), then the distorted model would predict block impacts whereas, in fact, the prototype would experience none, or a very limited number of impacts.

During this quarter, R. C. Dove visited Japan to confer and work with personnel at the JAERI Tokai Establishment. Because JAERI has conducted a significant amount of experimental seismic research in the area of reactor cores and components, this trip was especially valuable. A trip report containing details of JAERI's seismic research has been prepared for distribution. JAERI plans to test a "vertical slice, 1/2-scale" model of the VHTR core during February 1979 and R. C. Dove has been invited to participate in this test. This test will be conducted at Takesago, Japan.

2. Analysis of PCRVs

(P. D. Smith, Q-13)

After incorporation of changes found in Ref. 79, the Chen and Chen yield surface has continued to exhibit numerical difficulties. These problems appear to be caused by the discontinuity between the tension-compression region and the compression-compression region of the yield surface. A simplified hyperbolic yield surface has been investigated as a means of eliminating the discontinuity.

The basis of the revised surface is that it must be a surface of revolution about the hydrostatic axis and that it must have three constants that can be determined from the standard uniaxial tension, uniaxial compression, and biaxial compression tests. The generator for the simplified surface was chosen to be a hyperbola in octahedral shear and octahedral normal stress space

$$F(\sigma_{ij}) = (\tau - \beta)(\sigma - \alpha) = (-a^2) \ , \qquad (66)$$

where

σ_{ij} = stress tensor,

τ = octahedral shear stress obtained from σ_{ij},

σ = octahedral normal stress obtained from σ_{ij}, and

α, β, a = constants determined from the previously mentioned laboratory tests.

The surface is shown in octahedral space in Fig. 105. Following the Chen and Chen model, there are an initial yield surface and a failure surface, each described by Eq. (66) with a different set of constants associated with each surface. Figure 106 shows the close agreement between the simplified surfaces and experimental biaxial strength data. A simple linear interpolation is assumed for surfaces between the initial yield and failure surfaces. The constants that define these intermediate surfaces are

$$\beta = \beta_\phi + \kappa \, (\alpha_\mu - \beta_\phi) \, , \tag{67}$$

$$\alpha = \alpha_\phi + \kappa \, (\alpha_\mu - \alpha_\phi) \, , \tag{68}$$

and

$$a = a_\phi + \kappa (a_\mu - a_\phi) \, , \tag{69}$$

where the subscripts ϕ and μ refer to the initial yield and failure surfaces, respectively, and κ is the interpolation constant that varies between 0 and 1. Given a stress state (τ, σ) that lies on the current yield surface defined by α, β, and a, and a stress increment $(\delta\tau, \delta\sigma)$, the change in the interpolation parameter is

$$\delta\kappa = (B + \sqrt{B^2 - 4 \, AC} \,)/2A, \tag{70}$$

where

$$A = (\alpha_\mu - \alpha_\phi)(\beta_\mu - \beta_\phi) - (a_\mu - a_\phi)^2 \, , \tag{71}$$

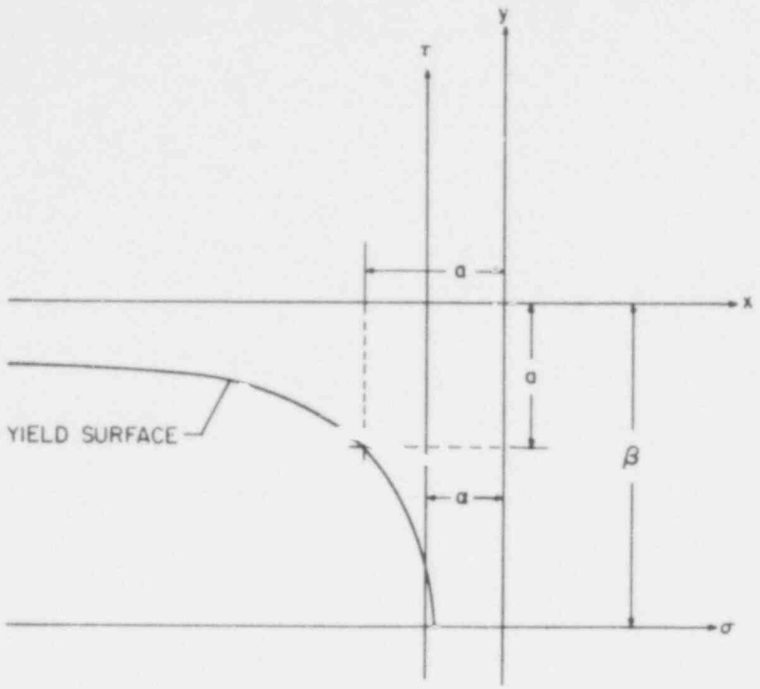

Fig. 105. Yield surface in octahedral space.

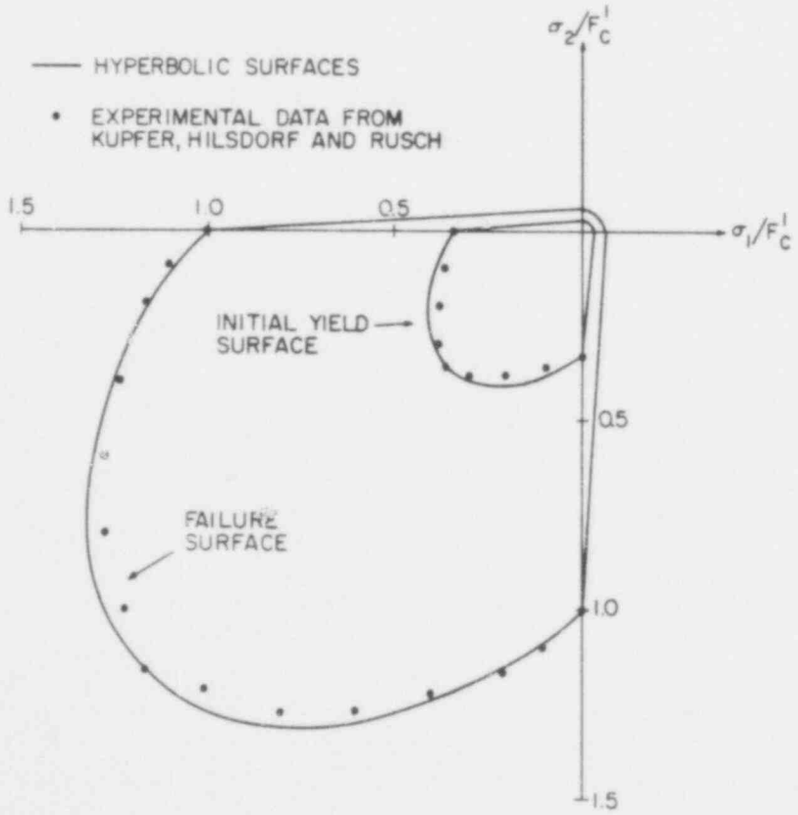

Fig. 106. Intersection of yield surface with σ_1 - σ_2 plane.

$$B = 2a(a_\mu - a_\phi) + (\beta_\mu - \beta_\phi)(\sigma + \delta\sigma - \alpha) + (\alpha_\mu - \alpha_\phi)(\tau + \delta\tau - \beta), \tag{72}$$

and

$$C = \delta\tau\delta\sigma + (\sigma - \alpha)\delta\tau + (\tau - \beta)\delta\sigma . \tag{73}$$

For a stress increment $(\delta\tau, \delta\sigma)$ that penetrates a yield surface described by α, β, and a, the elastic portion r of the stress increment is obtained by solving the quadratic equation,

$$[\delta\tau\delta\sigma]r^2 + \left[(\sigma - \alpha)\delta\tau + (\tau - \beta)\delta\sigma\right]r + \left[(\tau - \beta)(\delta - \alpha) - a^2\right] = 0 . \tag{74}$$

The outward normal to the surface described in Eq. (66) is

$$\frac{\partial F}{\partial \underset{\sim}{\sigma}} = \frac{1}{3\tau} \begin{Bmatrix} \tau(\beta - \tau) + (\alpha - \sigma)S_{11} \\ \tau(\beta - \tau) + (\alpha - \sigma)S_{22} \\ \tau(\beta - \tau) + (\alpha - \sigma)S_{33} \\ 2\,S_{12} \\ 2\,S_{23} \\ 2\,S_{13} \end{Bmatrix} , \tag{75}$$

where

$$\underset{\sim}{\sigma} = \left| \sigma_{11}, \sigma_{22}, \sigma_{33}, \sigma_{12}, \sigma_{23}, \sigma_{13} \right|^T , \tag{76}$$

and S_{ij} represents the deviatoric components of the stress tensor σ_{ij}. The elastic-plastic stress-strain matrix is formed using Eq. (75) in the usual fashion.[80]

The hardening parameter used in the elastic-plastic constitutive matrix is

$$H = \frac{dF}{d\varepsilon_\rho} , \tag{77}$$

where ε_ρ is a measure of the current plastic strain state. In this model, it is assumed that a uniaxial compressive stress-strain curve can be expressed in the form

$$d\phi/d\varepsilon_\rho = (2/\hat{\varepsilon}) \sqrt{(\phi_\mu - \phi_\phi)(\phi_\mu - \phi)} , \tag{78}$$

where

ϕ = the current uniaxial compressive yield strength of the material,

ε_ρ = uniaxial compressive strain,

ϕ_μ = the ultimate uniaxial compressive yield strength,

$\hat{\varepsilon}$ = uniaxial strain at ϕ_μ, and

ϕ_ϕ = uniaxial compressive yield strength.

Equation (77) can now be expressed as

$$H = \frac{dF}{d\varepsilon_\rho} = \frac{dF}{d\phi} \frac{d\phi}{d\varepsilon_\rho} . \tag{79}$$

By substituting a uniaxial compressive stress $-\phi$ into Eq. (66), the remaining derivative needed to find H is found to be given by

$$\frac{dF}{d\phi} = 2\left(\frac{\phi}{9}\right)^2 + \left(\frac{2\alpha - \sqrt{2}\,\beta}{3}\right)\left(\frac{\phi}{9}\right) - \left(\frac{\sqrt{2}\,\alpha\,\beta}{}\right) . \tag{80}$$

B. Phenomena Modeling and Systems Analysis

(P. A. Secker, Q-6)

The phenomena modeling and systems analysis task is concerned with the development, testing, and application of gas-cooled reactor (GCR) consolidated plant simulation computer programs. The Composite HTGR Analysis Program (CHAP) uses a model-independent systems analysis program called LASAN which has steady-state, transient, and frequency response solution capabilities. The

model-dependent portion of CHAP consists of linked modules, each representing a component, subsystem, or phenomenon of the overall HTGR plant model and having a standardized modular structure. The initial version (CHAP-I) models the 3 000-MW(t) HTGR. CHAP-II is currently under development and models the Fort St. Vrain (FSV) HTGR.

During the past quarter, FSV and 3 000-MW(t) model testing analyses were performed using complete plant models. Open loop and closed loop frequency response calculations were performed at 100% power for both FSV and the 3 000-MW(t) plants.

An improved numerical integration algorithm was developed using permuted sparse matrix procedures reducing storage and running time.

1. CHAP Transients

(P. A. Secker, K. R. Stroh, and C. E. Watson, Q-6; and R. B. Lazarus, C-3)

a. Parameter Studies

Steady-state calculations for both the 3 000-MW(t) large high-temperature gas-cooled reactor (LHTGR) and the FSV reactor were run using the CHAP models. These studies were performed to establish appropriate values of design parameters otherwise unavailable. All parameters were found for 100% of rated plant power and then fixed for the transient analyses. Table XVI shows the CHAP parameters modified to obtain the design specifications.

b. Rapid Load Changes

The CHAP models were used to predict plant response to rapid changes in load. The load demand was ramped from 100% to 25% at 0.5%/s. After 150 s, the load demand was held at 25%. Table XVII shows the initial conditions for the LHTGR prior to the load reduction demand.

TABLE XVI

CHAP DESIGN PARAMETERS

	CHAP Parameter	Design Specification
1.	Core channel orifice loss coefficients	Specified channel exit temperatures
2.	Width of side reflector gaps	Specified fraction of heat removal in side reflector at design
3.	Helium circulator turbine flow coefficient	Specified design flow rate in turbine
4.	High-pressure turbine flow coefficient	Specified feedwater flow rate
5.	Reheater heat transfer flowing coefficient	Specified helium temperature drop across reheater tube bundle
6.	Helium side loss coefficient in steam generator bundles	Specified circulator pressure rise

TABLE XVII

INITIAL CONDITIONS FOR 3 000 MW(t)

	Parameter	Value	
1.	Initial reactor power	3 000	MW(t)
2.	Circulator speed	6 750	rpm
3.	Total helium flow rate	1 409	kg/s
4.	Cold helium temperature	561	K
5.	Core average temperature	982.3	K
6.	Average helium temperature at core outlet	970.1	K
7.	Main steam temperature	785.6	K
8.	Reheat steam temperature	812.0	K
9.	Total feedwater flow	1 020.9	kg/s
10.	Main steam pressure	16 650	kPa
11.	HP turbine first-stage pressure	11 934	kPa

Figures 107a and b show the response of the LHTGR to the rapid load reduction. Feedwater flow rate, helium flow rate, and reactor power are shown in Fig. 107a. Reactor power is controlled to maintain a specified exit reheater steam temperature. The feed forward signal for control rod motion is the measured high-pressure turbine first stage pressure, which closely follows the load demand. The central control rod becomes fully inserted within 130 s after the transient begins. Feedback reactivity increases due to core cooling and causes the power to increase after 200 s. The control rods restore control after 318 s. Steady conditions are then achieved after 1 000 s. Figure 107b shows various key temperatures for plant variables.

2. Frequency Responses

We performed both open loop and closed loop frequency responses with the LHTGR plant model. Figure 108 shows the closed loop frequency response of reactor power to the plant load demand. A resonance is observed at 0.03 rad/s. However, the phase lag does not get below -180°, and the plant would be stable.

An open-loop frequency response of high-pressure turbine first stage pressure (control rod feed forward signal) to feedwater flow perturbation at 100% power is shown in Fig. 109. In this case, a resonance is observed at 0.02 rad/s; again, no instability is indicated.

The resonances observed on both of these Bode plots may be of interest because they would tend to produce small resonance fluctuations in the plant dynamic response with periods from 200 s to above 300 s. Similar frequency response calculations are under way for FSV.

3. LASAN Improvements

The linear system solver routine in the LASAN code was improved. The new algorithm solves $M\underline{x} = \underline{y}$ directly after permuting M into banded form. The old algorithm solved the equation by decomposing M into two matrices:

$$M = M_1 + M_2$$

and

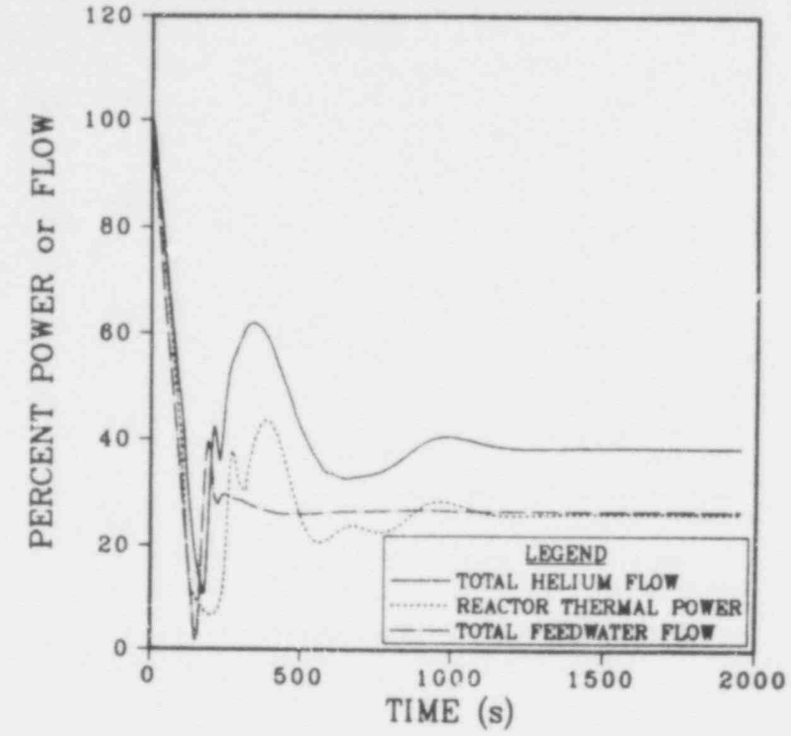

(a)

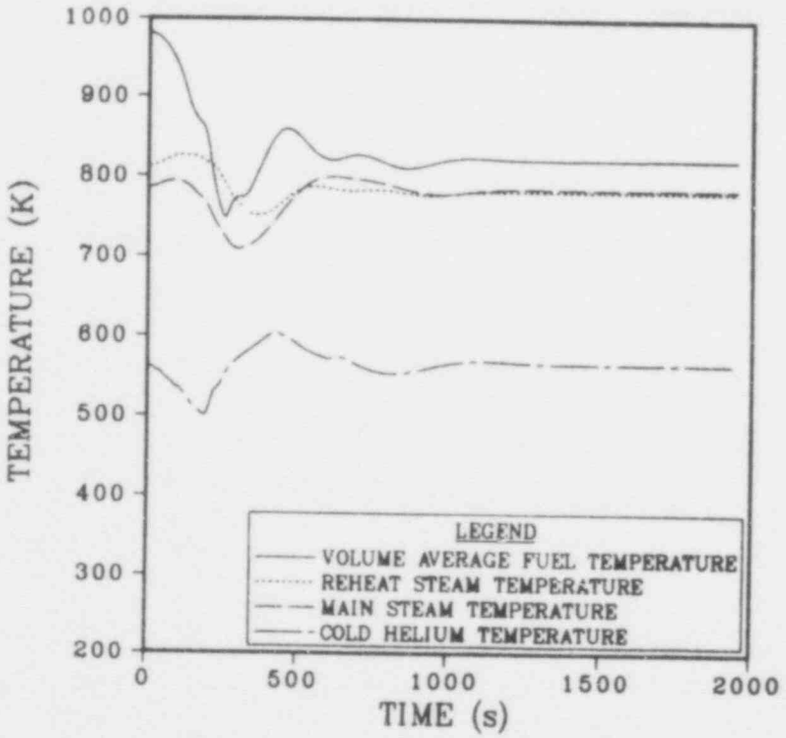

(b)

Fig. 107. Calculated response to a rapid load reduction.

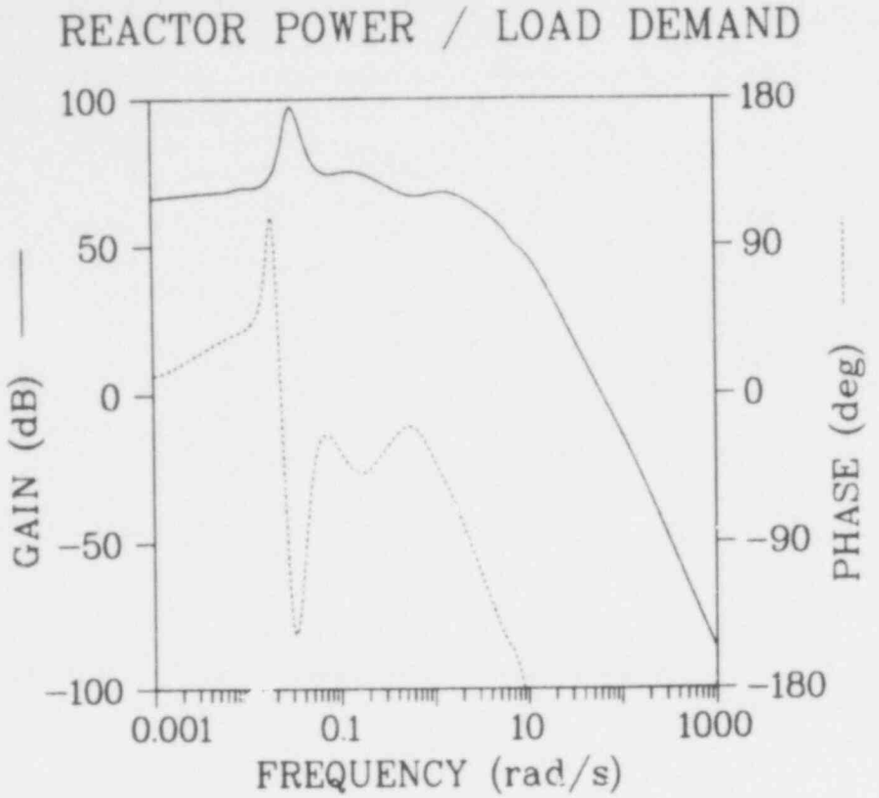

Fig. 108 Closed loop plant frequency response.

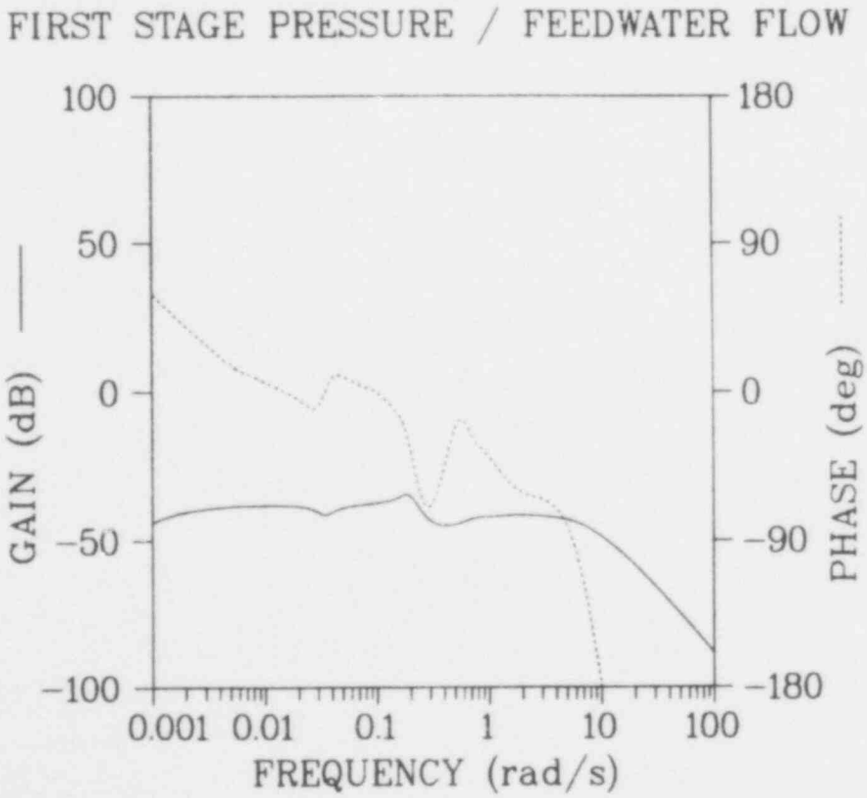

Fig. 109. Open loop plant frequency response.

iterating $M_1 \underline{x}_1 = \underline{y} - M_2 \underline{x}$. The objective was to find a decomposition with M_1 easy to invert that guarantees convergence by keeping the eigenvalues of $M_1^{-1} M_2$ small. Unfortunately, no fast but safe algorithm could be found which did not, on occasion, restrict the time step unduly.

The new banded algorithm utilizes the sparse properties of M. It is impractical to find the minimum bandwidth of a matrix. However, a heuristic algorithm was developed which does well and is quite fast.

A debugging tool was added to LASAN which helps the user identify the dependence of state variables on each of the other state variables. The Jacobi matrix is now displayed in terms of external state variable names on the user output.

New restart features were added to LASAN during this period. Multiple restart data sets can be obtained from a single run.

V. GCFR CORE DISRUPTIVE TEST PROGRAM

(D. L. Hanson, Q-13)

The basic assembly module of the GCFR core is a subassembly comprising 264 fuel rods, 6 corner support rods, 1 central rod (instrumented), and their surrounding duct. The duct is a right hexagonal cylinder. The purposes of this out-of-pile experimental program are to demonstrate the behavior of one of these GCFR core modules in the event of loss-of-core coolant flow or pressure and subsequent shutdown of reactor power to the level resulting from decay heat alone. The LOFA will be simulated in the Duct Melting and Fall-away Test (DMFT) and the loss-of-pressure accident will be simulated in the Depressurized Accident Condition (DAC) test. These experiments require the development of an electrically heated fuel rod simulator capable of delivering 2 kW of power while operating at surface temperatures exceeding 1 650 K, and the development of a fixture that will permit operation of an ensemble of 450 such rods (1 core module thermally guarded by segments of the 6 surrounding modules) at helium pressures up to 9.1 MPa. This Guarded Core Module (GCM) fixture will be the largest in a sequence of four test fixtures developed in the course of this program. The others are

- Ten-inch, single-rod fixture,
- One-meter, seven-rod fixture, and
- Full-length Subgroup (37-rod) fixture.

The GCM fixture will be used first for the DMFT and subsequently for the DAC test.

A. Program Planning

(D. L. Hanson, Q-13)

A meeting was held at General Atomic Company (GAC) in November to review LASL evidence from the FLS 1 test and subsequent spacer grid friction testing suggesting that the LASL mock spacer

grids contributed to the failure of simulated fuel rods in FLS 1 and that the prototype spacer grids give evidence of even greater potential for the same behavior. It was mutually agreed that LASL would utilize a design of its own creation to satisfy the need for spacer grids in FLS 2.

B. Analysis

(D. L. Hanson and A. J. Giger, Q-13)

Further work was accomplished on the frame that will be used to support the DMFT experiment within the GCM test fixture. To analyze the effect of high external pressure on the frame manifold with a low-pressure coolant within, a finite element model was made of the manifold. Figure 110 shows the current ring-shaped manifold design. The model was statically loaded by external application of 102 atm with 10.2 and 3.4 atm, respectively, in the lower and upper chambers. The resulting maximum principal stresses in the y-z plane are shown in Fig. 111. An exaggerated plot of the deformed shape is shown in Fig. 112. As a result of the analysis the welds are being relocated and the side wall thickness increased slightly to ensure better design margins.

An investigation was made of gas cooling for the support frame using a modification of a short program previously used to examine water cooling. The nominal design case, using nitrogen, is summarized in Table XVIII. An assumption of incompressibility was reasonably well met with an observed change in density of 10.4%. An increase in the film drop from 7.74-46.3 K results when changing from water to nitrogen. This, in effect, would allow slightly more, probably inconsequential, radial growth for the guard heater mount. More difficult to cope with would be the increase in the frame longitudinal growth. The decision for gas or water cooling has been deferred.

Postmortem analysis of FLS 1 continues. It has been determined that 18 of the 34 rods failed. Some localized melting at the tips of molybdenum blanket electrode rods has been observed.

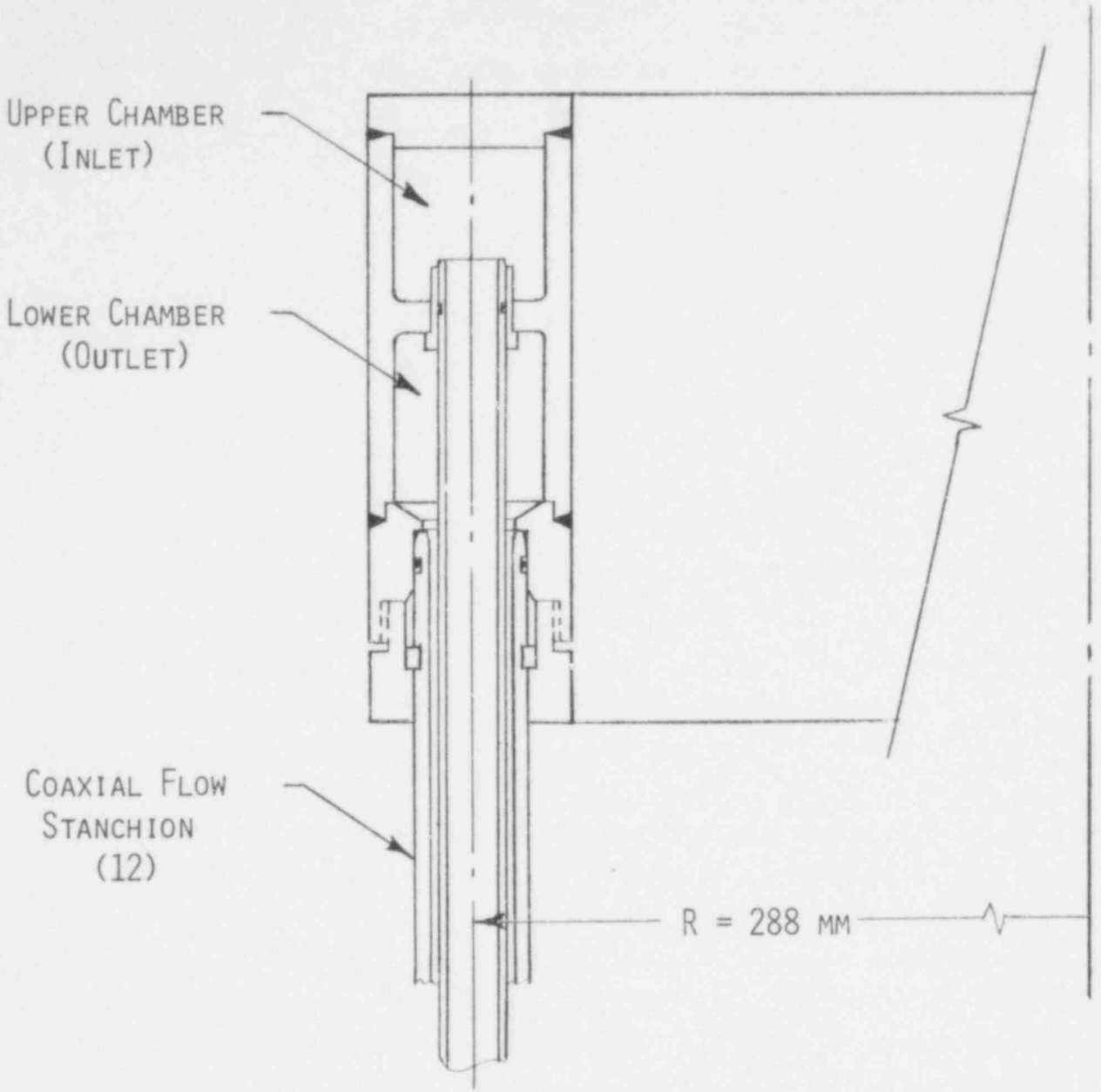

Fig. 110. Support frame manifold.

C. Design

(J. Churchman, SD-2; D. L. Hanson and A. J. Giger, Q-13)

271 Rod GCM Experiment

The support frame design was finished and detailing is 25% completed.

It was originally planned to react the pressure loads from the frame coolant pipes that pass through the top cover of the

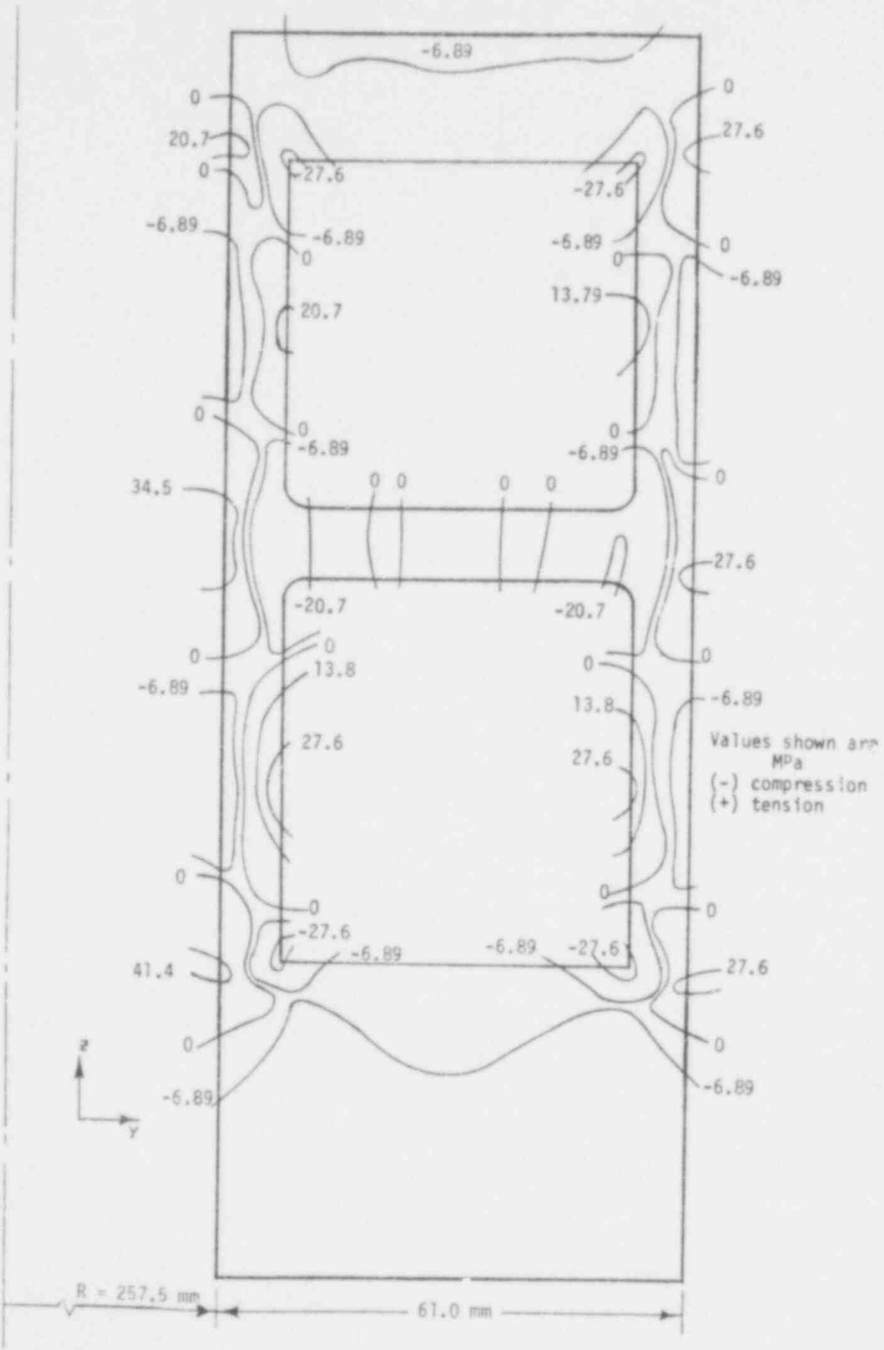

Fig. 111. Maximum principal stress in y-z plane.

pressure vessel (PV) onto the cover itself. Because this provided a redundant load path with the frame support, it was decided to accept this relatively high load, 34.8 kN, on the frame support.

A detailed design was completed for the uncooled plate to support the experiment on the frame; however, better analysis is required to establish the temperature regime of this part. Final design and release of the plate will be contingent on this.

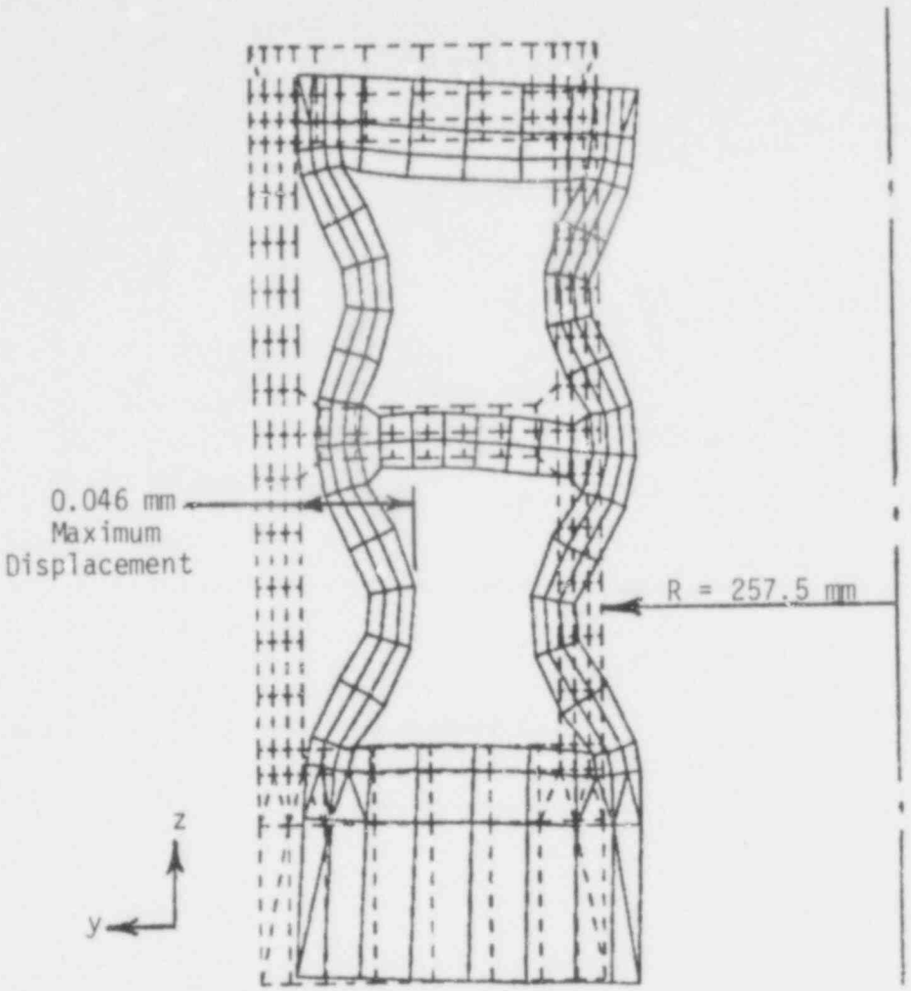

Fig. 112. Support frame manifold deformation.

TABLE XVIII

NOMINAL DESIGN OF DMFT SUPPORT FRAME WITH NITROGEN COOLING

Ring Material	C-1015
Stanchions (34.9 o.d. x 4.76 mm)	C-1015
Annulus Gap	2.38 mm
Coolant Rate	0.57 kg/s
Pressure	2.84 MPa
System Pressure Drop	36.5 kPa
Coolant Temperature Rise	29.3 K
ΔT, Film	46.3 K
Ring Diameter Increase	0.65 mm

A vertical adjustment downward of 101.6 mm was made on all the ports of the PV in order to make more space available for the top electrical contact. Difficulties are being encountered in designing this contact to carry 10 000 A, have a travel of 150 mm, and transmit small maximum loads to the experiment.

The bottom two sets of electrical passthrough ports (six holes) were eliminated from the PV because it appears to simplify electrical connection to the experiment to use the symmetrically located "balancing" port for the bottom gas port. If no through connections are made to the guard heater supports, as now seems likely, this leaves only three lateral connections, the upper electrical contacts for the guard heaters, to be made through the PV.

The results of brazing cladding into the core support plate for FLS 1 were not satisfactory; therefore, it is intended to braze individual fittings to the cladding and fasten these to the core support plate. The fittings have been designed, but because of fuel rod pitch change from 11.2-10.4 mm these are thin wall and relatively close tolerance parts. A pilot lot is planned for use on FLS 2.

D. Testing

(D. R. Bennett, R. Renfro, D. L. Hanson, and R. Ortega, Q-13)

1. Contact Resistance Test

In connection with the design of the top electrical contact for the first GCM test, an experiment was performed to examine the use of multiple ball bearings sandwiched between two plates as an electrical contact with two degrees of freedom. Contact resistance was measured through approximately 330, 2.4-mm-diam chromed steel ball bearings. After exposure to a current density of 0.9 amps/ball, which would be required in the design, approximately two-thirds of the bearings became charred, while several fused to the flat surfaces. This approach has been discarded.

2. Instrumentation

During the 37-rod FLS tests, data were scanned and recorded by the HP-3052A data acquisition system at a rate of about three

readings/s. Because DMFT tests will require much faster data acquisition times, benchmarking tests were conducted to ascertain more closely the limiting speed and capabilities of the system as presently configured.

The digital voltmeter (DVM) is the slowest device in the system and is thereby the limiting factor. The DVM (3455A) can internally determine the range of a voltage measurement with its auto range feature, or the voltage range can be specified in software. Careful software formatizing can equalize the two ranging techniques. Autocalibration of the system, necessary only at the test's initialization, can triple time requirements if used with every scan. The sixth significant digit acquired with high-resolution is unnecessary for thermocouple measurements, and is extremely time consuming. Optimization of all of these factors produced rates of 13.5 readings/s with 5 digit resolution. Hewlett Packard representatives indicate that 18-20 channels/s is the DVM's maximum speed; this discrepancy is being investigated.

With increasing knowledge of the HP-3052A system and careful software considerations, the speed and precision of the present system may be raised to its specification level. Upcoming instrumentation needs, dictating an increase beyond these levels, will require supplemental or new equipment to meet increased capacity and speed requirements.

3. Test Cell No. 1 Modifications

Construction of the test cell No. 1 modification (WA 16, TA-46) has begun. The 4- x 4.9- x 12.2-m, high-bay addition to the test cell will house the 15-ton pressure vessel and accompanying crane required for DMFT and DAC testing. At this point, footings have been dug; completion is expected within 90 days.

The crane hoist area and catwalks restrict the amount of usable space in the high-bay addition; therefore, interior layouts are being prepared that efficiently utilize space for equipment and test assemblies.

E. Fabrication and Procurement

(W. E. Dunwoody, Q-13)

The vendor for the GCM PV, March Metalfab Inc., has submitted the fabrication drawings and ASME pressure vessel code calculations for approval. The vendor's drawings are being checked and will be updated to reflect the latest design changes prior to the approval for fabrication. The calculations were reviewed and appear to be satisfactory.

Bids for the overhead bridge crane for the high-bay addition were received from two suppliers. Crane Hoist Engineering Co. (CHECO) is able to meet specified technical requirements, including those defining the minimum amount of horizontal crane travel required in the bay. Therefore, it has been requested that the order be placed with CHECO.

557 224

VI. CONTAINMENT SYSTEMS AND REACTOR SAFETY ANALYSES

(R. G. Gido, Q-6)

The following sections summarize the progress from two projects in the areas of containment systems and reactor safety funded by the NRC, Division of Systems Safety (DSS).

A. Containment Accident Long-Term Response

(D. E. Lamkin, Q-6)

A final report that describes the results of this effort has been prepared. This report includes the following three key items to provide a basis for the development of NRC licensing guidelines for qualification of safety-related equipment following a main steam line break inside the containment.

1. A new model for the treatment of condensation mass removal.
2. Justification for the use of a higher temperature difference or "driving potential" in containment heat transfer than is the current practice.
3. A model for the estimation of temperature, density, and velocity fields within the jet emanating from the postulated broken steam line.

Items 1 and 2 provide a firm basis for more realistically predicting the heat transfer boundary conditions for equipment located outside the jet. Item 3 provides a basis for heat transfer calculations within the jet.

B. Reactor Mass and Energy Release Audit Analysis

(G. J. E. Willcutt, Jr., Q-6)

We have completed initial TRAC simulations of Marviken Critical Flow Tests 1, 2, 4, and 7. Tests 1 and 2 used 0.3-m-diam nozzles with L/D of 3; Test 4 used a 0.509-m-diam nozzle with L/D of 3; and Test 7 used a 0.3-m-diam nozzle with L/D of 1. TRAC

mass fluxes agreed best with data for Test 4[13] and differed most with data for Test 7. Further investigation is required to verify and understand the differences.

A calculation of stagnation conditions at the nozzle entrance was added to TRAC. A separate program was written to calculate critical mass fluxes for the HEM, Moody, Henry-Fauske, Burnell and modified Zaloudek critical flow models using these stagnation conditions. A plot package compares each of these critical flow models with the TRAC and experimental results.

The TRAC simulation of Test 4[13] included a detailed model of the flare (expansion section) at the exit of the nozzle test section. We have since tested this nozzle model with the flare removed so the nozzle ends after the constant diameter section. We did this by coupling the nozzle entrance to a large plenum with fixed pressure and temperature boundary conditions. The steady-state mass fluxes with and without the flare agreed within 0.2%.

REFERENCES

1. L. J. Siefken, "FRAP-T4 - A Computer Code for the Transient Analysis of Oxide Fuel Rods," EG&G report CDAP-TR-78-027 (July 1978).

2. "TRAC-P1: An Advanced Best Estimate Computer Program for PWR LOCA Analysis, Vol. 1: Methods, Models, User Information, and Programming Details," Los Alamos Scientific Laboratory report LA-7279-MS (June 1978).

3. D. A. Niebruegge, E. L. Tolman, and C. W. Solbrig, "Best Estimate Fuel Rod Modeling Techniques," Nuclear Science and Engineering 68, 363-368 (1978).

4. J. A. Dearien, G. A. Berna, M. P. Bohn, J. D. Kerrigan, and D. R. Coleman, "FRAP-S3: A Computer Code for the Steady-State Analysis of Oxide Fuel Rods, Vol. 1: FRAP-S3 Analytical Models and Input Manual," EG&G report TFBP-TR-164 (October 1977).

5. R. J. Sand, L. J. Siefken, and B. W. Burnham, "Fuel Model Development for RELAP4/MOD7 Version 2," EG&G report CDAP-TR-78-025 (June 1978).

6. M. Bohn, EG&G Idaho Falls, Private Communication (December 1978).

7. J. M. Sorensen, "CHAST06, Core Heatup Analysis Model, Technical Description," General Electric Co. report NEDO-23728 (November 1977).

8. G. Carter, "SLOPE2 User's Guide," LASL Documentation LTSS-538 (October 1978).

9. A. R. Edwards and T. P. O'Brien, "Studies of Phenomena Connected with the Depressurization of Water Reactors," J. of British Nucl. Energy Society 9, 125-135 (April 1970).

10. K. D. Lathrop, "Reactor Safety and Technology Quarterly Progress Report for the Period April 1-June 30, 1976," Los Alamos Scientific Laboratory report LA-NUREG-6447-PR (August 1976).

11. R. W. Garner, "Comparative Analyses of Standard Problems - Standard Problem One (Straight Pipe Depressurization Experiments)," Aerojet Nuclear Company report I-212-74-5.1 (October 1973).

12. J. F. Jackson and M. G. Stevenson, "Nuclear Reactor Safety Quarterly Progress Report for the Period January 1-March 31, 1978," Los Alamos Scientific Laboratory report LA-7278-PR (NUREG/CR-0062) (June 1978).

13. J. F. Jackson and M. G. Stevenson, "Nuclear Reactor Safety Quarterly Progress Report for the Period July 1-September 30, 1978," Los Alamos Scientific Laboratory report LA-7576-PR (NUREG/CR-0522)(December 1978).

14. J. F. Jackson and M. G. Stevenson, "Nuclear Reactor Safety Quarterly Progress Report for the Period April 1-June 30, 1978," Los Alamos Scientific Laboratory report LA-7481-PR (NUREG/CR-0385)(October 1978).

15. S. Jacoby, "Experimental Data Report for LOFT Nonnuclear Test L1-5," EG&G report TREE-NUREG-1215 (June 1978).

16. K. A. Williams and D. R. Liles, "TRAC Calculations of ECC Bypass Phenomena in a 1/15 Scale Experimental Facility," ANS Annual Meeting (San Diego, CA, June 1978).

17. D. L. Batt, "Quick Look Report on LOFT Nuclear Experiment L2-2," EG&G report LOFT-TR-103 (December 1978).

18. P. A. Harris, T. K. Samuels, and H. J. Welland, "LOFT Experimental Operating Specification Vol. 2, NE L2 Series," EG&G report (July 1978).

19. B. J. Daly and F. H. Harlow, "Scaling and Constitutive Relationships in Downcomer Scaling," Los Alamos Scientific Laboratory report LA-7610 (NUREG/CR-0561)(1979).

20. B. J. Daly, "The Sensitivity of ECC Bypass and Lower Plenum Refill to Apparatus Scale Size and Lower Plenum Pressure in a PWR," Los Alamos Scientific Laboratory report (to be published).

21. C. J. Crowley, J. A. Block, and C. N. Cary, "Downcomer Effects in a 1/15 Scale PWR Geometry - Experimental Data Report," Creare, Inc. report NUREG-0281 (1977).

22. P. H. Rothe and C. J. Crowley, "Scaling of Pressure and Subcooling for Countercurrent Flow," Creare, Inc. report NUREG/CR-0464 (1978).

23. W. C. Rivard and M. D. Torrey, "Fluid Structure Response of a Pressurized Water Reactor Core Barrel During Blowdown," Los Alamos Scientific Laboratory report LA-7404 (1978).

24. W. C. Rivard and M. D. Torrey, "Numerical Simulation of Three-Dimensional Fluid-Structure Response," to be published in Proceedings of the American Nuclear Society Topical Meeting on Computational Methods in Nuclear Engineering (Williamsburg, VA, April, 1979).

25. W. C. Rivard and M. D. Torrey, "K-FIX: A Computer Program for Transient, Two-Dimensional, Two-Fluid Flow," Los Alamos Scientific Laboratory report LA-NUREG-6623 (1977).

26. W. C. Rivard and M. D. Torrey, "THREED: An Extension of the K-FIX Code for Three-Dimensional Calculations," Los Alamos Scientific Laboratory report LA-NUREG-6623, Suppl. 2 (1978).

27. D. A. Dahl, "MAPPER," Los Alamos Scientific Laboratory Program Library Write-Up, J5AJ.

28. W. C. Rivard, "Nonequilibrium Phenomena and Structural Interactions in LWR Blowdown Studies," 6th Water Reactor Safety Research Information Meeting (Washington, DC, November 1978). Copies of the film presented with this paper are available on loan from the author.

29. N. A. Fuchs, The Mechanics of Aerosols (Pergamon Press, New York, NY, 1964).

30. R. J. Brun, W. Lewis, P. J. Perkins, and J. S. Serafini, "Impingement of Cloud Droplets on a Cylinder and Procedure for Measuring Liquid-Water Content and Droplet Sizes in Supercooled Clouds by Rotating Multicylinder Method," National Advisory Committee for Aeronautics report NACA-1215 (1955).

31. G. C. Gardner, "External Water Separators; Performance of Knitted Wire Mesh and Corrugated Plate Separators," Chap. 7, Sec. 7.1 in Two-Phase Steam Flow in Turbines and Separators, M. J. Moore and C. H. Sieverding, Eds. (Hemisphere Publishing Co., Washington, DC, 1976).

32. D. A. Barnard, J. A. Ward, and P. B. Whalley, "A Preliminary Investigation of Two-Phase Flow Behavior Related to the Upper Plenum of a PWR," paper presented at the 6th Water Reactor Safety Research Information Meeting (Gaithersburg, MD, November 1978).

33. J. C. Dallman, W. L. Kirchner, and V. S. Starkovich, "De-Entrainment Phenomena from Droplet Cross Flow in Vertical Rod Bundles," American Nuclear Society Transactions 30, 381-384 (1978).

34. J. K. Dukowicz and T. D. Butler, "Status Report on Droplet Spray Modeling," Los Alamos Scientific Laboratory report LA-7567-PR (NUREG/CR-0522)(December 1978).

35. J. K. Dienes, C. W. Hirt, and L. R. Stein, "Computer Simulation of the Hydroelastic Response of a Pressurized Water Reactor to a Sudden Depressurization," Los Alamos Scientific Laboratory report LA-NUREG-6772-MS (1977).

36. "Design Response Spectra for Seismic Design of Nuclear Power Plants," U.S. Atomic Energy Commission Regulatory Guide 1.60, Rev. 1 (December 1973).

37. KFK Nachrichten Vol. 9, No. 2, 1977 Translation Series NUREG/TR-0038 (1977).

38. J. R. Travis, F. H. Harlow, and A. A. Amsden, "Numerical Calculation of Two-Phase Flows," Nuclear Science and Engineering 61, 1-10 (1976).

39. M. C. Yuen and L. W. Chen, "Heat Transfer Measurements of Evaporating Liquid Droplets," Intern. J. Heat Mass Transfer 21, 537 (1978).

40. W. C. Rivard, O. A. Farmer, T. D. Butler, and P. J. O'Rourke, "RICE: A Computer Program for Multicomponent Chemically Reactive Flows at All Speeds," Los Alamos Scientific Laboratory report LA-5812 (1975).

41. F. C. Prenger, "Optics Heat Pipe Test," Los Alamos Scientific Laboratory, private communication (July 1978).

42. F. C. Prenger, "Heat Pipe Thermal Control System for Stereographic Lens System," Los Alamos Scientific Laboratory, private communication (June 1978).

43. Ervin E. Underwood, Quantitative Stereology (Massachusetts, Addison-Wesley Publishers, New York, NY, 1970).

44. L. L. Smith, "SIMMER-II: A Computer Program for LMFBR Disrupted Core Analysis," Los Alamos Scientific Laboratory report LA-7515-M (NUREG/CR-0453)(1978).

45. A. Padilla, Jr., "High-Temperature Thermodynamic Properties of Sodium," Argonne National Laboratory report ANL-8095 (1974).

46. J. S. Rowlinson, Liquids and Liquid Mixtures (Plenum Press, New York, NY, 1969).

47. L. Leibowitz, "Update of Compilation of Sodium Properties," Reactor Development Program Progress Report, Argonne National Laboratory report ANL-RDP-74 (1978).

48. E. L. Wachspress, "Successive Overrelaxation," in Iterative Solution of Elliptic Systems (Prentice-Hall, New York, NY, 1966), Chap. 4.

49. L. A. Hageman, "The Estimation of Acceleration Parameters for the Chebyshev Polynominal and the Successive Overrelaxation Iteration Methods," Westinghouse report WAPD-TM-1038 (June 1972).

50. R. G. Steinke, "Optimum SIP Method Acceleration Parameters for the Neutron Diffusion Equation," Trans. Am. Nuc. Soc. 14, 206 (1971).

51. H. L. Stone, "Iterative Solution of Implicit Approximations of Multidimensional Partial Differential Equations," SIAM J. Num. Anal. 5, 3, p. 530 (1968).

52. G. Budkel, K. Kufner, and B. Stehle, "Benchmark Calculations for a Sodium-Cooled Breeder Reactor by Two- and Three-Dimensional Diffusion Methods," N.S.I.E. 64, 75-89 (1977).

53. Benchmark Problem Committee, "Argonne Code Center: Benchmark Problem Book" Argonne National Laboratory report ANL-7416, Supplement 2 (1978).

54. R. A. Hein, L. H. Sjodahl, and R. Szwarc, "Heat Content of Uranium Dioxide from 1200-3100 K," J. Nucl. Mater. 25, 99 (1968).

55. L. Leibowitz, L. W. Mishler, and M. G. Chasanov, "Enthalpy of Solid Uranium Dioxide from 2500 K to its Melting Point," J. Nucl. Mater. 29, 356 (1969).

56. C. Affortit and J. Marcon, "Chaleur Specifique a Haute Temperature des Oxydes d'Uranium et de Plutonium," Rev. Int. Hautes Temper. et Refract 7, 236 (1970).

57. R. Szwarc, "Defect Contribution to the Excess Enthalpy of Uranium-Dioxide - Calculation of the Frenkel Energy," J. Phys. Chem. Solids 30, 705 (1969).

58. D. A. MacInnes, "Electronic Contribution to the Thermodynamics of UO_2 - I. Specific Heat," Safety and Liability Dictorate, Culcheth, Cheshire, England (1978).

59. L. H. Aller, Astrophysics: The Atmospheres of the Sun and Stars (The Ronald Press Co., New York, NY, 1963).

60. D. R. Ferguson, "An Analysis of Transient Undercooling and Transient Overpower Accidents without Scram in the Clinch River Breeder Reactors," Argonne National Laboratory report ANL/RAS-75-29 (July 1975).

61. L. B. Luck, "Transient State Initialization of Quasistatic Neutronics Treatments," ANS 1978 Annual Meeting (San Diego, CA, June 1978).

62. C. R. Bell and J. E. Boudreau, "SIMMER-I Accident Consequence Calculations," ANS Trans. 27, 555 (1977).

63. P. E. Rexroth and A. J. Suo-Anttila, "An Analysis of SRI High Pressure Bubble Expansion Experiments," to be presented at the Specialists' Workshop on Predictive Analysis of Material Dynamics in LMFBR Safety Experiments (Los Alamos, NM, March 1979).

64. C. R. Bell, "SIMMER-II Analysis of LMFBR Postdisassembly Expansion," International Meeting on Nuclear Power Reactor Safety (Brussels, Belgium, October, 1978).

65. K. O. Reil, M. F. Young, and T. R. Schmidt, "Prompt Burst Energetics Experiments: Fresh Oxide/Sodium Series," Sandia Laboratories report SAND78-1561 (August 1978).

66. K. O. Reil, M. F. Young, W. J. Camp, and H. Plitz, "Prompt Burst Energetics Experiments: Uranium Carbide Series Preliminary Results," Sandia Laboratories report SAND78-0752 (1978).

67. M. F. Young, "Fuel Pin Modeling for the Prompt Burst Excursion (PBE) Experiments," Trans. Am. Nucl. Soc. 28, 489 (1978).

68. P. K. Mast, "The Los Alamos Failure Model (LAFM): A Code for the Prediction of LMFBR Fuel Pin Failure," Los Alamos Scientific Laboratory report LA-7161-MS (March 1978).

69. J. L. Straalsund, R. L. Fish, and C. D. Johnson, "Correlation of Transient-Test Data with Conventional Mechanical Properties Data," Nuc. Tech. 25, 531-540 (1975).

70. J. H. Scott and P. K. Mast, "Evaluation of the Effect of Shutdown Cracks in TREAT-Tested Fuel Pins," Trans. Am. Nucl. Soc. 27, 530 (1977).

71. P. K. Mast and J. H. Scott, "Fuel Pin Failure Models and Fuel-Failure Thresholds for Core Disruptive Accident Analysis," Int. Mtg. on Fast Reactor Safety and Related Physics, American Nuclear Society (Chicago, IL, October 1976).

72. P. K. Mast and J. H. Scott, "An Analysis of TOP Accidents in the FTR Using the Los Alamos Failure Model," Proc. ENS/ANS Topical Meeting on Nuclear Power Reactor Safety (Brussels, Belgium, October 1978).

73. R. D. Burns, III and J. H. Scott, "Statistical Analysis of Seventeen TREAT Experiments," Trans. Am. Nucl. Soc. 30, 463 (1978).

74. L. W. Deitrich, "Summary and Evaluation of Fuel Dynamics Transient-Overpower Experiments: Status 1974," Argonne National Laboratory report ANL-77-44 (June 1977).

75. R. L. Page, "Interim Report for TREAT Test H6," Argonne National Laboratory report ANL-RAS/78-44 (September 1978).

76. J. M. Cuttler, S Shalev, and Y. Dagan, "A High-Resolution, Fast-Neutron Spectrometer," Trans. Am. Nucl. Soc. 12, 63 (1969).

77. J. F. Jackson and M. G. Stevenson, "Nuclear Reactor Safety Quarterly Progress Report for the Period October 1-December 31, 1977," Los Alamos Scientific Laboratory report LA-7195-PR (April 1978).

78. W. L. Kirk, "HTGR Safety Research Program, April-June 1975," Los Alamos Scientific Laboratory report LA-6054-PR (September 1975).

79. W. F. Chen, H. Suzuki, and T. Y. Chang, "Analysis of Concrete Cylinder Structures under Hydrostatic Loading," Purdue University report CE-STR-78-2 (April 1978).

80. O. C. Zienkiewicz, The Finite Element Method (McGraw Hill, New York, NY, 1977), pp. 460-464.

☆U.S. Government Printing Office: 1979 – 627-013/91

Available from
US Nuclear Regulatory Commission
Washington, DC 20555

Available from
National Technical Information Service
Springfield, VA 22161

Microfiche	$ 3.00	126-150	7.25	251-275	10.75	376-400	13.00	501-525	15.25
001-025	4.00	151-175	8.00	276-300	11.00	401-425	13.25	526-550	15.50
026-050	4.50	176-200	9.00	301-325	11.75	426-450	14.00	551-575	16.25
051-075	5.25	201-225	9.25	326-350	12.00	451-475	14.50	576-600	16.50
076-100	6.00	226-250	9.50	351-375	12.50	476-500	15.00	601-up	-- 1
101-125	6.50								

1. Add $2.50 for each additional 100-page increment from 601 pages up.